DESIGN OF A HIGH SPECIFIC TORQUE INDUCTION MOTOR

A THESIS
SUBMITTED TO THE UNIVERSITY OF MANCHESTER
FOR THE DEGREE OF
DOCTOR OF PHILOSOPHY (PHD)
IN THE FACULTY OF ENGINEERING AND PHYSICAL SCIENCES

JOSE HERMILO CERON GUERRERO

SCHOOL OF ELECTRICAL & ELECTRONIC ENGINEERING
2015

CONTENTS

Final word count: 39661

LIST OF FIGURES

LIST OF TABLES

LIST OF ALGORITHMS

NOMENCLATURE

α_g	Gradient angle
α_τ	Heat transfer coefficient of unit frame surface (W/m^2K)
β	Parameter under analysis
δ	Input power factor angle
ΔR	Radius of an equivalent circle of the same cross sectional area as the coil
η	Machine efficiency
λ_{ei}	Geometrical permeance of end ring segment
λ_o^2	Ratio of the diameter of the airgap surface and the outer surface of the machine
μ_0	Magnetic permeability of free space ($4\pi \times 10^{-7} N/A^{-2}$)
ρ	End-ring material resistivity (Ωm)
σ	Electrical steel conductivity $(\Omega m)^{-1}$
τ_p	Pole pitch (m)
τ_{IM}	Thermal time constant of the induction motor (s)
ξ	Air density (kg/m^3)
A_{cu}	Area of copper per slot
A_c	Coil cross sectional area
A_T	Coefficient A in the torque equation
a	End-ring radial thickness (m)
A_i	End-ring cross-section (m^2)
A_v	Vehicle frontal area (m^2)
B_T	Coefficient B in the torque equation
b	End-ring axial width (m)
B	Magnetic loading (Wb/m^2)
B_m	Maximum flux density at the node concerned (T)
$\hat{B}_g$	Peak value of the sinusoidally distributed airgap flux density (T)
$\hat{B}_{cr}$	Peak rotor core flux density (T)
$\hat{B}_{cs}$	Peak stator core flux density (T)
$\hat{B}_{tr}$	Peak rotor tooth flux density (T)
$\hat{B}_{ts}$	Peak stator tooth flux density (T)
B_g	Peak value of the flux density in the airgap (T)

C_w	Aerodynamic drag coefficient
C_T	Coefficient C in the torque equation
D_{ir}	Average end-ring diameter (m)
D	Bore diameter (m)
D_T	Coefficient D in the torque equation
$d_{P_{TOT}}$	Core loss density (W/m^3)
D_o^2	Diameter of the outer surface of the machine (m)
D_f	Diameter of the stator frame (m)
d_t	Lamination sheet thickness (m)
D_r	Rotor outer diameter (m)
D_i	Stator bore (m)
E_T	Coefficient E in the torque equation
f	Frequency (Hz)
f_t	Tyre rolling resistance coefficient
G	Mass of the induction motor (kg)
g	The gravitation acceleration constant (9.81 m/s^2)
I_s	Stator current (A)
I_1	Stator line current
J_1	Current density (A/m^2)
k_e	Coefficient of excess loss $(W/(Ts^{-1})^{3/2}/m^3)$
k_h	Coefficient of hysteresis loss $(W.s/T^2/m^3)$
K_m	Coefficient to consider the increase of the frame surface due to its edges
k_{im}	Constant that includes machine geometry and wave-shape excitation variables
K_i	Current waveform factor
k_{d1}	Distribution factor
K_1	Electric loading (A/m)
K_e	Emf factor
K_p	Electrical power waveform factor
k_{p1}	Pitch factor
k_m	Rotational inertia coefficient
K_ϕ	Ratio of electric loadings on the rotor and the stator (A_r/A_s)
k	Skew factor
K_{el}	Specific electric loading (A/m)
k_{fill}	Slot filling factor
k_w	Winding factor
k_{wt}	Winding type constant
L_i	End-ring segment length (m)
L_{ew}	End winding inductance (H)
L_e	Effective stack length of the machine (m)
L_{ei}	Inductance of a end-ring segment (H)

L_f	Length of the stator frame (m)
L	Stack length (m)
l_{e2}	Straight portion of the end winding (m)
l_{ew}	Total perimeter of the end winding on one side (m)
m_v	Vehicle mass (kg)
n	Nominal rotor speed (RPM)
N_r	Number of rotor slots
N_s	Number of stator slots
N_{ph}	Number of series-connected conductors per phase
N_R	Number of rotor cage bars
n_s	Synchronous speed (RPM)
N_1	Turns per phase
p	Machine pole pairs
P	Number of poles
P_{jr}	Rotor copper losses (W)
P_R	Rated output of the machine (W)
P_{ir}	Stator iron losses (W)
P_{js}	Stator copper losses (W)
p_w	Winding pitch
q	Number of phases of the machine
q_1	Number of phases of each stator
q_1	Number of phases
q	Stator phases number
R_i	End-ring segment resistance (Ω)
S_1	Number of stator slots
$S_{T,\beta}$	Normalized sensitivity factor of the torque
T	Machine torque (Nm)
t_{wr}	Rotor tooth width (m)
T_{sr}	Stator/rotor turns ratio
t_{ws}	Stator tooth width (m)
v_0	Head-wind velocity (m/s)
V_1	Machine rated voltage (V)
V_s	rms applied phase voltage (V)
v	Vehicle speed (m/s)
X_{bar}	Rotor bar leakage reactance (H)
X_{diff}	Rotor differential leakage reactance (H)
X_{err}	Rotor end-ring leakage reactance (H)
X_1^{END}	Stator end-winding leakage reactance (H)
X_1^{SLOT}	Stator slot leakage reactance (H)
y_{cr}	Rotor core back depth (m)

y_{cs}	Stator core back depth (m)

ABSTRACT

Electric vehicles are a key technology in the reduction of our carbon footprint and this has motivated significant research interest. The electrical traction motor is one of the main areas of research in attempts to further improve electric vehicle performance. The permanent magnet motor is the predominant device in this application because of its high specific torque. However, it has suffered from market speculation in the raw magnet materials which has generated efforts to develop electrical machines which have a high specific torque and do not contain rare earth materials.

In the past the induction motor used to be the preferred motor for electric vehicles due to its low costs, low maintenance requirements, mature technology and robustness. The induction motor requires a higher specific torque to make it an alternative to permanent magnet machines. For this reason, this research had the primary aim of improving the specific torque of induction machines by undertaking a detailed review of the motor design because this process has conventionally focussed on the requirements for industrial applications.

The first stage of the work presented in this thesis consisted of identifying the designs already in use for this purpose and the potential technologies applicable to the induction motor that could be transferred from other electric traction machines. A full review of the design process was also conducted in order to identify the key areas of the process with special reference to the electromagnetic design which used finite element techniques as the main modelling tool.

New induction motor designs were developed which showed potential for improving the specific torque; two of these were selected for further refinement, prototyping and testing. Although these designs were modified to facilitate construction, some major difficulties were still encountered during the prototype rotor manufacture.

The test results were used to validate the design process and to identify further improvements in the designs. The issues encountered with the rotor manufacture prototype however lead to some overheating during the experimental testing. Comments about the design experience gained during this research are summarized including suggestions for further research.

DECLARATION

The University of Manchester
PhD by published work Candidate Declaration

Candidate Name: Jose Hermilo Ceron Guerrero

Faculty: Engineering and Physical Sciences

Thesis Title: Design of a High Specific Torque Induction Motor

Declaration to be completed by the candidate:

I declare that no portion of this work referred to in this thesis has been submitted in support of an application for another degree or qualification of this or any other university or other institute of learning.

Date: September 21, 2015

COPYRIGHT

[1]This excludes material already printed in academic journals, for which the copyright belongs to said journal and publisher. Pages for which the author does not own the copyright are numbered differently from the rest of the thesis.

DEDICATION

To my wife Elo and my son Benjamin.

Les agradezco su apoyo incondicional a lo largo de este proyecto, el cual no solo ha sido un paso en mi carrera sino tambien una experiencia para nuestra familia. Se que los cambios a los que se enfrentaron por acompañarme en este proceso no fueron faciles sobre todo por estar lejos del resto de nuestros familiares y nuestra tierra querida. Aun cuando no se que depara el futuro, me siento feliz de que continuaremos juntos en los nuevos proyectos que emerjan. No me queda nada mas que decir que los amo y adoro.

ACKNOWLEDGEMENTS

"There is a rule among living things that they shall conform. The blackbird with a white tail is killed by other blackbirds, or if he is lucky they just peck out the white feathers. This rule work on us too, and is possibly the greatest hindrance to our scientific progress. There is comfort in collectiveness."
Eric R Laithwaite

A young designer is like a child learning to walk, requiring a guide to giving the first steps into the science and art of electrical machinery design. Someone who shares his experience, knowledge and trust. I could not have a better guide than Professor Alexander C. Smith.

I want to thank the Federal Government of the Estados Unidos Mexicanos (the United Mexican States) for the financial support granted through scholarships from the Consejo Nacional de Ciencia y Tecnologia - CONACYT (the Mexican National Council for Science and Technology) and the Secretaria de Educacion Publica - SEP (the Mexican Ministry of Public Education).

I am sincerely grateful to Dr. Paul Tuohy for his invaluable support and advice during my research. I would also like to thank Dr. Edgar Peralta for his advice at the beginning of this project. My sincere thanks also goes to Dr. Gerardo Calderon, for his support and friendship. Thanks are also due to the mechanical workshop for building the prototypes used in this project.

The author is also grateful with all the free software community involved in the packages used in this thesis such as libreCAD, LaTeX and gnuplot.

Last but not the least, I would like to thank my parents, my family and friends in Mexico for their support, despite the distance.

THE AUTHOR

Jose Hermilo Ceron Guerrero received his BSc (Hons) and MSc (Hons) degrees in electrical engineering from the Instituto Politecnico Nacional - IPN (the Mexican National Polytechnic Institute) in 2008 and 2010 respectively. Since 2010, the author has been working in the research project described in this thesis. His main research interests include design, modelling, analysis, simulation and testing of electrical machines.

CHAPTER

ONE

INTRODUCTION

The induction motor is one of the major electromechanical power converters in use today. It offers reliability, simple construction, minimum maintenance requirements and low cost. Although, this electrical machine has been the predominant electric motor for fixed speed applications, the development of power electronics has expanded its use for variable speed applications.

Despite its advantages, the induction motor is considered the second best drive option for an electric vehicle because of its rotor copper losses and low harmonic requirements [1]. It has not been able to match the higher torque density of permanent magnet motors. However, researchers have shown renewed interest in reducing this performance gap in the face of the permanent magnets price speculation.

Mature technology is the main obstacle found and new design approaches are needed in order to improve induction motor torque densities.

1.1 Electric vehicles

Electric vehicles used in transportation employ electric propulsion with at least one electric motor coupled to the traction system in order to bring partial or full torque to the wheels. Electric vehicles appeared at the beginning of the 19th century and a lot of effort took place in their development until about 1930 [2]. However they were unable to offer an affordable means of transport across a wide range of travel.

Steam and later internal combustion engines on the other hand succeeded so that electric vehicles disappeared from the main market until the 1970s. It became necessary to find alternatives to fossil fuels due to concerns about carbon emissions and their sustainability in the long term. This vision produced a resurgence in electric vehicle research.

Current commercial hybrid vehicles are considered part of a transition to electric vehicles. On one hand, governments, institutions and individuals have realised the importance of the reduction of pollution because of the impact on global climate change. On the other hand, it is increasingly difficult to ignore the fact that internal combustion engine continues to be the main horsepower for ground vehicular transportation but at the expense of generating significant carbon footprint.

1.1.1 Key technologies

Figure 1.1 provides some clear examples of the key technologies and components inside electric vehicles. The electrical energy source, propulsion, body and energy management technologies are of crucial importance to the improvement of these means of transportation and there is a large interdependence between them [3].

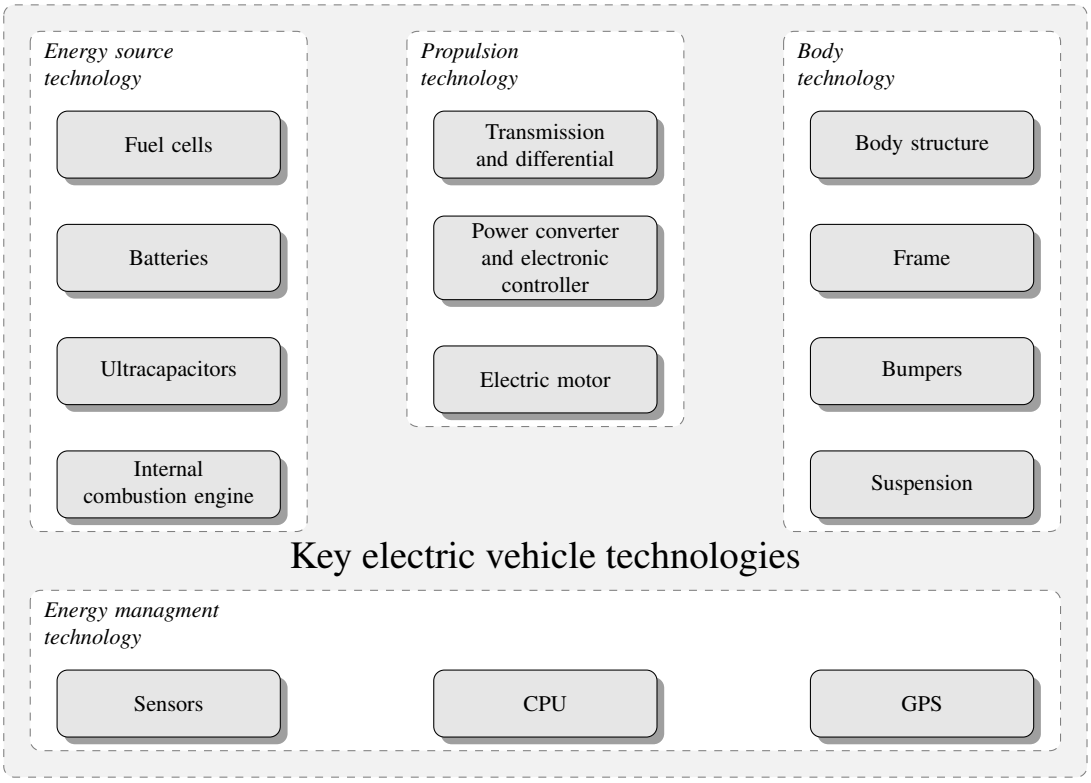

Figure 1.1: Some key technologies in electric vehicles

Electrical energy source technology involves power sources employed as batteries, fuel cells or ultracapacitors. This also considers the interaction and integration of the electric power sources with a fossil fuel engine. From the point of view of energy source technology, electrical vehicles can be classified into full electric or hybrid vehicles. Full electric vehicles obtain their power from batteries, fuel cells or ultracapacitors or a combination of them [4]. While hybrids make use of fossil fuels and the power from electrical energy storage which increases their efficiency [5].

Vehicle body technology is related to the mechanical structure of the vehicle; early electric vehicles did not receive much attention and many of them were constructed by adapting an internal combustion engine vehicle. Optimal chassis and body structure for an electric vehicle can only be done effectively by purpose-built design [3].

The propulsion system involves the interaction between electric motor, power converter and electronic controller as well as transmission and differential. Research efforts have focused on the best configuration which allows power transfer between the wheels and the motors with the best efficiency possible and low volume and weight. This has led to the tendency to integrate two or more components of the propulsion system into one single unit.

Maximising the available resources is fundamental in electric vehicles so that energy and management technology is crucial to make full use of all available energy resources.

1.1.2 Classification

Electric vehicles may be classified by their energy source: hybrid or full electric. This classification is the most commonly employed because this technology is one of the key issues for the propulsion system [5].

As shown in Figure 1.2, full electric propulsion may be divided into four basic topologies. Each one is described by a path following the arrows from the motor to the wheels. The longest path represents a converted vehicle where the internal combustion engine was replaced by the electric motor. This topology tends to be the heaviest and least efficient because it has more components. A second option involves changing the clutch-gearbox or automatic transmission by fixed gearing. The shortest path corresponds to a direct drive system and requires an electric motor with a high torque capability. The last topology is a drive where there is a fixed gearing between the wheels and the motor. The last two configurations require at least two drives to enable steering as they do not use a differential. If the whole powertrain is contained inside the wheel, it is normally denoted an in-wheel drive.

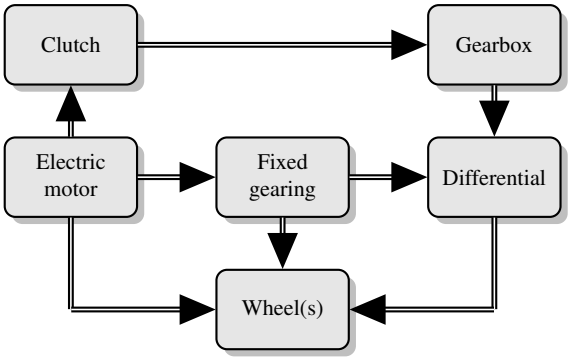

Figure 1.2: Powertrain topologies in full electric vehicles

Hybrid electric vehicles are subdivided further considering the extent of hybridization: micro, mild and full hybrids. A micro hybrid includes start/stop and regenerative braking technologies while a mild hybrid allows also the use of the electrical machine to temporarily boost propulsion. A full hybrid includes the operation modes mentioned previously but also permits the electric motor to provide full propulsion for the car [6].

As shown in Figure 1.3, the propulsion topologies in hybrid vehicles are classified based on the interaction between the traction electric motor and the internal combustion engine [5]. The most common these are [3]:

Series The mechanical output of the internal combustion engine is employed to produce electrical energy which feeds the traction electric motor or the energy storage system.

Parallel The motors only interact mechanically via the transmission system.

Series-Parallel Both machines are coupled to the transmission system and there is a generator driven by the internal combustion engine that provides energy support to the electrical system as in the series hybrid.

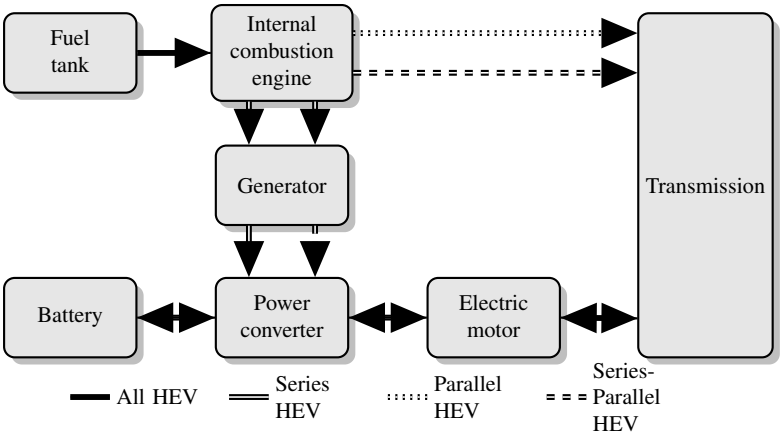

Figure 1.3: Powertrain topologies in hybrid electric vehicles

1.2 Traction requirements

The torque applied to the wheels needs to overcome the road load characteristics (F_{rlc}) when accelerating the vehicle [7]. This load is composed mainly of climbing resistance (F_{cr}), rolling resistance (F_{rr}) and aerodynamic drag (F_{ad}):

$$F_{rlc} = F_{cr} + F_{rr} + F_{ad} \tag{1.1}$$

The rolling resistance is related to the tyre deformation and is directly proportional to

the tyre rolling resistance coefficient (f_t), the vehicle mass (m_v) in kg and the gravitation acceleration constant ($g = 9.81m/s^2$):

$$F_{rr} = f_t m_v g cos(\alpha_g) \tag{1.2}$$

Another component of the road load characteristic, the climbing resistance represents the gravitational force over the electric vehicle. This resistance is also a function of the vehicle mass and gravity but it also includes the effect of the gradient angle (α_g) between the horizontal and the road.

$$F_{cr} = m_v g sin(\alpha_g) \tag{1.3}$$

The aerodynamic resistance represents the effect of turbulent and friction effects between air and the vehicle. This force is highly influenced by the vehicle speed (v) and the head-wind velocity(v_0), both in m/s. Other factors to calculate this resistance include the air density (ξ) in kg/m^3, the aerodynamic drag coefficient (C_w) and the vehicle frontal area (A_v) in m^2.

$$F_{ad} = 0.5 \xi C_w A_v (v + v_0)^2 \tag{1.4}$$

Both the climbing resistance and rolling resistance are considered constant in a basic analysis, while the aerodynamic drag is simply represented as a quadratic load [7], as shown in Figure 1.4.

The vehicle dynamics follows Newton's laws of motion and mechanics. The vehicle acceleration (a) varies directly proportional to the net force which is defined as the motive force available from the propulsion system (F) less the road load characteristic (F_{rlc}). The vehicle acceleration is also inversely proportional to the vehicle mass.

$$a = \frac{F - F_{rlc}}{k_m m} \tag{1.5}$$

where k_m is the rotational inertia coefficient [7].

If the change of gradient angle versus time and the acceleration profile, or the change of

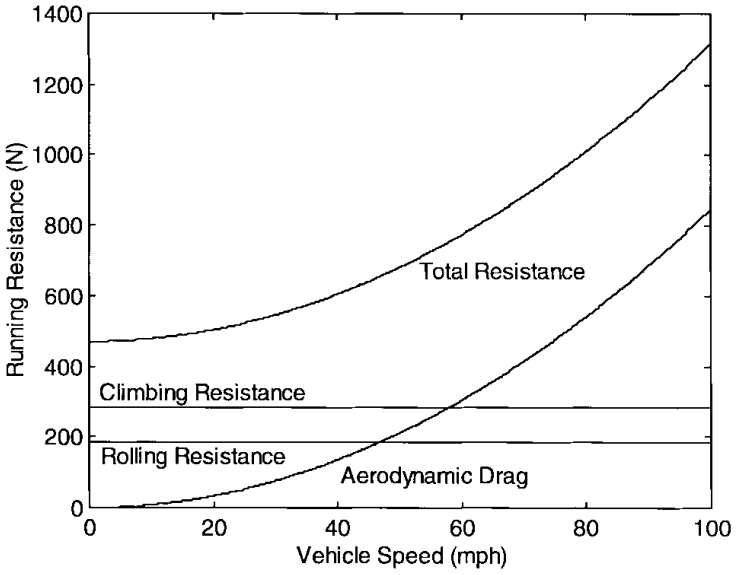

Figure 1.4: Typical road load characteristic [7]

speed versus time, during driving is known, it is possible to calculate the force F which has to be obtained from the propulsion system (Electrical or combustion engine). Historically drive cycles were used for emissions testing. A driving cycle is a benchmark for the evaluation of the performance of road vehicles. It contains a series of data representing the driving speed versus time profile for certain countries, regions or cities. The driving cycles also provide useful information about the traction requirements for a vehicle. Some of the more representative driving cycles are [8]:

US EPA FTP The Federal Test Procedure is issued by the US Environmental Protection Agency and is shown in Figure 1.5a. It is also known as the EPA75 and is based in the EPA Urban Dynamometer Driving Schedule (UDDS) which represents city driving conditions.

US EPA HWFET The Highway Fuel Economy Driving Schedule (HWFET) features highway driving conditions, Figure 1.5b.

European NEDC The New European Driving Cycle (NEDC), Figure 1.5c, compromises four Urban Driving Cycles and one Extra-Urban Driving Cycle.

Japan 10-15 Figure 1.5d presents this driving cycle which is in the Jisha Technical Standards. It represents the typical traffic flow of Japan and other Asia-Pacific cities.

The traction requirements for the electric motor are dictated by the drivetrain topology adopted. The maximum power requirement remains constant while the speed and the torque depend on the overall gear ratio in the transmission system. The maximum torque is usually limited in two drive regions as shown in Figure 1.6. The first region is represented by a constant torque from zero to base speed avoiding wheel slip. This is

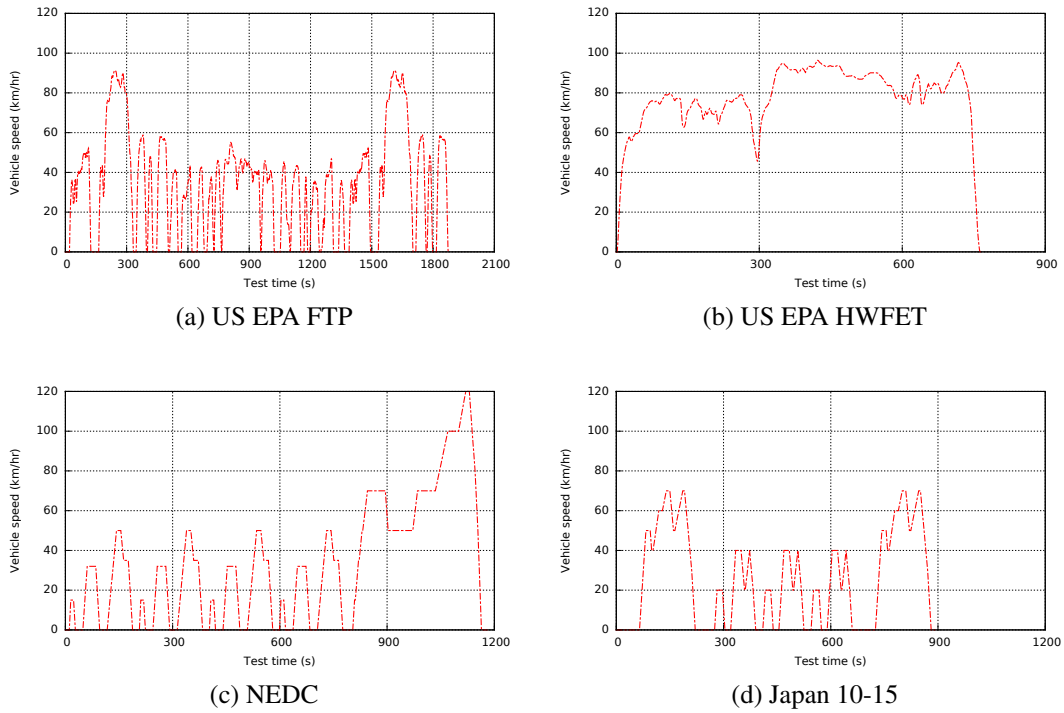

(a) US EPA FTP

(b) US EPA HWFET

(c) NEDC

(d) Japan 10-15

Figure 1.5: Driving cycles [8]

known as the constant torque region where the power varies linearly with the speed. The second region is known as constant power region and covers speeds above the base speed. The maximum power available is constant while the torque varies inversely with speed [7].

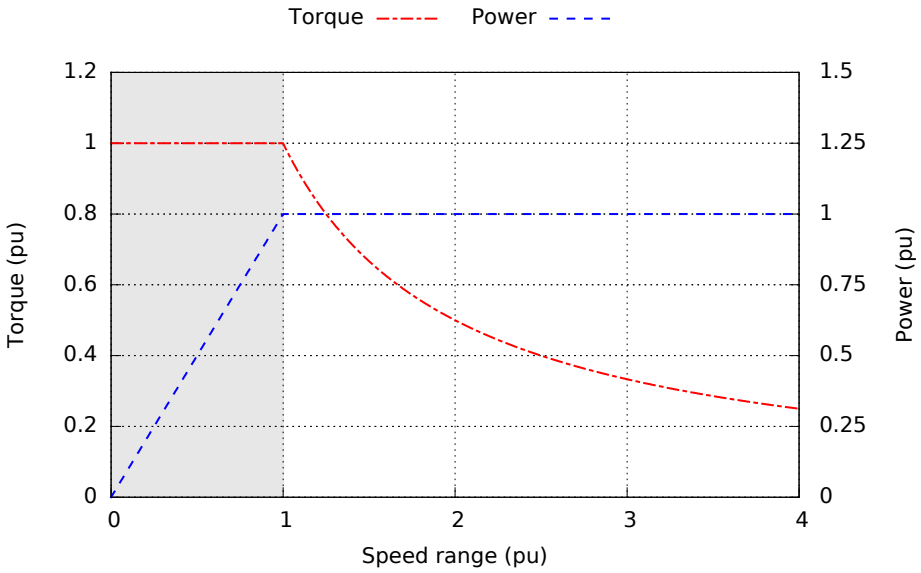

Figure 1.6: Torque and power requirements

The torque characteristic in Figure 1.6 represents the maximum requirements based on the corresponding driving cycle. The propulsion system would normally operate at lower torque levels most of the time. Nevertheless, these maximum requirements are directly proportional to the vehicle mass (Equation 1.5). In other words, minimization of the

vehicle mass would require a smaller motor which in turn would require a smaller power converter and power source system (Batteries, ultracapacitors, etc.). Minimization of the mass of all the components of an electric vehicle therefore is key in the vehicle design.

The values of maximum torque, base speed and maximum power requirements are calculated based on the initial acceleration and cruising at maximum vehicle speed [7]. In addition to these, the electric motor must be able to offer the following characteristics [3, 5]:

- High torque per unit of mass.
- High torque at low speed for starting and climbing.
- Wide speed range including constant torque and constant power regions.
- High efficiency over wide speed and torque ranges.
- High efficiency for regenerative braking.
- High reliability and robustness for various vehicle operating conditions.
- Reasonable cost.
- Low acoustic noise.

1.3 Electric motors

There are three main type of electric motors employed in electric vehicles: induction, synchronous permanent magnet and switched reluctance. All of them are ac machines but each one is based on different operating principles. Figure 1.7 shows typical structures of these to illustrate their differences clearly.

The comparison between different electrical machines is not straightforward. The advantages and weakness of each motor are well known and documented, the quantification of these is not a simple task. There are a large number of different qualities to take into account but the three most distinctive are specific torque/power, efficiency and speed range. It is important to note that torque and power density are considered together but they are not the same, this is clarified later in Section 1.5.

Each motor type has its own advantages and limitations. It is commonly considered that synchronous permanent magnet motors have the highest power/torque density and efficiency compared with the other two motor types [5]. However, their cost and efficiency at high speed are not as attractive. By contrast, the switched reluctance motor offers low cost and good performance at high speed but high torque density is not one of its virtues [5]. The induction motor offers a low cost, robust and reliable choice at the

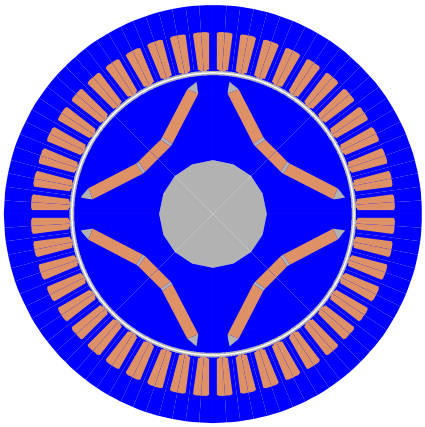

(a) Permanent magnet motor

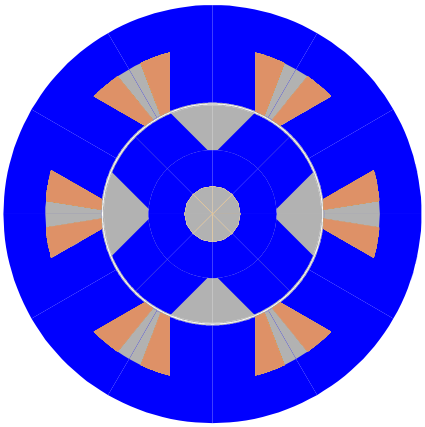

(b) Switched reluctance motor

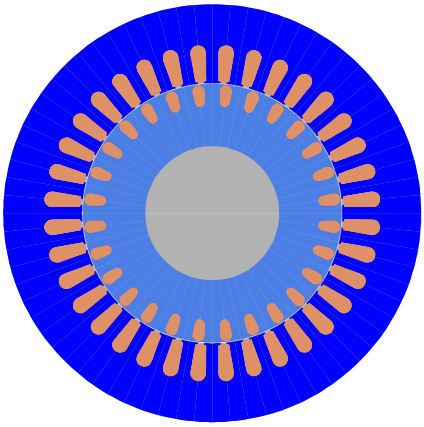

(c) Induction motor

Figure 1.7: Electric motors in electric vehicles

expense of the additional losses in the rotor cage and a lower torque density compared with the permanent magnet machine [5].

All these motors have comparable performance in terms of efficiency and speed range. They have expected efficiencies over 80 % for the whole operating range and they can achieve a wide speed range with the proper inverter and/or winding topology. However, the permanent magnet motor has a considerable advantage in terms of power/torque density [9] making it the main benchmark for comparison.

The sizing equation 1.6, which will be further analysed in Chapter 3, allows a designer to calculate the motor power for a given volume $D_o^2 L_e$ [10, 11]. It is employed to obtain the leading dimensions during the early design process. Although the dimensions obtained change during the design refinement, they allow one to obtain a fair comparison between all of these electrical motor types. The permanent magnet motor has the highest power density while the induction and switched reluctance have similar performances [10, 11].

$$P_R = \frac{1}{1+K_\phi}\frac{q}{q_1}\frac{\pi}{2}K_e K_i K_p \eta B_g K_{el}\frac{f}{p}\lambda_o^2 D_o^2 L_e \tag{1.6}$$

where

P_R - rated output of the machine (W)

K_ϕ - ratio of electric loadings of the rotor and the stator (A_r/A_s)

q - number of phases of the machine

q_1 - number of phases of each stator

K_e - emf factor

K_i - current waveform factor

K_p - electrical power waveform factor

η - machine efficiency

B_g - peak value of the flux density in the airgap (T)

K_{el} - total electric loading (A/m)

f - frequency (Hz)

p - machine pole pairs

λ_o^2 - ratio of the diameter of the airgap surface and the outer surface of the machine

D_o^2 - diameter of the outer surface of the machine (m)

L_e - effective stack length of the machine (m)

Equation 1.7 shows that the sizing equation can be also be presented in terms of torque [12]. This can be obtained from the previous equation using $P = \omega_r T$ and grouping the machine geometry and wave-shape excitation variables into a constant k_{im}. However, the same main components remain in the equation.

$$T = k_{im} K_{el} B D^2 L_e \tag{1.7}$$

where

T - machine torque (Nm)

k_{im} - a constant that includes machine geometry and wave-shape excitation variables

B - magnetic loading (Wb/m^2)

D - bore diameter (m)

It has been claimed in [12] using this equation that the torque density of a permanent magnet motor is about 2.3 times higher than the torque density of an induction machine for a given volume D^2L. This high torque density is mainly a consequence of the higher electric loading allowed in permanent magnet machines as they do not have to deal with the rotor copper losses. This result was obtained employing the values from Table 1.1 and assuming k_{im} has the same value for all the machines.

Table 1.1: Electric machine sizing [12]

Type	$B(Wb/m^2)$	$A(A_{rms}/m)@3min$	$A(A_{rms}/m)@30s$
Surface permanent magnet machine	0.82	6×10^4	8×10^4
Interior/inset permanent magnet machine	0.7	3×10^4	4.5×10^4
Induction machine	0.7	3×10^4	4.5×10^4
Variable/switched reluctance machine	0.8	3×10^4	4.5×10^4

Investigators have proposed the use of hybrid motors which integrate a combination of two or more types of electric machines [13]. The purpose is to overcome the disadvantages of each type at the expense of complex manufacture, higher costs and design requiring 3D finite element models in many cases [14]. Their equivalent circuits also become more complicated as they include more components and excitation sources [15].

The interest in hybrid motors surged as a result of the volatile material cost of permanent magnets. For this reason, most of them have permanent magnets combined with wound excitation or reluctance torques [16]. The integration of induction and permanent magnet motors is less common except as a low cost solution for line-start synchronous machines [13].

1.3.1 Induction motors for electric vehicles

Table 1.2 presents 25 different projects using induction motors for electric vehicles. All of them are part of the traction system for light ground road electric vehicles and have been designed specifically for this application. They have been ordered chronologically based on the year of the first relevant publication and labelled with the IM(Induction motor) prefix.

In sixteen of these projects a prototype was constructed whereas only nine do not report on any motor built until now. The prototypes were used to validate the design process.

Table 1.2: Induction motors in electric vehicles

Case No.	Prototype	Institutions	Countries	Years	References
IM1	Yes	General Electric Co	USA	1985	[17]
IM2	Yes	Westinghouse Motor Company Ltd.	Canada	1994	[18]
IM3	No	University of Sheffield	UK	1995	[19]
IM4	Yes	University of Rome	Italy	1995	[20]
IM5	Yes	Yokohama National University, Toshiba Corporation, Yaskaga Electric Mfg. Co	Japan	1996	[21]
IM6	No	Politecnico di Torino, Universita di Bologna	Italy	1996	[22]
IM7	Yes	Meidensha Corporation	Japan	1997	[23]
IM8	Yes	Ford Motor Co, McCleer Power Inc, Massachusetts Institute of Technology	USA	1998	[24]
IM9	Yes	Politecnico di Torino	Italy	1999	[25]
IM10	No	University of Tehran, University of Tabriz, The Ohio State University	Iran, USA	2000-2006	[26, 27]
IM11	No	Seoul National University, Dong-Eui University	Korea	2001	[28]
IM12	Yes	Darmstadt University of Technology	Germany	2006	[29]
IM13	Yes	Harbin Institute of Technology, FAW	China	2006	[30, 31]

Continued on next page

Table 1.2 – continued from previous page

Case No.	Prototype	Institutions	Countries	Years	References
IM14	Yes	Beijing Jiaotong University	China	2007	[32]
IM15	Yes	Traktionssysteme Austria GmbH, Technische Universität Darmstadt, Daimler Chrysler AG	Germany, Austria	2007-2008	[33, 34]
IM16	Yes	Central Calcutta Polytechnic, Jadavpur University	India	2008	[35]
IM17	Yes	Harbin University of Science and Technology, Harbin Institute of Technology	China	2008-2010	[36, 37]
IM18	No	University of Texas at Austin, TECO-Westinghouse Motor Company	USA	2009	[38]
IM19	No	University of Technology Sidney, Motor Design Ltd, University of Alberta, Glyndwr University	Australia, Canada, UK	2010-2012	[39–42]
IM20	Yes	Korea Institute of Industrial Technology, Suncheon First College, SRC Ltd	Korea	2012	[43]
IM21	No	Politecnico di Torino	Italy	2012	[44]
IM22	Yes	General Motors Company	USA	2012	[45]
IM23	Yes	Kyoto University, IMRA Material R&D Co., Research Institute for Applied Sciences, AISIN SEIKI Co.	Japan	2012	[46]
IM24	No	Sfax Engineering National School	Tunisia	2013	[47]
IM25	No	Central Mechanical Engineering Research Institute	India	2013	[48]

During the design phase, a lot of calculations and refinements took place to obtain the best possible design. However, the design process relies on a series of models which can only be validated when a prototype is built and tested.

Universities and research institutes have been involved in most of the projects (21) with eight having direct collaboration with industry. The remaining four projects have been developed by companies as the main participants. This confirms the research interest on this topic from both educational and commercial organizations including strong elements collaboration.

A total of 44 institutions, 28 universities/research institutes and 16 companies, have participated in these 25 projects. Most institutions have not been involved in more than one project with the exception of the Politecnico di Torino, the Westinghouse Motor Company and Harbin Institute of Technology which appear in 3, 2 and 2 projects respectively. The institutions come from 13 countries with the majority from Asia and Europe. However most of the projects (5) were developed in the USA. Collaboration between institutions from different countries on the other hand has been rare.

This research covers induction motor projects from 1985 to 2013. Although the time span covers almost three decades, most of the references have been published in the last one. This highlights the renewed interest in induction motors for electric traction applications.

1.3.2 Induction motor characteristics for electric vehicles

Each electrical machine produces a series of characteristics which define it. Some are dictated by its application requirements such as power, speed and torque, while others are restricted by the supply, including voltage, frequency and phases. Some are defined by the operating point of the machine, for example power factor and efficiency. The list is large and all of them are relevant during the design process. Table 1.3 illustrates some of the important characteristics of induction motors used in electric vehicles. Some values are empty because they were not available in the references or were in graphical form which makes it difficult to define a single value. Some references also presented multiple designs but only the one with best performance (Highest torque) is considered.

The first column identifies the vehicle type for which it was designed. Most of them were designed for a generic electric vehicle application. Some however were developed for very specific vehicles, IM18 for example is for a plug-in hybrid electric vehicle.

An algorithm base design code, called VICA, was employed to design IM18, a high speed induction motor at the University of Texas and TECO-Westinghouse [38]. A 100 kW peak-power water-glycol cooled machine was developed to fulfil the stringent requirements of a plug-in hybrid vehicle. The objective was to build a motor weighing 72 kg maximum, using a special aluminium housing with serpentine cooling channels

Table 1.3: Induction motors in electric vehicles

Case No.	Vehicle type	Voltage [V]	Power [kW]	Torque [Nm]	Speed [RPM]	Efficiency [%]	Power factor	Poles No.	Phases No.	Specific torque [Nm/kg]
IM1	EV	115.4	37.3	-	3800	>90	>0.85	2	3	0.95
IM2	EV	115	74.6	-	-	-	-	4	3	-
IM3	Converted EV	-	26	-	2000	-	0.81	6	3	-
IM4	EV		20	-	-	-	-	16	3	-
IM5	EV	60	0.75	-	1500	-	-	4	-	-
IM6	EV	63	17.5	55	3000	77	0.76	4	3	1.63
IM7	EV	150	45	-	2500	-	-	8/4	6	-
IM8	HEV	320	8	100	750	>80	-	12	3	4.92
IM9	HEV	-	4	-	1200	-	-	12	3	-
IM10	EV	96	11.19	-	1800	85.07	0.853	2	3	1.61
IM11	EV	170	15	-	3000	93	>0.8	4	3	1.33
IM12	EV	100	9	10.9	7867	-	-	4	-	0.62
IM13	HEV	-	40	106	3600	86	-	-	-	-
IM14	EV	200	40	129.13	2967	93.94	0.7992	4	3	-

Continued on next page

Table 1.3 – continued from previous page

Case No.	Vehicle type	Voltage [V]	Power [kW]	Torque [Nm]	Speed [RPM]	Efficiency [%]	Power factor	Poles No.	Phases No.	Specific torque [Nm/kg]
IM15	EV	-	8.2	-	2000	-	-	-	-	-
IM16	EV	-	-	-	-	-	-	4	3	-
IM17	PHEV	-	-	-	-	-	-	2	3	-
IM18	PHEV	200	50	-	4800	91.9	-	4	-	1.21
IM19	HEV	350	-	293	1475	95.2	0.68	8	3	8.08
IM20	EV	48	1.2	11.6	990	82.2	-	16	-	1.76
IM21	EV	173pk	50	110	4000	-	-	4	3	-
IM22	HEV	-	15pk	60pk	-	-	-	8	-	-
IM23	EV	-	20	-	1200	>92.3	-	8	3	-
IM24	EV	128	4.416	-	-	80	-	4	3	-
IM25	EV	34	3.5	23	1450	86	0.85	4	3	0.66

and a hollow shaft. Researchers reported that the prototype exceeded the weight limit and suggested the use of an aluminium rotor cage instead of the copper one used.

The machines presented have different voltage supplies ranging from 34 to 350 V. These values depend heavily on the battery or fuel cell technology employed. Despite some effort, it is clear that there is no a standard supply voltage. The voltage strategy also changes during operation in some cases affecting the design, for example in IM6.

Four design proposals are presented by researchers at the Torino Polytechnic and the University of Bologna [22]. They considered the power supply operating in PWM mode with a field oriented controller [22]. However all the designs were based and optimised for a voltage strategy which regulates the voltage supply even in the constant power operation region. Minimum active material weight was chosen as the objective function in a design process divided in two stages focusing on magnetic and electric circuits respectively.

The next column details the power rating. This is the power provided by the motor continuously at the base speed unless otherwise specified. The machines reviewed in this section range from 0.75 kW to 74.6 kW. The motors however with ratings under 10 kW are usually prototypes for validating a concept or the design process at reduced cost. After this preliminary validation, higher power versions were be built in order to drive an electric vehicle.

This is the case in IM11 developed by the Seoul National University and the Dong-Eui University [28]. Researchers employed a genetic algorithm called a new niching genetic algorithm to optimize the design of the induction motor for an electric vehicle [28]. Authors argued that this method is suitable in finding alternative optimal values based on different criteria specified by the designer. The optimization consisted of three stages. The first stage developed the basic motor topology and the selection of the optimization variables and constraints. The second stage covered the search for multiple optimal solutions using the proposed algorithm. The final stage selected the best motor design based on efficiency, power factor, stator winding temperature and material cost.

Power, torque and speed ratings are closely linked ($P = \omega_r T$) and are determined from the specified vehicle performance. Typical values of base speed at the wheel range from 300 RPM to 600 RPM. The use of a gearbox or a torque converter however allows a more convenient speed range for the power drive in terms of power density. This has been exploited in order to match with most common industrial fixed speeds; 14 of the projects use this.

One of the examples, IM3, was developed at the University of Sheffield. Researchers designed a three-phase induction machine with the capability of driving a Fiat Cinquecento [19]. The drivetrain consisted in a fixed ratio gearbox and a differential. A PWM inverter and six poles were selected, while minimization of the summation of harmonic winding factors divided by the harmonic numbers was employed as a criteria

for harmonic content reduction. During this iterative design process, the performance of the machine was evaluated using the conventional harmonic equivalent circuit. The researchers attempted to limit the leakage inductance because of the required wide speed range. They considered the modification of slot openings, airgap width and skew as ways of reducing the leakage reactances.

All the motors analysed have efficiencies over 77 % and power factors over 0.68. Efficiency affects the fuel consumption, whilst power factor influences the converter VA rating. None of these motors had a power factor over 0.9. The motor with one of the highest efficiency, IM14, also had one of the lowest power factors.

IM14 was developed at Beijing Jiaotong University employing design software, taking the design specifications in terms of geometry constraints, supply characteristics, required static and dynamic performances [32]. The software generated an optimal machine geometry employing a modified magnetic equivalent circuit and dynamic simulator as tools for optimization. During the dynamic simulation the effect of the control strategy was also considered.

15 of the machines analysed had 2, 4 or 6 poles which is also very common in industrial motors. The rest had 8, 12, 16 or no specified poles. Only one of the machines, IM7, allows pole changing with an 8/4 pole combination.

Meidensha Corporation developed a six-phase 4-8 pole-change induction motor (IM7) for electric cars [23]. This design attempts to obtain a wide speed range operation using a pole changing technique. The machine was controlled to operate in 8-pole mode during constant torque region and part of the constant power region and then changed to operate in 4-pole mode in order to extend the constant power operating region. The pole changing motor was employed to drive a prototype developed from a modified fossil fuel engine vehicle.

Nearly all of the machines are three phase machines which is standard in industry. Only one machine (IM7) had a different number of phases (six).

The last column of Table 1.3 corresponds to the specific torque for the cases where sufficient data was available. These specific torque values vary significantly and it is difficult to compare them objectively because there is no common benchmark. For example, the IM8 machines have one of the highest specific torque values but this is due to the high aspect ratio (a permanent magnet motor with the same aspect ratio would still have a higher specific torque). This design approach was not adopted here because the design methodology would require detailed end winding modelling and this would sensibly require full 3D modelling. Other researchers however have been exploring this design strategy, for example in [49]. Another example, the IM19 motor has the highest specific torque in part because of the high electrical loading which is possible due to a special cooling system [39, 40]. However, there is no prototype of this machine and also

transient simulations are necessary to validate the results. It will be shown later in this research that steady state simulations can neglect some important interactions between the stator and rotor which can lead to some misleading results.

1.3.3 Induction motor construction for electric vehicles

While the previous section focuses on the performance characteristics, this analyses some of the important constructional attributes of these machines in electric vehicles. Table 1.4 provides some data about the stator, rotor and cooling strategies.

Most of these induction motors are radial flux machines with the exception of one (IM4). This might be attributed to two reasons. First, the construction of axial machines is not standard which makes it more difficult and sometimes also more expensive to manufacture [50]. The other reason involves the design process. For example, some calculations in axial machines can not be simplified to a 2D analysis and require 3D simulations [51]. This 3D modelling can be avoided using an equivalent radial flux machine but it is not straightforward.

Researchers from the University of Rome (IM4) proposed the use of a differential double rotor machine with axial flux [20]. The rotor slots in this machine were skewed. The gearbox and differential are not necessary because each rotor is mechanically independent. In order to reduce costs, the prototype was produced by milling instead of progressive punching iron tape and open slots were employed. Although the prototype was built, no experimental results were presented in [20].

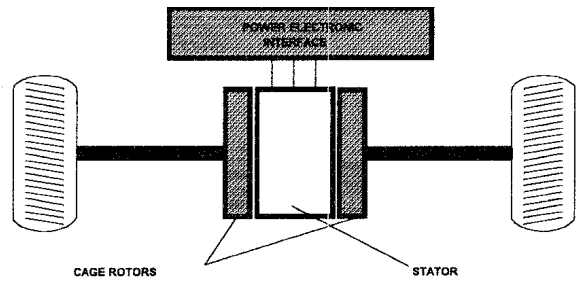

Figure 1.8: Differential double rotor motor [20]

The slot combination of the stator and rotor is one of the constructional features which affects the overall machine performance. The slot combination defines many of the harmonics present in the flux distribution. This has an important role in the useful torque produced. 48, 36 and 24 are the most common stator slot numbers in low power machines and is used in 5, 3 and 3 of these machines respectively. On the rotor, 38 and 53 are the most frequent slot numbers with 3 and 2 occurrences of each. 48/53 is the only repeated slot combination.

IM19 is one of the machines employing this slot combination. The traction motor for the

Table 1.4: Induction motors in electric vehicles

Case No.	Flux direction	Stator slots	Rotor slots	Stator core	Rotor core	Stator winding	Rotor winding	Cooling fluid
IM1	Radial	-	-	Conventional	Conventional	Conventional	Conventional	Transmission liquid
IM2	Radial	48	59	Conventional	Conventional	Diecast copper conductors	Copper squirrel cage	-
IM3	Radial	45	38 tapered	Conventional	Conventional	Conventional double layer	Copper squirrel cage	-
IM4	Axial	48	53/53 Differential rotors	Toroidally wound iron tape	Toroidally wound iron tape	Toroidal	Copper squirrel cage	Water
IM5	Radial	-	-	Rotary stator with slip rings	Differential	Conventional	Conventional	-
IM6	Radial	36	30	Conventional	Conventional	Conventional	Conventional	Water
IM7	Radial	-	-	Conventional	Conventional	6 phase pole changing windings	Conventional	-
IM8	Radial	-	-	Conventional	Conventional	Conventional	Conventional	Water
IM9	Radial	-	-	Conventional	Conventional	Conventional	Conventional	-
IM10	Radial	18	13	Conventional	Conventional	Conventional	Conventional	-

Continued on next page

Table 1.4 – continued from previous page

Case No.	Flux direction	Stator slots	Rotor slots	Stator core	Rotor core	Stator winding	Rotor winding	Cooling fluid
IM11	Radial	-	-	Conventional	Conventional	Conventional	Conventional	-
IM12	Radial	-	-	Conventional with cooling jacket	Conventional	Conventional with heat conductive resin	Copper squirrel cage	Water
IM13	Radial	-	-	Conventional	Conventional	Conventional	Conventional	-
IM14	Radial	36	33	Conventional	Conventional	Conventional	Copper squirrel cage	-
IM15	Radial	-	-	Conventional	Conventional	Conventional	Conventional	Water-Glycol
IM16	Radial	-	- Differential rotors	Conventional	Conventional	Conventional	Conventional	-
IM17	Radial	24	20	Conventional	Conventional	Conventional	Compound cage	-
IM18	Radial	48	38	Conventional	Conventional	Conventional	Conventional	Water-Glycol
IM19	Radial	48	53	Conventional	Conventional	Conventional	Copper squirrel cage	Water
IM20	Radial	90	124	Inner stator	Outer rotor	Conventional	Cage with reduced air porosity	-

Continued on next page

Table 1.4 – continued from previous page

Case No.	Flux direction	Stator slots	Rotor slots	Stator core	Rotor core	Stator winding	Rotor winding	Cooling fluid
IM21	Radial	48	40	Conventional	Conventional	Conventional	Conventional	Water
IM22	Radial	72	56	Conventional	Conventional	Bar winding	Conventional	-
IM23	Radial	24	38	Conventional	Conventional	High temperature superconductor	High temperature superconductor	Liquid nitrogen
IM24	Radial	24	40	Conventional	Conventional	Conventional	Conventional	-
IM25	Radial	36	24	Conventional	Conventional	Conventional	Conventional	-

2004 Toyota Prius electric vehicle was employed as the base for designing this induction machine [39]. The target was to keep the same performance at the same volume. The electric motor of the Toyota Prius hybrid vehicle is a permanent magnet synchronous motor with excellent performance. The development of a competitor for this machine represents a difficult task undertaken by researchers from the University of Technology Sydney, Motor Design Ltd and the University of Alberta [39, 40]. SPEED and Motorcad were the software employed. Although the same external dimensions were maintained, the performance was lower particularly during low speed operation. Similar results were also obtained for a switched reluctance motor redesigned from the Toyota Prius electrical motor [41]. Researchers however discovered that both machines could meet the desired performance after a careful refinement redesign process.

Conventional stator and rotor designs are the most common in these machines. A conventional machine has a construction similar to a typical industrial induction motor. Stator and rotor cores are composed of silicon-iron laminations with standard slot shapes. The stator windings are composed of random wound coils using magnet wire and the rotor has a die-cast aluminium squirrel cage.

An example of a conventional induction machine is IM8 described in [24]. The Ford Motor Co., McCleer Power Inc. and Massachusetts Institute of Technology presented a comparison between induction and variable reluctance machines and drives suitable for a starter-alternator in a hybrid vehicle [24]. For that application, one prototype of each machine type was designed, constructed and tested under the same specifications. Grouping coils was proposed so that they could be connected in series for starting and in parallel for generating, but it was not recommended due to space limitations. It was reported that the induction machine had a higher average thermal duty cycle than the variable reluctance machine while the variable reluctance machine had significant advantages for vehicle packaging and low rotor inertia. During balancing of the rotor for both machines, they were machined resulting in larger airgaps, so both rotors had to be rebuilt.

Only three machines present a non-conventional construction of the stator and rotor cores. The first, IM4, has cores wound toroidally using iron tape; it is the only axial flux motor included in these examples. The others, IM5 and IM20, employs standard silicon iron laminations. However, the IM5 stator was allowed to rotate with the use of slip rings while IM20 stator was located inside the rotor.

Researchers from the Yokohama National University, Toshiba Corporation and Yaskawa Electric Mfg. Co. developed IM5, a twin rotary motor [21]. Figure 1.9 illustrates this machine which was inspired by a three-phase four-pole high speed servomotor. The difference was that the stator became an outer rotor fed through slip rings. That machine avoided the use of a differential and a gearbox so that the outer and inner rotors were connected to each wheel. During stable operation, torque balance occurred between both

rotors producing the same behaviour as a conventional machine.

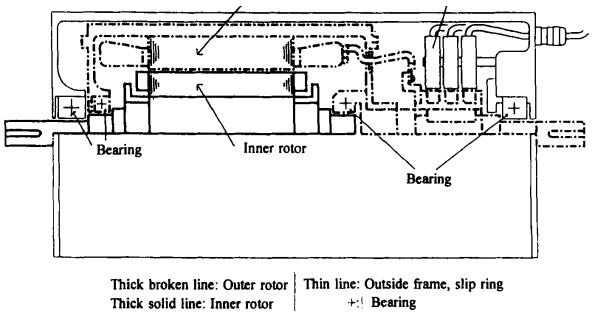

Figure 1.9: Twin rotary motor [21]

On the other hand, IM20 was an outer rotor induction motor with cage porosity reduced using a compression technique for casting [43]. It involved collaboration between the Korea Institute of Industrial Technology, Suncheon First College and SRC Ltd. Air porosity in the cage was reduced from 3.46 % to 0.81% enabling it to achieve a power density of 0.53 kW/kg.

There are more unconventional approaches in the windings than in the magnetic cores of the machines. Six motors have unconventional stator windings: toroidal, pole changing, conductive resin, bar, high temperature superconducting and die-cast copper. On the other hand, nine machines present a non standard industrial rotor cage. Six of them employ a copper squirrel cage. The remaining machines use a special compression technique during die-casting in order to reduce porosity and thus increase the conductivity or a high temperature superconducting cage.

IM23 was an induction machine designed for electric vehicles with both stator and rotor windings made of a high temperature superconducting material. Figure 1.10 shows the geometry of this device and its windings. Although this machine was cooled in a bulky cryostat with liquid nitrogen, researchers expected to reduce its size in future work [46]. The first part of the experimental results showed a higher torque density but a full test at nominal speed (1200 RPM) remains pending [46].

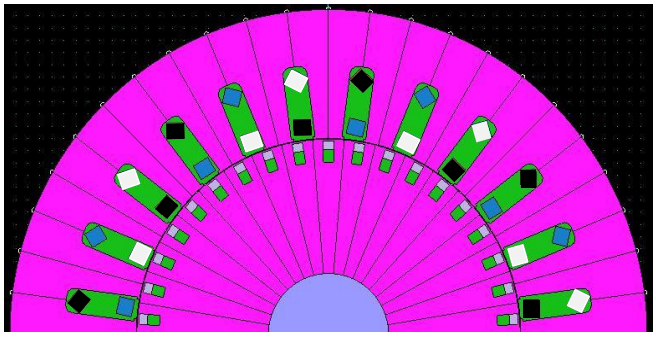

Figure 1.10: High temperature superconducting induction machine [46] (Magnetic cores are shown in pink; stator phases are shown in black, blue and white; and the superconducting cage is shown in grey.)

Finally, ten of these machines employ a liquid as a cooling fluid of which water and water-glycol are the most common. IM1 motor utilizes fluid in the transmission where it is contained. IM23 employs liquid nitrogen into a cryostat. Most of the remaining machines do not report the cooling fluid employed.

Induction motor (IM1) was developed as part of the Ford Company and General Electric Company Advanced Electric Power Train Program [17]. It employs an automatic shifting multi-speed transmission and a differential. Motor control was operated in pulse-width modulation (PWM) during the constant torque region and in six-step square wave mode during the power constant region. The motor was designed to be hermetically sealed in order to operate inside the car transmission. It was thus cooled by the automatic transmission fluid. A two pole winding was chosen because of the power factor and inverter requirements. Normally four-pole motors offer a better torque per unit volume. The authors tried to minimize the leakage inductance so that the desired pull-out torque could be achieved, however that was limited by harmonic currents.

1.3.4 Design methods for induction motors in electric vehicles

Each of the motor projects represents an effort to find a suitable propulsion motor for electric vehicles. Each one adopted a different design strategy for this application. Most of the design approaches can be classified into 4 categories based on the sizing equations 1.6 and 1.7. These 4 groups correspond to the 4 basic variables to which the machine power is proportional to for a given volume.

1.3.5 Machine geometry and wave-shape design approach

The machine geometry and wave-shape approach groups represent the designs where the focus is on the increase of k_{im} from Equation 1.7 or any of K_{ϕ}^{-1},K_e, K_i, K_p from Equation 1.6. This can be achieved by reducing the airgap flux harmonics, and employing a particular flux wave-shape with higher fundamental, among other techniques.

One of these approaches (IM10) was developed at the University of Tehran, the University of Tabriz and the Ohio State University [26, 27]. They suggested the use of a direct method for optimization of rotating electrical machines due to the large number of variables involved in the design process [26, 27]. Initially, rated power, peak speed, rated and peak torques were determined based on the expected performance of the vehicle. They then studied the influence of the pole number, base speed and slot shapes on the performance. Finally, the direct method was employed to determine the optimal design.

Another design strategy can be found in [30] and [31]. IM13 was developed for the propulsion system of a FAW hybrid vehicle at the Harbin Institute of Technology [30, 31]. A wide speed range operation was required, so the authors focused their efforts in reducing the leakage reactances and losses. This led them to study the specific effects of employing rectangular, trapezoidal or rectangular with inclined shoulder geometries rotor slots. Rectangular rotor slots were adopted because they found that this produced the lowest leakage and highest torque for the same slot area.

Other research has looked further into the relationship between torque ripple and the shape at the top and bottom of trapezoidal slots [47]. Two top and bottom topologies were compared, one rounded and the other straight. A trapezoidal slot with a rounded top and bottom was selected for IM24 because its torque ripple was 40.8 % lower.

The design process is different in each of the previous examples and it could also change during implementation. However, each designer attempts to define a procedure to refine and/or optimize. Reference [48] presents a detailed design algorithm for an induction motor for electric vehicles. It was implemented to design IM25 using Matlab. It was then refined with finite element simulations using the JMAG Designer software.

1.3.6 Electric loading design approach

Electric loading can be defined as the maximum continuous current in the machine without overheating. Some design approaches improve this to increase the torque. Some strategies for this include the use of thermally conductive resins, liquid cooling systems and improvement in the slot fill factor.

The design of IM15 is an example of this approach [33, 34]. Its water-glycol cooling system was fundamental to producing the required performance. This machine was part of a joint project between Traktionssysteme Austria GmbH, Technische Universität Darmstadt and Daimler Chrysler [33, 34]. The machine was designed considering the same electric powertrain (converter, batteries and ultracapacitors) and passive elements (housing and cooling).

The water cooling in IM21 was also fundamental in improving the electric loading [44]. Although the torque rating was achieved, this and the previous example were unable to deliver constant power over the base speed.

Improving the slot fill factor is another method for increasing the electric loading. It was done in IM22 using stator bar windings [45]. This project, from General Motors Company, also exploited some the advantages of induction machines such as low core losses at high speed, wider switching frequency range (low pole number) and higher transient overloading. However, stator eddy currents had to be taken into account during the design process.

Another method consists of using conductors composed of different materials. IM17 has a double cage rotor which looks to exploit the characteristics of a solid rotor [36, 37]. Each slot contained a two-section conductor. The top was composed of a magnetically and electrically conducting alloy whilst the bottom was made of aluminium. This design targeted a high torque and low current at starting.

1.3.7 Magnetic loading design approach

Magnetic loading is the average flux density over a magnetic pole. It is limited by the core material and its magnetic saturation. The use of cobalt iron laminations offers an option for increasing the magnetic loading but this solution is usually too expensive for electric vehicles.

Sometimes the best option was to test different laminations and geometries in order to find which offers the highest flux density in the airgap. IM2 was designed using this method [18]. It was developed by the Westinghouse Motor Company [18]. However, only an improvement of 1.2 % in efficiency was achieved.

1.3.8 Speed range design approach

Motor design can benefit from a high base speed in order to improve the power density. An example of this strategy allowed the development of the IM12 OSCAR electric vehicle motor [29]. In order to increase the power density, a high speed induction motor was proposed at the Darmstadt University of Technology [29]. It had to drive a lightweight electric vehicle named OSCAR, designed by AKASOL e.V. in Darmstadt [29]. This machine was coupled by an automatic two speed shifting gearbox because of difficulties matching the torque and power required outputs. The proposed high speed machine with two speed transmission (up to 22720 RPM) was compared with another motor with a high speed fixed ratio transmission (up to 18725 RPM) and a conventional air cooled induction machine (up to 13000 RPM). The performance of the three drives were compared under different drive cycles. Researchers concluded that the high speed induction motor with the two speed transmission had the best performance. An unconventional cooling jacket was used and the stator end windings were coated with a heat conducting resin to reduce temperature.

The use of a direct drive eliminates the necessity for gearbox and differential but might not increase the motor torque density. Nevertheless, this can bring a higher torque density for the whole powertrain. This was applied to IM9, a high pole number induction motor developed at Torino Polytechnic [25]. This machine was located between the internal combustion engine and the gearbox. 12 poles were selected due to space restrictions in

order to minimize the overall size of the complete drivetrain. This induction machine was designed to operate as starter, generator or motor.

The use of a direct drive requires at least two motors to allow steering, unless a differential motor is employed. IM16 is a differential induction machine developed at Central Calcutta Polytechnic [35]. This motor had two rotors which are connected directly to the wheels without requiring a mechanical differential. Both rotors were squirrel cage with double bearings at each end and were powered by a single stator as shown in Figure 1.11. A four-pole three-phase motor was designed, analysed, built and tested for both motor and generator operation.

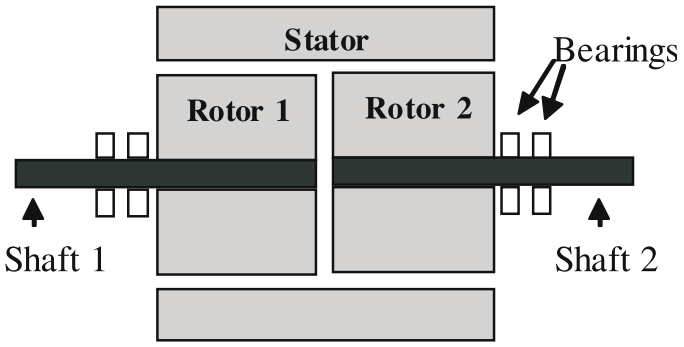

Figure 1.11: Differential induction machine [35]

1.3.9 Summary

This appendix analyses some of the main induction machines developed for electric vehicles described in the literature. Most of these motors have considered all the specific requirements for electric traction but they have generally failed to offer novel designs. This is a result of the predominant influence of industrial squirrel cage induction motor. It is true that the use of new designs sometimes offers little improvement to justify a change in the status quo. But if standard induction machines continue to be used, there would be little room for improvement. Only new approaches could effectively offer a way to obtain machines with better performance. These new designs could be obtained by exploiting the improvements already achieved in other machine types for electric vehicles.

1.4 Prospects for electric vehicles

Electric vehicles appeared as early as the 1830s [2]. They struggled at that time because of the requirements for better batteries in order to compete with steam powered alternatives. By the end of the 19th century, new batteries renewed interest in electric vehicles until the

early years of the 20th century when gasoline competitors like the Ford model T forced them out of the market [2] due to the higher energy storage density of fossil fuels against batteries.

During the 1970s, fuel prices and environmental concerns renewed interest again in electric automobiles [2]. DC motors were the best alternative at that time but the use of ac machines and in wheel drives were already predicted [52]. By year 2000, these predictions became a reality as shown in Table 1.5 [3].

Table 1.5: Electric vehicles in 2000 [3]

Model	Vehicle type	Electric motor type
Fiat Panda Elettra	Full electric	Series dc motor
Mazda Bongo	Full electric	Shunt dc motor
Conceptor G-Van	Full electric	Separately excited motor
Suzuki Senior Tricycle	Full electric	PM dc motor
Fiat Seicento Elettra	Full electric	Induction Motor
Ford Th!nk City	Full electric	Induction Motor
GM EV1	Full electric	Induction Motor
Honda EV Plus	Full electric	PM brushless motor
Nissan Altra	Full electric	PM brushless motor
Toyota RAV4	Full electric	PM brushless motor
Chloride Lucas	Full electric	Switched reluctance motor
Toyota Prius	Hybrid	PM brushless motor
Honda Insight	Hybrid	PM synchronous motor

The induction machine was the preferred option for electric traction according to a survey carried out by Chang in 1994 [53]. In contrast, Table 1.6 illustrates the more recent tendency favouring the use of permanent magnet machines just ten years later. It is also noticeable that the development of full electric vehicles has been slower compared with hybrid vehicles.

This change in the preferred electrical machine for electric vehicles was a result of higher power/torque density electrical traction motors and long-term low-cost expectations for permanent magnet motors [54]. However, in 1999 some researchers predicted that induction and permanent magnet machines would have similar cost tendencies as can be seen in Figure 1.12 [55]. The cost reductions were predicted as a result of technology improvements and mass production [55].

The cost predictions were rather disappointing. The expected cost reductions never happened because of fluctuating raw materials costs. Permanent magnets are made of rare earth elements. China became the main source since the beginning of the 1990s but now its own internal demand for rare earth metals is about to overcome production levels [56]. Despite new mining activities in the USA, Canada, Australia and South Africa, rare earth materials supply is expected to continue to be tight. Their prices are expected to remain high and unpredictable [56].

Table 1.6: Electric vehicles in 2010 [3, 58]

Model	Vehicle type	Electric motor type	Power output	Torque	Voltage
Toyota Prius V, IV, III, II	Hybrid	PM AC synchronous motor	60 kW	207 Nm	650 V maximum
Toyota Camry 11	Hybrid	PM AC synchronous motor	105 kW @ 4500 rpm	270 Nm @ 0-1500 rpm	650 V maximum
Honda CR-Z, Z-EX	Hybrid	PM AC synchronous motor	10 kW @ 1500 rpm	79 Nm. @ 1000 rpm	-
Honda Insight	Hybrid	PM AC synchronous motor	10 kW @ 1500 rpm	79 Nm @ 1000 rpm	-
Honda Civic Hybrid Sedan	Hybrid	PM motor	15 kW @ 2000 rpm	103 Nm	-
Honda FCX Clarity	Full electric	PM AC synchronous motor	100 kW	256 Nm @ 0-3056 rpm	-
Ford 2011 Fusion	Hybrid	PM AC synchronous motor	79 kW @ 6500 rpm	-	275 V
Chevrolet Volt	Hybrid	PM AC synchronous motor	112 kW	370 Nm	-
Nissan Leaf	Full electric	High response synchronous AC motor	80 kW	280 Nm	-
Nissan Altima	Hybrid	PM AC synchronous motor	105 kW @ 4500 rpm	270 Nm @ 0-1500 rpm	650 V maximum
Mitsubishi i-MiEV	Full electric	PM AC synchronous motor	47 kW	180 Nm	-

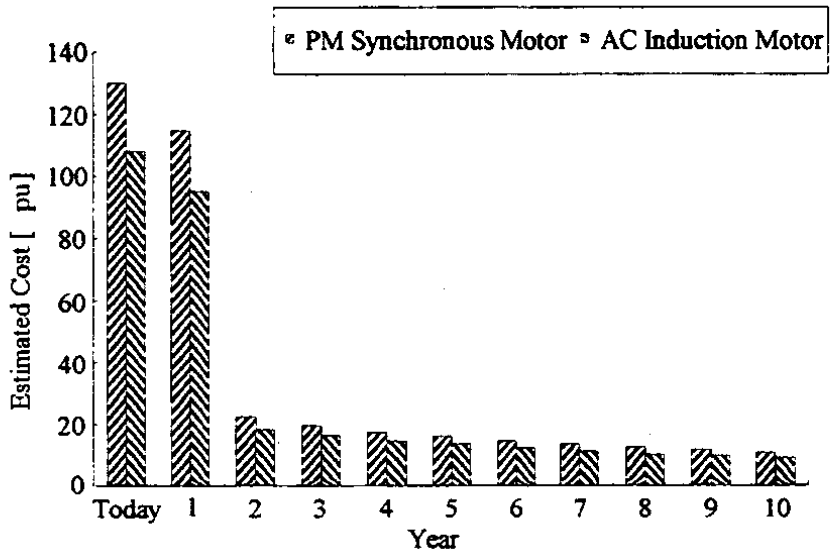

Figure 1.12: Induction motor and permanent magnet motor cost in 1999 [55]

These uncertainties have motivated researches into alternatives. For example, permanent magnet motors with ferrite instead of rare earth materials or machines with wound field claw pole rotors represent some of the state of the art research in Japan [57].

It is expected that there will be an increase in the number of passenger light road vehicles in the next decades. Figure 1.13 provides the market expectations in California. By 2030, hybrid vehicles might represent 11 % of on-road Californian vehicles. On the other hand, full electric and plug-in hybrid vehicles are expected to show a significant increase in their sales between 2018-2027 [59]. This figure also shows how hybrid electric vehicles are a transition technology from the internal combustion engines to the full electric powertrains.

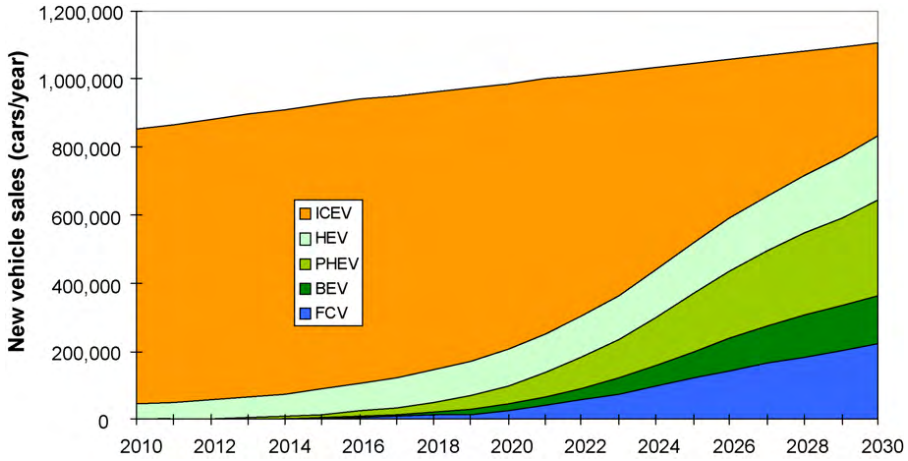

Figure 1.13: Projected vehicle sales in California by type: Internal Combustion Engine Vehicle (ICEV), Hybrid Electric Vehicle (HEV), Plug in Hybrid Electric Vehicle (PHEV), Battery Electric Vehicle (BEV) and Fuel Cell Vehicle (FCV) [59]

1.5 High power/torque electrical machines with wide speed range

Power electronics has driven the opportunity to use ac electrical machines in a wider range of applications. This has also imposed a change in their operational requirements. On one side, they have been required to operate under different conditions and environments than typical in industry. On the other, designers are required to produce machines with improved performance. Higher power/torque and a wide speed range are some of the main requirements imposed on electric machines for electric vehicles.

Power and torque densities are often employed as benchmarks. This is because the power and torque of an electric motor are directly proportional for a fixed speed ($P \propto T$). Power density is the power per volume in units of kW/m^3. Similarly, torque density is the torque capability per volume in Nm/m^3. They must not be confused with the power and torque to weight ratios, also known as specific power and specific torque, in kW/kg and Nm/kg respectively.

Nevertheless, some machines have been classified into two categories: high torque and high power. Although clear definitions of these have not been introduced, an attempt to define them is presented here. High torque machines can be defined as electric motors with improved torque at nominal speeds under 3600 RPM (typical maximum industrial speed at 60 Hz). High power machines are generally understood to have higher power per unit volume or mass than typical industrial machines at speeds over 3600 RPM.

Both machine categories are suitable for electric vehicles, however most of them fall into the high torque category. This might be explained by the fact that the machine is expected to produce sufficient torque to eliminate the necessity for a gearbox, differential and other mechanical components.

Reference [60] presents research about both high power and torque designs, labelled as extreme operating conditions, for large and medium machines. The authors describe the advantages and drawbacks of each operating condition. First, they describe how high speed machines increase their power at the same ratio as speed. They also highlight the improvement in cooling and consequently in electric loading with speed. But this is done at expense of higher core and winding losses. They then mentioned the advantages of using short length and large diameters in order to achieve high torque. They also presented the main disadvantages such as higher winding losses, increased leakage inductances and limited structural size.

Furthermore, this research also mentioned that these extreme operating conditions share common problems. For example, further research is considered necessary to produce models or data about the magnetic properties of the materials at these operating conditions. Available data is usually given for a limited number of frequencies (50 and

60 Hz). It also noted the necessity of using 3D analysis and multi-physics models as a consequence of their complex structures.

Although there is great interest in increasing the torque and power, most of the machines developed have conventional structures. This can be caused in part because radical structural changes sometimes produce minor improvements that does not justify their implementation. It may also be as a result of the superior performance of permanent magnet machines and the technological maturity of induction machines.

An important conclusion can be inferred from this: many of the important advances in higher power and torque might not have been developed for induction machines. However, much of this research can be applied to the design of any electric machine and must be considered.

1.6 Project aims and objectives

The main aim of this work is to analyse the design of conventional induction motors for automotive drive applications with the intention of taking a non-conventional look at the design process and developing new designs that are optimised in terms of specific torque for automotive drives. The following tasks are considered key objectives in order to accomplish the main project objective:

- Compare several designs in terms of specific torque with a common simulation tool.
- Full literature review of current design strategies in induction machines for electric vehicles.
- Identify designs already developed for other applications and for other electrical machines which might be suitable for induction machines used in electric traction.
- Propose and refine different designs based on the literature review.
- Validate the simulation tool employed with an experimental test program.
- Validation of design techniques and methodologies.

Notwithstanding there is a great variety of hybrid electric light ground vehicles in the market, it is possible to identify the common performance requirements. All the new designs have to observe these traction requirements which have been already mentioned in Section 1.2. Four specific properties have also been stipulated with recommended values:

Continuous power: 60 kW. Power ratings vary from 10 to 100 kW depending on the electric type and size of the vehicle. The selected power rating was based on the

Toyota Prius electrical motor which is considered one of the most successful in the market [61, 62].

Base speed: 1500 RPM. A powertrain topology was considered where the electric motor is coupled to the wheels by a differential. Considering that the base speed of a light ground electric vehicle at the wheels ranges from 300 RPM to 600 RPM and typical gear differential ratios vary from 3 to 5, the base speed for the electric motor would be between 900 RPM to 3000 RPM. The selected value should facilitate the search of a benchmark.

Rms per phase voltage: 400 V. Tables 1.6 and 1.3 shows that there is no standard rated voltage for motors employed in electric vehicles. A industrial voltage rating was selected to facilitate finding a benchmark.

Speed range ratio: 4. This property usually varies from 2 to 6 times the base speed but the optimal value depends on the powertrain topology adopted. Researchers have however identified that a value between 3 to 4 is the most common value [63].

1.7 Significance of this research project

There has been a growing interest recently in electric vehicles and their powertrains with the development of electric traction motors a key task. The permanent magnet motor has become the favourite motor for such applications because of its better power/torque density, efficiency and speed range [1].

The permanent magnet motor however has suffered from price speculation of the raw magnet materials. The price uncertainty is result of a growing demand and the entrance of more expensive new suppliers [56]. Unpredictable political issues also play an important role in the costs of rare earth materials [56].

Questions have been also raised about whether the induction motor might have been overlooked when judged as the second best option for automotive applications [64]. Despite the permanent magnet motor having a better overall performance, the fuel consumption savings are still less than 1 % compared with induction and switched reluctance motors [34, 65]. These savings are calculated using the same hybrid electric vehicle and energy management system under average driving cycles [34].

Other investigators have gone even further and criticised the validity of the standard steady state efficiency maps [66]. They argue that efficiency should be determined under dynamic operation with optimal flux for each driving cycle [66].

Despite the differences in power/torque densities, some researchers have claimed that induction and permanent motors could achieve the same peak torque using the same inverter and having the same stack length and outer diameter [44]. The difference in

power/torque density appears during continuous operation where the permanent magnet machine can handle approximately 45 % more torque for the same maximum heat dissipated [44].

This illustrates some of the reasons why several investigators consider the induction motor a worthy rival to take into account [67]. The induction machine is of importance to industry being the most commonly used machine type. It offers mature technology, low cost, low maintenance, simple construction, reliability and robustness. Figure 1.14 shows how the induction motor was expected to retain at least 20 % share of the electric vehicle European market by 2015 [68]. This prediction proved to be quite optimistic and the permanent magnet machines continue to dominate the market due to the lack of alternative high specific torque electrical machines without rare-earth materials. This would encourage further research as the shown in this thesis.

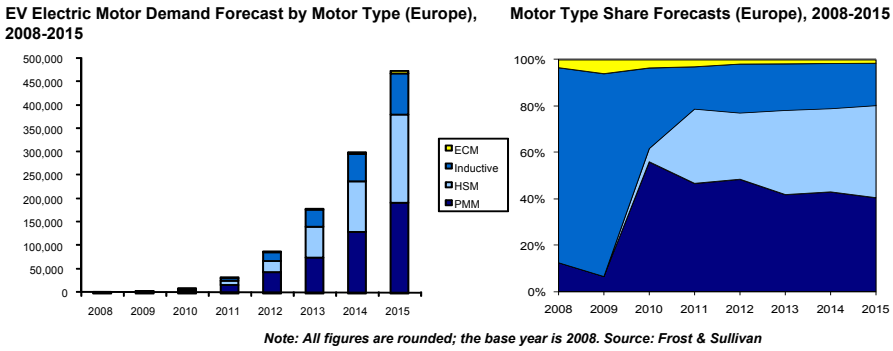

Figure 1.14: European commercialization forecast for EV electric motor type: Electric Corner Modules (ECM is an in wheel permanent magnet motor drive), Permanent Magnet Motor (PMM), Hybrid Synchronous Motor (HSM) and Inductive (Induction motor) [68]

Research has concentrated on the standard squirrel cage induction motor, but in terms of novel design approaches, little has been done. Its design has been highly influenced and optimized to line-start standard fixed speed industrial requirements. Variable speed design follows similar paths, dictated by industrial requirements for material and cost reduction as the main objectives.

The research described in this thesis represents an effort towards new design approaches. The work focuses on the key motor parameters: specific torque; efficiency; and a wide operating speed range.

1.8 Thesis structure

Chapter 1 introduces the importance and challenges of induction motors in electric vehicles. It covers the basics of electric vehicles including key technologies, classification, topologies and traction requirements in order to define clearly the importance and the aims of this project.

Chapter 2 gives a review of the typical design process for induction motors and also includes electric machines with high performance. This provides background to understanding the limitations of current designs and recognize the necessity of some changes in the current industrial-based designs. It is also discusses the tools available and required for modelling and simulation to justify the selection of finite element analysis.

Chapter 3 deals with explaining a common design methodology proposed for the design and comparison of the new designs. It also includes the selection and simulation of benchmark machines which were used as a starting point for the new designs. This is included with the aim of explaining and justifying the assumptions and limitations of the models and methodologies used.

The proposed designs are summarized in Chapter 4, including their models and simulations obtained using the finite element method. On the other hand, Chapter 5 focuses on analysing the simulation results and comparing them in order to select the best designs. This chapter also includes the description of some manufactured machines and their basic experimental results obtained.

The conclusions to this research work are summarized in Chapter 6 with suggestions of future research in order to improve the proposed designs and their comparison. Suggestions of improving its models and methodologies employed are also included.

1.9 References

[1] Inc. Raymond R. Fessler BIZTEK Consulting. *Assessment of Motor Technologies for Traction Drives of Hybrid and Electric Vehicles*. Tech. rep. 4000080341. 820 Roslyn Place, Evanston, IL 60201-1724: for UT Battelle, LLC, Oak Ridge National Laboratory, 2011.

[2] *Electric and Hybrid Vehicles*. URL: `http://www.ieeeghn.org/wiki/index.php/Electric_and_Hybrid_Vehicles`.

[3] C.C. Chan, "The state of the art of electric and hybrid vehicles", *Proceedings of the IEEE*. 90, 247 –275. (2002).

[4] A.F. Burke, "Batteries and Ultracapacitors for Electric, Hybrid, and Fuel Cell Vehicles", *Proceedings of the IEEE*. 95, 806 –820. (2007).

[5] Z.Q. Zhu and D. Howe, "Electrical Machines and Drives for Electric, Hybrid, and Fuel Cell Vehicles", *Proceedings of the IEEE*. 95, 746 –765. (2007).

[6] M. Ehsani, Yimin Gao, and J.M. Miller, "Hybrid Electric Vehicles: Architecture and Motor Drives", *Proceedings of the IEEE*. 95, 719 –728. (2007).

[7] M. Ehsani, K.M. Rahman, and H.A. Toliyat, “Propulsion system design of electric and hybrid vehicles”, *Industrial Electronics, IEEE Transactions on*. 44, 19 –27. (1997).

[8] *Dynamometer Drive Schedules*. URL: `http://www.epa.gov/nvfel/testing/dynamometer.htm`.

[9] M.R. Harris. “Comparative electromagnetic parameters for alternative motor types”. In: *Motors and Drives for Battery Powered Propulsion, IEE Colloquium on*. 1993, pp. 3/1 –3/4.

[10] Surong Huang et al., “A general approach to sizing and power density equations for comparison of electrical machines”, *Industry Applications, IEEE Transactions on*. 34, 92–97. (1998).

[11] Surong Huang and Guodong Xie, “Evaluation of switched-reluctance machine through generalized sizing equations”. English, *Journal of Shanghai University (English Edition)*. 2, 117–121. (1998).

[12] J.M. Miller and Institution of Electrical Engineers. *Propulsion Systems for Hybrid Vehicles*. IEE power and energy series. Institution of Electrical Engineers, 2004.

[13] Z.Q. Zhu and C.C. Chan. “Electrical machine topologies and technologies for electric, hybrid, and fuel cell vehicles”. In: *Vehicle Power and Propulsion Conference, 2008. VPPC ’08. IEEE*. 2008, pp. 1 –6.

[14] I. Ozawa, T. Kosaka, and N. Matsui. “Less rare-earth magnet-high power density hybrid excitation motor designed for Hybrid Electric Vehicle drives”. In: *Power Electronics and Applications, 2009. EPE ’09. 13th European Conference on*. 2009, pp. 1 –10.

[15] Y. Amara et al., “Hybrid Excitation Synchronous Machines: Energy-Efficient Solution for Vehicles Propulsion”, *Vehicular Technology, IEEE Transactions on*. 58, 2137 –2149. (2009).

[16] F. Leonardi et al. “Design considerations and test results for a doubly salient PM motor with flux control”. In: *Industry Applications Conference, 1996. Thirty-First IAS Annual Meeting, IAS ’96., Conference Record of the 1996 IEEE*. Vol. 1. 1996, 458 –463 vol.1.

[17] John L. Oldenkamp and Steven C. Peak, “Selection and Design of an Inverter-Driven Induction Motor for a Traction Drive System”, *Industry Applications, IEEE Transactions on*. IA-21, 259 –265. (1985).

[18] N. M. Elkasabgy and C. Di Pietro, “The effects of various magnetic materials on lamination design for stator-rotor diecasting of induction motors for electric vehicle applications”, *Journal of Applied Physics*. 75, 6039 –6041. (1994).

[19] A. Harson, P.H. Mellor, and D. Howe. “Design considerations for induction machines for electric vehicle drives”. In: *Electrical Machines and Drives, 1995. Seventh International Conference on (Conf. Publ. No. 412)*. 1995, pp. 16 –20.

[20] F. Caricchi, F. Crescimbini, and E. Santini. “Axial flux electromagnetic differential induction motor”. In: *Electrical Machines and Drives, 1995. Seventh International Conference on (Conf. Publ. No. 412)*. 1995, pp. 1 –5.

[21] Atsuo Kawamura, Tomoki Yokoyama, and Tsuneo Kume, “ADTR-motor drive for electric vehicle”, *Electrical Engineering in Japan*. 116, 94–105. (1996).

[22] Z. Zhang, F. Profumo, and A. Tenconi, “Improved design for electric vehicle induction motors using an optimisation procedure”, *Electric Power Applications, IEE Proceedings* -. 143, 410 –416. (1996).

[23] M. Mori et al. “A control method of an inverter-fed six-phase pole change induction motor for electric vehicles”. In: *Power Conversion Conference - Nagaoka 1997., Proceedings of the*. Vol. 1. 1997, 25 –32 vol.1.

[24] J.M. Miller et al. “Starter-alternator for hybrid electric vehicle: comparison of induction and variable reluctance machines and drives”. In: *Industry Applications Conference, 1998. Thirty-Third IAS Annual Meeting. The 1998 IEEE*. Vol. 1. 1998, 513 –523 vol.1.

[25] L. Ferraris et al. “Iron losses analysis with different supply techniques in high poles number induction motors for automotive applications”. In: *Industrial Electronics, 1999. ISIE ’99. Proceedings of the IEEE International Symposium on*. Vol. 2. 1999, 651 –655 vol.2.

[26] Jawad Faiz and M. B. B. Sharifian, “Optimal design of an induction motor for an electric vehicle”, *European Transactions on Electrical Power*. 16, 15–33. (2006).

[27] M. Faiz et al., “Optimum Design of Induction Motors for Electric Vehicles”, *Electric Machines & Power Systems*. 28, 1177–1194. eprint: `http://www.tandfonline.com/doi/pdf/10.1080/073135600449053` (2000).

[28] Dong-Hyeok Cho, Hyun-Kyo Jung, and Cheol-Gyun Lee, “Induction motor design for electric vehicle using a niching genetic algorithm”, *Industry Applications, IEEE Transactions on*. 37, 994 –999. (, Jul/Aug, 2001).

[29] B. Eberleh and Th. Hartkopf. “A high speed induction machine with two-speed transmission as drive for electric vehicles”. In: *Power Electronics, Electrical Drives, Automation and Motion, 2006. SPEEDAM 2006. International Symposium on*. 2006, pp. 249 –254.

[30] Song Liwei et al. “The research of induction motor driving system for hybrid electric vehicle”. In: *Vehicle Power and Propulsion Conference, 2006. VPPC ’06. IEEE*. 2006, pp. 1 –4.

[31] Chu Shumei, Dai Ying, and Song Liwei. “Rotor Slots Design of Induction Machine for Hybrid Electric Vehicle Drives”. In: *Vehicle Power and Propulsion Conference, 2006. VPPC ’06. IEEE*. 2006, pp. 1 –3.

[32] Huijuan Liu et al. “Design and Simulation of An Inverter-fed Induction motor for Electric Vehicles”. In: *Vehicle Power and Propulsion Conference, 2007. VPPC 2007. IEEE*. 2007, pp. 112 –115.

[33] H. Neudorfer. “Comparison of three different electric powertrains for the use in high performance Electric Go-Kart”. In: *Electrical Machines and Power Electronics, 2007. ACEMP ’07. International Aegean Conference on*. 2007, pp. 21 –26.

[34] H. Neudorfer, N. Wicker, and A. Binder. “Comparison of three different electric powertrains for the use in hybrid electric vehicles”. In: *Power Electronics, Machines and Drives, 2008. PEMD 2008. 4th IET Conference on*. 2008, pp. 510 –514.

[35] S. Sinha et al., “The Differential Induction Machine: Theory and Performance”, *Sadhana*. 33, 663–670. (2008).

[36] Li Weili et al. “Analysis of the influence of rotor material on IMCCR temperature field”. In: *Vehicle Power and Propulsion Conference, 2008. VPPC ’08. IEEE*. 2008, pp. 1 –5.

[37] Weili Li, Junci Cao, and Xiaochen Zhang, “Electrothermal Analysis of Induction Motor With Compound Cage Rotor Used for PHEV”, *Industrial Electronics, IEEE Transactions on*. 57, 660 –668. (2010).

[38] J. Herbst et al. “Challenges in the design of a 100 kw induction motor for a PHEV application”. In: *Vehicle Power and Propulsion Conference, 2009. VPPC ’09. IEEE*. 2009, pp. 408 –413.

[39] D.G. Dorrell et al. “Comparison of permanent magnet drive motor with a cage induction motor design for a hybrid electric vehicle”. In: *Power Electronics Conference (IPEC), 2010 International*. 2010, pp. 1807 –1813.

[40] D.G. Dorrell et al. “Modern electrical machine analysis and design techniques applied to hybrid vehicle drive machines”. In: *Industrial Electronics (ISIE), 2010 IEEE International Symposium on*. 2010, pp. 3728 –3733.

[41] D.G. Dorrell et al. “Comparison of different motor design drives for hybrid electric vehicles”. In: *Energy Conversion Congress and Exposition (ECCE), 2010 IEEE*. 2010, pp. 3352 –3359.

[42] D.G. Dorrell et al., “Analysis and Design Techniques Applied to Hybrid Vehicle Drive Machines -Assessment of Alternative IPM and Induction Motor Topologies”, *Industrial Electronics, IEEE Transactions on*. 59, 3690 –3699. (2012).

[43] A. Hyun Rok Cha et al. “Design of outer rotor type induction motor having high power density for in-wheel system”. In: *Electrical Machines and Systems (ICEMS), 2012 15th International Conference on*. 2012, pp. 1 –4.

[44] G. Pellegrino et al., “Comparison of Induction and PM Synchronous Motor Drives for EV Application Including Design Examples”, *Industry Applications, IEEE Transactions on*. 48, 2322 –2332. (2012).

[45] S. Jurkovic et al. “Electric machine design and selection for General Motors e-Assist Light Electrification Technology”. In: *Energy Conversion Congress and Exposition (ECCE), 2012 IEEE*. 2012, pp. 906 –913.

[46] D. Sekiguchi et al., “Trial Test of Fully HTS Induction/Synchronous Machine for Next Generation Electric Vehicle”, *Applied Superconductivity, IEEE Transactions on*. 22, 5200904. (2012).

[47] Jalila Kaouthar Kamoun et al. “An induction motor FEM-based comparative study: Analysis of two topologies”. In: *Ecological Vehicles and Renewable Energies (EVER), 2013 8th International Conference and Exhibition on*. 2013, pp. 1–5.

[48] P. Mishra and S. Saha. “Design modeling and simulation of low voltage squirrel cage induction motor for medium weight electric vehicle”. In: *Advances in Computing, Communications and Informatics (ICACCI), 2013 International Conference on*. 2013, pp. 1697–1704.

[49] P.M. Tuohy et al., “Rim-drive marine thruster using a multiple-can induction motor”, *Electric Power Applications, IET*. 7, 557–565. (2013).

[50] D.J. Patterson et al. “A comparison of radial and axial flux structures in electrical machines”. In: *Electric Machines and Drives Conference, 2009. IEMDC ’09. IEEE International*. 2009, pp. 1029 –1035.

[51] P. Wu and K.J. Tseng. “Finite element analysis of axial-gap induction motors”. In: *Power Electronics and Motion Control Conference, 2004. IPEMC 2004. The 4th International*. Vol. 2. 2004, 571–576 Vol.2.

[52] Edward P. Cornell, R.H. Guess, and Fred G. Turnbull, “Advanced motor developments for electric vehicles”, *Vehicular Technology, IEEE Transactions on*. 26, 128–134. (1977).

[53] L. Chang, “Comparison of AC drives for electric vehicles-a report on experts’ opinion survey”, *Aerospace and Electronic Systems Magazine, IEEE*. 9, 7 –11. (1994).

[54] J.G.W. West. “Propulsion systems for hybrid electric vehicles”. In: *Electrical Machine Design for All-Electric and Hybrid-Electric Vehicles (Ref. No. 1999/196), IEE Colloquium on*. 1999, pp. 1/1 –1/9.

[55] Pill-Soo Kim, Yong Kim, and Byung-You Hong. “A method for future cost estimation of hybrid electric vehicle”. In: *Power Electronics and Drive Systems, 1999. PEDS ’99. Proceedings of the IEEE 1999 International Conference on*. Vol. 1. 1999, 315–320 vol.1.

[56] P.C. Dent and M.H. Walmer. “4.6: Supply chain sustainability - rare earth materials”. In: *Vacuum Electronics Conference (IVEC), 2010 IEEE International*. 2010, pp. 57 –58.

[57] T. Kosaka et al. “State-of-art of research and development of vehicle motors”. In: *ECCE Asia Downunder (ECCE Asia), 2013 IEEE*. 2013, pp. 153–158.

[58] *Commercial brochures from the mentioned manufacturers*. 2010.

[59] Guihua Wang, “Advanced vehicles: Costs, energy use, and macroeconomic impacts”, *Journal of Power Sources*. 196, 530 –540. (2011).

[60] Ma Weiming and Wang Dong. “Key technologies of large and medium power electromechanical energy conversion under extreme operating conditions”. In: *Electrical Machines and Systems, 2008. ICEMS 2008. International Conference on*. 2008, pp. 2755 –2760.

[61] T. A. Burress et al. *Evaluation of the 2010 Toyota Prius Hybrid Synergy Drive System*. Tech. rep. ORNL/TM-2010/253. Oak Ridge, Tennessee 37831: Oak Ridge National Laboratory, 2011.

[62] J. S. Hsu et al. *Report on Toyota/Prius Motor Torque Capability, Torque Property, No-Load back EMF, and Mechanical Losses - Revised May 2007*. Tech. rep. ORNL/TM-2004/185. Oak Ridge, Tennessee 37831: Oak Ridge National Laboratory, Oak Ridge Institute for Science, and Education, 2007.

[63] E. Hall, S.S. Ramamurthy, and J.C. Balda. “Optimum speed ratio of induction motor drives for electrical vehicle propulsion”. In: *Applied Power Electronics Conference and Exposition, 2001. APEC 2001. Sixteenth Annual IEEE*. Vol. 1. 2001, 371 –377 vol.1.

[64] M. Zeraoulia, M.E.H. Benbouzid, and D. Diallo, “Electric Motor Drive Selection Issues for HEV Propulsion Systems: A Comparative Study”, *Vehicular Technology, IEEE Transactions on*. 55, 1756 –1764. (2006).

[65] D. Bucherl et al. “Comparison of electrical machine types in hybrid drive trains: Induction machine vs. permanent magnet synchronous machine”. In: *Electrical Machines, 2008. ICEM 2008. 18th International Conference on*. 2008, pp. 1 –6.

[66] A.M. Bazzi and P.T. Krein. “Comparative evaluation of machines for electric and hybrid vehicles based on dynamic operation and loss minimization”. In: *Energy Conversion Congress and Exposition (ECCE), 2010 IEEE*. 2010, pp. 3345 –3351.

[67] T. Finken, M. Felden, and K. Hameyer. “Comparison and design of different electrical machine types regarding their applicability in hybrid electrical vehicles”. In: *Electrical Machines, 2008. ICEM 2008. 18th International Conference on*. 2008, pp. 1 –5.

[68] Frost & Sullivan. *Thought Leadership Report: Industrial Opportunities in the Electric Vehicles Segment*. Tech. rep. M46B-10. 2009.

CHAPTER

TWO

LITERATURE REVIEW

2.1 Introduction

This chapter covers the basic background for the design of induction motor for the electric vehicle applications. This begins with an introduction to the evolution of the design process from the early days. A review is then presented of the key parts of the process including comments about its actual implementation for electric vehicles.

2.2 Brief history of the design of induction motors

The induction machine was invented by Nikola Tesla in 1888 [1]. Since then researchers have continued to improve this electromechanical converter. The history of this development is valuable in the design of induction machines because it includes both the successes and failures over time [2].

The period from its invention until about 1900 was considered by Lamme to be the "golden age" of induction machines [2]. Some of the first induction machines were designed using simple trial-and-error methods. Analytical calculations however became rapidly necessary to achieve better designs. During this short period, most of the significant advances in induction machines had their origins or were developed for first time: overlapping distributed windings; polyphase (three-phase) and single-phase motors; squirrel cage rotors; double cage rotors; semi-closed slots; stationary primary and rotating secondary configuration; resistive starting methods; pole changing windings; operation as a generator; autotransformer starting; amongst others [2, 3].

Even the first traction applications for induction motors occurred in those years. Locomotives with induction machines were unsuccessful except for auxiliary generation

purposes [2]. Some warships were also built in the USA including a primitive series hybrid electric powertrain [2]. The 19th century was an exciting period for the design of all electric machines: for example some concepts such as modular, toroidal and transversal windings were already in use [4].

The next period could be denominated the age of analytical analysis in induction motors which covers mainly the first half of the 20th century [2]. This name was also proposed by Lamme who was contemporary of others designers such as Behrend, Say and Alger [5–7]. The design was based on sizing equations and analytical expressions similar to those currently found, these equations however included many constants obtained by experience [8]. Some graphical methods were also relevant during this era for use in the design and analysis of induction machines [9].

In addition to the improvements in the calculations, there were some important advances in other areas: laminations, insulation, standardization and cast aluminium rotors [9]. Nevertheless, the basic structure developed during the golden age remained essentially unchanged. It is during these years that the induction motor became the predominant motor in industrial fixed-speed applications.

The third design stage might be called the "age of computer assisted design" covering a large part of the second half of the 20th century [10–14]. Some investigators developed their career during more than one age such as Alger. This motivated him to review their history in the USA: Figure 2.1 illustrates the size reduction of the induction motors from 1903 to 1974 [9]. If this figure were to be continued for some decades more, it is very likely to show a further reduction in the motor volume.

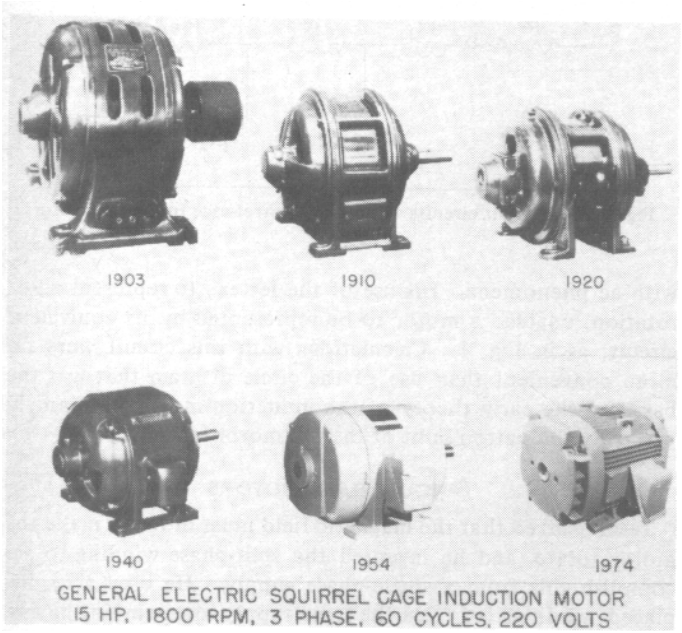

Figure 2.1: Induction motor evolution [9]

Computers have helped to continue the development of designs with reduced volume. However computers brought other important changes to the design process as well. On

one hand, they have allowed the development of numerical techniques for the design and analysis of induction machines for instance winding functions (WF), magnetic equivalent circuits (MEC) and finite elements (FE). On the other hand, they have facilitated the search for the best design using formal optimization procedures. There were few designs however which did not have their background in the golden age.

The contemporary era could be denominated the "age of special application design" for the induction machine. This age was facilitated by three conditions. First, researchers proposed designs for special applications which were less influenced by standard industrial induction motor designs [15, 16]. Laithwaite could be considered a pioneer of this age and he also defined the concept of induction machines for special purposes [17]. Second, computers started to become powerful enough to allow a more direct design approach utilizing numerical techniques like finite elements. Third, there has been an increased number of applications requiring designs with improved performance in power/torque density, efficiency and speed range.

This latest design age is still in development; the industrial induction motor is expected to be used in many of the latest applications. The new designs would be used when the application requirements and costs justify it. For electric vehicles, a brief review in the previous chapter was done of the existing designs in literature and it was found that most of them tend to be highly influenced by the standard industrial approaches. Nevertheless some designs presented in the previous chapter could be considered examples of bespoke induction machines.

2.3 Design process

The design of electrical machines is considered to be both art and science. It requires creativity and experience from the designer to develop the machine structure. The required calculations to predict and improve the performance are rigorously scientific.

There are six basic stages during the design process which are repeated and could be interrupted to restart at any previous stage until a satisfactory design is obtained:

Topology definition. This first stage involves the determination of the basic shape of the machine. Most of the creative activity takes place during this stage. The designer has to deal with a series of choices based on application requirements, manufacturing restrictions and cost limitations, amongst other factors. Many decisions rely on the design criteria and the experience of the designer, for instance winding type and materials selection, whilst others are given constraints including temperature limits and torque output required.

Initial outline. Once the structural topology is clearly defined, the next step consists of

obtaining the initial geometrical dimensions. This is commonly done through the use of analytical expressions or similar previous designs. Researchers have made significant efforts to obtain these dimensions as close as possible to the final design.

Dimensional refinement. Following this, an iterative refinement methodology is applied in order to achieve the best possible design. This activity requires performance evaluation which can be calculated for example with the following tools: analytic expressions, general harmonic analysis or winding functions, magnetic equivalent circuits and finite elements. It is important to establish a refinement criteria.

Prototype construction. This includes the preparation of diagrams and drawings with all the specifications necessary for manufacture. Each component is manufactured separately taking into balance the cost and quality. For example machining could be employed instead of casting for some elements to reduce the prototype costs when the performance is not significantly affected. The machine is then assembled to include finishing procedures such as adding resins to the stator windings and rotor balancing.

Machine test. This requires the preparation of a test rig and definition of a test protocol for performance evaluation. It has to reproduce the operational conditions which the machine will withstand.

Experimental data analysis. The experimental results from the previous stage are essential to validate the design process. If significant differences exist from the calculated values, the designer can identify the source and improve the methodology.

The costs involved in the manufacture and testing of one prototype are very high and the time involved could be many months. For these reasons, many researchers today focus their attention on the first three stages of the design process and commonly only one prototype is built.

2.3.1 Design philosophy

The designer is the key in this facet of induction machine design by contributing creativity to the process. Although an infinite number of designs are often possible, the standard topologies are preferred. This can be explained by the fact that design in engineering is evaluated in an objective manner favouring machines which offer reliability, low cost production and high efficiency, amongst others attributes.

This paradox has made it quite difficult to justify the design of unconventional machines. Since the first decades of 20th century, it has been reported that many researchers had the perception that little could be improved in their designs [2]. Evolution of the induction machine however has shown the contrary.

The designer has to make decisions through the whole procedure but the first stage is the most crucial and dominates the whole process. The most important decision is usually whether to adopt a conventional topology or not. In most cases a standard industrial motor topology is justifiably selected almost by default.

2.3.2 Design strategies

This subsection covers some examples of design strategies focusing on the first three stages because some references have not reported if a prototype was fully developed and many of the main choices are made at this stage of the process. More detail about the conventional induction machines labelled as IM3 and IM18 can be found in the previous chapter.

The strategy employed to develop IM3 is summarized in Algorithm 1 [18]. A squirrel cage induction motor topology was selected, the remaining choices consisted of the selection of some basic parameters like pole and slot numbers and the calculation of the dimensions. The minimum pole number was selected considering the space envelope restrictions. A rough method was then introduced to consider the airgap harmonics. This proceeded to the minimization of $\sum \frac{k_{wm}}{n}$ where k_{wn} is the n'th harmonic winding factor and n the harmonic number. The harmonic equivalent circuit parameters were calculated and employed to evaluate the performance over the complete speed range. The iteration continued until the voltage across the magnetizing reactance, V_m, converged.

Researchers identified some potential improvements to IM3: open rotor slots and wide stator slot openings; larger airgap; and an unskewed rotor. However, each one has its drawbacks including reduced power factor and increased harmonic content in the airgap field.

Input: Initial parameter values
initialization;
repeat
    Calculate machine dimensions and winding details;
    Calculate equivalent circuit parameters;
    Analyse equivalent circuit;
until V_m *converged*;

Algorithm 1: Design process in IM3 [18]

IM14 utilized a similar approach to the previous one. Algorithm 2 shows the whole process where the main difference is the second iterative loop [19]. This included the selection and design of the control strategy to evaluate the dynamic performance. The

procedure was iterated until the dynamic requirements were achieved. This approach compared the results between a magnetic equivalent circuit and a dynamic simulator.

Input: Initial parameter values
initialization;
repeat
  repeat
    Determine motor geometry;
    Material selection;
    Calculate electromagnetic parameters;
    Calculate static characteristic of the motor
  until *Static requirements satisfied*;
  Define control strategy;
  Evaluate dynamic performance;
until *Dynamic requirements met*;

Algorithm 2: Design process in IM14 [19]

Algorithm 3 illustrates a more commercial approach [20]. First, the customer requirements were checked for consistency. The program then searched a database for the most suitable motor. If the requirements match any of the designs, the design process was effectively complete in a matter of seconds. If not, the closest match in the database was employed as benchmark and the design parameters adjusted in order to meet the requirements. The performance and manufacturing (Costs) were then simulated. The machine design was completed in minutes if the extrapolation was successful. If all the previous steps failed, the program began to engage in a Monte-Carlo design synthesis. The matching design in this case was completed in hours if any was found [20].

Many of the previous approaches used the sizing equation to determine the airgap or full machine envelope as a starting point in the design. The stator and rotor were then designed and dimensioned in a relatively separate manner. However, others have started from the shaft dimension through the rest of the geometry to the outside: rotor core back, rotor slots and tooth, cage, rotor slot openings and tips, airgap, stator slot openings and tips, stator slots and tooth, stator windings and stator core back frame [21]. This approach was used to search for the smallest machine for the required performance [22]. If the output torque requirement was not satisfied, the machine dimensions were increased [22]. The advantage of this approach was that the motor performance could be computed when only the rotor was designed. This allowed the refinement to start before the full machine dimensions were obtained [23].

Previous examples might present the design as a simple process. But this is a result of hard work to synthesize the design process in order to facilitate optimization. However, even single choices inside this process are difficult tasks. For example, the design of the

```
Input: Customer requirements
initialization;
if Customer requirements are consistent then
    Search database for suitable motor;
    if Customer requirements match designs in the database then
        Report all matching design (Seconds);
    else
        Pick out the closest match in the database;
        Adjust the design parameters to provide the required performance;
        Simulate performance and manufacturing (Costs);
        if Extrapolation is succesful then
            Report matching design (Minutes);
        else
            Engage Monte-Carlo design synthesis;
            if Design synthesis is successful then
                Report matching design (Hours);
            else
                Stop
            end
        end
    end
else
    Stop
end
```

Algorithm 3: Commercial design approach [20]

stator winding distribution is complex enough to be treated separately as an optimization problem using genetic algorithms [24].

The machine topology is normally known at the beginning of the design process and its refinement consists in determining the best dimensions. But if the topology is part of the search for the best design, this is called topology optimization. This search generates a large number variables so that a traditional method is applied to the final refinement when the basic structure is defined [25]. This method is still under development but it is expected that it would find the whole 3D topology of an electrical machine in the future [26]. This method had been applied for example to find the topology of stator slots [27]. The slot geometry was conformed by a series of points with the optimal position determined by an evolution strategy [27].

Another optimization topology technique is called the density method. It has been applied to a transformer in conjunction with the finite element method [25]. Each finite element

had an associated normalized density between 0 and 1. The value 0 represented air while 1 was a magnetic material. Figure 2.2 illustrates how the core shape is obtained after this optimization method determined the normalized density for each element [25].

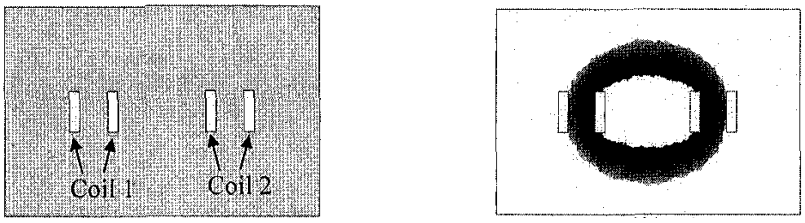

(a) Initial core (b) Final core

Figure 2.2: Topology optimization [25]

2.3.3 Summary

This section has described the typical process followed during the design of an induction machine including examples both for general purpose and electric vehicle applications. Little difference was found between induction machines for electric vehicles and industrial induction motors in most cases.

The search of new topologies is a promising technique which could lead to a radical changes in the design of electrical machines, specially if this is done in 3D. However, this approach is still in premature stage and is restricted by the huge computational costs associated with the search of topologies using techniques such as the finite element method.

2.4 Modelling tools

The design process requires tools to calculate the dimensions and performance of the induction machine under development. There are three main categories for electromagnetic calculations: analytic, magnetic equivalent circuit and finite element method. Each one has its advantages and disadvantages so that choosing one is not straightforward [28]. These techniques can be used directly to evaluate the performance or to calculate the equivalent circuit parameters of the machine.

The equivalent circuit of an induction motor is a relatively simple representation but at the same time a powerful model which allows one to evaluate the machine performance and the impact of any change of parameters on such performance. The simple equivalent circuit model employed is described in Figure 2.3. This model is valid only for the fundamental field. R_1 and jX_1 represent respectively the resistance and the leakage reactance of the stator. jX_m represents the magnetizing reactance of the motor and R'_2

and jX_2' are the resistance and leakage reactance of the rotor. k is the skew factor to take into account the effect of the skew in the rotor slots and s is the slip of the induction motor.

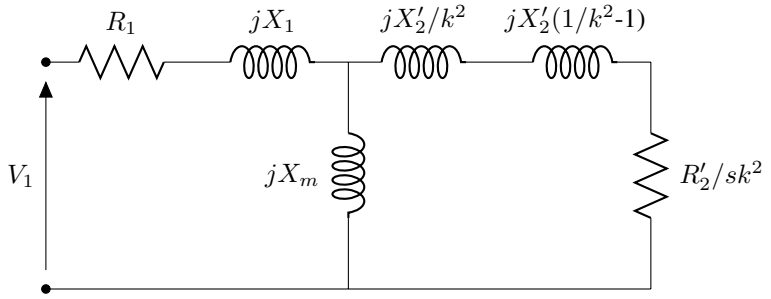

Figure 2.3: Fundamental induction motor equivalent circuit of one phase

2.4.1 Analytical methods

A great number of analytic expressions can be found in literature to determine the motor dimensions and parameters. Many of these formulae were obtained from theoretical analysis and/or experimental data. These analytical methods sometimes simplify the calculation of complex phenomena such as the slot leakage flux with the calculation of constants [29]. Despite the simple construction of the squirrel cage for example, calculation of the effective resistance and reactance under different slip frequencies of the slots [30] and end-rings is not straightforward [31, 32]. The inductances of the machine end windings are notoriously difficult to calculate accurately even with the simplification of representing them as current conducting filaments [33–35].

Other analytical methods are the winding function and the generalized harmonic analysis. Although there are some differences in their approach, both methods use the Fourier analysis to represent the airgap, winding distributions, voltages and currents [12, 36–39]. These techniques are simple to program, fast and require low computational costs. These methods can be modified to include saturation [40, 41] and non-uniform airgap distributions [42]. Nevertheless, some parameters need to be calculated by other methods such as the leakage inductance calculations.

2.4.2 Magnetic equivalent circuit method

The magnetic equivalent circuit is a method in which the machine is divided into small magnetic circuits denominated “flux tubes” [13]. These are represented by a reluctance network which is coupled to the circuit equations. Solving the resulting system matrix allows one to calculate the dynamic performance of the electrical machine. Saturation can be also included by this method. Some researchers consider it a promising tool for

the design of electrical machines specially for 3D topologies; notwithstanding, it has been largely overtaken by the finite element method [43–45].

This method has been used successfully to simulate both squirrel cage and wound rotor induction machines [46–48]. However, its main weaknesses are the difficulty to model eddy currents accurately and its requirement of prior knowledge of the flux directions [49, 50]. Both issues could be solved by using smaller elements like in the finite element method but this generates a trade-off between model accuracy and computational costs [49, 50].

2.4.3 Finite element method

The finite element method is a numerical technique to the solution of field problems represented by partial differential equations. It originated in mechanical analysis but it has been applied in many engineering areas: structural mechanics, fluids dynamics, heat analysis, electromagnetic problems, amongst others. This method divides the problem domain into small elements with a defined shape and imposes boundary conditions. The problem is reduced to a finite number of equations which allows an approximate solution to be obtained. Its accuracy increases with the number of elements but the computational resources needed also increase.

This method has been used extensively for the design and analysis of electrical machines. It allows the designer to consider devices with complicated geometries, induced eddy currents and non-linear materials. Both 2D and 3D versions have been developed but 2D simulations are preferred specially in radial machines to reduce computational costs. Transient and steady state conditions can be simulated as well. The finite element method can also be employed to determine the parameters of the equivalent circuit [51]. There are several available commercial software packages which utilize the finite element method in electrical machines: Flux, Comsol, Opera and FEMM for example.

The software available allows definition and analysis of complicated geometric topologies. It also does not depend on empirical constants which might not be accurate for unconventional designs and are commonly used in many analytical methods. Finite element models do not require the division of the machine into sections where the flux direction is known. There are disadvantages in terms of computational and time requirements so the simulations were developed using 2D representations of the designs.

Flux 2D (Version 11.1) and Opera 2D (Version 16.1) would be described as examples of the finite element software packages employed suitable for research. Figure 2.4 illustrates the process to create a model for an induction machine for both packages. Although Flux 2D requires more steps to prepare the models, the processes are very similar. The difference is that Opera 2D defines the geometry, mesh, magnetic and electrical properties

Flux 2D

- **Define parameters**
  - Stator
    - Geometry
    - Circuit
    - Auxiliary
  - Rotor
    - Geometry
    - Circuit
    - Auxiliary
- **Geometry**
  - Define coordinate systems
    - Stator
    - Rotor
  - Define periodicity
  - Define transformations
    - Stator
    - Rotor
  - Draw geometry and create faces
    - Windings
      - Stator
      - Rotor
    - Cores
      - Stator
      - Rotor
    - Airgap
    - Shaft
- **Mesh**
  - Define and assign mesh lines
    - Windings
      - Stator
      - Rotor
    - Cores
      - Stator
      - Rotor
    - Airgap
    - Shaft
  - Mesh geometry

Opera 2D

- **Define parameters**
  - Stator
    - Geometry
    - Circuit
    - Auxiliary
    - Material
    - Mesh
  - Rotor
    - Geometry
    - Circuit
    - Auxiliary
    - Material
    - Mesh
- **Create regions**
  - Stator windings
    - Geometry
    - Properties
    - Mesh
  - Stator core
    - Geometry
    - Properties
    - Mesh
  - Rotor windings
    - Geometry
    - Properties
    - Mesh
  - Rotor core
    - Geometry
    - Properties
    - Mesh
- **Prepare solver**
  - Define solver
  - Define airgap
  - Generate mesh
  - Create circuit

Figure 2.4: Flux 2D and Opera 2D base algorithms

of each region at the same time while Flux 2D does it separately.

The first step in the preparation of the induction motor models was the definition of auxiliary parameters. These are variables and constants containing information about the dimensions, circuit parameters, mesh and material properties. Flux 2D offers the

Flux 2D

- **Physics**
  - Define application
  - Define materials
    - Windings
      - Stator
      - Rotor
    - Cores
      - Stator
      - Rotor
    - Airgap
    - Shaft
  - *Define circuit*
  - Define mechanical sets
    - Stator
    - Rotor
    - Airgap*
  - Define and assign region faces
    - Windings
      - Stator
      - Rotor
    - Cores
      - Stator
      - Rotor
    - Airgap
    - Shaft
- ***Circuit***
  - Define equipotentials
    - PT1
    - Stator
    - Rotor
  - Define stator elements
    - Resistances
    - Inductances
    - Coil conductors
    - Voltage sources
  - Define rotor elements
    - Resistances
    - Inductances
    - Squirrel cage

Opera 2D

- **Auxiliar solution file**
  - Recalculate parameters
  - Save case

Figure 2.4: – continued from previous page

advantage that when the value of an auxiliary parameter is modified, the parts of the model where it was employed are modified as well. For instance, if the width of the teeth was defined using a variable and this was changed after the geometry was created, Flux 2D would update the geometry whilst Opera 2D would only modify the value of the

variable.

The next three steps are related to defining the geometry, mesh and material properties. Although both programs allow the user to prepare each of them separately, in Opera 2D it is better to define them together. These steps therefore were described separately for each software package.

Flux 2D requires the definition of coordinate systems, periodicity and auxiliary geometric transformations (rotation) prior to the creation of the geometry. First points and then lines are created to form the boundaries of cores, windings and other components in the machine. A command is then used to create geometrical faces using the previous drawings. One advantage of Flux 2D is that it permits the user to create geometrical regions with multiple boundaries, for instance a circular ring area. Figure 2.5a shows the geometry of the 5.5 kW benchmark motor created in Flux 2D.

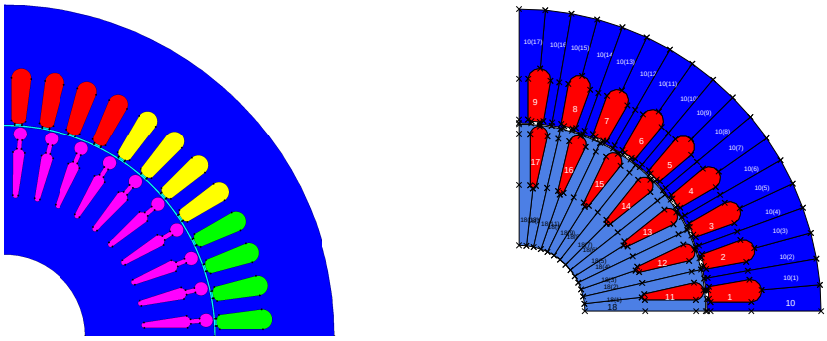

(a) Flux 2D (b) Opera 2D

Figure 2.5: Geometry

Both finite element analysis programs require definition of some auxiliary properties before mesh creation. Flux 2D allows the user to assign these properties for points, lines and faces. It also permits the user to define global mesh properties for automatic meshing of the whole geometry. The mesh can be generated after this step as shown in Figure 2.6.

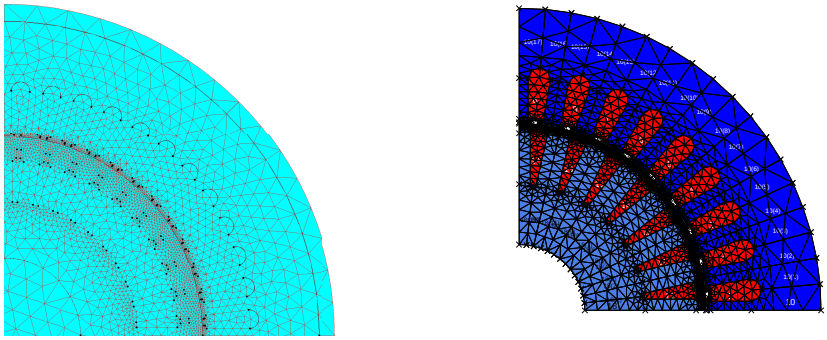

(a) Flux 2D (b) Opera 2D

Figure 2.6: Mesh

The next step is denominated "define the physics" according to the Flux 2D manual.

Initially, the application or problem type is defined. The next step is to define the materials and mechanical sets (groups of regions with the same motion). The previous information is used to define and assign the face regions. A face region group together with geometrical faces which are of the same material, belong to the same mechanical set and are part of the same element in the auxiliary electrical circuit.

An electrical circuit needs to be created to represent how the active electrical conductive components are connected to the power source, including end effects not represented by the 2D simplification of the problem. The equipotential connections are first defined and drawn which allows the creation and interconnection of resistances, inductors, voltage sources, coil conductors, solid conductors, squirrel cages, amongst other components. A section of the circuit for the Flux 2D model of the 5.5 kW benchmark motor is illustrated in Figure 2.7a.

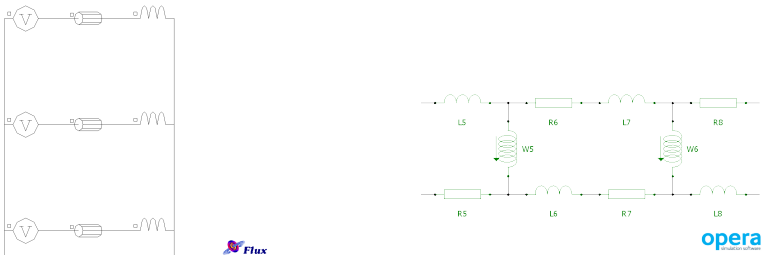

(a) Flux 2D (b) Opera 2D

Figure 2.7: Circuit connections

Opera 2D completes the last three steps together, defining all the properties with default values if they are not specified (Figures 2.5b and 2.6b). For this purpose, Opera 2D requires of the creation of regions. At the beginning of the definition of each region, the program requires specification of the material, associated elements of the auxiliary electrical circuit, symmetry and geometrical transformations. The coordinates are then specified point by point requiring the user to indicate the curvature, boundary conditions and mesh properties for the lines between them. This process is more straightforward than in Flux 2D but it requires some additional steps: definition of the solver and airgap, generation of the mesh and the auxiliary circuit. Opera 2D also requires auxiliary files with commands to guide the solution of the problem.

Both Flux 2D and Opera 2D offers two ways of interaction with the user: graphical user interface (GUI) or command-line. For the command-line interaction, Flux 2D uses a programming language called Pyflux (Python including the Flux 2D commands) whilst Opera 2D uses its own programming language. All the steps previously mentioned (with the exception of the auxiliary electrical circuit creation in Opera 2D), solution and post-processing of the results can be automated with the use of command files [52]. They have the extensions *.py for Flux 2D and *.comi for Opera 2D. Command files allow the user to generate libraries which can be employed on multiple projects. For example, a

specific slot geometry can be contained in a library and easily included in various different designs.

Both finite element packages allow rotor skew to be considered by means of a series of interconnected 2D slice models. Opera 2D however only allows these models for transient simulations. Figure 2.8 shows an example of the skew models for Opera 2D.

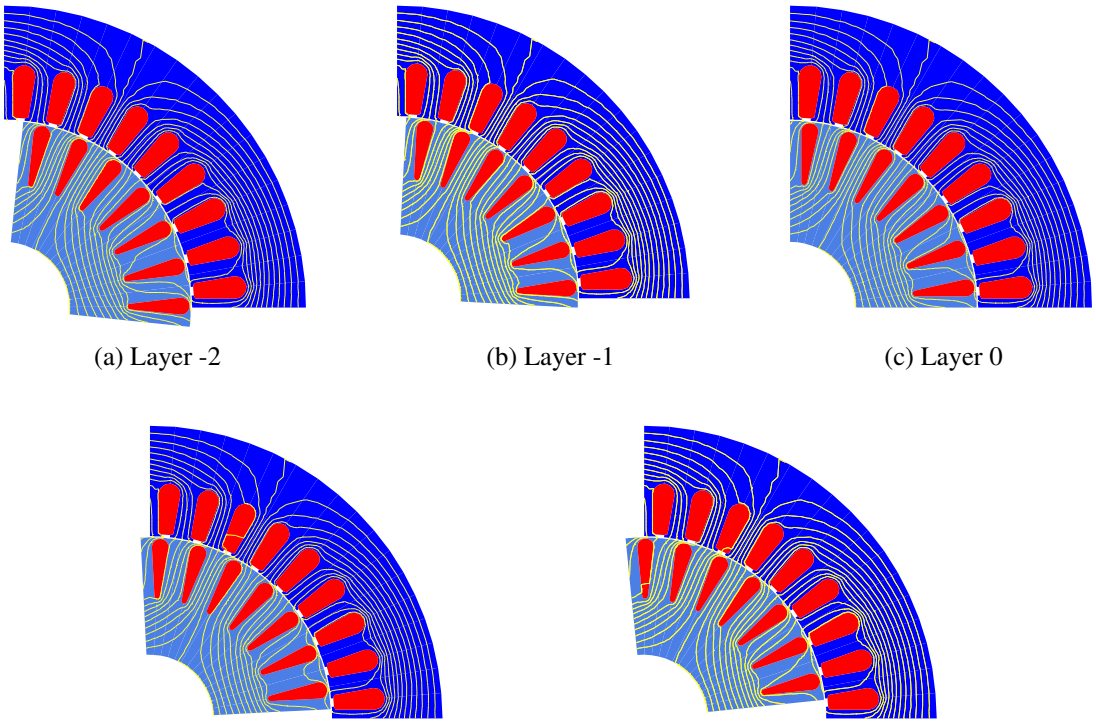

(a) Layer -2 (b) Layer -1 (c) Layer 0

(d) Layer 1 (e) Layer 2

Figure 2.8: Skew model in Opera 2D

2.4.4 Summary

This section has presented briefly the tools available for the design and performance evaluation of new designs. Special attention was given to the finite element method because it offers the highest accuracy when the designer is exploring novel or uncommon motor topologies.

2.5 Induction motor topology

Most of the induction machine designs available for traction applications are based on the industrial, fixed-speed, three-phase induction motor. However, if the designer decides to opt for an unconventional machine, a full review of choices in the basic structure and materials is needed. This section intends to cover this gap and also includes some

examples of unconventional high power/torque induction machines which were not designed for electric vehicle traction.

2.5.1 Structure

One of the initial choices involves the topology of the flux path. Axial and transverse flux designs present the inconvenience of requiring 3D models. Radial designs are simpler because they can normally be designed effectively using 2D models. All the models developed during this project were restricted to be 2D due to this simplicity as a first stage but further research must certainly explore 3D designs.

Even a simple decision such as the pole number selection become a complex procedure to determine the best option [53]. Sometimes, this may be dictated by the space available [54] or by the application speed [55]. The pole number can be also influenced by the operational strategy as in the case of pole changing windings [56].

Three phase stator windings are the predominant topology. But it is recognized that a higher phase number offers a series of advantages: reduced harmonics in the airgap field, lower torque pulsations and better fault tolerance [57–60]. For the case of the rotor, the selection of parameters such as the number of slots and their best shape is not straightforward even for squirrel cage machines [61–64].

It is important to note that the design process also becomes more difficult when the machine requirements are extreme, for example a high speed induction machine to operate under a high temperature environment [65]. This kind of application requires the consideration of designs with improved cooling which might require segmented core structures for example [66]. The structural design is also affected if the cooling circuits have components inside the active material area of the machine [67].

2.5.2 Materials

Materials used in the design of induction machines can be classified according to the active materials as part of the energy conversion process into two basic categories: magnetic and conducting. The selection of these materials during the design process is key in achieving the desired performance. The designer has to evaluate if standard materials are employed or if the application justifies the utilization of other special materials.

Magnetic materials for induction motors usually consists in laminations of a soft magnetic alloy. The most common is silicon iron whilst other alloys are reserved for special purposes. For example, cobalt iron has the highest magnetic flux density saturation as shown in Figure 2.9 but its costs are very high and vulnerable to market

speculation [68]. Cobalt iron laminations therefore are usually restricted to applications where the cost is not restrictive such as aerospace [69]. Other examples of soft magnetic lamination materials for special purposes will be mentioned in 2.5.8.

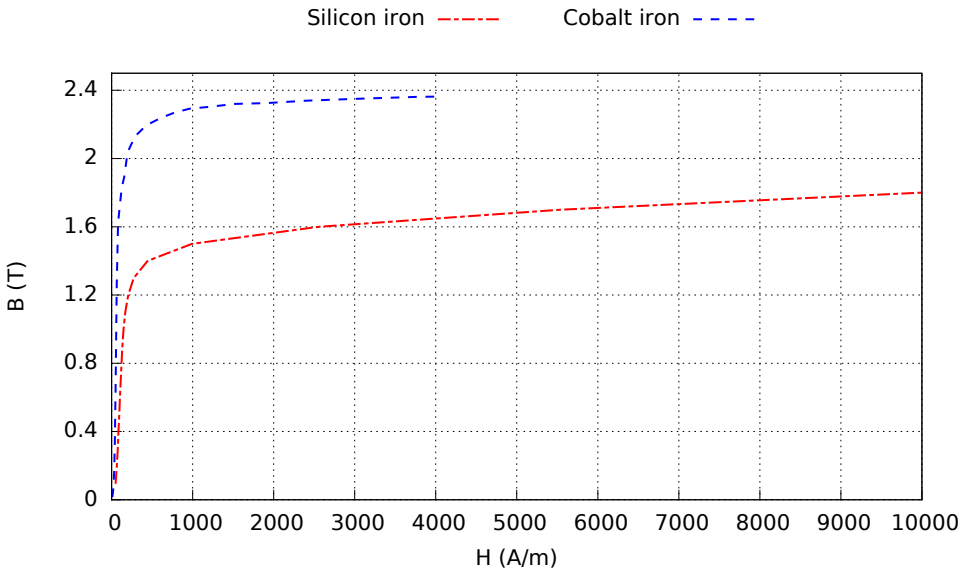

Figure 2.9: Silicon iron and cobalt iron laminations properties

An alternative to lamination material is composite materials. These are compacted iron powder particles coated by an insulating compound [70]. A study in the use of composite materials in electrical machines highlighted the possibility of constructing motors with complex geometries, for example axial-radial flux machines [71, 72]. However, the use of composite materials has not been completely satisfactory particularly for machines which require a high magnetic flux density [71]. The manufacturing process also requires moulding instead of machining for use in induction motor cores for example in order to prevent undesired eddy currents [73]. These disadvantages prevented their consideration during this project.

Amorphous and nanocrystalline materials also offer promising improvements in the efficiency of electric machines [74, 75]. Their main limitations lie in their manufacturing techniques and costs for mass production which is the reason they were not explored during this research.

Aluminium and copper are the most common conducting materials employed in induction machines. Both metals can be used to fabricate the stator windings whilst aluminium is the preferred material for the squirrel cage construction in the rotor. Thanks to the advances in copper casting technology, the fabrication of copper rotor cages offers potential for higher efficiency [76, 77].

The choice of active material is extremely important during the design process, other non-active materials are needed of course and are equally important although they are not directly involved in the energy conversion process. Some of these materials constitute parts of the insulation, cooling and structural systems. They can however have a major

influence over the electric loading. For example, high thermal conductivity resins can be employed to impregnate the machine windings which improves the thermal performance. Their use inside the slots is also necessary but it tends to reduce the fill factor and make coil assembly difficult unless coils are preformed and pressed [78].

2.5.3 Drive integration

An electric drive system couples the electric motor to the mechanical system and to the electronic power converter. There is a tendency to group and/or eliminate components of the powertrain. This allows weight and volume reduction and can also improve the performance. The interpretation and implementation of this concept differs but it increasingly attracts research interest.

One example of this tendency is known as direct drive which is an electric machine which has been designed to be coupled to the mechanical load through minimum mechanical components. This eliminates the necessity for gearboxes, differentials, clutches, amongst others. However, this means the electrical machine must operate with higher torques and lower speeds.

High torque is also a common requirement in ship propulsion and a good example of that is the ALSTOM advanced induction machine [79]. This machine was carefully designed for ship propulsion with the special requirements for naval applications. Power densities close to those of permanent magnet synchronous motors were obtained in this motor as a result of 15 years of continued improvement. The "pin-vent lamination" cooling employed is key in achieving only 20 % less torque than a permanent magnet motor [79].

Another high torque density induction machine for marine propulsion was designed in [55]. Authors searched for the best induction motor topology to compete against a permanent magnet motor. They achieved a design with only 15 % less torque density than a permanent magnet motor. The authors found that pole numbers were an important factor to high torque density. Adopting a design strategy to maximize the torque density, it was shown that between eight and ten poles allowed higher torque densities using air ducts.

Researchers from the University of Manchester and Rolls-Royce developed a multiple-can rim-drive induction machine [15]. This was employed as a bidirectional thruster for a tidal stream turbine. Figure 2.10 shows the multiple layers of the multi-can rotor instead of a squirrel cage. Cans provide a simple structure and protection from the sea environment. It operates under a very low duty cycle (4 times a day for approximately 2 minutes).

The naval industry is not the only one with developments in low speed high torque machines, many examples can also be found in the pulp, paper and cement industries amongst others. In these industrial applications, it has been found that an induction

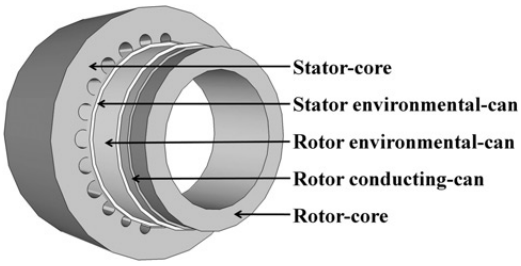

Figure 2.10: Rim-drive motor [15]

motor direct drive option is strongly recommended for applications with speeds over 600 RPM [80]. While for processes demanding between 300 and 600 RPM a comparison of direct drive and geared solutions should be undertaken [80]. Geared solutions are usually the best option for application under 300 RPM [80].

The direct drive integration of electrical machines has been adopted across the ranges from large scale applications down to miniature sizes. The biggest power ratings can be found in specific industries such as cement, paper and naval. Miniature applications include areas such as biomedical and bioengineering. Figure 2.11, for example, shows a small induction motor pump with impeller integrated with the rotor suitable for biomedical purposes [81].

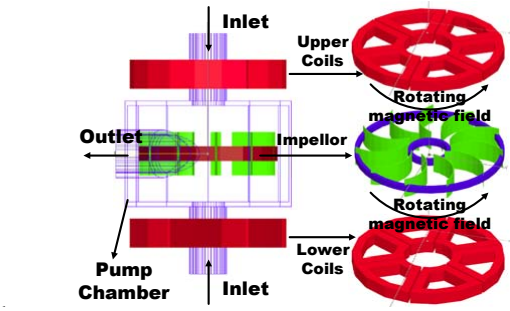

Figure 2.11: Inductively-driven shaft-less pump [81]

Wound induction machines are an alternative for variable speed direct drive applications. The stator is connected directly to the main supply and the speed can be regulated through resistances or power electronics connected to the rotor windings via slip rings [82, 83].

The Universidade Federal de Santa Catarina and WEG designed, constructed and tested a wound rotor induction motor without slip rings. As shown in Figure 2.12, power was transferred to the rotor through three rotary transformers attached to the machine shaft. The main disadvantage was the lower power factor as a consequence of the transformers [84].

Another approach to direct drive is the use of magnetic gears. These devices offer a compact solution but they also employ permanent magnets. An example of a permanent magnet machine integrated with the magnetic gear is shown in Figure 2.13 [85].

Integration can also take place with the power converter. For example, a permanent

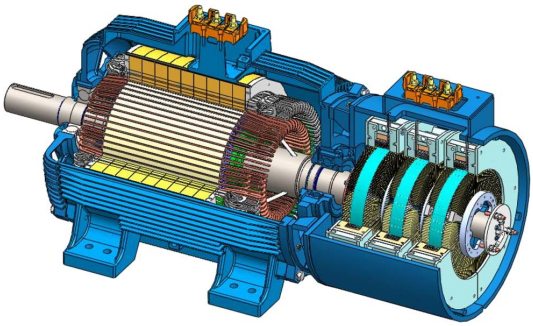

Figure 2.12: Doubly-fed induction machine with rotary transformers [84]

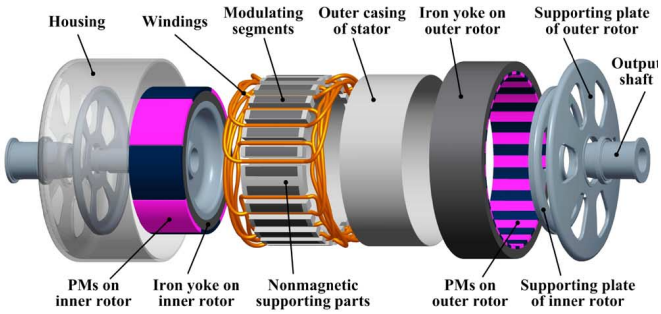

Figure 2.13: Integrated magnetic-geared machine [85]

magnet motor uses concentrated windings and composite materials [86]. Figure 2.14 illustrates how each section has its own corresponding power electronic module. This constructional integration was quite straightforward but more complex structure machines are expected to appear in the future [86].

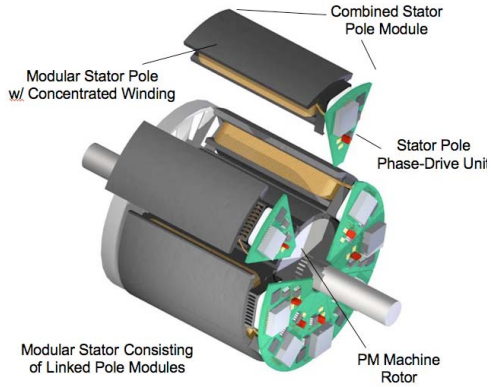

Figure 2.14: Integrated modular motor drive [86]

Most of these direct drive machines presented in this section have further potential to improve the design of induction machines with specific torque levels close to the permanent magnet machines. However, most of them, except the canned rotor induction motor, were not further explored during this research because they require of 3D simulations.

2.5.4 Non-sinusoidal airgap flux distribution

The use of a non-sinusoidal airgap flux distribution allows an increase in the peak of the fundamental field without saturating the core. This gives a higher torque production because the magnetic loading is increased. For example, an eight-pole five-phase induction machine design employed a rectangular flux distribution and a multiphase concentrated winding to improve the core utilization [87]. Researchers showed that multiphase PWM drives operate with a conventional multiphase induction machine in a satisfactory manner but not optimally. Hence authors applied Fourier analysis to study and evaluate the performance of their proposed machine claiming a 10 % torque increase [88].

An improvement of up to 40 % more torque was achieved using a non-sinusoidal airgap flux distribution in [89]. Figure 2.15 shows how third harmonic currents were injected to reshape the flux distribution and obtain a higher fundamental without saturation in a six-phase induction machine composed of two three-phase groups displaced by thirty electrical degrees. The injection of third harmonic currents synchronized with the fundamental was also employed in a seven-phase four-pole high torque density induction motor at the University of Bologna [90–92].

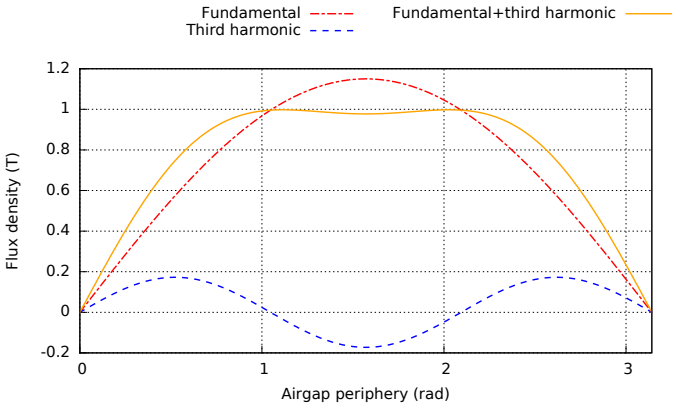

Figure 2.15: Third harmonic injection

Although this technique has been explored in detail by several authors, further potential exists in its combination with other techniques. So, some of the designs explored during this research were combined with the third harmonic current injection.

2.5.5 Special flux paths

There are two main airgap flux trajectories in rotating electrical machines: radial and axial. Radial is the most common because it is simple to design and manufacture. Some researchers claim that axial is more compact and allows the ability to divide the machine into modules [93, 94]. However, the equations were oversimplified and assumed that all of the axial area can be utilized and this may overstate the advantages of axial machines [95].

Permanent magnet motors can adopt complex structures more easily compared with induction motors. This is because they can tolerate higher harmonics in the flux distribution without a significant performance deterioration due to the rotor mainly responds to the fundamental flux. For example, Figure 2.16 illustrates the stator of a three-phase transverse flux permanent magnet motor [96]. Transverse flux machines are more complex to design requiring 3D analysis techniques. Manufacture is also more difficult. Each phase is a section with a claw-pole structure shifted from the other phases [96]. An induction motor version might be feasible. But further research is necessary to determine if the torque density can be improved.

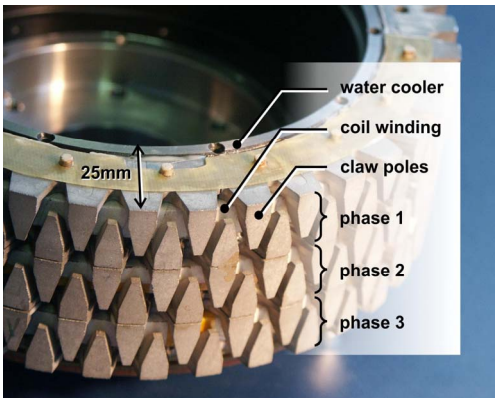

Figure 2.16: Transverse flux motor [96]

Electrical motors with complex flux paths are sometimes necessary when the machine has to fit into unconventional spaces. A particular motor example adapted to its spacial environment is the downhole pump [97]. This machine has an adapted stator geometry to accommodate four large axial channels. Figure 2.17 shows a section of this machine including one of the axial channels.

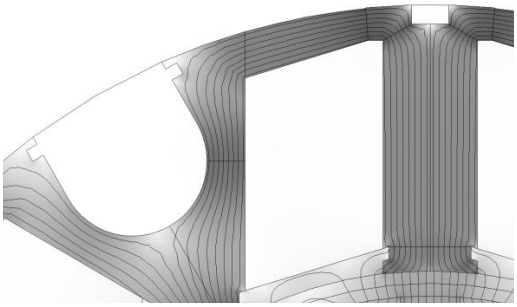

Figure 2.17: Motor with large axial channels [97]

The flux path can also be modified by the inclusion of slits in the magnetic core. This technique has been used to improve the torque production in solid rotors [98]. Nevertheless, the presence of slits requires a balance between performance improvement and maintaining the mechanical strength of the rotor specially for high speed applications. The slit inclusion technique will be further explored during this research because it could help to modify the leakage paths.

2.5.6 Multiple rotors and/or stator

Investigators have proposed machines with multiple rotors and/or stator in order to improve the torque density or to eliminate the necessity for a differential. For induction machines, this implies the presence of two or more airgaps which increases the magnetizing current requirements with implications in terms of power factor and efficiency. Nevertheless, these structural changes allow a reduction of the flux leakage and an improved cooling area which might justify the complex manufacture [99]. For this reason, multiple stators designs were considered and explored in this project.

A high torque induction motor with free rotating magnets inside the rotor and a rectangular flux density distribution was developed in Japan [100, 101]. Researchers claimed an improvement of up to 30% in torque due to the increase in the magnetic flux linkage inside the rotor [100]. The structure of this unconventional machine is shown in Figure 2.18.

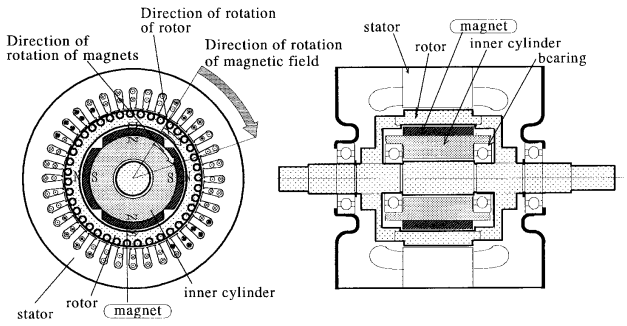

Figure 2.18: Induction motor with free-rotating magnets inside its rotor [101]

Double stator construction has also been applied successfully to improve the torque in a solid rotor motor [102]. This rotor was composed of a hollow structure which resulted in a low inertia. The power factor and efficiency were also improved in this machine.

Each rotor or stator can be of a different type in these machines. This is useful for example in a variable transmission system [103]. Figure 2.19 shows how the internal combustion engine drives the inner wound induction rotor and the transmission system is coupled to the permanent magnet middle rotor. This machine eliminates any mechanical coupling between the wheels and the motors. However, it requires slip rings which increases the maintenance requirements and costs.

2.5.7 Special windings

Unconventional windings have been adopted to increase the slot fill factor and/or reduce leakage inductances. These modifications improve the torque density, power factor and efficiency but at the expense of a more complex manufacturing process.

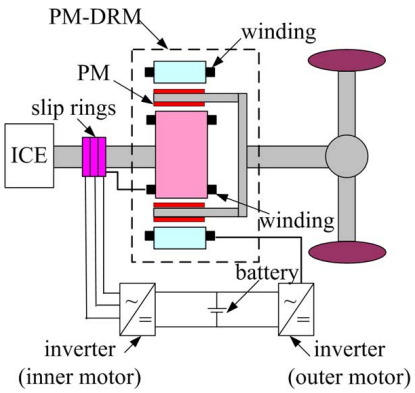

Figure 2.19: Hybrid double-rotor motor [103]

There are six main approaches to increase the fill factor in the stator [104]: employing skilled and very experienced workers; preform the windings; use of rectangular, hexagonal, foil or triangular wire profiles; utilizing modular windings; post-forming direct compression of the windings employing single press or multi-impact techniques; and preforming the coil by encapsulation with a thermoplastic material or water. The first solution is not suitable for mass production. The next four techniques are the most common employed whilst the last one is still at the conceptual stage [104].

Preformed windings are well known in industry but they are usually reserved for large machines due to cost and space restrictions. Researchers at the Hyundai Mobis Co have built a permanent magnet motor for electric vehicles with windings formed by individual square conductors welded to the end turns [105]. Similar compact stator construction could be obtained by employing preformed windings inserted into open slots [106]. The slots can then be closed with magnetic wedges improving the airgap flux distribution, power factor, efficiency and magnetizing current [106].

A slot fill factor of up to 85 % was achieved at Mitsubishi Electric with the 9G stator motor [107]. Figure 2.24 shows how the preformed distributed windings were inserted into the flat core composed of laminated strips, the stator was then shaped mechanically to form a ring. This option was not explored during this research because of the manufacture facilities limitations.

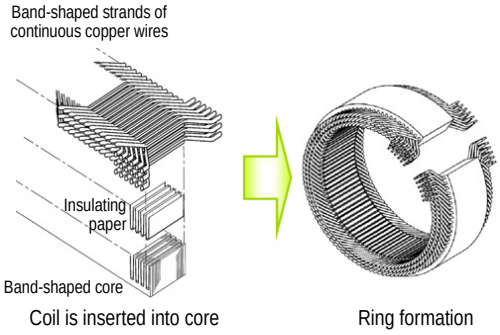

Figure 2.20: Manufacturing of the 9G stator [107]

A new planar preformed winding was proposed for an in-wheel axial flux permanent magnet machine [108]. Figure 2.21 illustrates the manufactured coils which were inspired by printed circuit techniques. These windings were core-less which meant a large airgap making them less suitable for induction motors. Nevertheless, improved versions of this winding type are worth further research. However, this machine was not considered for further developed in this research due to its complex modelling using 2D tools.

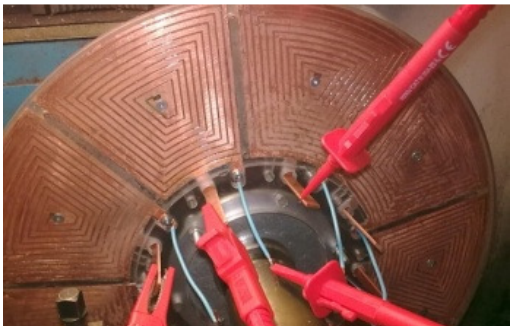

Figure 2.21: Planar windings [108]

Modular windings are concentrated coils which do not overlap offering a more compact construction. This allows an increase in the slot fill factor and a reduction in the length of the end windings; for this reason a modular winding design is presented later in this project. A review of this winding type was presented by General Electric focusing on the advantages and challenges for each motor type [109, 110]. Another review focusing on the manufacture and the utilization of complex core constructions can be found in [111].

These windings have also been applied successfully mainly in permanent magnet machines to improve the torque density. In contrast, their implementation in induction machines usually increases the machine size due to the required very short-pitched coils for a low harmonic content in the airgap flux distribution. A modular high voltage five-phase induction motor has been proposed to improve the insulation [112]. Figure 2.22 shows the stator diagram of this machine which was 30% bigger than the conventional design. Despite the reduced end winding dimensions, the efficiency was lower as a result of the increased turns per phase winding. Modular windings have been also applied to a six-pole single phase induction motor but a 23° skew angle was required to reduce the harmonics [113]. This single phase machine kept the same volume of active material and achieved a significant reduction in the end winding size.

Toroidal machines are another type with non-overlapping and short-end windings. Researchers from Newcastle University developed a toroidal winding induction motor [114]. The main disadvantage was that the coils only linked half of the airgap flux per pole. Three methods of construction were considered: segmented stator; preformed flat strap core which is ring shaped after winding; and open slot construction [115]. The second of these methods was employed to built a machine as shown in Figure 2.23. It was claimed that a 55 % slot fill factor could be achieved. A toroidal design is included

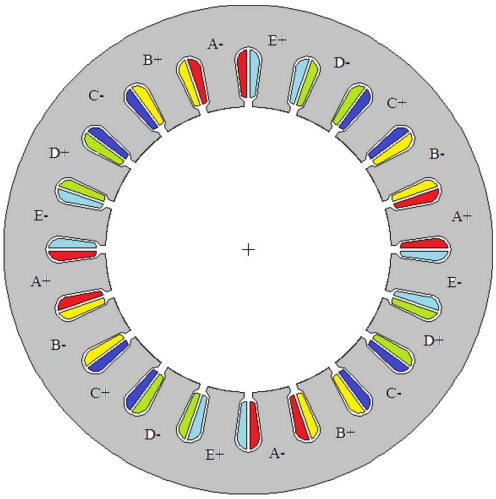

Figure 2.22: Modular winding induction machine [112]

in this thesis because of its compacted coils and end-windings which could potentially improve the specific torque.

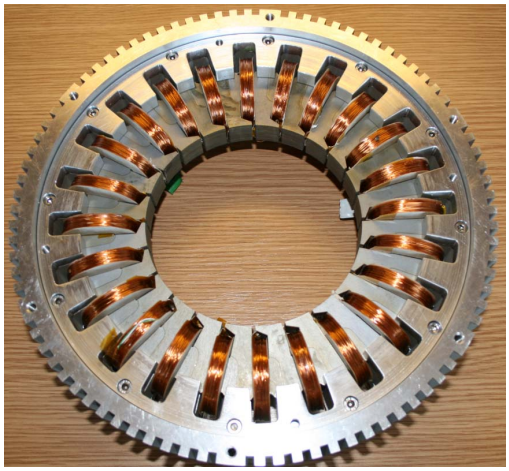

Figure 2.23: Stator of a toroidal wound induction motor [115]

Non-conventional designs have also been implemented in the rotor. An alternative to the squirrel cage winding was developed by Hitachi [116]. Figure 2.24 shows this special rotor structure composed of compacted copper clad steel wires aligned in the radial direction. This rotor, called a matrix rotor, explored the use of a magnetically anisotropic solid material for improving the torque production [116]. A more detailed numerical analysis was presented 23 years later [117].

Another solid rotor structure with improved performance was the spiral sheet rotor [118]. This was composed of a series of lamination sheets compacted in a spiral as shown in Figure 2.25. Its main advantage consisted in a wide slip range without exceeding the thermal and mechanical limits. It was suitable for variable load regimes with frequent start and stops, requiring low starting currents. The main drawback was the complex manufacture so it was not further explored during this project.

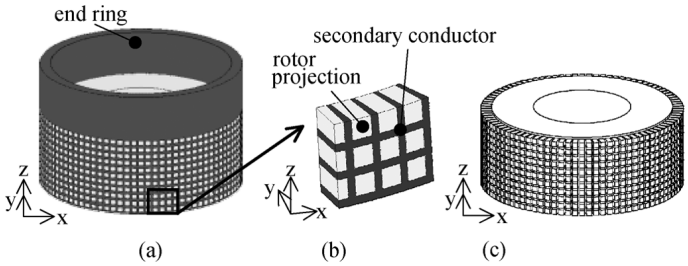

Figure 2.24: Matrix-rotor induction motor [117]

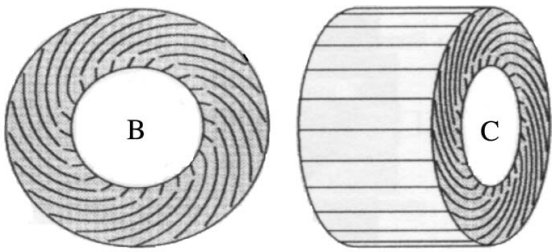

Figure 2.25: Spiral sheet rotor [118]

Finally, the importance of the cooling system should be highlighted as it determines the maximum electric loading. A direct cooling system in the stator windings is reported to be an effective way of improving the torque density [119].

2.5.8 Special magnetic cores

It is well known that the use of cobalt iron laminations in electrical motors allows the reduction of the volume and mass. Some researchers have reported a size improvement of about 10 % [120]. This is because of the higher magnetic loading compared with the standard silicon iron laminations. Nevertheless, the cost of cobalt iron materials is high and fluctuating, restricting its application mainly to the aeronautical and space industries.

The use of low silicon content electrical laminations is a more economical approach to increase the magnetic loading [119]. A similar method was explored during this project by using a solid rotor core. Another affordable technique to improve this loading consists of using grain-oriented silicon iron laminations. This was implemented using a segmented core construction of a synchronous permanent magnet machine [121]. Some researchers have proposed the use of grain-oriented silicon iron only in the teeth of a switched reluctance motor [122]. The developed machine is shown in Figure 2.26. Although a higher torque was achieved, this construction resulted in a weaker mechanical structure and more complex manufacture. A segmented induction motor with grain oriented laminations was developed during this research due to its higher magnetic loading.

Anisotropic materials increase the complexity of the simulation models. For this reason,

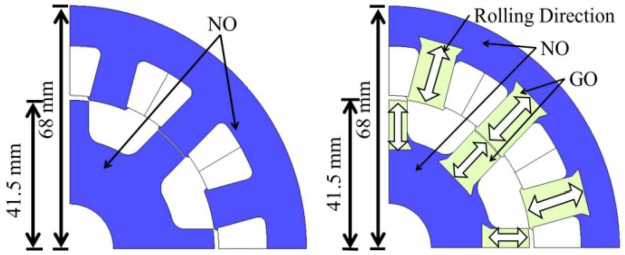

Figure 2.26: Switched reluctance motor with grain-oriented electric steel [122] (Grain oriented - GO, Non oriented - NO)

investigators have proposed the use of shifted laminations of grain oriented silicon steel as shown in Figure 2.27 [123]. An equivalent isotropic model could then be employed for simulation purposes [123]. This research is still in its early stages and has not been applied to a rotating electrical machine.

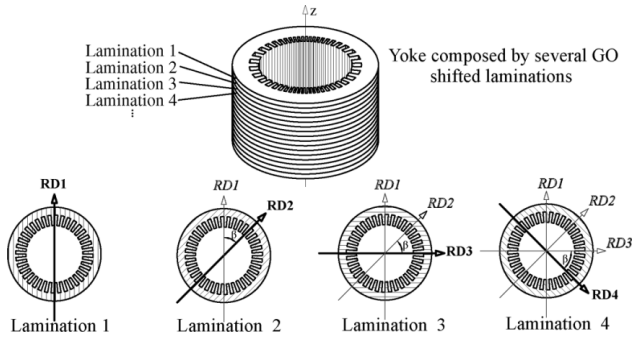

Figure 2.27: Grain-oriented steel assembly for rotating electrical machines [123] (Radial direction - RD)

In the windings section, the benefits of open slots were mentioned at the expense of higher harmonic torques. It was suggested that the use of magnetic wedges could compensate for the undesired effects. Another solution consists in the use of laminations with unequal stator teeth [120]. But this requires of transient simulations which over difficult the design process.

2.5.9 Summary

This section reviewed the changes and novel topologies in electrical machines which explore the use of materials and topologies for higher power/torque production. Although many of the machines presented are not induction machines, most of the design changes could be implemented in induction motors.

2.6 Induction machine operation

The design of induction machines is highly influenced by the duty cycle. As mentioned in the previous chapter, the traction motor would be operating dynamically dictated by the driving cycle and the interaction of the components of the drivetrain. This section aims to highlight some of the operational conditions for the induction machine which have an important influence in the design.

2.6.1 Speed-range considerations

The design procedure for electrical machines is also influenced by the converter operation in variable speed applications where voltage becomes typically the main restriction above base speed [124–126]. The optimal speed ratio is of significant importance due to its influence over volume and weight for the drivetrain. Typical values might be between 1 to 5 whilst one study suggests that the optimal value is about 3 for a 4 pole induction motor [127].

Changing connections can be used to overcome the voltage limit above base speed and wide speed range operation. For example, open winding machines driven by a cascaded inverter topology [128]. This has been reported to increase the high-speed power density of an induction motor by approximately 73 % [128].

The ratio between the pull out and the nominal torque at base speed is a good indicator of the speed range that can be achieved whilst maintaining constant power output by a particular induction machine [129]. In other words, the speed range ratio at constant power is approximately equal to the ratio between the pull out torque and the nominal torque at base speed [129].

2.6.2 Dynamic considerations

According to [130], the traction motor must withstand 3 different duty cycle modes at base speed: continuous, intermittent and peak. During the first, the electric motor could operate continuously for any period of time [130]. The intermittent mode involves the ability of the motor to provide from 4/3 to 5/3 of the continuous torque for short time transients(<30 s) [130]. Finally, peak torque required is about 2.5 times the continuous torque in order to overcome engine crankshaft stiction - cold start (<50 ms) [130].

2.6.3 Thermal considerations

As the designs tend to further exploit the materials of an induction machine, there tends to be an impact on the thermal performance requiring the machine to operate at higher temperatures. This is highly dependant on the dynamic operation. For the continuous operating mode, the temperature must not exceed the limits imposed by the materials. However, for intermittent and peak modes of operation the induction motor in electric vehicles tends to operate safely within the temperature constraints. This is because of the relatively large thermal time constant of an induction machine compared with the cycle times mentioned for these operating conditions (30 s and 50 ms). References [131, 132] present Equation 2.1 which allows the designer to estimate rapidly the thermal time constant of an induction motor (τ_{IM}). For example, the authors in [131, 132] found that the thermal time constants were larger than 10 minutes for motors under about 1 kW with the tendency to increase for larger machines.

$$\tau_{IM} = \frac{420G}{K_m L_f \pi D_f \alpha_\tau} \tag{2.1}$$

where

G - mass of the induction motor (kg)

K_m - coefficient to consider the incremease of the frame surface due to its edges

L_f - length of the stator frame (m)

D_f - diameter of the stator frame (m)

$\alpha_\tau = 14 + 56\frac{n}{n_s}$, - heat transfer coefficient of unit frame surface (W/m^2K)

2.6.4 Summary

This section has described the three main operating conditions that need considering when designing an induction machine. This can be summarised as the influence of speed range, dynamic and thermal considerations on the nominal rating of the machine. For the case of electrical vehicles, the speed range and thermal requirements impose the most important restrictions.

2.7 Conclusions

A review of the design process has become necessary to find alternative options to standard designs and to identify procedures which might have been neglected. It would

also be useful to evaluate as many new designs as possible in order to identify the opportunities and challenges. This would need benchmarks to be defined in order to make an objective comparison and selection of the best designs. Manufacture and experimental tests would also deliver valuable results and experience for discussion.

This chapter has presented a review of the design process from a historical and technical prospective. History shows that the design of electrical machines is a process which has been in constant evolution contradicting the perception that the induction motor can not be improved significantly. The technical challenges include the proposition of new design methodologies focusing on the creative side of the process without ignoring the rigorous calculations required, for example using finite elements.

The maturity of induction machines requires a review from the very beginning of the design process in order to obtain new designs capable of being competitive for electric vehicle applications. This could be done by proposing new topologies. However, few authors have done this because radical changes are perceived to produce only small improvements which makes it difficult to justify the change in the manufacture process of this mature industry.

This research is intended to challenge this tendency by searching and evaluating new designs considering the operational requirements and constraints discussed in this chapter.

2.8 References

[1] Nikola Tesla, "A New System of Alternate Current Motors and Transformers", *American Institute of Electrical Engineers, Transactions of the*. V, 308–327. (1888).

[2] B.G. Lamme, "The story of the induction motor", *American Institute of Electrical Engineers, Journal of the*. 40, 203–223. (1921).

[3] H.E. Green, "A short history of the induction motor", *Students' Quarterly Journal*. 12, 34–36. (1941).

[4] W.B. Esson, "Notes on the design of multipolar dynamos", *Electrical Engineers, Journal of the Institution of*. 20, 265–289. (1891).

[5] B.A. Behrend. *The Induction Motor and Other Alternating Current Motors: Their Theory and Principles of Design*. McGraw-Hill, 1921.

[6] M.G. Say and E.N. Pink. *The performance and design of alternating current machines: transformers, three-phase induction motors and synchronous machines*. Engineering degree series. Sir I. Pitman & sons, Ltd., 1936.

[7] P.L. Alger. *Induction Machines: Their Behavior and Uses*. Gordon and Breach, 1970.

[8] Comfort A. Adams, "The Design of Induction Motors; With Special Reference to Magnetic Leakage", *American Institute of Electrical Engineers, Transactions of the*. XXIV, 649–684. (1905).

[9] Philip L. Alger and R.E. Arnold, "The history of induction motors in America", *Proceedings of the IEEE*. 64, 1380–1383. (1976).

[10] E. Levi. *Polyphase motors: a direct approach to their design*. A Wiley-Interscience Publication. Wiley, 1984.

[11] P. Cochran. *Polyphase Induction Motors, Analysis: Design, and Application*. Electrical and Computer Engineering. Taylor & Francis, 1989.

[12] S. Williamson and E.R. Laithwaite, "Generalised harmonic analysis for the steady-state performance of sinusoidally-excited cage induction motors", *Electric Power Applications, IEE Proceedings B*. 132, 157 –163. (1985).

[13] V. Ostović. *Dynamics of saturated electric machines*. SPRINGER VERLAG GMBH, 1989.

[14] E.S. Hamdi. *Design of small electrical machines*. Design and measurement in electronic engineering. Wiley, 1994.

[15] P.M. Tuohy et al., "Rim-drive marine thruster using a multiple-can induction motor", *Electric Power Applications, IET*. 7, 557–565. (2013).

[16] T.A. Lipo. *Introduction to AC Machine Design*. Wisconsin Power Electronics Research Center, University of Wisconsin, 2004.

[17] E.R. Laithwaite. *Induction Machines for Special Purposes*. Newnes international monographs on electrical engineering and electronics. George Newnes, 1966.

[18] A. Harson, P.H. Mellor, and D. Howe. "Design considerations for induction machines for electric vehicle drives". In: *Electrical Machines and Drives, 1995. Seventh International Conference on (Conf. Publ. No. 412)*. 1995, pp. 16 –20.

[19] Huijuan Liu et al. "Design and Simulation of An Inverter-fed Induction motor for Electric Vehicles". In: *Vehicle Power and Propulsion Conference, 2007. VPPC 2007. IEEE*. 2007, pp. 112 –115.

[20] J.A. Moses et al. "A computer-based design assistant for induction motors". In: *Industry Applications Society Annual Meeting, 1991., Conference Record of the 1991 IEEE*. 1991, 1–7 vol.1.

[21] M. Nurdin, M. Poloujadoff, and A. Faure, "Synthesis of squirrel cage motors: a key to optimization", *Energy Conversion, IEEE Transactions on*. 6, 327 –335. (1991).

[22] A. Boglietti et al. "Induction motor design methodology based on rotor diameter progressive growth". In: *Energy Conversion Congress and Exposition (ECCE), 2011 IEEE*. 2011, pp. 3104 –3111.

[23] Dong-Hyeok Cho, Hyun-Kyo Jung, and Cheol-Gyun Lee, “Induction motor design for electric vehicle using a niching genetic algorithm”, *Industry Applications, IEEE Transactions on*. 37, 994 –999. (, Jul/Aug, 2001).

[24] A.C. Smith and D. Delgado. “Automated AC winding design”. In: *Power Electronics, Machines and Drives (PEMD 2010), 5th IET International Conference on*. 2010, pp. 1 –6.

[25] Jin-Kyu Byun, Song-Yop Hahn, and Il-Han Park, “Topology optimization of electrical devices using mutual energy and sensitivity”, *Magnetics, IEEE Transactions on*. 35, 3718 –3720. (1999).

[26] D.-H. Kim, J.K. Sykulski, and D.A. Lowther, “The Implications of the Use of Composite Materials in Electromagnetic Device Topology and Shape Optimization”, *Magnetics, IEEE Transactions on*. 45, 1154 –1157. (2009).

[27] Jang-Sung Chun, Hyun-Kyo Jung, and Joong-Suk Yoon, “Shape optimization of closed slot type permanent magnet motors for cogging torque reduction using evolution strategy”, *Magnetics, IEEE Transactions on*. 33, 1912 –1915. (1997).

[28] S. Williamson and A.C. Smith. “Induction motor modelling-choosing the tool to do the job”. In: *Modeling the Performance of Electrical Machines (Digest No: 1997/166), IEE Colloquium on*. 1997, pp. 1/1–1/4.

[29] A. F. Puchstein, “Calculation of Slot Constants”, *American Institute of Electrical Engineers, Transactions of the*. 66, 1315 –1323. (1947).

[30] S.A. Swann and J.W. Salmon, “Effective resistance and reactance of a rectangular conductor placed in a semi-closed slot”, *Electrical Engineers, Proceedings of the Institution of*. 110, 1656 –1662. (1963).

[31] S. Williamson and M.A. Mueller, “Calculation of the impedance of rotor cage end rings”, *Electric Power Applications, IEE Proceedings B*. 140, 51 –60. (1993).

[32] Stephen Williamson and Rich Schiferl, “An Investigation of the Influence of Deep-Bar Effect on the Resistance of Cage Rotor End-Rings”, *Industry Applications, IEEE Transactions on*. IA-23, 696 –704. (1987).

[33] M. Freese. “Analytic calculation of turbo generator end winding inductances using Neumann’s formula”. In: *Power Electronics Electrical Drives Automation and Motion (SPEEDAM), 2010 International Symposium on*. 2010, pp. 1597 –1602.

[34] M. Freese. “Comparison between an analytic method and a numerical calculation to determine the end winding inductances of a turbo generator”. In: *Electrical Machines (ICEM), 2010 XIX International Conference on*. 2010, pp. 1 –5.

[35] C.J. Carpenter, “The application of the method of images to machine end-winding fields”, *Proceedings of the IEE - Part A: Power Engineering*. 107, 487 –500. (1960).

[36] J.F. Eastham and S. Williamson, “Generalised theory of induction motors with asymmetrical airgaps and primary windings”, *Electrical Engineers, Proceedings of the Institution of*. 120, 767 –775. (1973).

[37] S. Williamson and A.C. Smith, “Field analysis for rotating induction machines and its relationship to the equivalent-circuit method”, *Electric Power Applications, IEE Proceedings B*. 127, 83 –90. (1980).

[38] S. Williamson and A.C. Smith, “Equivalent circuits for cage induction motors with inter-bar currents”, *Electric Power Applications, IEE Proceedings* -. 149, 173 –183. (2002).

[39] S. Williamson and A.C. Smith, “A unified approach to the analysis of single-phase induction motors”, *Industry Applications, IEEE Transactions on*. 35, 837 –843. (, Jul/Aug, 1999).

[40] B.J. Chalmers and R. Dodgson, “Saturated leakage reactances of cage induction motors”, *Electrical Engineers, Proceedings of the Institution of*. 116, 1395 –1404. (1969).

[41] J.C. Moreira and T.A. Lipo. “Modelling of saturated AC machines including air gap flux harmonic components”. In: *Industry Applications Society Annual Meeting, 1990., Conference Record of the 1990 IEEE*. 1990, 37 –44 vol.1.

[42] T. Lubin et al., “Comparison Between Finite-Element Analysis and Winding Function Theory for Inductances and Torque Calculation of a Synchronous Reluctance Machine”, *Magnetics, IEEE Transactions on*. 43, 3406 –3410. (2007).

[43] M. Amrhein and P.T. Krein. “Magnetic Equivalent Circuit Simulations of Electrical Machines for Design Purposes”. In: *Electric Ship Technologies Symposium, 2007. ESTS ’07. IEEE*. 2007, pp. 254 –260.

[44] M. Amrhein and P.T. Krein. “Magnetic Equivalent Circuit Modeling of Induction Machines Design-Oriented Approach with Extension to 3-D”. In: *Electric Machines Drives Conference, 2007. IEMDC ’07. IEEE International*. Vol. 2. 2007, pp. 1557 –1563.

[45] M. Yilmaz and P.T. Krein. “Capabilities of finite element analysis and magnetic equivalent circuits for electrical machine analysis and design”. In: *Power Electronics Specialists Conference, 2008. PESC 2008. IEEE*. 2008, pp. 4027 –4033.

[46] Jong-Ho Jeong, Eun-Woong Lee, and Hyun-Kil Cho. “Analysis of transient state of the squirrel cage induction motor by using magnetic equivalent circuit method”. In: *Electrical Machines and Systems, 2003. ICEMS 2003. Sixth International Conference on*. Vol. 2. 2003, 720 –723 vol.2.

[47] S.D. Sudhoff et al., “Magnetic Equivalent Circuit Modeling of Induction Motors”, *Energy Conversion, IEEE Transactions on*. 22, 259 –270. (2007).

[48] M. Sawahata et al. “Magnetic flux density analysis of wound rotor induction motor by permeance model”. In: *Electrical Machines and Systems, 2009. ICEMS 2009. International Conference on*. 2009, pp. 1 –6.

[49] H. Gholizad et al. “Motional eddy currents analysis in moving solid iron using magnetic equivalent circuits method”. In: *Wireless Communications and Applied Computational Electromagnetics, 2005. IEEE/ACES International Conference on*. 2005, pp. 533 –536.

[50] A. Davoudi et al., “Reduced-Order Modeling of High-Fidelity Magnetic Equivalent Circuits”, *Power Electronics, IEEE Transactions on*. 24, 2847 –2855. (2009).

[51] S. Williamson and M.J. Robinson, “Calculation of cage induction motor equivalent circuit parameters using finite elements”, *Electric Power Applications, IEE Proceedings B*. 138, 264 –276. (1991).

[52] *Dynamic Design of a Reluctance Synchronous Machine utilising Python Scripting in Flux* 60 (Apr. 2010).

[53] Feng Liang et al., “Selection of the pole number of induction machines for variable speed applications”, *Industry Applications, IEEE Transactions on*. 31, 304 –310. (, Mar/Apr, 1995).

[54] L. Ferraris et al. “Iron losses analysis with different supply techniques in high poles number induction motors for automotive applications”. In: *Industrial Electronics, 1999. ISIE ’99. Proceedings of the IEEE International Symposium on*. Vol. 2. 1999, 651 –655 vol.2.

[55] R. Lateb et al. “Performances comparison of induction motors and surface mounted PM motor for POD marine propulsion”. In: *Industry Applications Conference, 2005. Fourtieth IAS Annual Meeting. Conference Record of the 2005*. Vol. 2. 2005, 1342 –1349 Vol. 2.

[56] M. Osama and T.A. Lipo. “Modeling and analysis of a wide speed range induction motor drive based on electronic pole changing”. In: *Industry Applications Conference, 1996. Thirty-First IAS Annual Meeting, IAS ’96., Conference Record of the 1996 IEEE*. Vol. 1. 1996, 357 –364 vol.1.

[57] J.M. Apsley et al., “Induction motor performance as a function of phase number”, *Electric Power Applications, IEE Proceedings* -. 153, 51–60. (2006).

[58] S. Williamson and S. Smith. “Pulsating torque and losses in multiphase induction machines”. In: *Industry Applications Conference, 2001. Thirty-Sixth IAS Annual Meeting. Conference Record of the 2001 IEEE*. Vol. 2. , 30 Sep-4 Oct, 2001, 1155 –1162 vol.2.

[59] E. Levi et al., “Multiphase induction motor drives - a technology status review”, *Electric Power Applications, IET*. 1, 489 –516. (2007).

[60] H.E. Jordan, Jr. Zowarka R.C., and S.B. Pratap, “Nine-phase armature windings design, test, and harmonic analysis”, *Magnetics, IEEE Transactions on*. 41, 299–302. (2005).

[61] J. Le Besnerais et al., “Optimal Slot Numbers for Magnetic Noise Reduction in Variable-Speed Induction Motors”, *Magnetics, IEEE Transactions on*. 45, 3131 –3136. (2009).

[62] Jae-Woo Kim, Byung-Taek Kim, and Byung Il Kwon, “Optimal stator slot design of inverter-fed induction motor in consideration of harmonic losses”, *Magnetics, IEEE Transactions on*. 41, 2012 –2015. (2005).

[63] Seok-Bae Park et al., “Stator slot shape design of induction motors for iron loss reduction”, *Magnetics, IEEE Transactions on*. 31, 2004 –2007. (1995).

[64] S. Williamson and C.I. McClay, “Optimization of the geometry of closed rotor slots for cage induction motors”, *Industry Applications, IEEE Transactions on*. 32, 560 –568. (, May/Jun, 1996).

[65] D. Gerada et al. “Design considerations of high-speed induction machines for high-temperature applications”. In: *Electrical Machines, 2008. ICEM 2008. 18th International Conference on*. 2008, pp. 1 –6.

[66] R. Wrobel, P. Mellor, and D. Holliday. “Thermal analysis of a segmented stator winding design”. In: *Energy Conversion Congress and Exposition (ECCE), 2010 IEEE*. 2010, pp. 1290 –1297.

[67] M.M. Baggu, H.L. Hess, and K. Rink. “Thermal modeling of "direct lamination cooling (DLC)" induction motor for hybrid electric vehicle applications”. In: *Vehicle Power and Propulsion, 2005 IEEE Conference*. 2005, pp. 468 –472.

[68] B. Frederic, W. Thierry, and F. Herve. “The use of iron-nickel and iron-cobalt alloys in electrical engineering, and especially for electrical motors”. In: *Electrical Insulation Conference and Electrical Manufacturing Expo, 2007*. 2007, pp. 394 –401.

[69] M. Centner, R. Hanitsch, and U. Schafer. “Comparison of high-speed induction motors employing cobalt-iron and silicon electrical steel”. In: *Electrical Machines, 2008. ICEM 2008. 18th International Conference on*. 2008, pp. 1 –6.

[70] M. Persson et al. “Soft magnetic composite materials-use for electrical machines”. In: *Electrical Machines and Drives, 1995. Seventh International Conference on (Conf. Publ. No. 412)*. 1995, pp. 242 –246.

[71] A. Jack. “Experience with using soft magnetic composites for electrical machines”. In: *New Magnetic Materials - Bonded Iron, Lamination Steels, Sintered Iron and Permanent Magnets (Digest NMo. 1998/259), IEE Colloquium on*. 1998, pp. 3/1 –3/4.

[72] A.G. Jack, B.C. Mecrow, and C.P. Maddison. “Combined radial and axial permanent magnet motors using soft magnetic composites”. In: *Electrical Machines and Drives, 1999. Ninth International Conference on (Conf. Publ. No. 468)*. 1999, pp. 25 –29.

[73] M. Morimoto. “Induction motor made of iron powder core”. In: *Power Electronics Conference (IPEC), 2010 International*. 2010, pp. 1814 –1817.

[74] A. Boglietti et al. “Preliminary considerations about the adoption of unconventional magnetic materials and structures for induction motors”. In: *Industry Applications Society Annual Meeting, 1988., Conference Record of the 1988 IEEE*. 1988, 188 –194 vol.1.

[75] Akihiro Makino et al., “Low core losses and magnetic properties of Fe85-86Si1-2B8P4Cu1 nanocrystalline alloys with high B for power applications (invited)”, *Journal of Applied Physics*. 109, 07A302 –07A302–5. (2011).

[76] J.L. Kirtley et al. “Improving Induction Motor Efficiency with Die-cast Copper Rotor Cages”. In: *Power Engineering Society General Meeting, 2007. IEEE*. 2007, pp. 1 –6.

[77] D.T. Peters et al. “Copper in the squirrel cage for improved motor performance”. In: *Electric Machines and Drives Conference, 2003. IEMDC’03. IEEE International*. Vol. 2. 2003, 1265 –1271 vol.2.

[78] M.W. Wichmann, T.D. Boyer, and C.T. Keller. “Coil encapsulation with thermoplastic resins”. In: *Electrical Insulation Conference, 1997, and Electrical Manufacturing Coil Winding Conference. Proceedings*. 1997, pp. 525 –528.

[79] C. Lewis. “The Advanced Induction Motor”. In: *Power Engineering Society Summer Meeting, 2002 IEEE*. Vol. 1. 2002, 250 –253 vol.1.

[80] S. Evon and R. Schiferl. “Direct drive induction motors”. In: *Pulp and Paper Industry Technical Conference, 2004. Conference Record of the 2004 Annual*. , 27 Jun-1 Jul, 2004, pp. 49 –54.

[81] P. Wu, C. Chang, and K.J. Tseng. “New concept of multi-phase inductively-driven shaft-less centrifugal pumps”. In: *Electric Machines and Drives, 2005 IEEE International Conference on*. 2005, pp. 398 –403.

[82] Yuefeng Liao. “Design of a brushless doubly-fed induction motor for adjustable speed drive applications”. In: *Industry Applications Conference, 1996. Thirty-First IAS Annual Meeting, IAS ’96., Conference Record of the 1996 IEEE*. Vol. 2. 1996, 850 –855 vol.2.

[83] M. Stiebler. “Doubly-fed asynchronous machine for low voltage drives”. In: *Electrical Machines (ICEM), 2010 XIX International Conference on*. 2010, pp. 1 –6.

[84] M. Ruviaro et al., “Analysis and Test Results of a Brushless Doubly Fed Induction Machine With Rotary Transformer”, *Industrial Electronics, IEEE Transactions on*. 59, 2670 –2677. (2012).

[85] Linni Jian et al., “Integrated Magnetic-Geared Machine With Sandwiched Armature Stator for Low-Speed Large-Torque Applications”, *Magnetics, IEEE Transactions on*. 48, 4184 –4187. (2012).

[86] N.R. Brown, T.M. Jahns, and R.D. Lorenz. “Power Converter Design for an Integrated Modular Motor Drive”. In: *Industry Applications Conference, 2007. 42nd IAS Annual Meeting. Conference Record of the 2007 IEEE*. 2007, pp. 1322 –1328.

[87] H.A. Toliyat, T.A. Lipo, and J.C. White, “Analysis of a concentrated winding induction machine for adjustable speed drive applications. I. Motor analysis”, *Energy Conversion, IEEE Transactions on*. 6, 679 –683. (1991).

[88] H.A. Toliyat, T.A. Lipo, and J.C. White, “Analysis of a concentrated winding induction machine for adjustable speed drive applications. II. Motor design and performance”, *Energy Conversion, IEEE Transactions on*. 6, 684 –692. (1991).

[89] R.O.C. Lyra and T.A. Lipo. “Torque density improvement in a six-phase induction motor with third harmonic current injection”. In: *Industry Applications Conference, 2001. Thirty-Sixth IAS Annual Meeting. Conference Record of the 2001 IEEE*. Vol. 3. , 30 Sep - 4 Oct, 2001, pp. 1779 –1786.

[90] D. Casadei et al. “Torque maximization in high-torque density multiphase drives based on induction motors”. In: *Energy Conversion Congress and Exposition (ECCE), 2010 IEEE*. 2010, pp. 3896 –3902.

[91] D. Casadei et al. “Control of a high torque density seven-phase induction motor with field-weakening capability”. In: *Industrial Electronics (ISIE), 2010 IEEE International Symposium on*. 2010, pp. 2147 –2152.

[92] L. Zarri et al. “Maximum-torque-per-ampere control of high torque-density multiphase drives based on induction motors”. In: *Energy Conversion Congress and Exposition (ECCE), 2012 IEEE*. 2012, pp. 495 –502.

[93] K.R. Pullen and H. Mansir. “High power density air cooled motor generators for automotive applications”. In: *Electrical Machine Design for All-Electric and Hybrid-Electric Vehicles (Ref. No. 1999/196), IEE Colloquium on*. 1999, pp. 7/1 –7/5.

[94] F. Profumo, Zheng Zhang, and A. Tenconi. “Axial flux machines drives: a new viable solution for electric cars”. In: *Industrial Electronics, Control, and Instrumentation, 1996., Proceedings of the 1996 IEEE IECON 22nd International Conference on*. Vol. 1. 1996, 34 –40 vol.1.

[95] M.U. Lamperth, A. Beaudet, and M. Jaensch. “Disc Motors for Automotive Applications”. In: *Hybrid and Eco-Friendly Vehicle Conference, 2008. IET HEVC 2008*. 2008, pp. 1 –5.

[96] A. Kleimaier and B. Hoffmann. “Axial flux motor "DYNAX ®"- A compact electric drive for automotive power trains”. In: *Electric Drives Production Conference (EDPC), 2011 1st International*. 2011, pp. 1 –4.

[97] A. V. Matveev et al. “A novel permanent magnet motor with large axial channels for downhole applications with high-torque requirements”. In: *Power Electronics, Machines and Drives (PEMD 2012), 6th IET International Conference on*. 2012, pp. 1 –6.

[98] Y. Gessese and A. Binder. “Axially slitted, high-speed solid-rotor induction motor technology with copper end-rings”. In: *Electrical Machines and Systems, 2009. ICEMS 2009. International Conference on*. 2009, pp. 1 –6.

[99] K. Ziolko. “Basic Problems of Increasing the Density of Unit Power of Electric Machines”. In: *EUROCON, 2007. The International Conference on “Computer as a Tool ”*. 2007, pp. 1818 –1825.

[100] Yoshiyuki Shibata, Nuio Tsuchida, and Koji Imai, “High torque induction motor with rotating magnets in the rotor”, *Electrical Engineering in Japan*. 117, 102–109. (1996).

[101] Y. Shibata, N. Tsuchida, and K. Imai, “Performance of induction motor with free-rotating magnets inside its rotor”, *Industrial Electronics, IEEE Transactions on*. 46, 646 –652. (1999).

[102] M.E. Missiry, “New form of unlaminated rotor motor”, *Magnetics, IEEE Transactions on*. 20, 1786 –1788. (1984).

[103] Chen Yunyun et al., “Electromagnetic Performance Analysis of Double-Rotor Stator Permanent Magnet Motor for Hybrid Electric Vehicle”, *Magnetics, IEEE Transactions on*. 48, 4204 –4207. (2012).

[104] D. Jaksic. “"Getting rid of the air "or how to maximize winding fill factor (ID 81)”. In: *Electric Drives Production Conference (EDPC), 2011 1st International*. 2011, pp. 84 –87.

[105] Dae-Sung Jung et al. “Optimum Design of the Electric Vehicle Traction Motor Using the Hairpin Winding”. In: *Vehicular Technology Conference (VTC Spring), 2012 IEEE 75th*. 2012, pp. 1 –4.

[106] G. Madescu et al. “Effects of stator slot magnetic wedges on the induction motor performances”. In: *Optimization of Electrical and Electronic Equipment (OPTIM), 2012 13th International Conference on*. 2012, pp. 489 –492.

[107] Wakaki Miyaji and Atsushi Oohashi, “New Generation (9G) Alternator”, *ADVANCE Magazine*. 121. (2008).

[108] N. Takorabet et al. “Design and optimization of a permanent magnet axial flux wheel motors for electric vehicle”. In: *Electrical Machines (ICEM), 2012 XXth International Conference on*. 2012, pp. 2635–2640.

[109] A.M. EL-Refaie, “Fractional-Slot Concentrated-Windings Synchronous Permanent Magnet Machines: Opportunities and Challenges”, *Industrial Electronics, IEEE Transactions on*. 57, 107 –121. (2010).

[110] A. El-Refaie. “Fractional-slot concentrated-windings: A paradigm shift in electrical machines”. In: *Electrical Machines Design Control and Diagnosis (WEMDCD), 2013 IEEE Workshop on*. 2013, pp. 24–32.

[111] M. Inoue et al. “An evaluation of concentrated and distributed windings in interior PM and claw pole motors”. In: *Power Electronics and ECCE Asia (ICPE ECCE), 2011 IEEE 8th International Conference on*. , 30 May-3 Jun, 2011, pp. 176 –183.

[112] A.S. Abdel-Khalik and S. Ahmed, “Performance Evaluation of a Five-Phase Modular Winding Induction Machine”, *Industrial Electronics, IEEE Transactions on*. 59, 2654 –2669. (2012).

[113] Tae-Uk Jung et al. “Improved Design for Driving Characteristics in Single Phase Induction Motor with Concentrated Winding”. In: *Power Electronics Specialists Conference, 2007. PESC 2007. IEEE*. 2007, pp. 2418 –2422.

[114] B.B. Jensen et al., “Performance of a Folded-Strip Toroidally Wound Induction Machine”, *Industrial Electronics, IEEE Transactions on*. 59, 2217 –2226. (2012).

[115] B.B. Jensen and A.G. Jack. “Toroidally wound induction machines”. In: *Electrical Machines (ICEM), 2010 XIX International Conference on*. 2010, pp. 1 –5.

[116] M. Ito et al., “Magnetically anisotropic solid rotor of an induction motor”, *Energy Conversion, IEEE Transactions on*. 3, 427 –432. (1988).

[117] Y. Kawase et al., “Magnetic Field Analysis of Matrix-Rotor Induction Motor Using Parallel Computing System”, *Magnetics, IEEE Transactions on*. 47, 1062 –1065. (2011).

[118] R. Mujal-Rosas and J. Orrit-Prat, “General Analysis of the Three-Phase Asynchronous Motor With Spiral Sheet Rotor: Operation, Parameters, and Characteristic Values”, *Industrial Electronics, IEEE Transactions on*. 58, 1799 –1811. (2011).

[119] K.M. Rahman and S.E. Schulz, “Design of high-efficiency and high-torque-density switched reluctance motor for vehicle propulsion”, *Industry Applications, IEEE Transactions on*. 38, 1500 –1507. (, Nov/Dec, 2002).

[120] M. Galea, T. Hamiti, and C. Gerada. “Torque density improvements for high performance machines”. In: *Electric Machines Drives Conference (IEMDC), 2013 IEEE International*. 2013, pp. 1066–1073.

[121] S. Cicale et al. “Design of a Permanent Magnet Synchronous Motor with Grain Oriented electrical steel for Direct-drive elevators”. In: *Electrical Machines (ICEM), 2012 XXth International Conference on*. 2012, pp. 1256–1263.

[122] Y. Sugawara and K. Akatsu. “Characteristics of a Switched Reluctance Motor using Grain-Oriented electric steel sheet”. In: *ECCE Asia Downunder (ECCE Asia), 2013 IEEE*. 2013, pp. 1105–1110.

[123] S. Lopez et al., “Grain Oriented Steel Assembly Characterization for the Development of High Efficiency AC Rotating Electrical Machines”, *Magnetics, IEEE Transactions on*. 45, 4161 –4164. (2009).

[124] R. Curiac and H. Li. “Specific design considerations for AC induction motors connected to adjustable frequency drives”. In: *Pulp and Paper Industry Technical Conference (PPIC), Conference Record of 2010 Annual*. 2010, pp. 1 –6.

[125] John L. Oldenkamp and Steven C. Peak, “Selection and Design of an Inverter-Driven Induction Motor for a Traction Drive System”, *Industry Applications, IEEE Transactions on*. IA-21, 259 –265. (1985).

[126] M.P. Magill and P.T. Krein. “Examination of design strategies for inverter-driven induction machines”. In: *Power and Energy Conference at Illinois (PECI), 2012 IEEE*. 2012, pp. 1 –6.

[127] E. Hall, S.S. Ramamurthy, and J.C. Balda. “Optimum speed ratio of induction motor drives for electrical vehicle propulsion”. In: *Applied Power Electronics Conference and Exposition, 2001. APEC 2001. Sixteenth Annual IEEE*. Vol. 1. 2001, 371 –377 vol.1.

[128] B.A. Welchko and J.M. Nagashima. “A comparative evaluation of motor drive topologies for low-voltage, high-power EV/HEV propulsion systems”. In: *Industrial Electronics, 2003. ISIE ’03. 2003 IEEE International Symposium on*. Vol. 1. 2003, 379 –384 vol. 1.

[129] N.A. Patil, J.S. Lawler, and J.W. McKeever. “Determining constant power speed ratio of the induction motor from equivalent circuit parameters”. In: *Southeastcon, 2008. IEEE*. 2008, pp. 460–467.

[130] J.M. Miller and Institution of Electrical Engineers. *Propulsion Systems for Hybrid Vehicles*. IEE power and energy series. Institution of Electrical Engineers, 2004.

[131] A. Shenkman, M. Chertkov, and H. Moalem, “Thermal behaviour of induction motors under different speeds”, *Electric Power Applications, IEE Proceedings* -. 152, 1307–1310. (2005).

[132] M. Chertkov and A. Shenkman, “Determination of the heat state of normal load induction motors by a no-load test run”, *Electric Machines & Power Systems*. 21, 355–369. (1993).

CHAPTER

THREE

DESIGN METHODOLOGY

3.1 Introduction

This chapter describes the basic procedure followed in the development of new motor designs with the aim of increasing the specific torque. It includes also the description of the procedures followed for the initial dimensional calculations and the modelling using finite elements. An introduction to the designs developed during this research is explained at the end of this chapter.

3.2 General methodology

The previous two chapters have identified that the standard squirrel cage topology is the most commonly employed in the design of induction motors for electric vehicles. For this reason a design strategy is needed to introduce and evaluate new designs. The methodology followed during this research can be summarized as follows:

Machine requirements and initial outline. The first stage consists in the determination of the performance requirements for an induction motor driving a light ground vehicle. These requirements could be used to select an industrial induction motor with a similar performance for use as a benchmark. The initial outline could be also obtained using analytical expressions to calculate the main geometric dimensions at the outset of the design.

Finite element analysis software. This part describes the software packages selected for the simulation of new motor designs.

Design search and analysis. This is one of the main parts of this research and includes a review of a series of new topologies for high specific torque. The new design is

presented in detail including the simulation results and their analysis.

Design selection. After a discussion and comparison of the new designs, two of them were selected for manufacture.

Manufacture. The construction process of the two prototypes.

Experimental tests. The experimental rig was prepared and used to test the new machines.

Results analysis. Conclusions and discussion of the results obtained by simulation and experiments were developed during this stage.

The first two stages were the necessary precursor for the development of new induction machine designs. They are included in this chapter whilst the remaining stages are explained in the subsequent chapters.

3.3 Machine requirements and initial outline

The initial specifications used during the design process were based on the motor for the toyota Prius described in section 1.6. However, this rating was changed later in order to produce a prototype which would be feasible to manufacture and test without exceeding the budget and the test facilities capabilities of the laboratory. The rating was reduced from 55 kW to 7.5 kW initially and later further to 5.5 kW. The last reduction was because there was one machine available with this rating and the stator could also be used for the new prototypes. All these machines are of the same family and manufacturer. Their dimensions were used to generate the benchmark machines and the initial designs using analytical methods.

3.3.1 Analytical calculations

The first outline for any new designs can be obtained from direct modifications to the benchmark geometry or using analytical calculations. The basic equations are briefly described in this section whilst the criteria for the selection of values such as the number of pair poles, phases, slots, etc. are discussed in subsequent sections. The first equation involves the determination of the D^2L_e product from the following torque sizing equation [1]:

$$T = \sqrt{2}k_w K_{el}\hat{B}_g \cos(\delta)\frac{\pi D^2 L_e}{4} \tag{3.1}$$

where

k_w - winding factor

K_{el} - specific electric loading

$\hat{B}_g$ - peak value of the sinusoidally-distributed airgap flux density

δ - input power factor angle

D - bore diameter of the machine (m)

Le - stack length of the machine (m)

D^2L_e allows the diameter and length of the stator bore to be obtained considering the space restrictions or assuming a specific aspect ratio. Another key calculation consisted in determining the number of series-connected conductors per phase (N_{ph}) using Equation 3.2 [1]. The winding constant (k_{wt}) is a factor introduced to consider the winding type. For example, its value was 1 for distributed windings and 2 for toroidal windings.

$$\hat{B}_g = \frac{k_{wt} q p V_s}{\sqrt{2}\pi f D L_e N_{ph}} \tag{3.2}$$

where

q - stator phases number

p - number of pole pairs

V_s - rms applied phase voltage (V)

The stator tooth width, t_{ws} (m), and the stator core-back depth, y_{ds} (m) were calculated using the values of the peak stator tooth flux density, $\hat{B}_{ts}$ (T); the peak stator core flux density, $\hat{B}_{cs}$ (T) and the number of stator slots, N_s [1].

$$\hat{B}_{ts} = \frac{\hat{B}_g D}{p t_{ws}} \sin\left(\frac{p\pi}{N_s}\right) \tag{3.3}$$

$$\hat{B}_{cs} = \frac{\hat{B}_g D}{2p y_{ds}} \tag{3.4}$$

Equation 3.5 can be used to calculate the stator current, I_s (A) [1]. The stator current then allows the area of the conductors required to be determined which in turn permits the slot area, depending on the slot filling factor assumed, to be calculated. The procedure to obtain the slot dimensions varies depending on the slot type but it is based on the dimensions previously mentioned. The dimensions of the rotor can then be calculated using a similar procedure. The analytical expressions for this and further detailed calculations for the induction motor have been included in Appendix B.

$$I_s = \frac{\pi D K_{el}}{2 q N_{ph} k_w} \tag{3.5}$$

3.3.2 Additional assumptions and restrictions

Additional assumptions or limitations adopted to those already mentioned in previous chapters:

All the new designs were evaluated using a 2D finite element model. 3D effects which could not be modelled such as the end-windings were included and/or calculated by analytical expressions.

All the new designs were rated at 25 % of their pull out torque. This was done with the intention of achieving a speed range of approx 4 times the base speed [2]. This assumption allows us to compare all the new designs at the base speed. A full review of the torque-speed curves of the new designs through the whole speed range would have demanded an excessive amount of computing time.

Optimal flux level control not considered. Induction machines usually operate at full flux levels during the constant torque region in variable speed applications. Some researchers have suggested that this is inefficient, especially at reduced loads [3]. This affects the power converter control and requires knowledge of the load regime and algorithms fast enough for operation in real time. Predefining the flux levels for different loads by building data tables has been proposed. The controller uses these tables as a reference based on the load [3]. The savings would depend on the machine and the motion cycle but improvements in efficiency can be reached for loads under 2/3 of rated load according to [3].

The previous option only changes the set point in the control depending on the load required. It does not consider the dynamic behaviour of the machine and the high current peaks during transients. This produces a performance degradation during

dynamic behaviour. Specific techniques to deal with this situation are needed. An example is presented using an heuristic approximation of the optimal flux levels in [4].

3.4 Finite element models

This section contains some brief information related to the finite element models used. This is relevant to all the designs presented in the next chapters unless otherwise specified.

3.4.1 Mesh density

Mesh definition is a trade off between computational resources and model accuracy. If the mesh is too fine, the time required to solve the model would be excessive or could even exceed the computer resources available. On the other hand, if the mesh is too coarse, the solution could become inaccurate.

The procedure for meshing followed the recommendations provided by the Flux user manual: the initial mesh was generated with the airgap elements as close to equilateral as possible. In most cases, the airgap is small enough to ensure all the airgap elements have an appropriate size if they are close to equilateral. The rest of the elements can be resized in an iterative process. Initially the problem was solved using a dense mesh, the mesh was then relaxed and the model solved again. This process was repeated until the simulation results start to diverge, for example by more than 1 %.

3.4.2 Boundary conditions

The finite element method requires the definition of the boundary conditions around the problem. Two boundary conditions were used in the models for the induction motor designs investigated:

Dirichlet boundary: This boundary condition allow the user to define a fixed value of magnetic potential, usually zero. This effectively creates a flux line around the outer diameter of the stator core. This prevents any flux leakage into the air space surrounding the machine which is a good approximation when the stator core-back is not heavily saturated. If the stator core-back is saturated, an airspace surrounding the model core is added and the Dirichlet boundary is then moved to the outer perimeter of the airspace.

Symmetry boundary: This boundary allows the user to reduce the size of the problem by defining periodic conditions between two symmetry lines. This allows the

problem to be reduced to one magnetic/electric pole for example.

3.4.3 Materials

An important aspect in the modelling of electrical machines are the B-H curves required for the core laminations. Initially, the B-H curves available in the Flux 2D and Opera 2D material library were used but the results obtained were different than expected particularly in terms of the core losses. The B-H data at 50 Hz for each design was subsequently obtained from a compendium of lamination steel data published by the Electric Motor Education and Research Foundation [5] with the exception of the properties of grain-oriented steel which were obtained from [6].

3.4.4 Pre and post-processing

Flux 2D and Opera 2d were used in the simulation of the induction motor designs in both steady and transient states. The recommended practices for configuring and selecting options for the solver were followed [7–10]. All the models presented were voltage driven and in the steady state Opera 2D for example allows the user to use a static geometry and mesh and uses a pseudo-magnetostatic solution by adjusting the parameters using slip frequency to model the rotor speed. Transient simulations on the other hand cannot apply these simplifications and require a moving geometry and mesh which results in much higher computational times.

The choice of time step size in the transient simulations is a crucial trade off between computational time and accuracy in the finite element models. This time step selection could be validated against steady state simulations if applicable, analytical simulations based on measured equivalent-circuit machine parameters or experimental data. For steady state conditions, Flux 2D recommends using a time step based on the maximum allowed electrical angular movement of the rotor, for example one 20th of a full electrical pole angle. For transient simulations, Flux 2D recommends a time step of one 20th of the time period of one cycle of the fastest transient frequency under analysis.

Similar criteria can be used in Opera 2D. However Opera 2D has other disadvantages during transient solutions compared to Flux 2D. The main issue being that it is not straightforward to start a transient simulation at a particular slip condition. The user is forced to simulate the full start up of the machine even if the start up simulation is not required. Opera 2D recommends increasing the step size during the start up to ignore initial starting transients and speed up the solution. Another option is to fix the rotor speed to a value close to the expected final speed at the supply connection to the machine and then release the rotor speed and let the machine achieve the final steady state conditions.

Post-processing of the models included obtaining the most important parameters such as the magnetic flux, current distributions and losses. This stage also includes the calculation of torque which was determined using the virtual-work method in both Opera 2D and Flux 2D [7–10]. This method calculates the torque by determining the magnetic energy as a function of a virtual angular rotation of the rotor.

3.5 Finite element model in Flux 2D

This section describes an example of the procedure to create a finite element model of an induction machine in Opera 2D and Flux 2D. Both software packages allow the creation of models using the user graphical interface or to drive the software by script files. All the models employed were developed with script files. However, the graphical user interface was very useful to generate the initial script files. Detailed examples of the scripts can be found in Appendix C.

The initial models were created following the recommendations and examples found in the user manual and the user guide for Flux 2D [9, 10]. Initial models were created using the graphical interface while all the actions were recorded in a script file. The script file generated is in Pyflux language (Python+Flux defined commands). Once the script language was analysed, it was divided into several files to facilitate the creation and analysis of more models. The first file (Appendix C.1.1) is a general file whose only function is to call all the remaining files as the model script was strongly subdivided in order to facilitate debugging.

3.5.1 Parameters

The first couple of files are the parameters files (Appendix C.1.1). The first one is for the stator and defines first the geometrical parameters such as lengths and diameters. It also includes circuit parameters such as frequency, voltage, stator winding resistance, etc. The last part of this file uses the previous parameters to define the coordinates of the points used to draw the slots. These coordinates were denominated auxiliary parameters.

The second file corresponds to the rotor parameters defining also geometric, circuit and auxiliary parameters in a similar way than in the stator.

3.5.2 Geometry

Appendix C.1.3 presents the corresponding files to create the motor geometry. It was also subdivided into stator and rotor files. This section begins with the rotor file because it is more convenient in Flux 2D to create the geometry from the centre outwards.

The first part of the rotor script corresponds to the creation of the coordinate systems employed to facilitate the drawing of the slots and later to define the mechanical movement. The transformations commands follow which allow duplication of the slots. The slots begin with the creation of the points and then the segments (straight or curved) which join these points. Once a closed surface can be defined by the drawing segments, the command buildFaces() is applied which allows the creation of the geometrical surfaces. Auxiliary counters are used to record the number of points, lines and geometrical faces. The constant application of the buildFaces command is very important to keep order in the auxiliary counter of the geometrical faces.

The creation of the slots can be done in two ways. One is building one slot and then apply a transformation to define the rest. The other is to draw independently each slot using loops, for example using a "for" loop. The second method is more complicated but offers the possibility of drawing more complex asymmetrical slots.

The next step consists in the drawing of the shaft and the rotor core. This process is similar to the slots, the points are created, then the segments and finally the command to build faces is applied as necessary.

The process for the remaining stator geometry is very similar to that used in the rotor.

3.5.3 Mesh

There are two basic ways to control the mesh in Flux 2D. One consists in activating the automatic method to mesh the problem based on auxiliary user defined coefficients. The other method is to define mesh operations and apply them to the geometry. The second method was used because the automatic method tends to create a very dense mesh. Although this is necessary to solve the problem, during debugging it is convenient to have a coarse mesh in order to quickly identify any issue. Once the debugging process is finished, the parameters can be adjusted to increase the mesh density and to obtain the solutions. The mesh operations are referred to the geometry using the number of points, lines or faces (This is assigned automatically and sequentially by Flux 2D). This process is very simple if the auxiliary counters were generated properly during the geometry files. The two files corresponding to the stator and rotor meshes can be found in Appendix C.1.4.

3.5.4 Physics

The stator and rotor physics files (Appendix C.1.5) are composed of three main parts. The first file is the definition of the problem type to be solved (Steady state or transient, 2D or 3D, etc.). The second part consists of the definition of the properties of the

materials including the corresponding BH curves for the magnetic materials. The final part consists of the definition of the "mechanical sets" which are command definitions of the mechanical rotation of the rotor or the fixed position of the stator.

3.5.5 Circuit

The circuit definition can be also driven by script. The first components to be drawn are the equipotential segments which are the lines that interconnect the circuit components. The script also contain the definition of the external inductances used to represent the end-winding leakage. The voltage sources are also included in these scripts as well as the coils representing the stator windings. For the rotor, there is a macro defined model of the squirrel cage which facilitates the rotor circuit creation. The corresponding files for the circuit build can be found in Appendix C.1.6.

3.5.6 Regions

Appendix C.1.7 includes the scripts that finalise the model. These files begin with the creation of the region faces which are objects that link the coils from the circuit and/or the mechanical sets with the geometrical faces. The region faces can be also used to define boundary conditions, for example zero magnetic potential on the outer boundary of the model. The process to assign the region faces with the geometry faces also requires the auxiliary counters defined during the creation of the geometry.

These scripts were created during the implementation of Pyflux in Flux 2D. At this point Flux 2D was still subdivided into three programs: preprocessor, solver and post-processor. The script detailed here was created when only Pyflux was implemented in the preprocessor. The solving and post-processing was only possible using the graphical interface or by an old and more complex scripting method which is now obsolete.

3.6 Finite element model in Opera 2D

The process described here was based on the user manual and the user guide for Opera 2D [7, 8]. Similar to Flux, the graphical interface was used to generate the initial scripts which were later used to develop the new designs. Similar to Flux a main file is used to call all the necessary subroutines and is included in Appendix C.2.1.

3.6.1 Parameters

Unlike the Flux philosophy, Opera prefers to define everything at once which simplifies the process. The main disadvantage of opera is parametrization. You can define parameters and use them to define the geometry, materials, mesh, etc but they pass the actual value through. When you modify the parameter, the model does not change.

The opera strategy makes the models easier to assembly but if you need to change the model, it is better sometimes to start again.

The procedure is similar to Flux 2D: including parameters for the geometric, circuit and auxiliary coordinates for the slot geometry. The parameters files also include the material properties and the mesh parameters. Review of the mesh size was done in a similar manner to Flux 2D. The files for the stator and rotor parameters are in Appendix C.2.2.

3.6.2 Stator

Appendix C.2.3 shows the files necessary for the basic creation of the stator. The basic process to create a region is as follows: define the region properties such as material, density, conductivity, associated circuit component, symmetry, rotation amongst others. The geometry is then defined point by point and line by line simultaneously. The process continuous until the shape is closed.

The first file in Appendix C.2.3 corresponds to the creation of the stator slots. The second one illustrates the method for drawing the stator core. It is important to notice that in Opera it is not recommended or even possible to define the core with a single surface. This is in part because Opera does not allow surfaces defined by more than one continuous line, for example the use of a circular ring is not allowed. You can create the face but the solver will stop. It is necessary in this case to create two surfaces to define a circular ring.

3.6.3 Rotor

Appendix C.2.4 includes the files for the rotor. The process is basically the same as the stator. It should be noted that the segmentation of the core in Opera tends to produce a denser mesh than in the Flux models.

3.6.4 Solver

Unfortunately, the circuit creation can not be done easily by command in Opera 2D. It is better to create a file family which cover most cases. In addition there is no squirrel cage model predefined.

Appendix C.2.5 shows the solver file. Initially you define the solver (type, frequency, non-linearity, iterations, tolerance, amongst others). It is important to note that although Opera allows you to define the parameters in terms of frequency, the solver does not update properly these parameters during the solving process. It is necessary to solve each point of the torque-slip curve in an individual file.

The next step in this file is the creation of the airgap. Opera can handle up to three airgaps and defines the airgap as a circular ring. The rest of the geometry is defined as background region which assumes the properties of air for solving. The mesh is then generated and the circuit file associated is loaded.

3.6.5 Auxiliary

Appendix C.2.6 is necessary as each point of the torque-slip curve are in different files. This file is in charge of saving these files with different names, solving them and storing the necessary data as required in an output file.

3.6.6 Summary

This section has illustrated the process for the finite element modelling used for the design of an induction motor. The process was covered for Flux 2D and Opera 2D. Both software packages have common procedures but although the Opera 2D models tend to be faster to develop, the Flux 2D models are more user friendly to parametrize, solve and post-process the solution.

3.7 Thermal models

The new designs developed were evaluated using the thermal model described in [11]. This is a simplified thermal model for variable speed induction motors as shown in Figure 3.1. The thermal model include three heat sources: P_{ir} stator iron losses (W), P_{js} stator copper losses (W) and P_{jr} rotor copper losses (W) [11]. The thermal model considers only the thirteen most influential thermal resistances [11]:

R_{eca} Thermal resistance representing the forced convection between the motor case and air cooling

R_0 Thermal resistance between the motor case and the external air

$R_{ia,ec}$ Thermal resistance between the internal air and the case ends

R_{sy1} Radial thermal resistance of the stator yoke inner half

R_{sy2} Radial thermal resistance of the stator yoke outer half

R_{st} Radial thermal resistance of the stator teeth

$R_{cu,ir}$ Thermal resistance between the stator windings and the stator core

$R_{ew,ec}$ Thermal resistance between the stator end-windings and the motor case

$R_{ew,ia}$ Thermal resistance between the stator end-windings and the internal air

$R_{s,ag}$ Thermal resistance between stator and airgap

$R_{r,ag}$ Thermal resistance between rotor and airgap

R_{sig} Radial thermal resistance between the stator and the motor case

R_{shf} Axial thermal resistance of the shaft

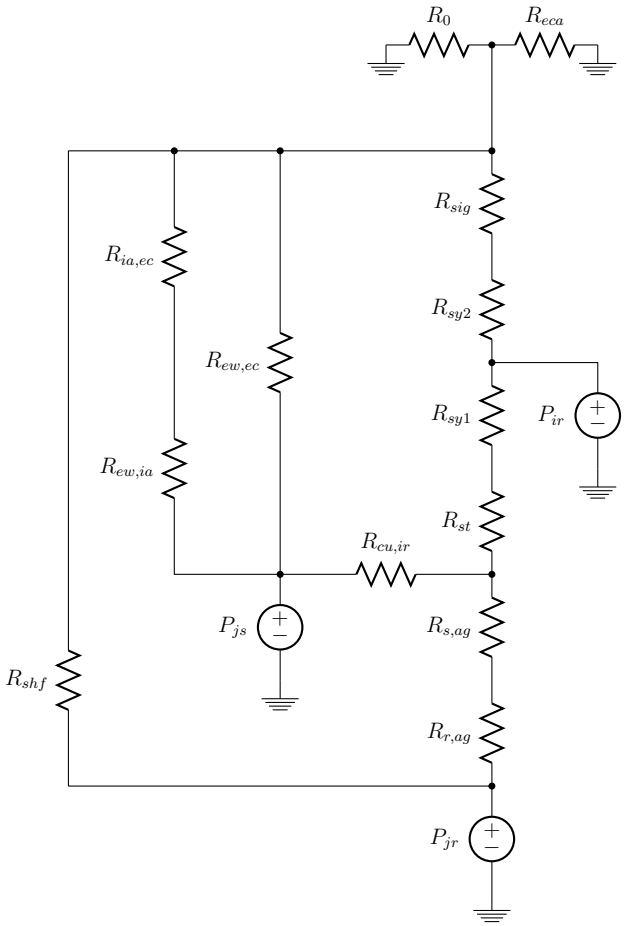

Figure 3.1: Thermal model employed [11]

All the corresponding equations for this model have been included in Appendix D.

3.8 Benchmark motors

A 55 kW induction motor was selected as a benchmark machine based on the requirements established previously. This machine was used to compare the performance of new designs during the first part of this research. It was subsequently decided that a smaller power rating was required to facilitate all the experimental work. For this reason another two benchmark machines were selected consisting of a 7.5 kW and a 5.5 kW induction motor. The last two machines used the same laminations but different stack length. The specification of the construction and performance of these benchmarks can be found in Appendix A.

The three benchmark motors were obtained from industrial induction machines but with some minor modifications. The rotor bar shape was changed to trapezoidal bars with rounded tops and bottoms and the aluminium cage material was substituted by copper. The bar area was scaled by the copper to aluminium conductivity ratio in the two smaller benchmark motors. Figure 3.2 illustrates the difference between the industrial and the benchmark induction motors.

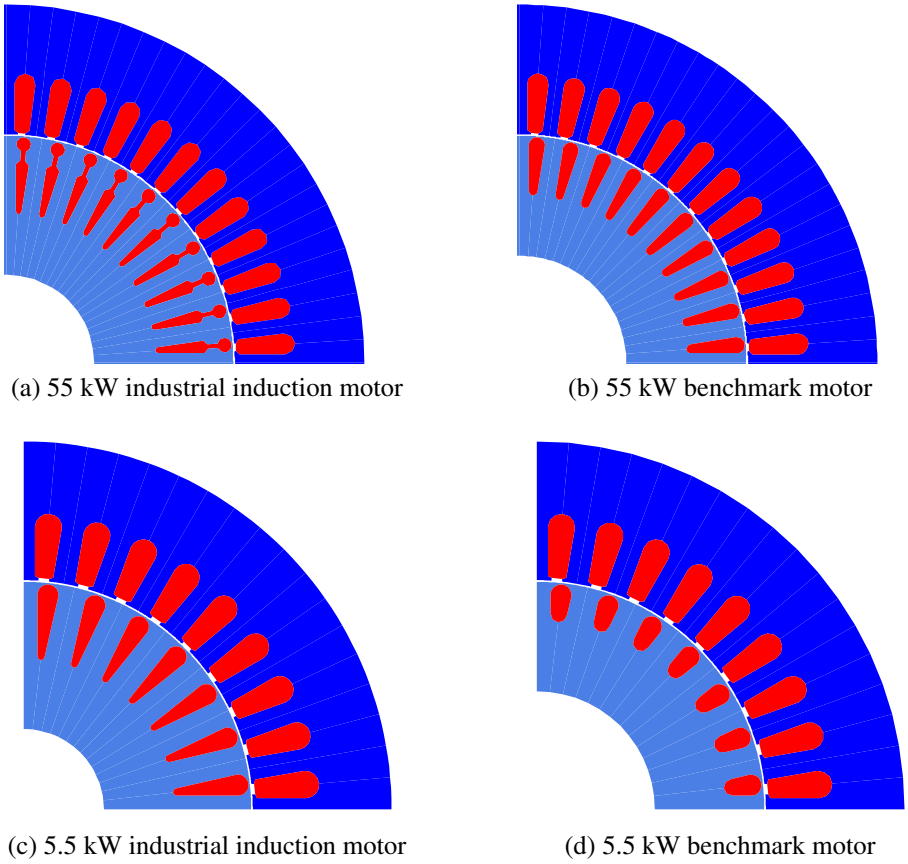

(a) 55 kW industrial induction motor

(b) 55 kW benchmark motor

(c) 5.5 kW industrial induction motor

(d) 5.5 kW benchmark motor

Figure 3.2: Benchmark motors

Figure 3.3 shows the stator of the benchmark industrial induction motor and the original aluminium cage rotor which was also tested for comparison with the new designs.

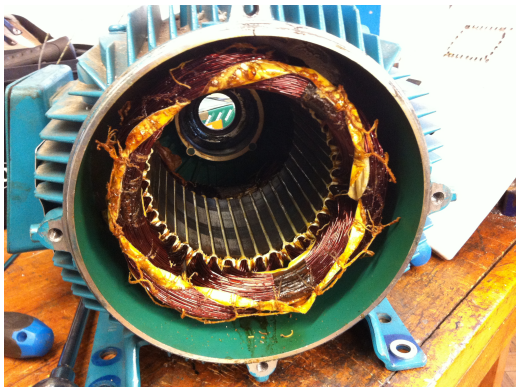

(a) Stator

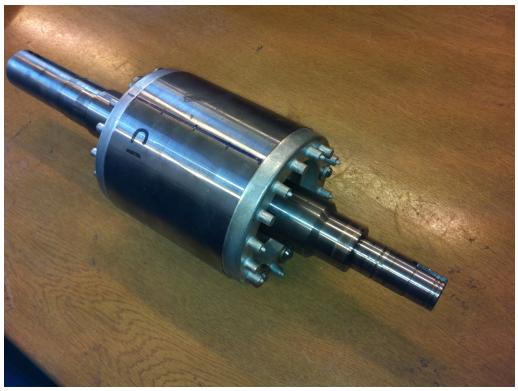

(b) Rotor

Figure 3.3: 5.5 kW industrial induction motor

For this purpose, the next section details the performance analysis of one of the benchmark motors used as an example of a typical induction motor. The 5.5 kW benchmark machine was selected because it has the same rating as the motors which were considered for prototyping, experimental test and further analysis.

3.8.1 5.5 kW benchmark motor performance

The performance of the 4-pole, 5.5 kW benchmark motor was evaluated using the finite element software Opera 2D, focusing on four important operating conditions: no load, nominal torque, maximum torque and locked rotor. Figure 3.4 illustrates the benchmark machine performance under no load conditions. The torque produced and the slip are almost zero whilst the rotor rotates close to its synchronous speed, 1500 RPM. The equipotential field lines shows how the magnetic field follows the expected distribution. The flux density shows a sensible distribution without areas of significant saturation whilst the current distribution is concentrated in the stator as expected.

The performance of the 5.5 kW benchmark induction motor during nominal rated load operation is shown in Figure 3.5. The field distribution is very similar to that on no-load as expected because even on load the stator and rotor load currents largely cancel each other to leave the dominant magnetizing field pattern in the finite element solution. No significant saturation can be detected in the flux density distribution. The current density naturally is higher in the rotor slots. It should be noted however that the current density displayed in the stator slots was calculated including the air space between conductors and the slot insulation. The conductor current densities in the conductors of this benchmark machine have similar values for both the stator and rotor.

Figure 3.6 shows the performance of the benchmark motor operating at maximum torque. Distortion in the equipotential field lines is more evident whilst some areas of saturation appear in the flux density distribution. The current density values are much higher than

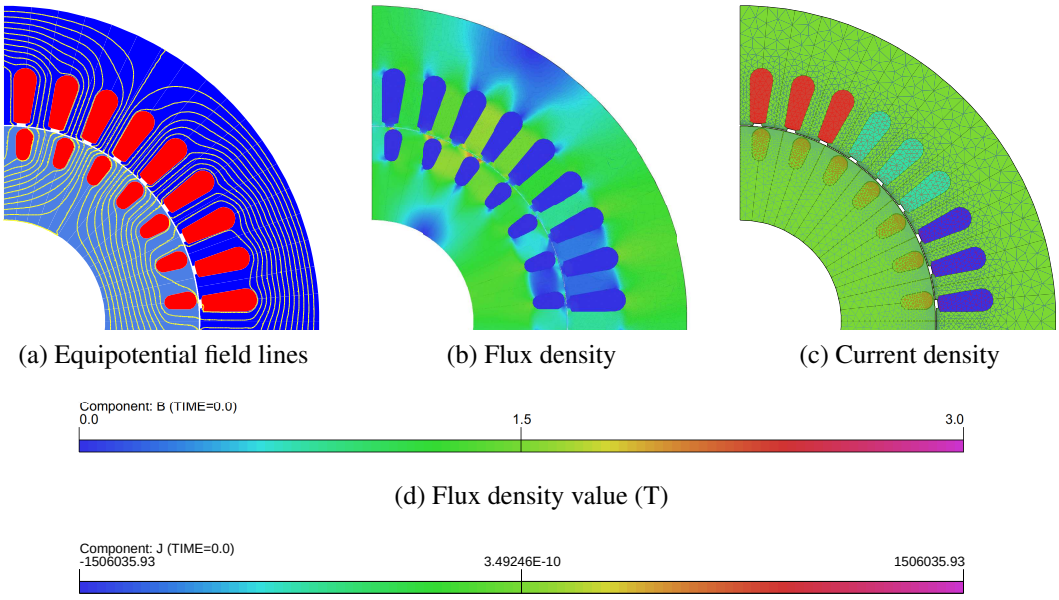

(a) Equipotential field lines (b) Flux density (c) Current density

(d) Flux density value (T)

(e) Current density value (A/m^2)

Figure 3.4: 4-pole, 5.5 kW benchmark motor under no load conditions

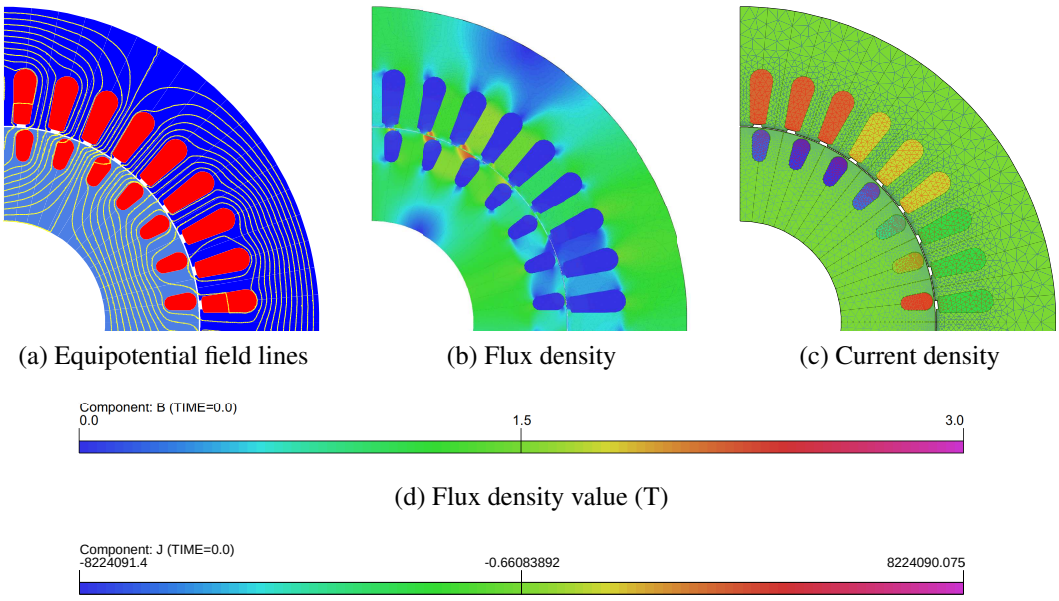

(a) Equipotential field lines (b) Flux density (c) Current density

(d) Flux density value (T)

(e) Current density value (A/m^2)

Figure 3.5: 5.5 kW benchmark motor under nominal load conditions

in the previous operating conditions as expected and these can be allowed only for short periods of time before overheating occurs.

The performance when the rotor is locked at standstill is illustrated in Figure 3.7. The magnetic field distribution is now quite different from the no-load case and saturation is present in some areas of the teeth. The current density now reaches its highest value with the current distribution in each rotor bar following a largely sinusoidal variation around the rotor as expected.

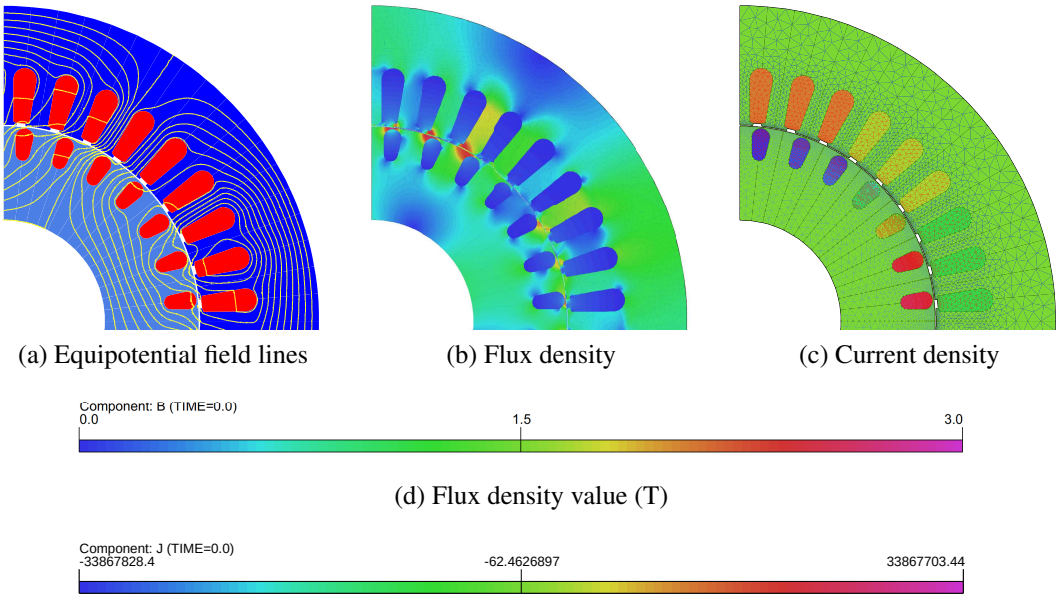

(a) Equipotential field lines (b) Flux density (c) Current density

(d) Flux density value (T)

(e) Current density value (A/m^2)

Figure 3.6: 5.5 kW benchmark motor at maximum torque

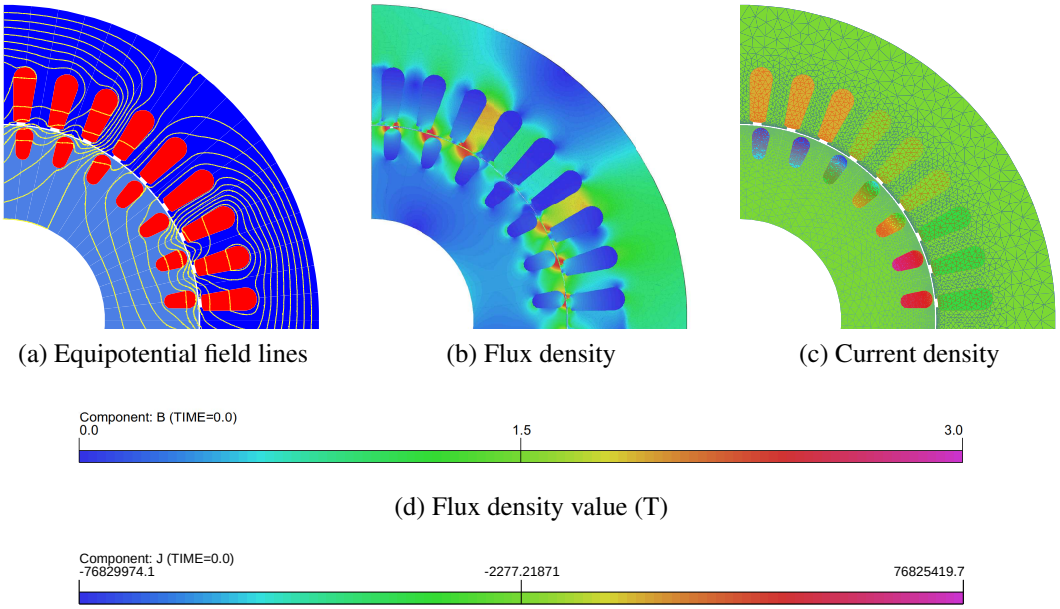

(a) Equipotential field lines (b) Flux density (c) Current density

(d) Flux density value (T)

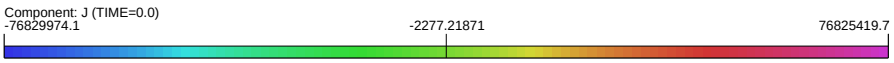

(e) Current density value (A/m^2)

Figure 3.7: 5.5 kW benchmark motor under locked rotor conditions

The analysis of the airgap flux density distribution is an important tool in the design of electrical machines. It enables the designer to identify undesired flux harmonics present in the machine. Figure 3.8 presents the airgap flux density distribution under the various operating conditions. It can be seen how the harmonic content of the flux density distribution increases with increasing load.

Figure 3.8 is clear in terms of observing the distortion in the airgap flux distribution with

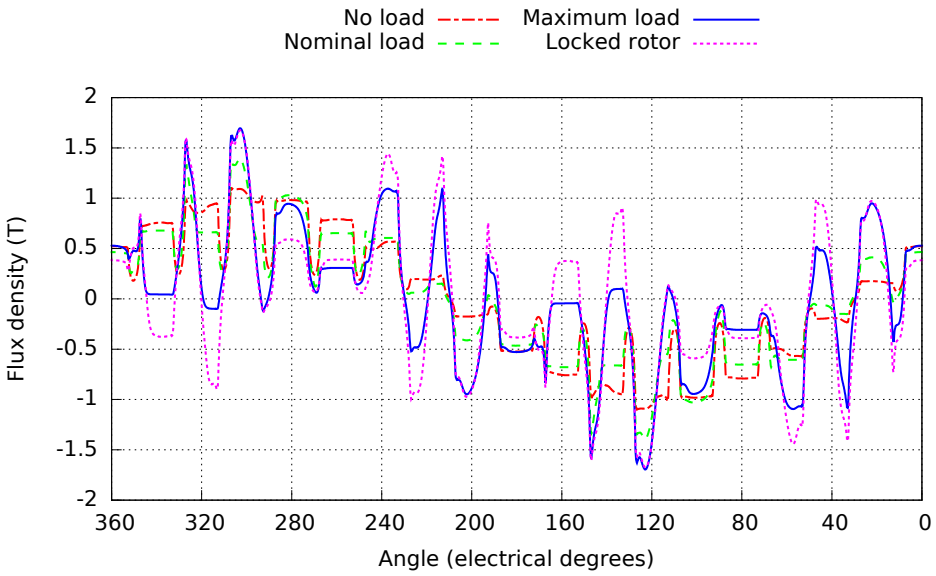

Figure 3.8: Airgap flux density distribution

the application of mechanical load, but it is difficult to evaluate this quantitatively. For this purpose, a Fourier harmonic analysis is used for comparing the changes in the airgap field distribution as shown in Figure 3.9.

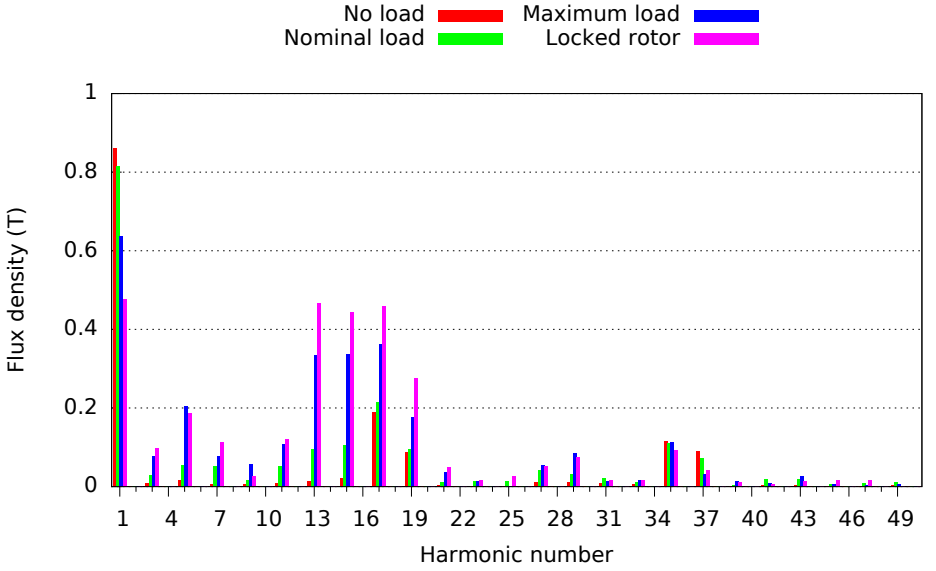

Figure 3.9: Harmonic analysis of the airgap flux density distribution

The fundamental airgap field reduces as the load increases as expected. This is caused by the increasing voltage drop across R_1 and X_1 in the per-phase equivalent circuit as the load current increases. The fundamental airgap field is proportional to the voltage across X_m in the equivalent circuit and this reduces as the voltage drop across R_1 and X_1 increases.

Increasing load also shows an increase in certain harmonic fields in Figure 3.9. The significant harmonics in Figure 3.9 are the main stator and rotor slotting harmonics given by $N_s/p \pm 1$ and $N_r/p \pm 1$ where N_s and N_r are the stator and rotor slot numbers and

p is the pole pairs. In the benchmark motor, this corresponds to 17, 19 and 13, 15 which correlates with Figure 3.9.

Figure 3.10 presents a series of graphs which illustrate the performance of the benchmark motor. Torque, phase current, power factor and efficiency were analysed and compared with the initial industrial induction motor. The performance of the benchmark motor is better in each aspect than the industrial motor. As mentioned in the previous chapter, the cage of the benchmark machine was made of copper with a slot area scaled by the copper to aluminium conductivity ratio whilst the industrial cage was made of aluminium with a larger slot area.

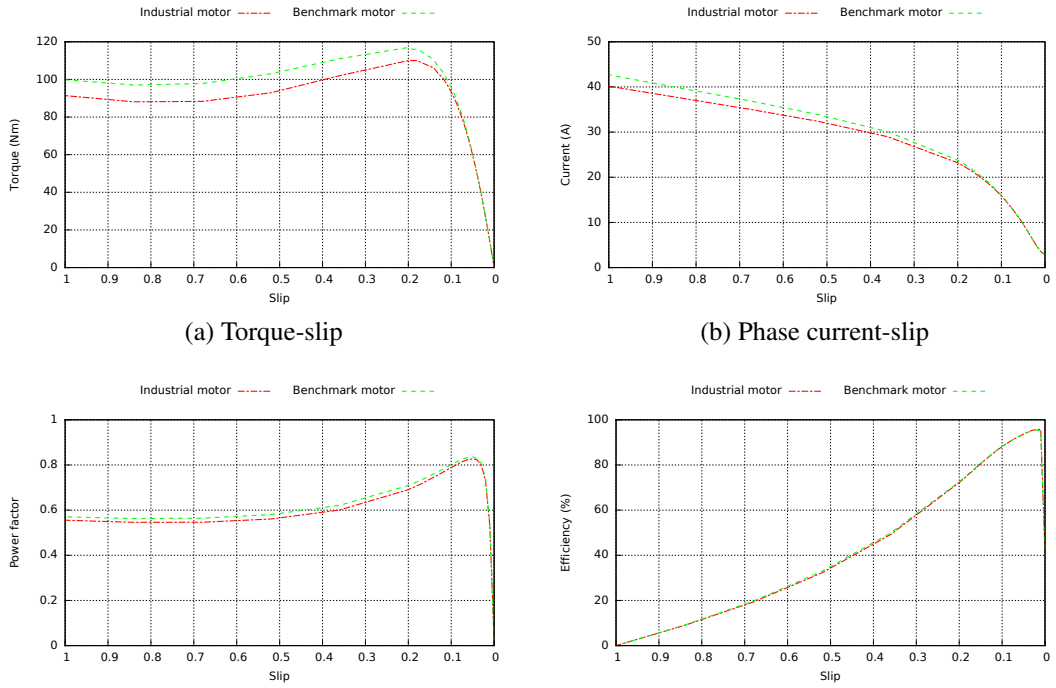

(a) Torque-slip

(b) Phase current-slip

(c) Power factor-slip

(d) Efficiency-slip

Figure 3.10: Performance curves of the 5.5 kW benchmark motor

The performance of the benchmark motor was also simulated over the full speed (frequency) range. Figure 3.11 illustrates the torque-speed curves for different operating frequencies from 50 Hz to 200 Hz. This figure also displays the required load torque for a 5.5 kW powertrain including the constant torque region under the 1500 RPM nominal speed and the constant power region for higher speeds. The benchmark motor was clearly not able to meet the torque requirements across the whole constant power region specially at the highest speeds. In this case, the designer would need to increase the torque capacity of the design to increase the available speed range. This would usually mean increasing the size of the machine.

Figure 3.11 only includes frequencies equal or higher than the nominal, 50 Hz, covering exclusively the behaviour during the constant power region. This means that the supply voltage was held at its maximum value while the airgap flux levels and hence torque

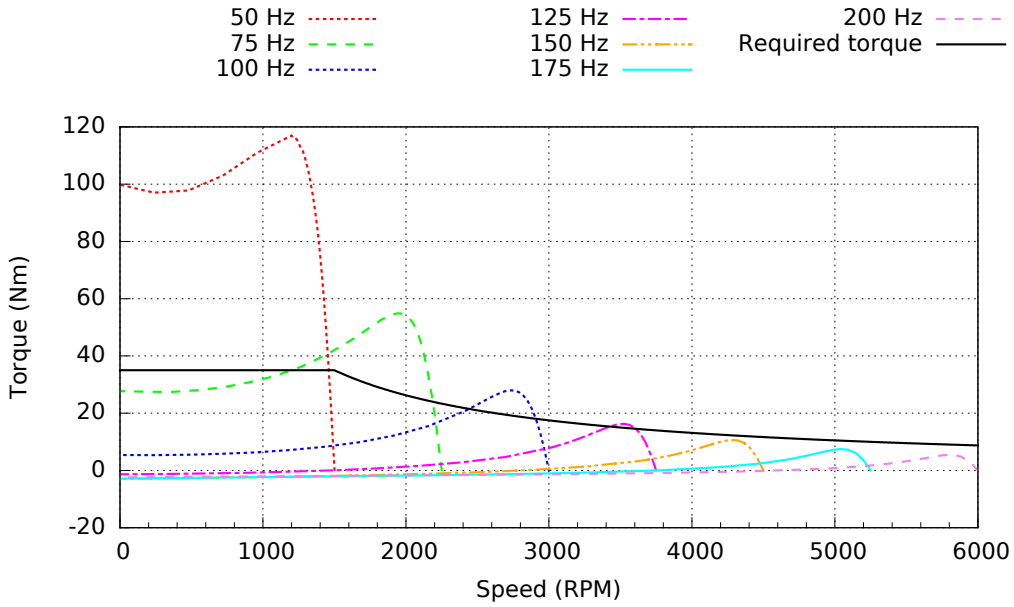

Figure 3.11: Torque speed curves for different operating frequencies

reduce as the frequency increases. Curves for the constant torque operating region were not calculated because the motor can fully meet the torque requirements using the basic V/f control strategy.

Torque is negative at large slip for the highest frequency simulations as shown in Figure 3.11. This is due to the high harmonic airgap flux distribution result of the high slip and the lower flux levels.

The steady-state finite element simulations give valuable results for the conventional induction motor designs. However, more accurate results can be obtained by employing transient simulations [12]. For this reason, the benchmark motor was simulated using a finite element transient model under the following load profile:

0.0 s to 0.2 s: The rotor speed is fixed to 1500 RPM and the stator energized.

0.2 s to 1.0 s: The rotor speed is no longer fixed and the machine operates under no load conditions.

Over 1.0 s The machine mechanical load is increased at a constant rate of 45 Nm/s^2.

Figure 3.12 illustrates the results obtained with the transient simulation. This shows the initial torque oscillations during the stator energization and the subsequent stable operation under no load conditions. The load torque is then increased until the machine can no longer produce enough torque and the motor stalls and the speed drops to zero.

Figure 3.12 might not however be easy to interpret. But if the results are referred to the motor slip as shown in Figure 3.13, it can be seen that the transient results follows the steady state simulations performed previously.

The object of the transient analysis of the induction motor is to obtain as much information

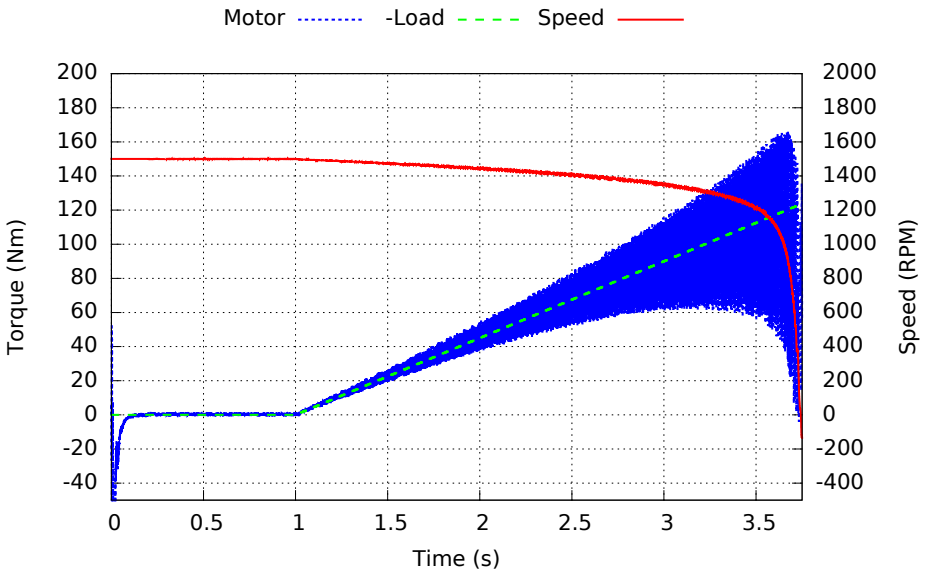

Figure 3.12: Transient simulation of the 5.5 kW benchmark motor

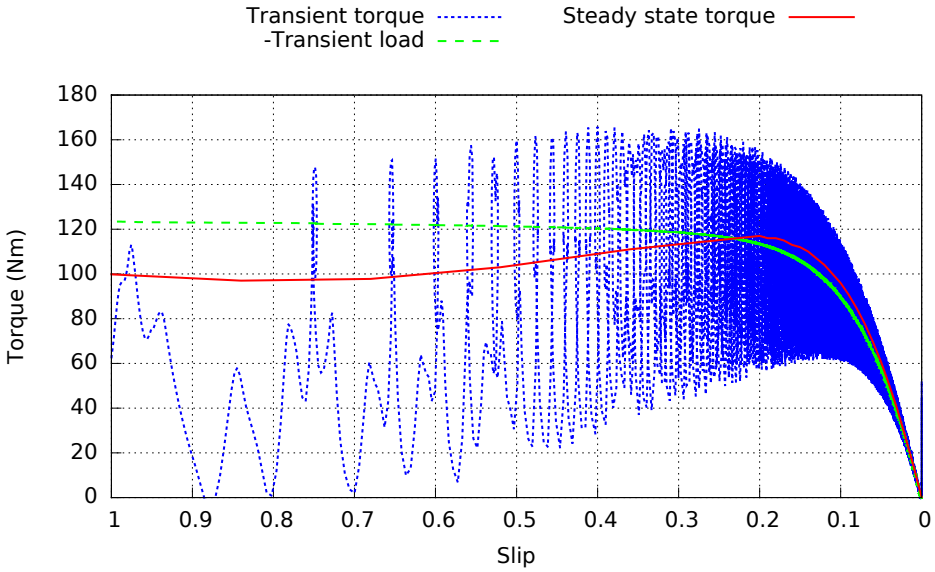

Figure 3.13: Transient torque-slip curve

as possible in only one transient simulation. This is because a more appropriate method of obtaining the transient torque-slip curve is to perform a finite element transient simulation for each load condition which would be extremely time consuming. For example, the time required to simulate 1 second of the transient model of this benchmark motor in Opera 2D was between 1 to 2 days.

The steady state finite element simulations however are usually sufficient in most cases for calculating the performance of the machine at different points on the torque-slip curve. Some special design approaches however can only be represented using transient models. The transient simulation presented in this section might look redundant for obtaining the torque-slip curve but it allows the transient results of the benchmark machine to be compared and also to validate the mechanical load profile for use in other models.

3.8.2 Experimental test rig

Figure 3.15 shows the laboratory test rig employed to test the industrial benchmark machine and the two prototype rotors. The rotor under test was installed in the industrial motor stator and frame. The mechanical shaft of the test machine was coupled to a Ward-Leonard speed control system and the stator windings supplied by a variac. A more detailed description of the equipment used is:

DC motor. Figure 3.14 shows this Invensys/Brook Crompton shunt dc motor with a power rating of 22 kW and nominal speed of 1500 RPM.

Power analyser. A wide band power analyser system Norma D 6000, which was connected between the test motor and the variac.

Torque transducer. Sensor model TORQSENSE E300 RWT - 40 Nm, and display model TORQSENSE transducer display E302.

DC power supply unit (PSU). Model Lambda GEN 300-5. This is a 1500 W dc supply with voltage and current ranges 0-300 V or 0-5 A.

Variac. Connected to a 400 V three-phase supply, regulating the voltage from 0 to 115 %.

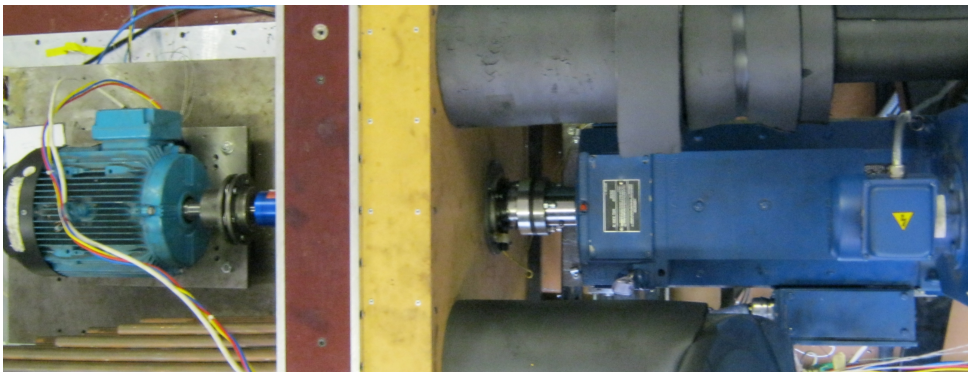

Figure 3.14: Motor under test (Left) coupled to the DC machine (Right)

3.8.3 Test procedure

The test rig described was used to record the performance of the various rotors at different operating speeds. The procedure can be summarized as follows:

- The Ward-Leonard speed control system was started and the test motor speed controlled to the nominal speed (1500 RPM). The machine under test was excited at nominal current and the system was left operating at this point for approximately 30 minutes in order to allow the test system to warm up and reach its operating temperature.
- The voltage at the terminals of the test motor was then increased from 0 V to the required test voltage using the variac.

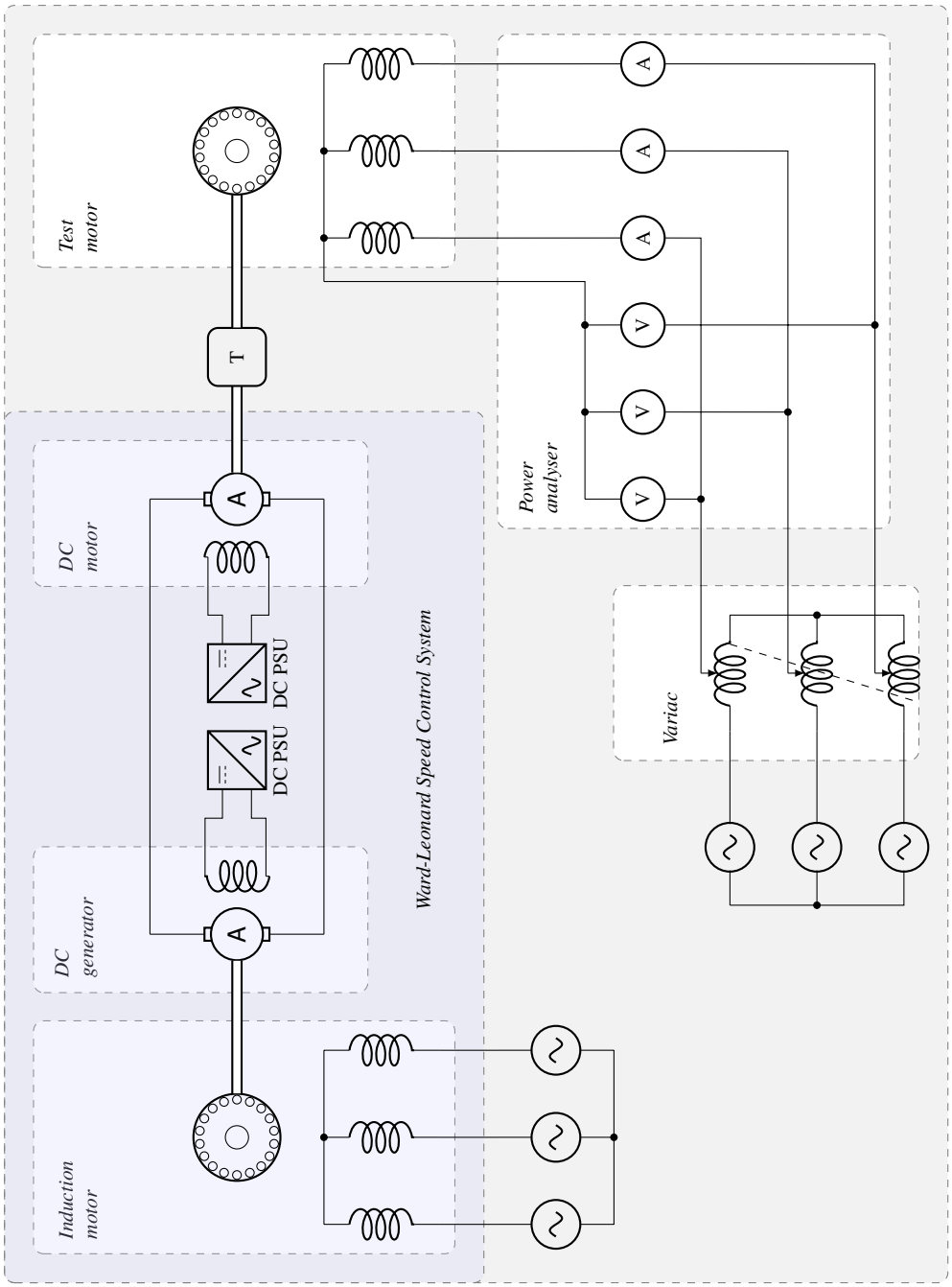

Figure 3.15: Experimental test-rig

- Speed, torque, voltages, currents, active power and power factor were recorded as quickly as possible to prevent significant changes in temperature.
- The speed was reduced to the next operating point. Operating points were defined in small speed steps (∼20 RPM) at low slip and in large steps (∼100 RPM) for large slip (∼>0.2).
- The last two steps were repeated until the full speed range was covered. For operating points at high slip values, the speed was increased to nominal speed after the measurements were recorded in order to allow the machine to cool down before continuing to the next operating point.

3.8.4 Experimental test results

Experimental tests were carried out to validate the finite element models. Test measurements were performed at two test voltages (100 V and 200 V). Figure 3.16 shows the simulated and test results for the original 5.5 kW industrial motor at 100 V. The simulated and test results for the industrial motor show good correlation at low slip values.

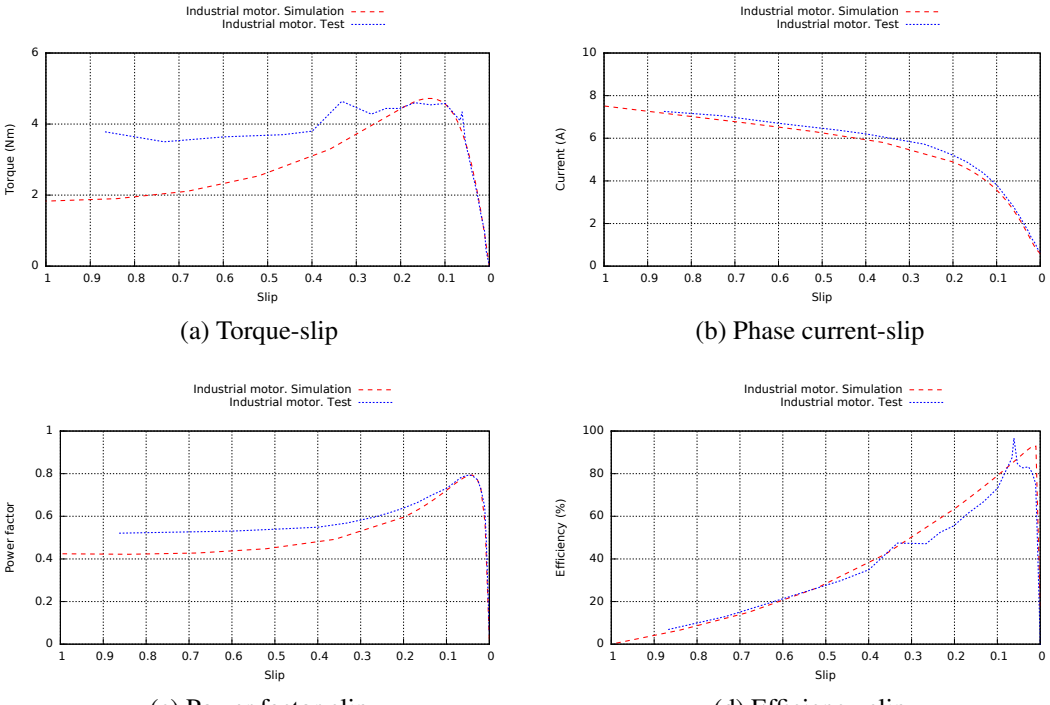

(a) Torque-slip

(b) Phase current-slip

(c) Power factor-slip

(d) Efficiency-slip

Figure 3.16: Performance of the 5.5 kW induction motor at 100 V (26 simulation points and 22 measurement points)

Some of the differences between the simulation and test results were attributed to variations in the rotor temperature. At high slip values, the rated current density can be exceeded even at reduced voltage level tests. This can result in overheating in the test

machine, particularly in the rotor, which in turns affects the cage resistance. Figure 3.17 shows how the torque-slip curve is affected by the rotor temperature. The test result was also plotted for direct comparison and shows the sensitivity of the cage resistance to temperature at higher slip values.

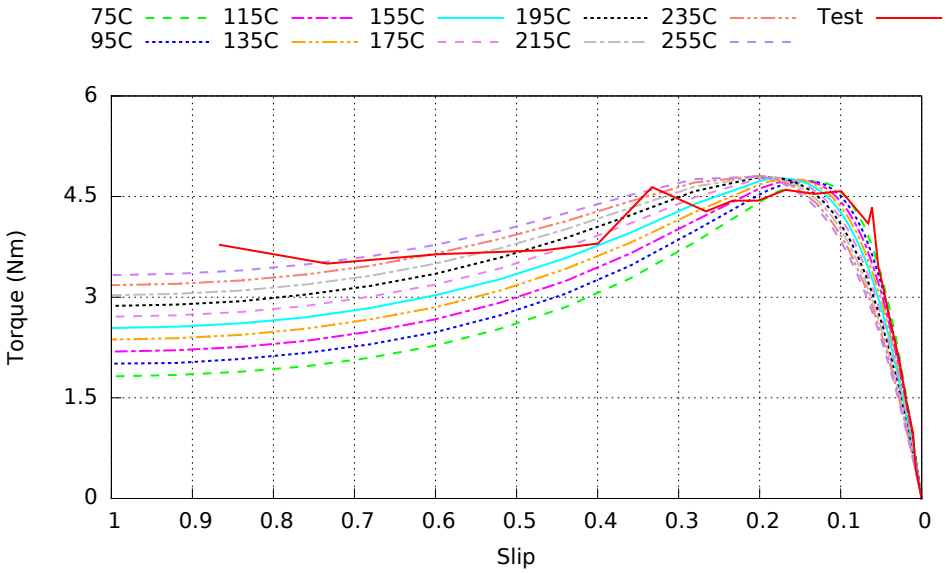

Figure 3.17: Torque-slip characteristic for the industrial rotor at 100 V and different rotor temperatures

Figure 3.18 illustrates the results obtained at 200 V which have the same tendency as those at 100 V. The machine would normally operate at low slip values where the model shows a stronger correlation with the experimental results.

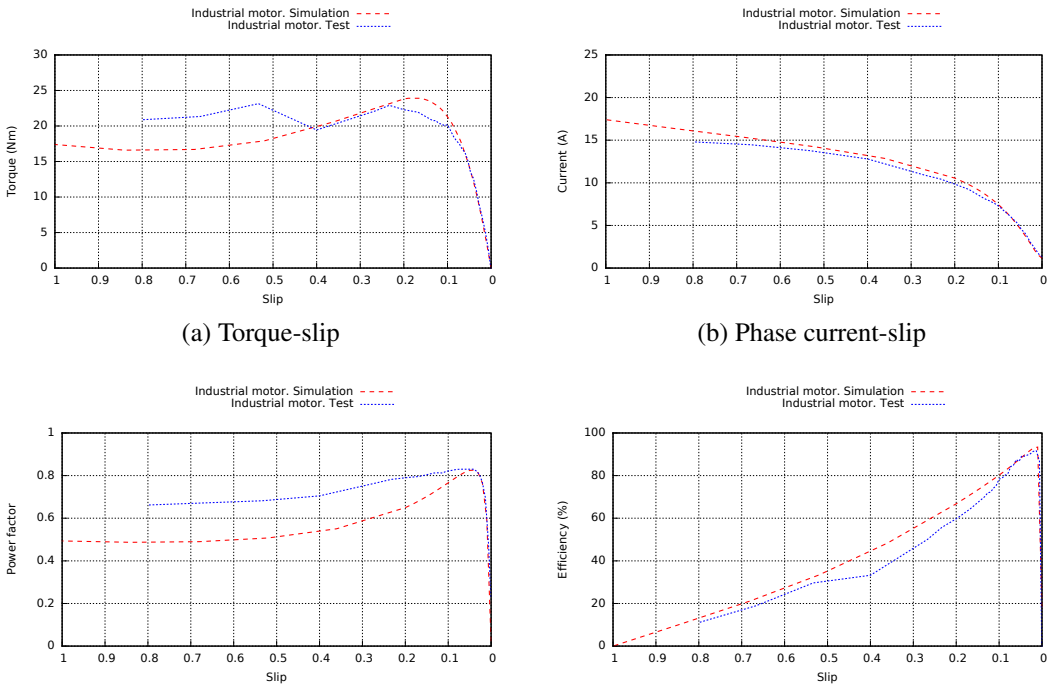

(a) Torque-slip

(b) Phase current-slip

(c) Power factor-slip

(d) Efficiency-slip

Figure 3.18: Performance of the 5.5 kW induction motor at 200 V

3.9 Equivalent circuit parameters sensitivity

Part of the design strategy consisted in identifying which motor parameters have a major influence on torque production. A sensitivity analysis of the induction motor was conducted based on the methodology described in [13, 14]. The torque equation in terms of the variables in the equivalent circuit can be given as [13, 14]:

$$T = \frac{E_T}{s\left\{\left[A_T + \frac{B_T}{s}\right]^2 + \left[C_T - \frac{D_T}{s}\right]^2\right\}} \tag{3.6}$$

where the coefficients are

$$A_T = R_1\left(X_2' + X_m\right)$$
$$B_T = R_2'\left(X_1 + X_m\right)$$
$$C_T = X_1 X_2' + X_m\left(X_1 + X_2'\right) + X_m^2\left(k^2 - 1\right)$$
$$D_T = R_1 R_2'$$
$$E_T = \frac{90 R_2' k^2 X_m^2 V_1^2}{\pi n_s}$$

V_1 - machine rated voltage (V)

n_s - synchronous speed (RPM)

k - skew factor

Equation 3.7 calculates the normalized sensitivity factor for the torque $S_{T,\beta}$ and represents the percentage torque change when the parameter β (R_1, R_2', X_1, X_2', or X_m) was modified by one per cent [13, 14].

$$S_{T,\beta} = \frac{\beta}{T}\frac{\partial T}{\partial \beta} \tag{3.7}$$

Table 3.1 illustrates the results of the sensitivity analysis for a typical 55 kW industrial induction motor design. Four operating conditions were considered: no load, full load, pull out torque and locked rotor. The most important results are those evaluated at pull out torque because this highlights how the maximum torque is restricted by the parameters of the equivalent circuit. The rotor leakage was identified as the most influential factor limiting the maximum torque, followed by the stator leakage and the stator resistance. The minus sign indicates a reduction in the torque production with the increase of that

particular parameter, hence their minimization was crucial in any new designs. Similar results would be obtained for the other industrial induction motors.

Table 3.1: Sensitivity analysis for 55 kW industrial induction motor

Parameter	No load	Full load	Pull out torque	Locked rotor
Torque [Nm]	2.5	363.7	1115.4	863.8
Slip	0.0001	0.0171	0.0981	1.0
R_1	0.145	0.145	0.145	0.145
R_2'	0.116	0.116	0.116	0.180
X_1	0.335	0.335	0.335	0.335
X_2'	4.37	2.466	0.952	0.465
X_m	24.1	24.04	23.76	18.1
k	0.9976	0.9976	0.9976	0.9976
S_{T,R_1}	-0.00031	-0.03579	-0.12093	-0.15253
$S_{T,R_2'}$	-0.99970	-0.70252	-0.00214	0.8120
S_{T,X_1}	-0.02741	-0.05839	-0.26894	-0.78801
$S_{T,X_2'}$	-0.00002	-0.24030	-0.71165	-1.08586
S_{T,X_m}	0.02748	0.03702	0.10368	0.21458

3.10 Design search

Knowledge of the influence of each of the motor parameters allows the designer to identify potential areas of improvement in torque production. The following design concepts were based on this analysis but also using the sizing equation and/or other analytical equations.

3.10.1 Distributed rotor bar induction motor

Reducing the rotor leakage inductance X_2' is one method of increasing peak torque production. This parameter has three main components as described in Equation 3.8: the bar leakage inductance, the differential leakage and the endring leakage. Equation 3.9 shows the dependency of the differential leakage X_{diif} on the number of rotor slots. Increasing the number of rotor slots therefore would reduce the differential leakage. This suggested that dividing the rotor bars into a series of small distributed bars would improve the torque in a similar manner to the matrix motor [15, 16].

$$X_2' = T_{sr}\left(X_{bar} + X_{diff} + \frac{X_{er}}{2N_R sin^2\left(p\pi/N_R\right)}\right) \tag{3.8}$$

where

T_{sr} - stator/rotor turns ratio ($T_{sr} = \frac{4m\left(N_{ph}k_w\right)^2}{N_R}$)

X_{bar} - rotor bar leakage reactance (H)

X_{diff} - rotor differential leakage reactance (H)

X_{err} - rotor end-ring leakage reactance (H)

N_R - number of rotor cage bars

$$X_{diff} = \frac{\mu_0 \omega w d \pi}{4 g N_r} \left(\sin^{-2}\left(\frac{p\pi}{N_r}\right) - \left(\frac{N_r}{p\pi}\right)^2 \right) \tag{3.9}$$

3.10.2 Induction motor with third harmonic current injection

Equation 3.1 shows that an increase in the fundamental aigap flux distribution would directly increase the torque developed in the machine. This would ultimately be restricted by saturation, but if a flux distribution with a higher fundamental component were used without exceeding the saturation point, it would be possible to obtain more torque. This can be achieved by the injection of third harmonic current as reported in [17–20]. Although this has been studied in detail, this method could easily be combined with other techniques to further increase the maximum torque and this has not been fully explored.

3.10.3 Wound rotor induction motor

The reduction of the harmonic content of the airgap flux distribution plays a key role in the design of induction machines because a cage rotor will respond to most harmonics. One method to reduce this effect is to use a wound rotor. Although a wound rotor is less compact and robust than a cage rotor, the better harmonic tolerance of the induction design can improve the torque density. Any harmonic field that couples with the rotor cage produces a negative torque at the normal operating slip. Removing these harmonics therefore would increase the net output torque.

3.10.4 Induction motor with tooth slits

The stator leakage reactance X_1 comprises two components as shown in Equation 3.10. The stator slot leakage paths within one phase tend to combine and cancel in the inner

teeth of this phase. This gives as a result a leakage path as shown in Figure 3.19. One means to reduce this leakage is the introduction of thin slits in the teeth and this would also increase the torque.

$$X_1 = X_1^{SLOT} + X_1^{END} \tag{3.10}$$

where

X_1^{SLOT} - stator slot leakage reactance (H)
X_1^{END} - stator end-winding leakage reactance (H)

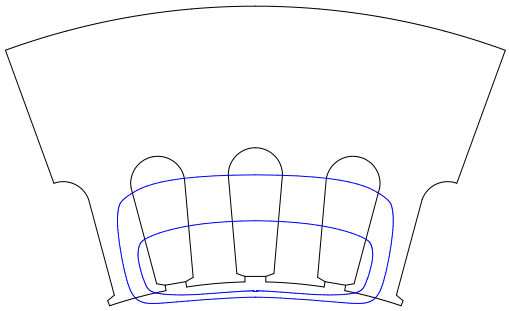

Figure 3.19: Stator slot leakage paths for one stator phase band

3.10.5 Double stator induction motor

Equations 3.11 and 3.12 were taken from reference [21]. These equations are based on the sizing equation.

$$J_1 = 2q_1 N_1 I_1 / (S_1 A_{cu}) \tag{3.11}$$

where

J_1 - current density (A/m^2)
q_1 - number of phases
N_1 - turns per phase
I_1 - stator line current
S_1 - number of stator slots
A_{cu} - area of copper per slot

$$K_1 = 2q_1 N_1 I_1/(\pi D_r) \tag{3.12}$$

where

K_1 - electric loading (A/m)

D_r - rotor outer diameter (m)

Reference [21] also shows that any slot shape could be substituted for an equivalent rectangular slot with width (w_e) and depth (d_e). The area of such a slot is determined from Equation 3.13.

$$A_{cu} = w_e d_e k_{fill} \tag{3.13}$$

where

k_{fill} - slot filling factor

Combining Equations 3.11, 3.12 and 3.13, the relationship between the electric loading and the current density, Equation 3.14 can be established. This equation shows how to increase the electric loading and in turn the torque. Almost all the components of this equation are relatively fixed with the exception of the slot depth (d_e). If d_e is increased, the torque produced also would be increased.

$$K_1 = \frac{S_1 w_e d_e k_{fill}}{\pi D_r} J_1 \tag{3.14}$$

However increasing the slot depth also increases the stator slot leakage reactance as part of X_1. A better method is to add a second stator which would increase the net electric loading in the machine to $K_1 + K_2$ where K_2 is the electric loading of the second stator. The normal difficulty of doing this is finding the space needed to add the second stator. The design concept explored here is to remove the back iron of the rotor and insert the second stator inside the rotor cage. The rotor cage would then form a rim situated between two airgaps to the two stator windings. Torque would then be produced between the rotor field and the stator surface current density of the conventional stator but also with

the additional stator. Potentially this could significantly increase the torque developed, however cooling would also be critical.

3.10.6 Modular induction motor

Although modular windings tend to make an induction motor bigger, the advantage of separated coils offers some advantages for pole changing [22]. It is expected that a modular induction motor would have a lower peak torque compared to an equivalent industrial induction motor. However, using pole change operation would allow the rating of the modular induction machine to be half of the peak torque. This is because the machine only has to cover a 2:1 speed range before pole changing. This would increase the allowed rating which would be seen as an increase in the specific torque.

3.10.7 Solid rotor core induction motor

As shown in Equation 3.1, increasing the fundamental aigap flux distribution would increase directly the torque produced in the machine. Some non-laminated iron alloys have better magnetic properties than silicon iron but at the expense of much higher iron losses. However, these iron losses are dependant on the frequency. The induction motor in an electric vehicle could work at low slip most of the time. The frequency in the rotor core would also be low which could allow the use of these alloys.

3.10.8 Induction motor with grain oriented laminations

Recalling also Equation 3.1, the use of grain oriented laminations, which have improved magnetic properties along the grain axis, to increase the fundamental airgap flux distribution would in turn increase the maximum torque. For this purpose, the stator could be constructed using a series of segments of grain oriented material in the radial direction.

3.10.9 Canned rotor induction motor

Looking at Equation 3.9, another way to reduce the differential leakage and increase the torque is to increase airgap. This is normally not a good design rule because of the increase in the magnetizing current and lower performance (efficiency and power factor). However if part of the larger airgap was filled with a thin copper can this might produce a net increase in the torque. The selection of the can thickness was made in such way that the torque produced was equal to the double stator induction motor. The can thickness

was rounded up to the closest commercial copper sheet thickness in order to facilitate manufacture.

3.10.10 Toroidal induction motor

Similar to the modular motor, the toroidal induction motor allows pole changing in order to achieve a wide speed range [23, 24]. The rating of the toroidal machine has a 2:1 ratio between the peak torque and the nominal torque. This would also allow better use of the machine capabilities. Besides, toroidal windings could offer important space savings (compacted, shorter and non-overlapped end-windings) once manufacture techniques are improved [24].

3.11 Conclusions

This chapter provides a review of the basic methodology for the development of new induction motor designs for electric vehicles. It covers the initial requirements through to the new preliminary design concepts. Special attention was focused on the finite element software used to asses the new motor designs.

3.12 References

[1] A C Smith. *Design of Electrical Machines, Lecture notes*. 2012.

[2] N.A. Patil, J.S. Lawler, and J.W. McKeever. “Determining constant power speed ratio of the induction motor from equivalent circuit parameters”. In: *Southeastcon, 2008. IEEE*. 2008, pp. 460–467.

[3] R. Mecke. “Energy-efficient control of induction machines with variable rotor flux”. In: *Power Electronics and Applications (EPE), 2013 15th European Conference on*. 2013, pp. 1–10.

[4] J.-F. Stumper, A. Dotlinger, and R. Kennel, “Loss Minimization of Induction Machines in Dynamic Operation”, *Energy Conversion, IEEE Transactions on*. 28, 726–735. (2013).

[5] *Lamination steels, Third edition. A Compendium of Lamination Steel Alloys Commonly Used in Electric Motors*. The Electric Motor Education and Research Foundation, 2009.

[6] H Witte. *FEA Simulations of Magnets with Grain Oriented Steel*. Tech. rep. BNL-98381-2012-IR. USA: Brookhaven National Laboratory, 2012.

[7] Cobham Technical Services. *Opera2d User Guide*. Cobham CTS Litmited, 2011.

[8] Cobham Technical Services. *Opera2d User Manual*. Cobham CTS Litmited, 2011.

[9] Cedrat. *Induction Machine Tutorial*. Magsoft corporation, 2006.

[10] Cedrat. *User Guide Flux*. 2012.

[11] A. Boglietti et al., "A simplified thermal model for variable-speed self-cooled industrial induction motor", *Industry Applications, IEEE Transactions on*. 39, 945 –952. (, Jul/Aug, 2003).

[12] A. Stermecki et al. "Determination of the starting and operational characteristics of a large squirrel cage induction motor using harmonic and transient FEM". In: *Electrical Machines, 2008. ICEM 2008. 18th International Conference on*. 2008, pp. 1–5.

[13] I. Sanchez and P. Pillay. "Sensitivity analysis of induction motor parameters". In: *Southeastcon '94. 'Creative Technology Transfer - A Global Affair'., Proceedings of the 1994 IEEE*. 1994, pp. 50 –54.

[14] S. Ansuj, F. Shokooh, and R. Schinzinger, "Parameter estimation for induction machines based on sensitivity analysis", *Industry Applications, IEEE Transactions on*. 25, 1035 –1040. (, Nov/Dec, 1989).

[15] Y. Kawase et al., "Magnetic Field Analysis of Matrix-Rotor Induction Motor Using Parallel Computing System", *Magnetics, IEEE Transactions on*. 47, 1062 –1065. (2011).

[16] M. Ito et al., "Magnetically anisotropic solid rotor of an induction motor", *Energy Conversion, IEEE Transactions on*. 3, 427 –432. (1988).

[17] R.O.C. Lyra and T.A. Lipo. "Torque density improvement in a six-phase induction motor with third harmonic current injection". In: *Industry Applications Conference, 2001. Thirty-Sixth IAS Annual Meeting. Conference Record of the 2001 IEEE*. Vol. 3. , 30 Sep - 4 Oct, 2001, pp. 1779 –1786.

[18] D. Casadei et al. "Torque maximization in high-torque density multiphase drives based on induction motors". In: *Energy Conversion Congress and Exposition (ECCE), 2010 IEEE*. 2010, pp. 3896 –3902.

[19] D. Casadei et al. "Control of a high torque density seven-phase induction motor with field-weakening capability". In: *Industrial Electronics (ISIE), 2010 IEEE International Symposium on*. 2010, pp. 2147 –2152.

[20] L. Zarri et al. "Maximum-torque-per-ampere control of high torque-density multiphase drives based on induction motors". In: *Energy Conversion Congress and Exposition (ECCE), 2012 IEEE*. 2012, pp. 495 –502.

[21] V.B. Honsinger, "Sizing Equations for Electrical Machinery", *Energy Conversion, IEEE Transactions on*. EC-2, 116–121. (1987).

[22] A.S. Abdel-Khalik and S. Ahmed, “Performance Evaluation of a Five-Phase Modular Winding Induction Machine”, *Industrial Electronics, IEEE Transactions on*. 59, 2654 –2669. (2012).

[23] B.B. Jensen et al., “Performance of a Folded-Strip Toroidally Wound Induction Machine”, *Industrial Electronics, IEEE Transactions on*. 59, 2217 –2226. (2012).

[24] B.B. Jensen and A.G. Jack. “Toroidally wound induction machines”. In: *Electrical Machines (ICEM), 2010 XIX International Conference on*. 2010, pp. 1 –5.

CHAPTER

FOUR

SIMULATION RESULTS

4.1 Introduction

This chapter explores different potential designs to increase the specific torque of induction motors for electric vehicles. The following sections describe the new designs which were introduced in the previous chapter. This review presents a more detailed description of each motor with the initial improvements expected and some simulation results compared with the respective benchmark.

4.2 Distributed rotor bar induction motor

The selection of the slot number for both stator and rotor is a balance between the electric and magnetic circuits during the design process. The advantages/disadvantages of increasing or reducing the number of slots have to be considered carefully in terms of the desired motor performance. The stator slots are difficult to vary in general because they are largely fixed by the pole-number and the winding design. To investigate the influence of rotor slot number, a distributed bar rotor was developed that significantly increased the rotor bar number. The conventional squirrel cage rotor was replaced by a mesh of small hexagonal elements which were distributed to allow the flux paths to pass through the rotor in the radial direction as shown in Figure 4.1. It is a similar use of the active materials to the anisotropic rotor of the matrix motor mentioned in Section 2.5.7. This design uses the same stator as the 55 kW benchmark motor.

The laminations required for both the stator and rotor of the considered distributed bar motor are shown in Figure 4.1a. The main difference with a typical induction motor lamination is that the cage elements were distributed in groups (160) each composed of a pair of subgroups each one. Each subgroup pair was aligned in the radial direction but

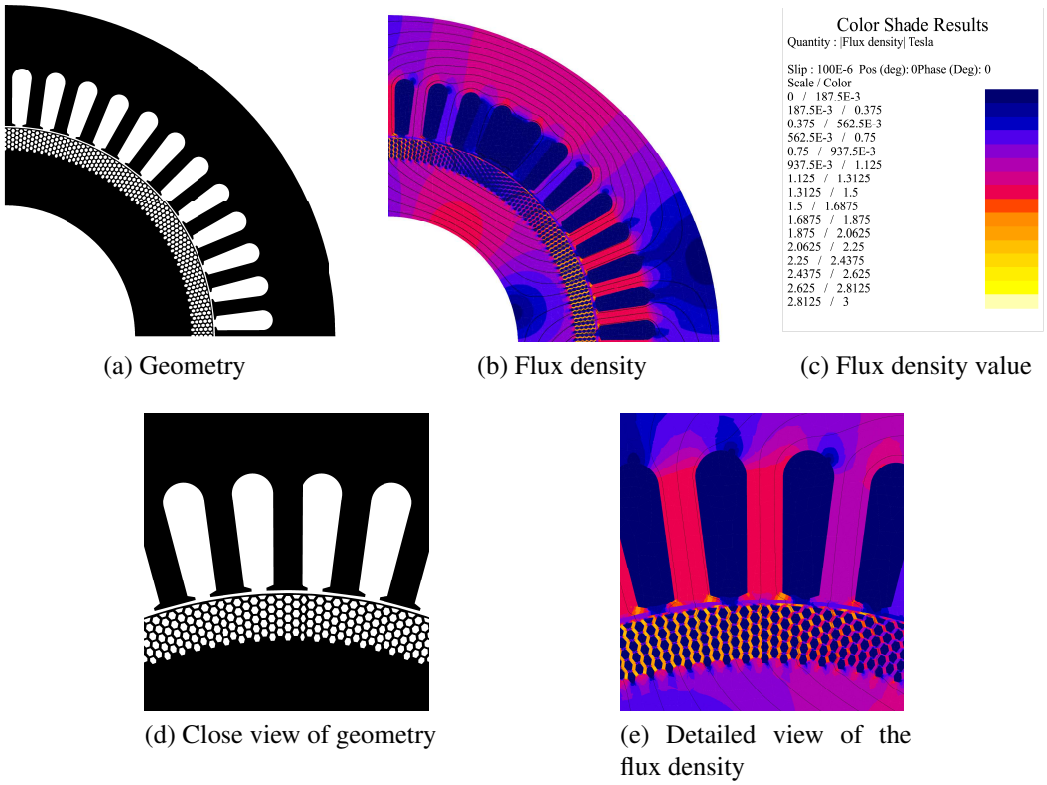

(a) Geometry (b) Flux density (c) Flux density value

(d) Close view of geometry (e) Detailed view of the flux density

Figure 4.1: Distributed rotor bar induction motor under no load conditions

shifted to maximize the space utilization. One subgroup was composed only of complete hexagonal elements (5) while the other subgroup by one trapezoidal (half hexagon) element and hexagonal elements (4) as shown in Figure 4.1d. In simpler terms, each bar of the benchmark motor was replaced by a mesh of 40 smaller elements (5x8 in the radial and tangential directions respectively). The distance between the sides of the elements of each subgroup is constant in the tangential direction in order to keep the tooth width constant. For this reason, the hexagonal elements closest to the coreback are narrower than those closest to the airgap. The standard rules for the selection of the number of rotor slots were not expected to apply in this rotor. The numbers of groups and elements to form this cage were selected only in order to have geometrical elements close to a regular hexagon whilst this cage area was maintained the same as the industrial cage area scaled by the copper to aluminium conductivity ratio. This distributed cage therefore occupied a smaller area than the copper cage 55 kW benchmark motor because its slots have the same slot area as the aluminium cage.

Each cage group was considered as a single component in the electric circuit of the cage in order to simplify the model. If each element were considered separately in the electric circuit for this particular cage, there would be a circuit with 1600 solid conductor components plus all the interconnecting end-ring circuit components (About 11520 components more). The use of symmetry can reduce this by a factor of 4 but the number of components would be prohibitively large. It would also require a means of calculating the resistance and inductance of the end-ring components in the radial and tangential

direction which is clearly not straightforward.

The flux density distribution and the equipotential field lines under no load conditions for the distributed rotor bar induction motor in Figures 4.1b and 4.1e show similar distribution and paths to the industrial motor.

Figure 4.2 illustrates the simulated performance of the distributed bar rotor in comparison to the benchmark motor. It is clear that there is an increment in the maximum torque but at the expense of other performance factors. A reduction in the rotor harmonic leakage was expected because of the better distribution of currents in the rotor. Manufacture of the rotor however represents the main obstacle to this type of machine.

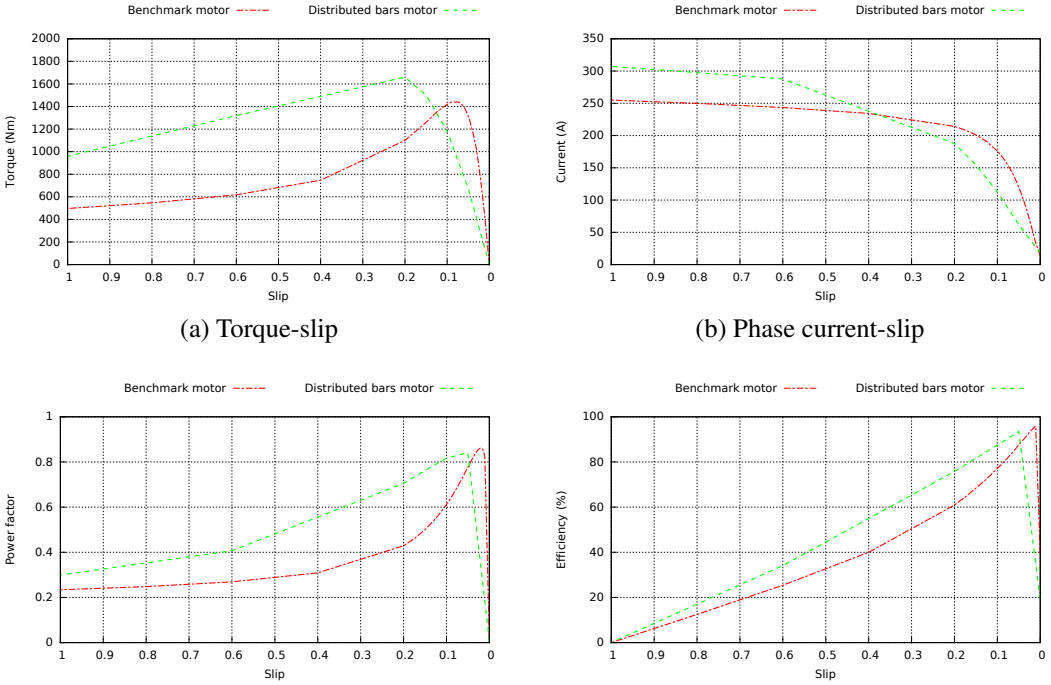

(a) Torque-slip

(b) Phase current-slip

(c) Power factor-slip

(d) Efficiency-slip

Figure 4.2: Performance curves of the distributed bar induction motor

The 55 kW benchmark motor was employed as a reference for comparison and the results are illustrated in Figure 4.2. The new design had a higher maximum torque but at a higher slip than the maximum torque of the benchmark motor.

In simple terms the slip at which peak torque occurs is determined by the ratio of the rotor resistance to the rotor leakage reactance so Figure 4.2a suggests the distributed bar rotor has a lower rotor leakage as expected. The rotor reactance is composed of the rotor end-ring reactance, slot reactance and the harmonic (or differential) leakage reactance. Because the rotor bar number has been increased, the harmonic differential leakage would be expected to reduce although it is difficult to asses the influence on the rotor slot leakage.

Another useful measure of the rotor performance is the torque per unit current squared which is a good indication of the effective rotor resistance. Using the standstill figures, the rotor resistance was also found to be higher for the distributed bar rotor than the

normal cage rotor. This would also increase the slip at peak torque but would not increase its magnitude. Figure 4.2b also shows that the input current at standstill is higher for the distributed bar rotor which would also indicate that the rotor leakage reactance is lower to compensate for the higher rotor resistance.

The geometry of the small bar elements shown in Figure 4.1 had the best performance compared with several other bar shapes considered, for instance round, trapezoidal, square, amongst others. Figure 4.3 illustrates a couple of examples: round and rhombus.

(a) Round (b) Rhombus

Figure 4.3: Induction motors with distributed rotor bar

Although further research is still needed however for the distributed bar rotor particularly because the modelling and simulation became more complex, it was decided however to explore more simple motor designs. This was based on the expected excessive manufacture and costs. Lamination cutting was predicted to be more difficult and expensive due to the size of the elements of the distributed bar rotor. But the main challenge was the manufacture of the cage. Die-casting was not expected to be suitable in practical and economic terms while machining was considered not to be suitable for mass production.

In order to help with manufacture, the hexagonal elements were changed for round bars and their number reduced as shown in Figure 4.4. It could be considered a simpler version of the distributed round bar motor resulting in effectively a double rotor cage topology which would be easier to manufacture and each rotor bar is modelled individually. This and the next designs were based on the 5.5 kW benchmark motor in order to help with prototyping and testing.

Unfortunately the performance gain was lost as a large magnetic flux leakage occurs between the two layers of rotor bars. The main problem with the rotor bar design in Figure 4.4 is that the inner layer of bars are effectively magnetically short-circuited. Figure 4.5 shows the reduced torque obtained while the power factor and efficiency do not change significantly compared with the benchmark motor. Slits between the bars could be helpful in reducing the leakage flux but this might make the rotor mechanically weaker.

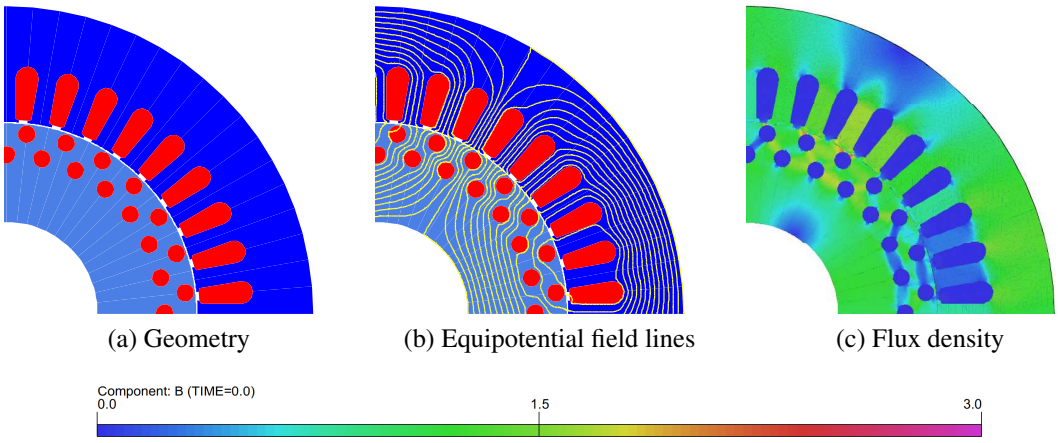

(a) Geometry (b) Equipotential field lines (c) Flux density

(d) Flux density value (T)

Figure 4.4: Round slot, double cage rotor induction motor under no load conditions

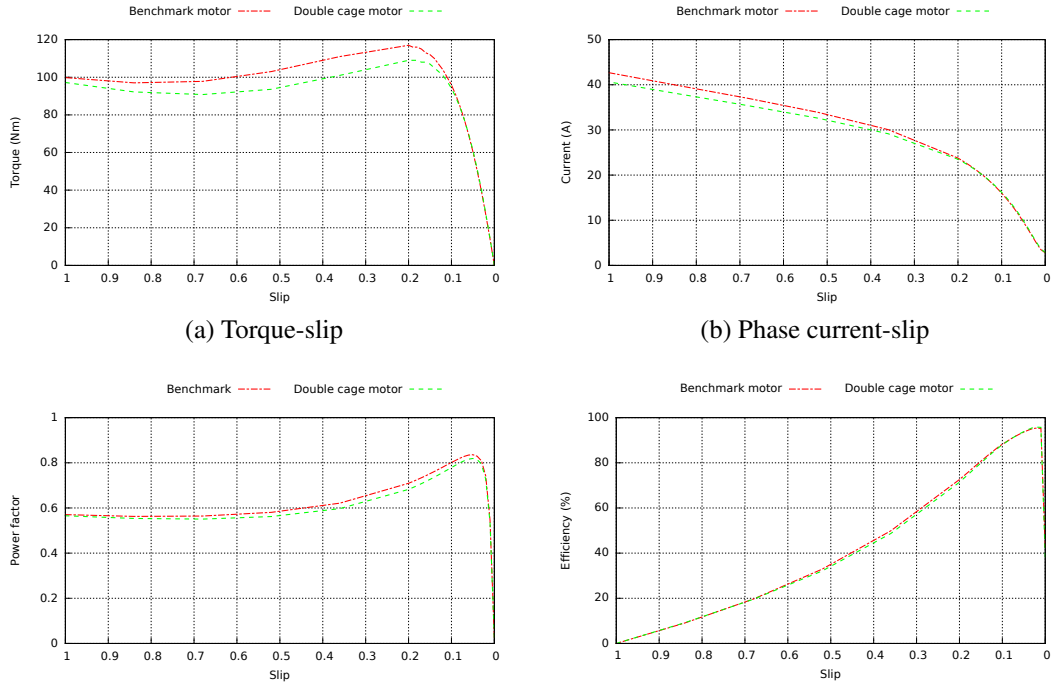

(a) Torque-slip (b) Phase current-slip

(c) Power factor-slip (d) Efficiency-slip

Figure 4.5: Performance curves of the round slot, double cage rotor induction motor

Figure 4.6 shows a modified version of the previous design with a reduced space between the slot layers to reduce the bar leakage flux and the round slots of the top layer were replaced with rectangular bars. The rectangular bar area was scaled from the area of a bar of the industrial motor by the copper to aluminium conductivity ratio. The round bar had the maximum area that allowed 1 mm separation from the rectangular bars and the distance between round bars was equal to the tooth width of the industrial motor. The rectangular bar has a lower resistance than the round bar but the same as the industrial bar. The round bar resistance is a little more than the double that of the rectangular bar resistance.

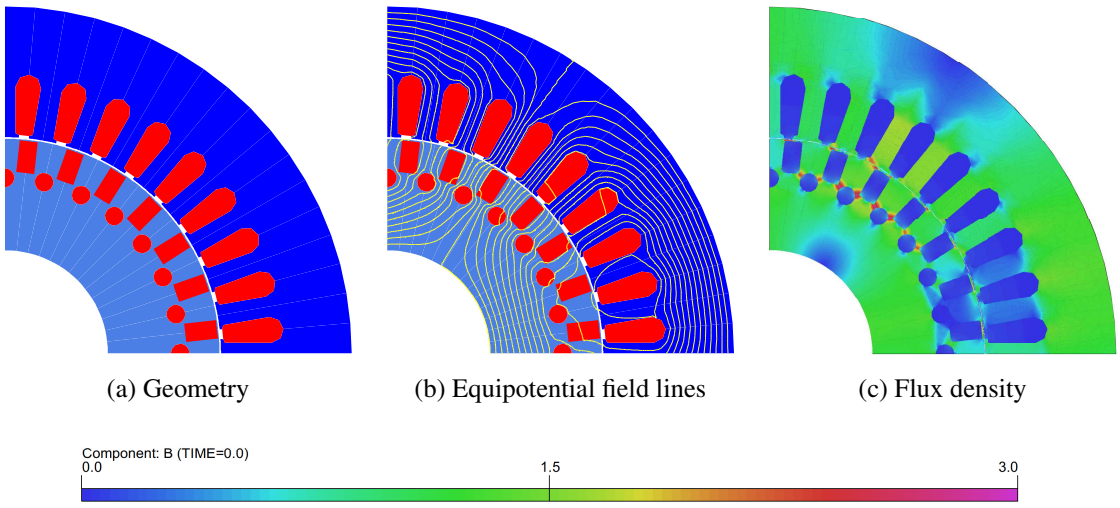

(a) Geometry (b) Equipotential field lines (c) Flux density

(d) Flux density value (T)

Figure 4.6: Double cage rotor induction motor under no load conditions

Each layer had its own separated end-ring. Both separated and single end-ring configurations were simulated and it was found that separated end-rings produced a slightly better performance. This improvement however was thought to be a consequence of the modified end-ring impedances used in both models.

This motor design showed a higher peak torque compared to the benchmark machine but at the expense of a higher phase current and lower power factor and efficiency as illustrated by Figure 4.7. Although the ratio of torque improvement is not as high as in the design with small hexagonal elements, its construction and testing can be relatively easily implemented.

The higher torque production is assumed to be a result of a reduction in the rotor differential leakage as a consequence of the larger number of effective rotor slots than the benchmark motor. The lower rotor resistance is also reflected in the torque-slip curve with a maximum torque at a lower slip value. On the other hand, the increment in the phase current is attributed to the higher magnetizing current needed as a result of the saturated bridges around the round bars.

4.3 Induction motor with third harmonic current injection

Third harmonic current injection has been reported as a technique to increase the torque of an induction motor. This technique allows the amplitude of the fundamental magnetic flux wave to increase but at the expense of adding higher harmonics which introduce torque pulsations. Although this technique is more related to the machine control than

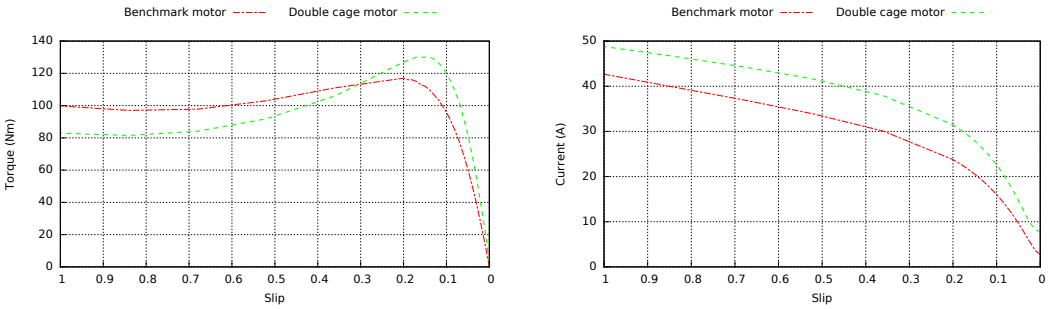

(a) Torque-slip

(b) Phase current-slip

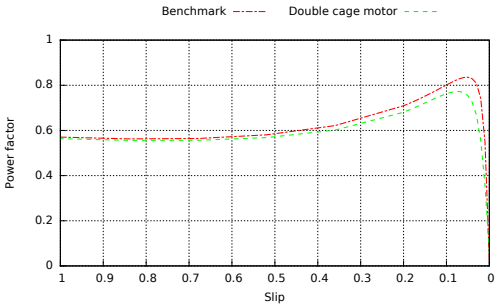

(c) Power factor-slip

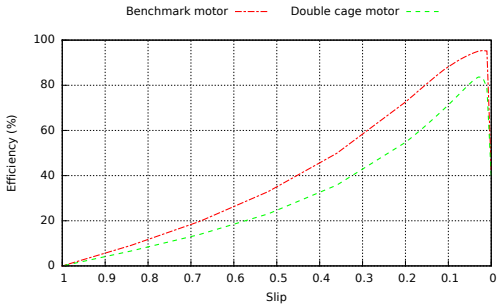

(d) Efficiency-slip

Figure 4.7: Performance curves of the double cage rotor

to the design, it requires the designer to consider the effect of torque pulsations and their reduction.

The main advantage of this method lies in the fact that it can be used in conjunction with other methods for torque improvement. This technique is simple to implement and the topology of the machine remains almost unchanged. From a design point of view, stator and rotor corebacks need to be wider in order to keep the flux density within the design levels. This approach however requires some important changes to be made to the control because of the higher losses and torque pulsations [1, 2].

Figure 4.8 shows the field distribution for the 55 kW benchmark motor before and after implementation of the third harmonic current injection. These field distributions correspond to an operating point close to the maximum torque (About 0.1 slip). It is clear that the general saturation levels in the magnetic circuit increase particularly in the corebacks. This is because in both cases the same induction motor was employed with the only difference in the voltage source. In the case without third harmonic injection the motor was supplied with a sinusoidal voltage supply. In the case with third harmonic current injection two sinusoidal voltage supplies connected in series were used. The series voltage sources consisted of one with 50 Hz nominal frequency and a higher peak voltage (1.15 pu) while the other had a 150 Hz frequency, 0.15 pu peak voltage [3–5].

Figure 4.9 shows the electromagnetic torque obtained with a couple of transient simulations in Flux 2D. Both simulations start at the same operating condition, close to maximum load. Without harmonic current injection, the torque pulsations are caused by

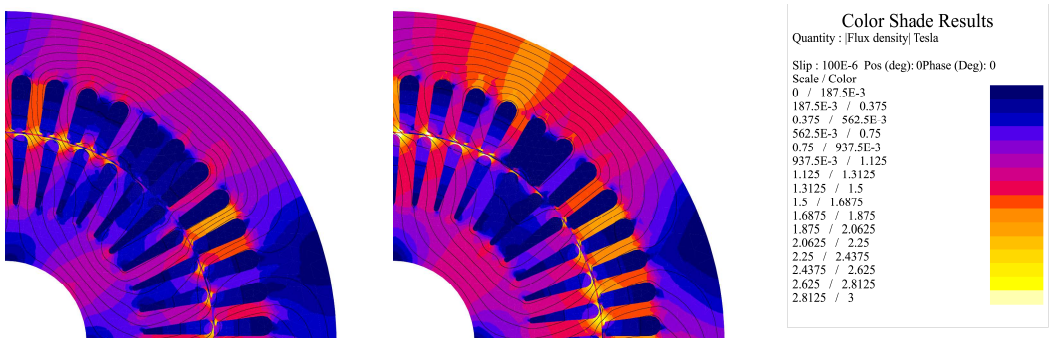

(a) Without third harmonic (b) With third harmonic (c) Flux density value

Figure 4.8: Induction motor with third harmonic current injection under no load conditions

the slotting and the interaction of the higher order mmf harmonics. The second case however considers the injection of third harmonics and it is clear from Figure 4.9 that a higher average torque is produced as predicted, but also the torque pulsations are increased significantly.

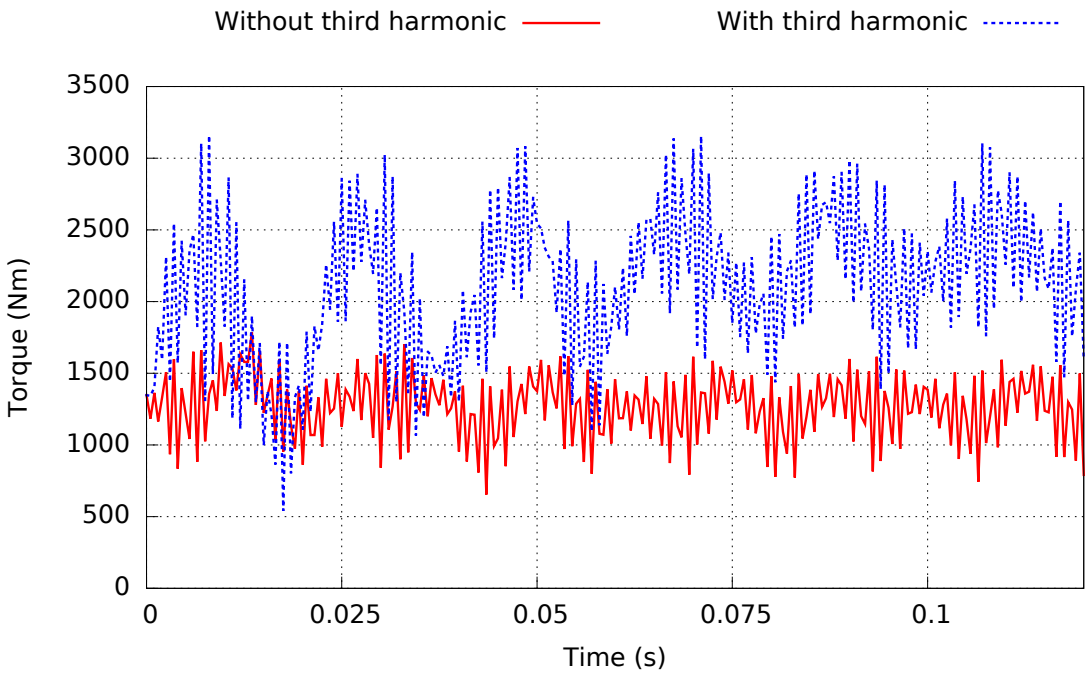

Figure 4.9: Transient simulation of the induction motor with third harmonic current injection

One of the main design disadvantages of the third harmonic current injection is its computational requirements for simulation. It requires transient simulations because the circuit sources have different frequencies (50 and 150 Hz). The transient simulation step for this method has also to be reduced compared with the time step used in the benchmark motor because of the higher frequency (150 Hz).

4.4 Wound rotor induction motor

Wound induction motors have been used in the past for variable speed applications because of the simplicity in their control. This can be done through the variation of the resistance connected to the rotor windings. However this requires slip rings and part of the energy is lost in these resistances. Power converters connected to the rotor windings instead of resistances have also been used in order to eliminate these resistive losses.

A normal cage rotor is a robust and cost effective rotor construction but it will respond to most of the mmf harmonics produced by the stator winding. This restricts the options available in the stator winding design because its field distribution should have a low harmonic content.

For this reason, a different approach to the design of wound rotor induction motors was adopted. A wound rotor including a three phase distributed winding was used so the rotor would only respond to the stator mmf harmonics that were also produced by the rotor winding. A five-phase concentrated winding was employed in the stator to maximise the fundamental field [6, 7]. An outer rotor topology was also selected to provide more space for the distributed rotor windings. Figure 4.10 shows the geometry, equipotential field lines and flux distribution for this machine under no load conditions. The winding distributions for one phase at the stator and the rotor are shown in Figure 4.11.

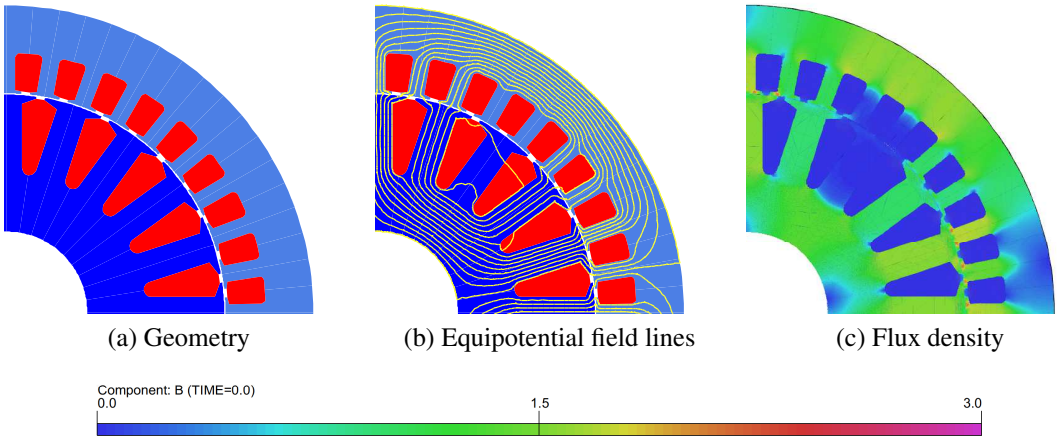

(a) Geometry (b) Equipotential field lines (c) Flux density

(d) Flux density value (T)

Figure 4.10: Wound rotor induction motor under no load conditions

A lower performance however was obtained because this machine employed the same active volume as the 7.5 kW benchmark squirrel cage rotor induction motor. In other words, the available active space was insufficient because of the increased area required by the wound rotor windings. This constrained the motor outer diameter and the available slot area for both stator and rotor windings and as a result produced relatively high resistance windings. This is reflected in Figure 4.13 by the peak torque occurring at a relatively high slip compared to the normal slip in the benchmark motor. However a

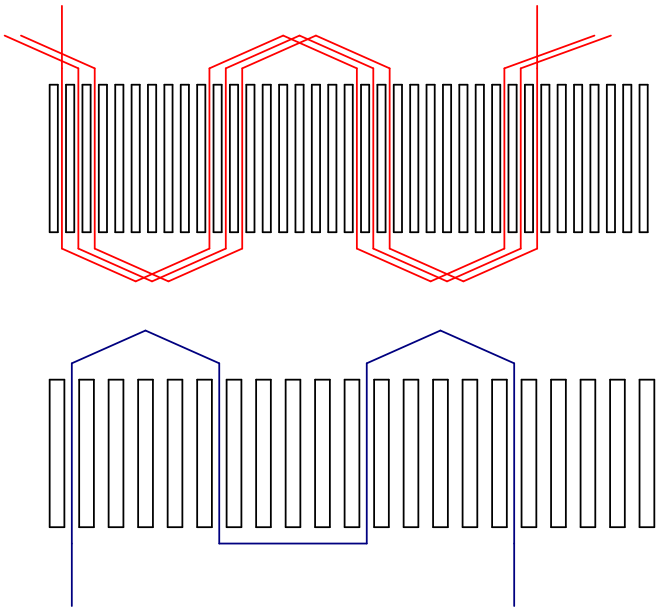

Figure 4.11: Wound rotor winding layout for one phase at the stator (red) and the rotor (blue)

higher maximum pull out torque was achieved. The performance was further improved (about 40 %) using third harmonic current injection as shown in Figure 4.12. The third harmonic injection was simulated by adding to the stator phase circuit a series voltage source with three times the fundamental frequency.

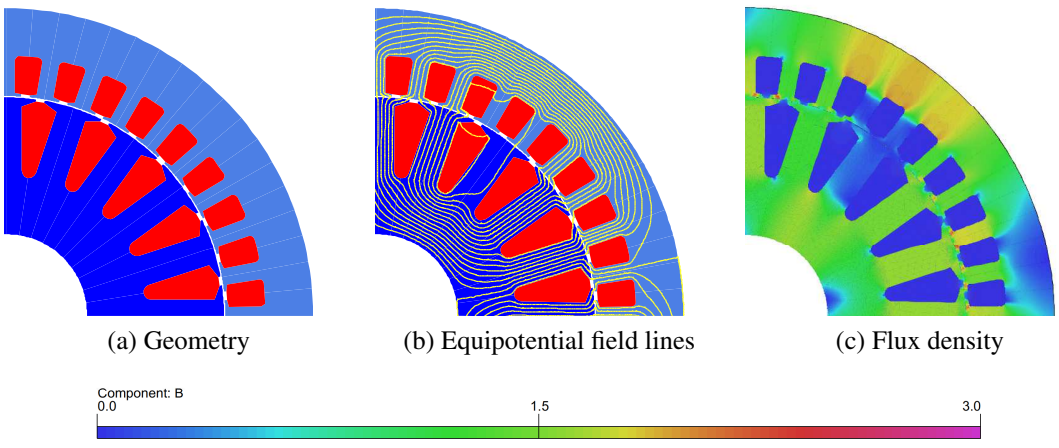

(a) Geometry (b) Equipotential field lines (c) Flux density

(d) Flux density value (T)

Figure 4.12: Wound rotor induction motor with third harmonic current injection under no load conditions

The use of the third harmonic current injection to increase the torque production in squirrel cage induction motors has been already covered extensively in the literature, as mentioned in section 2.5.4. This method however is particularly useful because it could be implemented in conjunction with most of the other techniques and topologies for torque improvement. This case of a wound outer rotor induction motor with third harmonic current injection is an example.

Figure 4.13 presents the torque-slip curves for the wound rotor induction machine using Opera 2D. The torque-slip curve of the wound rotor induction motor with third current injection however was obtained by employing a transient simulation for each loading condition.

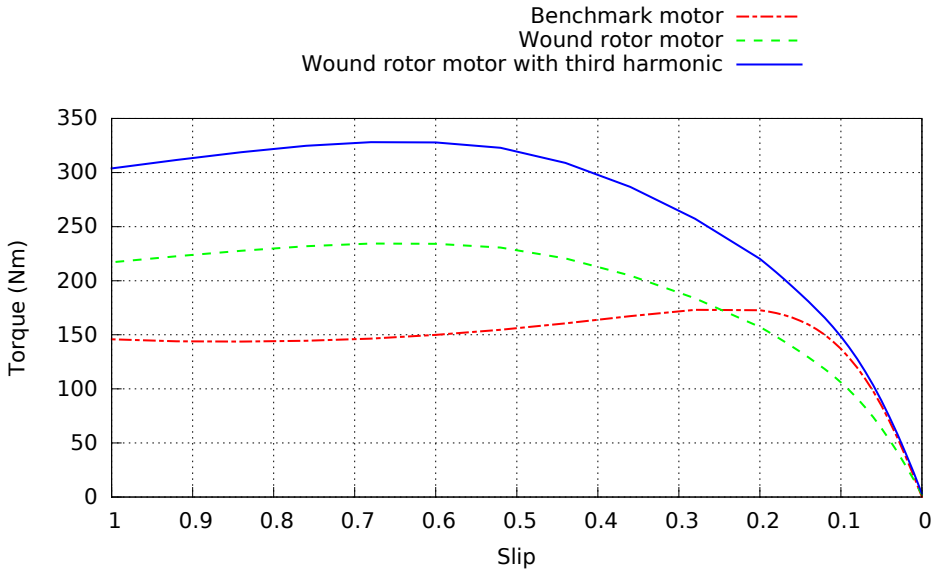

Figure 4.13: Torque-slip curves for the wound rotor induction motor

Although the wound rotor induction motor design produces a higher peak torque, the relatively high slip at which this occurs make it more suitable for other type of applications and not an the electric vehicle. This design illustrated the use of third harmonic current injection method with other techniques for torque improvement.

4.5 Induction motor with tooth slits

The leakage inductances are key influential parameters for maximum torque. Their reduction therefore is an obvious means to increase the specific torque. One option to achieve this leakage reduction was to insert thin slits in the rotor and stator teeth as shown in Figure 4.14. This design was based on the 55 kW benchmark induction machine. Slits have been used in high speed solid rotor induction motors previously to increase power/torque [8].

The slits unfortunately required thinner slots to avoid saturation in the teeth. The modification to the slot area however tends to increase the leakage, so again it becomes a trade-off between the two counter-balancing effects and Figure 4.15 shows that the net effect of the slits is minimal although a small gain of 2 % in starting torque was achieved. This improvement was considered insignificant to justify the mechanical weakness produced in the core structure by introducing the slits.

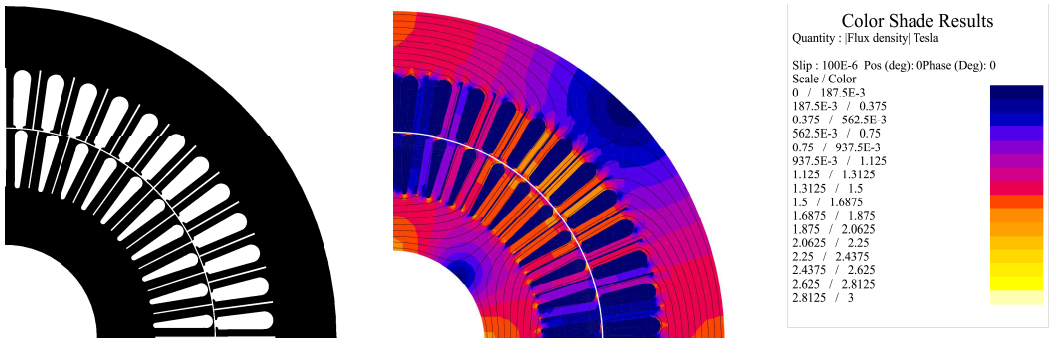

(a) Geometry (b) Flux density (c) Flux density value

Figure 4.14: Induction motor with tooth slits under no load conditions

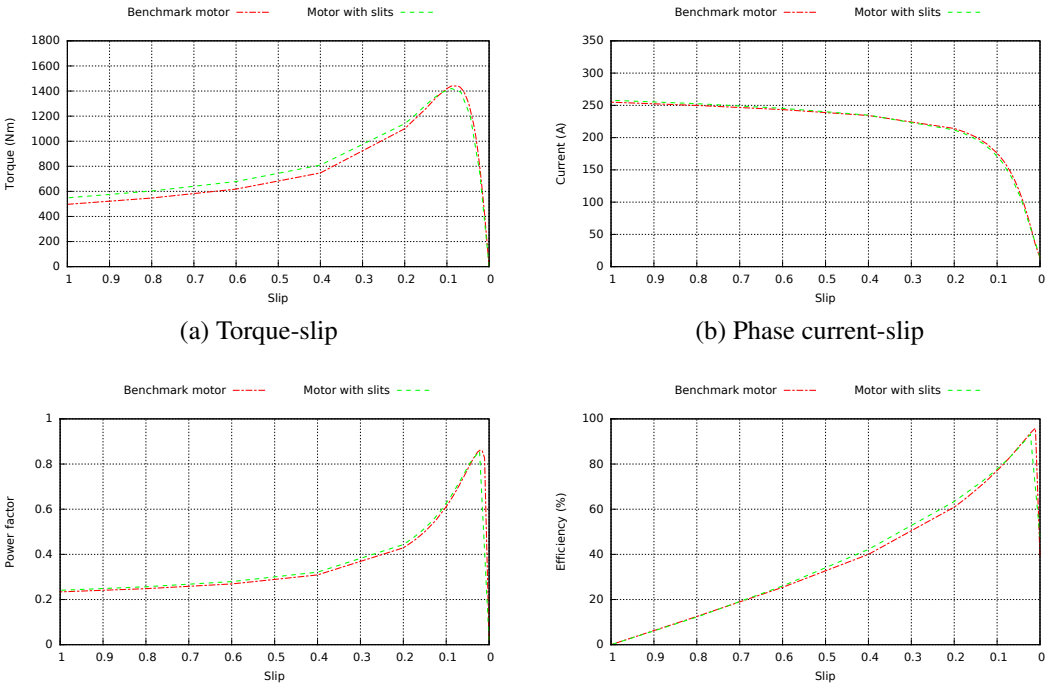

(a) Torque-slip (b) Phase current-slip

(c) Power factor-slip (d) Efficiency-slip

Figure 4.15: Performance curves of the induction motor with tooth slits

4.6 Double stator induction motor

Multiple airgap topologies have been applied successfully in other types of electrical machines as reported in section 2.5.6. Permanent magnet motors have also taken the lead in the use of multiple stators or rotors for performance improvements [9, 10]. There might also be some potential in the use of this technology in induction machines to increase the electric loading; reduce the field harmonics; or improve the excitation of the magnetic circuit.

Initially the space available inside an induction motor rotor was considered without any major modifications of the single airgap machine used as a reference. A double stator induction motor topology was then used in order to take advantage of the space inside

the rotor as shown in Figure 4.16a. The rotor coreback and shaft were replaced in the 7.5 kW benchmark motor by an inner stator whilst the rest of the geometry remained unchanged. This inner stator had the same magnetic loading as the outer stator and a reduced number of slots in order to improve the slot fill factor. The inner stator however had very limited space in this machine size for the windings. This space restriction reduces as the machines becomes larger or could be accommodated by increasing the outer diameter of the machine.

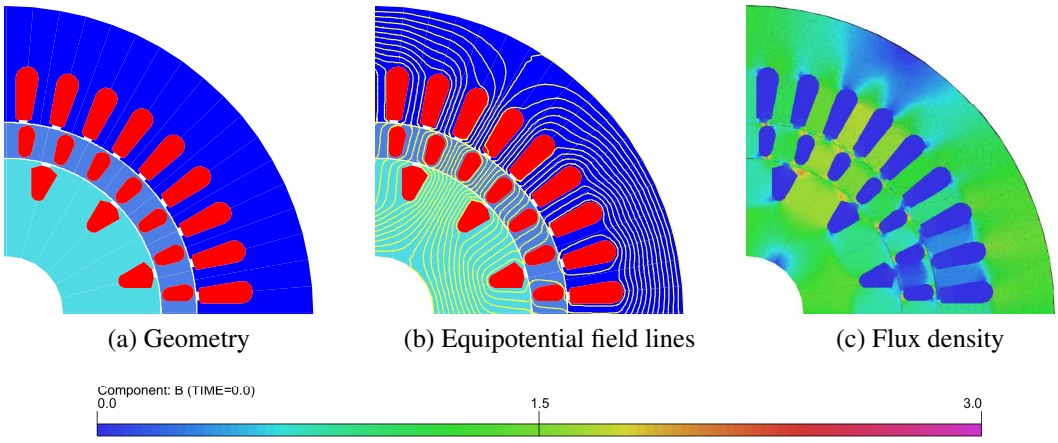

(a) Geometry (b) Equipotential field lines (c) Flux density

(d) Flux density value (T)

Figure 4.16: Double stator induction motor under no load conditions

The active rotor area was reduced and the rotor was assumed to be attached mechanically to the shaft via the end-rings. Mechanical coupling to the rotor would be one of the main challenges in this design and would have to guarantee electrical insulation between the cage and the shaft. The mechanical weakness could be offset by the opportunities for improving the cooling because of the two airgaps and the possibility of implementing a direct cooling system on the inner section of the motor. The design strategy was then to achieve maximum torque production without worrying about the mechanical coupling. If a design with improved performance was found, then the coupling would be designed and modelled to check its effect in the performance.

Figure 4.16b presents the equipotential field distribution for this motor which is clearly similar to that of the standard induction motor whilst Figure 4.16c details the flux density distribution for this design. It should be noted that some small saturation areas are evident under no load conditions.

One of the interesting features of this design is the magnitude of the mmf harmonics. There is no requirement that the winding design for the two stators is the same except for pole number. The two stators can also be rotated with respect to each other to produce a phase shift between the two windings. This can be used to reduce the magnitude of some of the major mmf harmonics, for example the 5th, at the expense of a small reduction in the fundamental mmf.

There are two methods for achieving the phase shift. One was rotating one stator to change the mechanical angle between the stators while the other option would be to modify the phase angle between the voltage sources of the two stators. Mechanical shifting was selected because it was easier to implement in the finite element model.

This interesting feature with the two stators shifted at different angles to obtain more torque is illustrated in Figure 4.17. This shows that the torque produced by each stator of the double stator motor (DS) at different phase shifts varies and compares them with the respective benchmark motor (B).

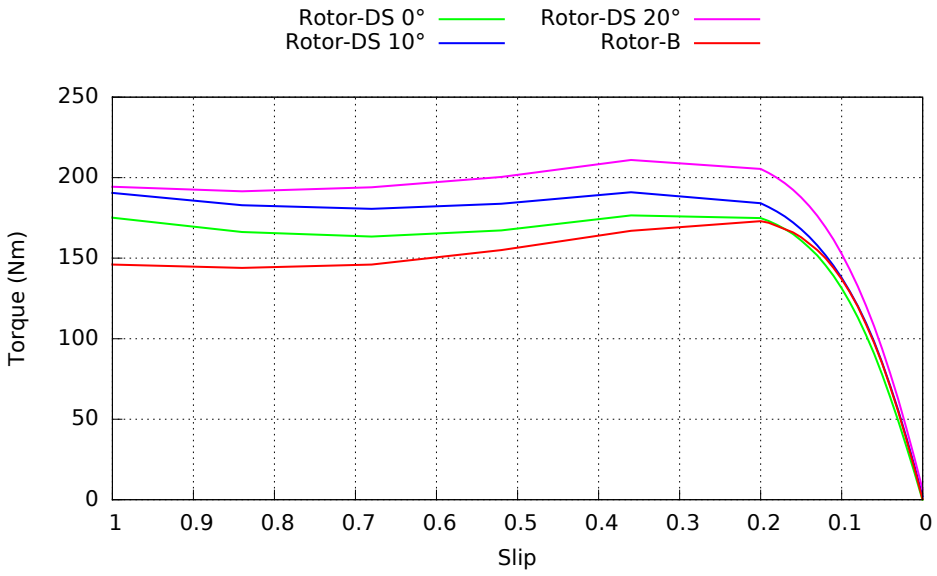

(a) Rotor torque

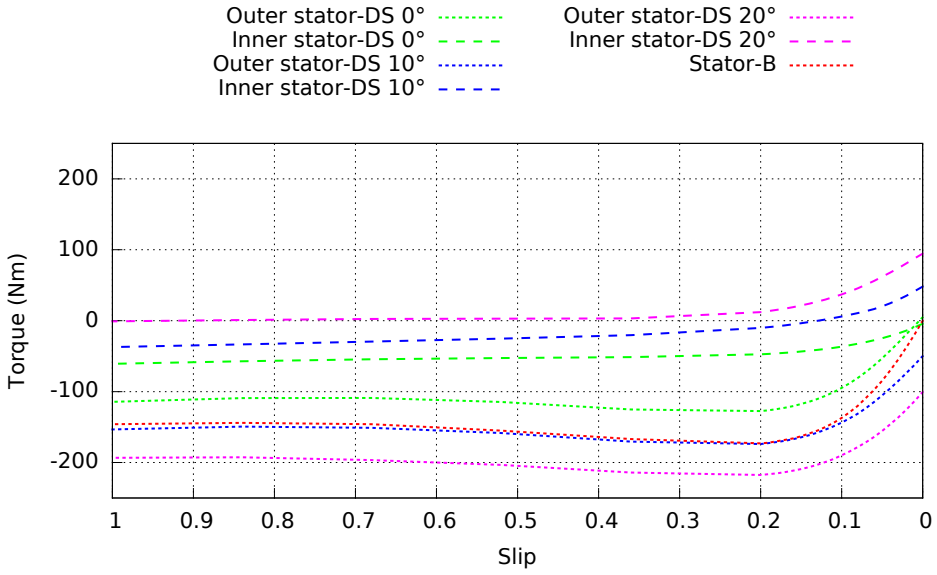

(b) Stator(s) torque

Figure 4.17: Torque-slip curves of the double stator induction motor at different angular mechanical shift between the two stators

For benchmark motor (B), the torque in the stator and rotor had the same magnitude but in opposite directions as expected. In the double stator configurations (DS), the torque

produced on the rotor has the same magnitude as the summation of the torques from the two stators. The torque produced on the rotor rotation was considered to be positive.

The maximum rotor torque increased with the phase shift angle as shown in Figure 4.17. At a slip close to 0, each stator produced a torque but in opposite directions of almost the same value which resulted in no torque output at the rotor. The inner stator torque tended to have the same direction as that produced by the outer stator as the phase shift angle increased. At the 20° phase shift angle, the inner stator torque tends to 0 Nm as the slip angle increases.

Figure 4.18 compares the harmonic flux distribution at the mid-radius of the rotor for the benchmark motor and the double stator motor at different phase shift angles. The double stator shows a slightly higher fundamental flux than the benchmark motor. The phase shift modifies the harmonic content in the flux distribution effecting mainly the 3rd, 5th and 7th harmonics. The 20° phase shift angle seems to improve the torque production because of the higher fundamental and third harmonic with a lower 5th and 7th harmonic content.

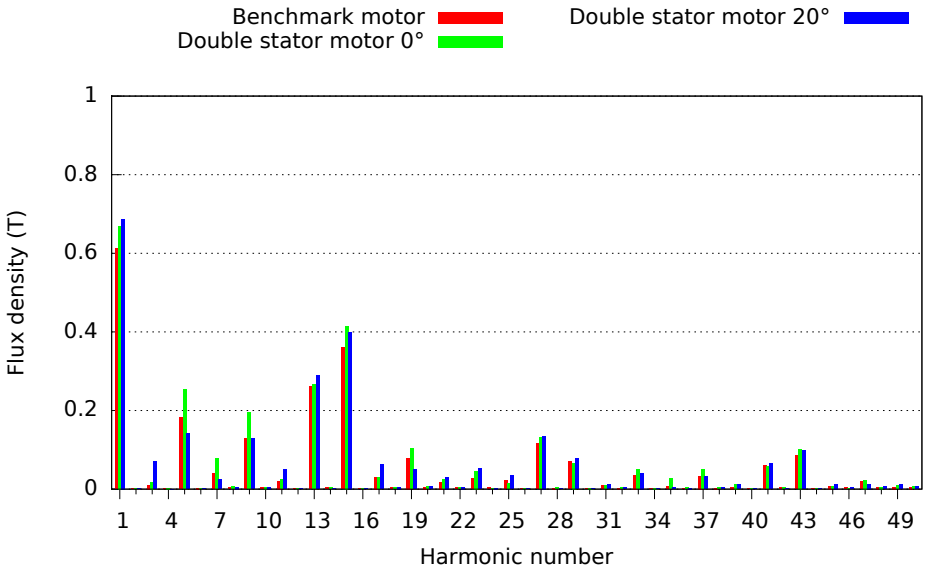

Figure 4.18: Harmonic analysis of the flux density distribution

Despite the double stator machine having an increased stator conductor area of about 20 %, Figure 4.17 showed that there is not a large improvement in the rotor torque using the double stator compared with the benchmark motor. This is believed to be a consequence of the limited space available at this machine size limiting the additional electric loading produced by the inner stator. The benefits however of adding a second stator and increasing the electric loading are expected to improve at larger machine sizes.

The highest torque was obtained at a mechanical phase shift angle between the two stators of 20° . The performance curves in Figure 4.19 show however that the improvement in the torque was only obtained at the expense of a deterioration in the power factor and efficiency and an increased phase current.

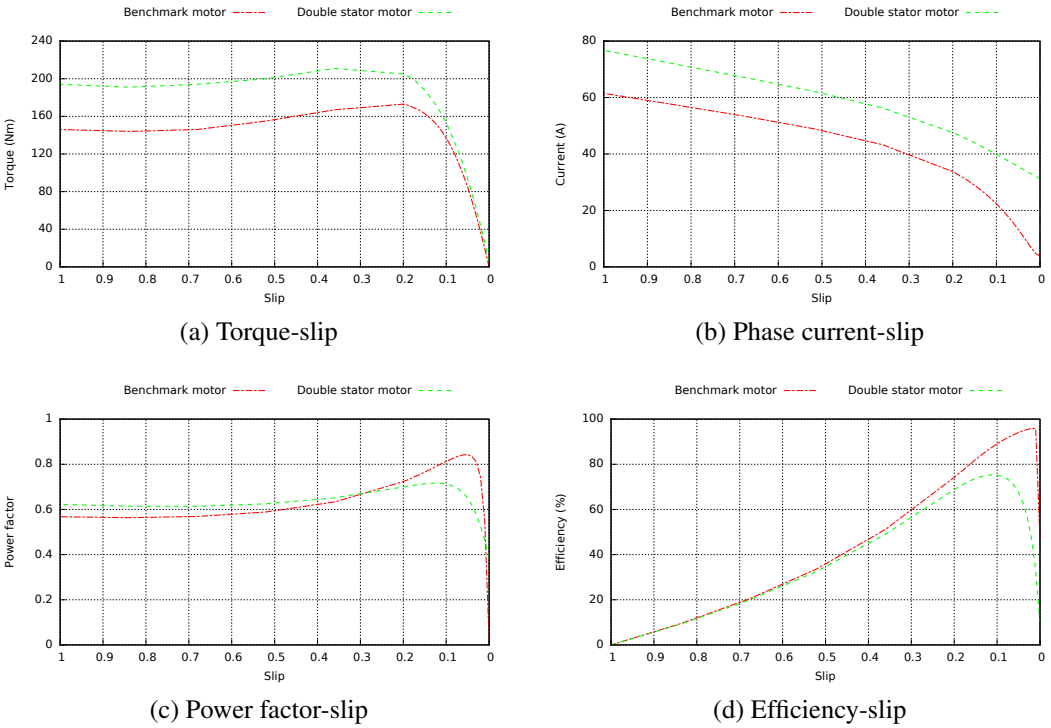

(a) Torque-slip

(b) Phase current-slip

(c) Power factor-slip

(d) Efficiency-slip

Figure 4.19: Performance curves of the double stator induction motor with stators shifted 20°

The phase angle between the stators distorts the flux distribution and more tooth saturation occurs as shown in Figure 4.20 and this was thought to be one factor in the performance degradation. There might also be changes in the differential leakage which can reduce the active torque-producing current. Figure 4.20 corresponds to no load conditions for the double stator induction motor with stators mechanically shifted 20°.

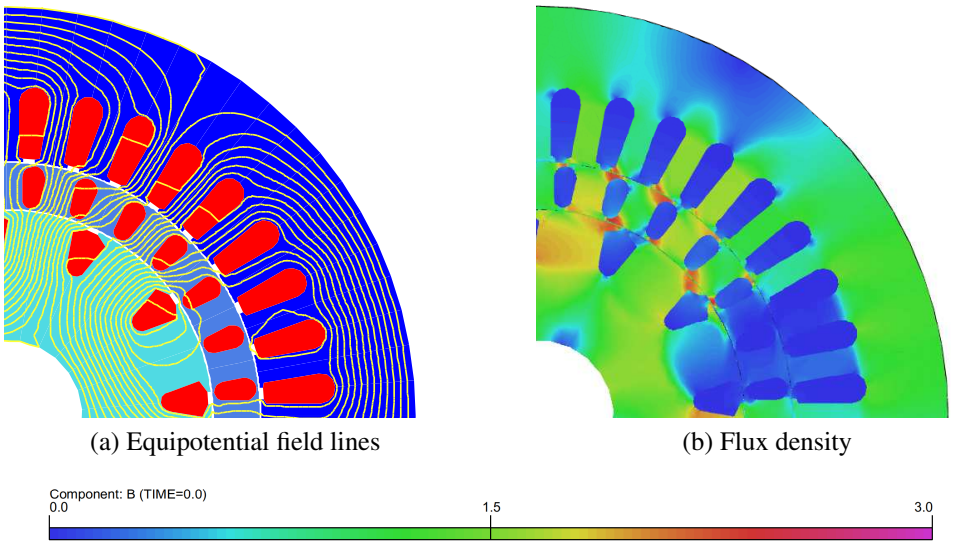

(a) Equipotential field lines

(b) Flux density

(c) Flux density value (T)

Figure 4.20: Double stator induction motor with stators mechanically shifted 20° under no load conditions

A 55 kW version of the double stator motor was also developed. Unlike the previous example, this does not use the same topology for the outer stator and the rotor but instead has the same active volume as the corresponding benchmark motor. The geometry of the laminations is shown in Figure 4.21.

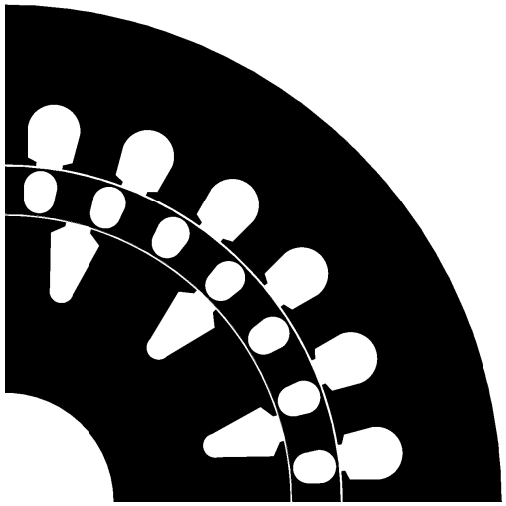

Figure 4.21: 55 kW double stator induction motor

For this design, the torque produced at different phase angles between the two stators was analysed using the torque and current maps shown in Figure 4.22. These figures illustrate the best phase shift for torque production, but the phase current generally increases as the phase shift angle increases.

These maps show again how the current requirements increased with the phase angle between the stators. The torque however also increased with the phase angle between the stators. It should be noted that the increase in the torque is not symmetric with the direction of phase shift.

Although the lack of active space in the designs prevented significant improvement in the performance and the ability to compensate for the double airgap, further research is necessary in these special machines. Some developments made are still at the conceptual stage and were inspired by the double stator induction motor, these are described in the remaining part of this section.

The first concept was an induction motor similar to the induction machine with free-rotating permanent magnets inside its rotor, described in section 2.5.6. The main difference is that this motor has a salient-pole wound-field rotor instead of the permanent-magnet inner rotor. Figure 4.23 illustrates the basic structure but it requires transient simulations in the design process because of the ac and dc excitation. It has also the disadvantage of requiring brushes. Figure 4.23 shows the equipotential and density flux distribution of this machine when the dc field is excited.

Further design is necessary to refine the pole shape and dimensions but this was not possible because of the lack of time. The importance of this machine however is more at

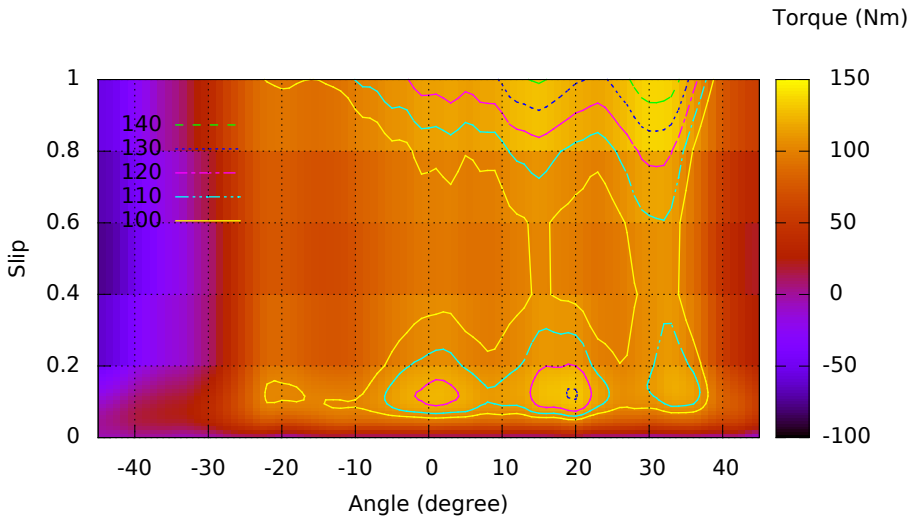

(a) Torque

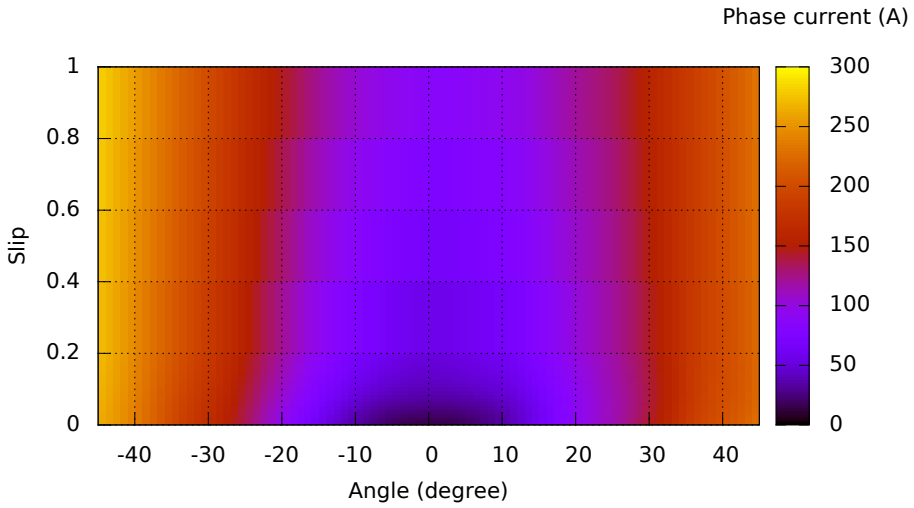

(b) Phase current

Figure 4.22: Double stator induction motor performance maps

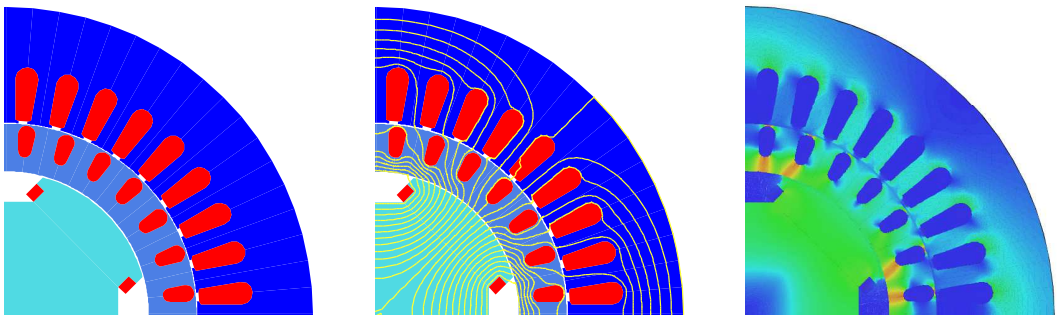

(a) Geometry (b) Equipotential field lines (c) Flux density

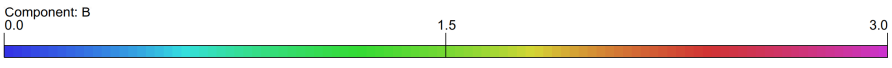

(d) Flux density value (T)

Figure 4.23: Double rotor induction motor under no load conditions

a conceptual level. The stator and the squirrel cage rotor operate as in a normal induction machine whilst the salient-pole rotor rotates freely following the main field at synchronous speed. The salient-pole rotor would not produce torque because its only function is to provide additional excitation to the magnetic circuit.

Figure 4.24 presents the equivalent circuit for an induction motor with a double rotor [11, 12]. The main difference with from the standard equivalent circuit is the inclusion of an induced voltage E_0 in the magnetizing part of the circuit. This is produced by the free-rotating inner rotor. The expected improvement in performance would be a result of the reduction in the magnetizing current which reduces the current and voltage drop across R_1 and X_1. The voltage induced in the rotor would then be higher producing a higher torque.

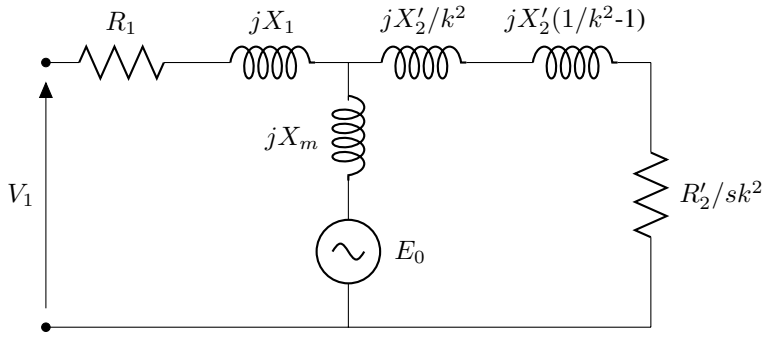

Figure 4.24: Fundamental one-phase equivalent circuit for the induction machine described in Figure 4.23 [11]

Further research would also be necessary in order to evaluate the benefits and drawbacks of the use of a claw pole rotor instead of a salient-pole structure but this is out of scope of this research [13–19].

Theoretically, the inner salient-pole free-rotating rotor could be replaced by a stator which is controlled to produce the same effect. In this case a similar specific torque improvement could be expected.

It would also possible to simulate the case when the inner rotating field rotates at a different speed. To achieve this, each stator could be supplied by its own inverter which would allow each to have different frequencies. This feature could be beneficial for a wide speed range.

Figure 4.25 presents four cases to illustrate this concept using the machine from Figure 4.16. Case A presents no-load starting from 0 RPM using a transient simulation whilst case B is also no-load starting but with an initial rotor speed of 1500 RPM. Both simulations achieve the same steady state behaviour but case B requires less time to achieve it which would reduce the simulation time. Case C presents starting on load with the rotor speed already at 1500 RPM. Case D presents a similar starting strategy with the initial rotor speed of 1500 RPM under load but with excitation at different frequencies

for each stator. Unfortunately case D is unstable and the rotor speed tends towards zero, this model however is interesting and requires further development.

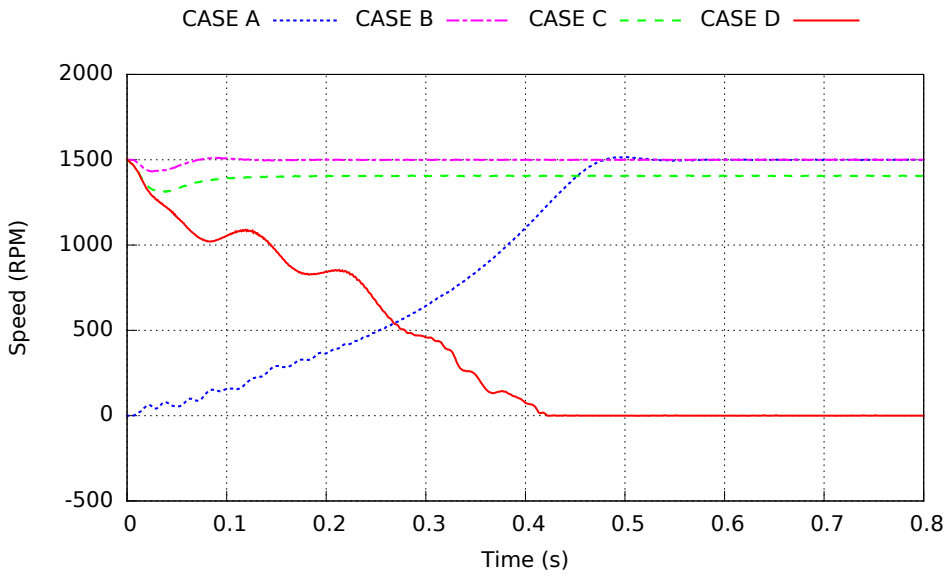

(a) Speed

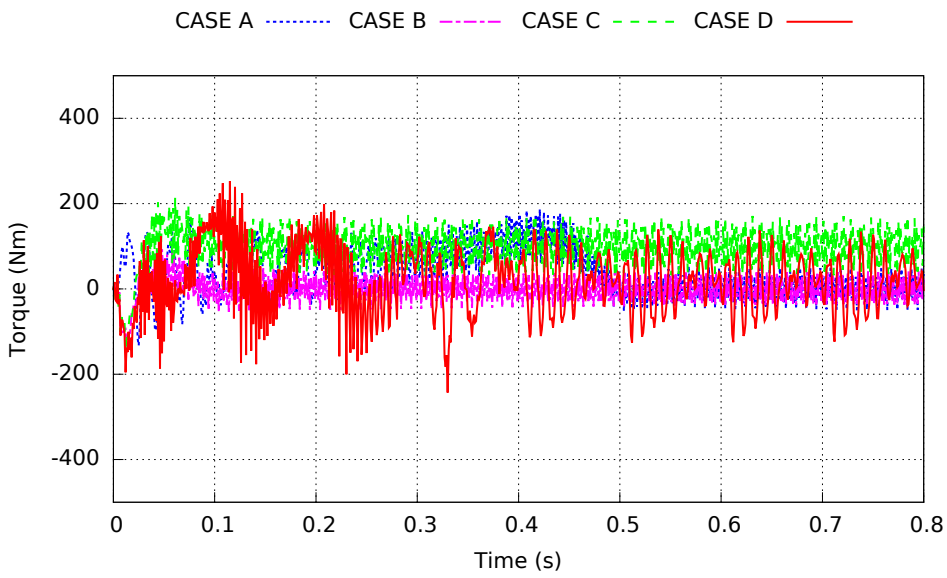

(b) Torque

Figure 4.25: Transient simulations of the double stator induction motor

4.7 Modular induction motor

Modular windings have been used in permanent magnet motors because they are easy to wind and more compact with reduced end winding dimensions and leakage reactance [20]. Modular windings have been considered for induction machines but the volume has to be increased to compensate for the extra turns needed to maintain the fundamental flux density and overcome the low short-pitch factor [20]. In addition, the higher harmonic content of these types of windings results in high losses in the

conventional rotor cage winding [20]. As a result, modular windings are not normally considered suitable for induction machines.

To reduce the magnetic flux harmonics produced by a modular winding and prevent it increasing the volume of the motor, an alternative option is to use a double stator and use the phase shift to improve the harmonic content. This modular double stator winding machine was developed based on the 55 kW benchmark motor as shown in Figure 4.26. Each stator used a three-phase modular winding whilst the squirrel cage consisted of 16 slots.

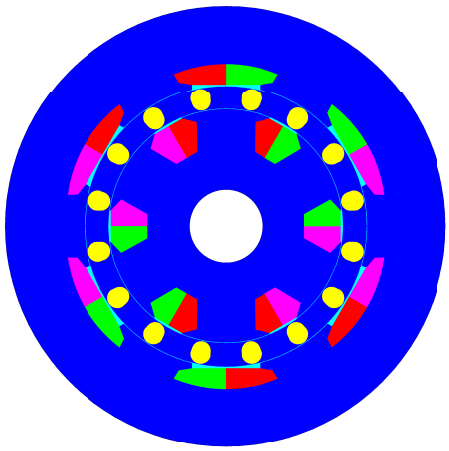

Figure 4.26: Double modular stator induction motor

The results obtained from a steady state simulation gave similar torque values to the benchmark machine. Transient simulations were also undertaken to assess the torque pulsations. Large torque pulsations were evident in the 2D transient finite element simulations of the double modular stator motor. Stator skew was then investigated to reduce the torque pulsations. Skewing 30 mechanical degrees of the double modular stator was an effective way of reducing the torque pulsations as shown in Figure 4.27.

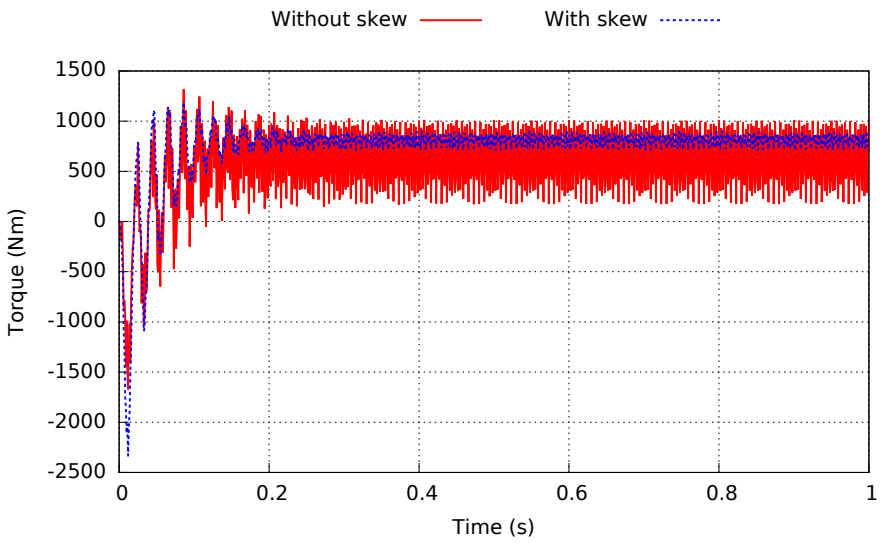

Figure 4.27: Transient simulation of the double modular stator induction motor

A large skew angle of the modular motor however was needed resulting in the skew of both stators as an alternative to avoid weakening the rotor structure. A more detailed view of the skew effects on the rotor is presented in Figure 4.28. This model however has not considered the increase in the slot fill factor as a result of using the modular windings which would produce a higher specific torque.

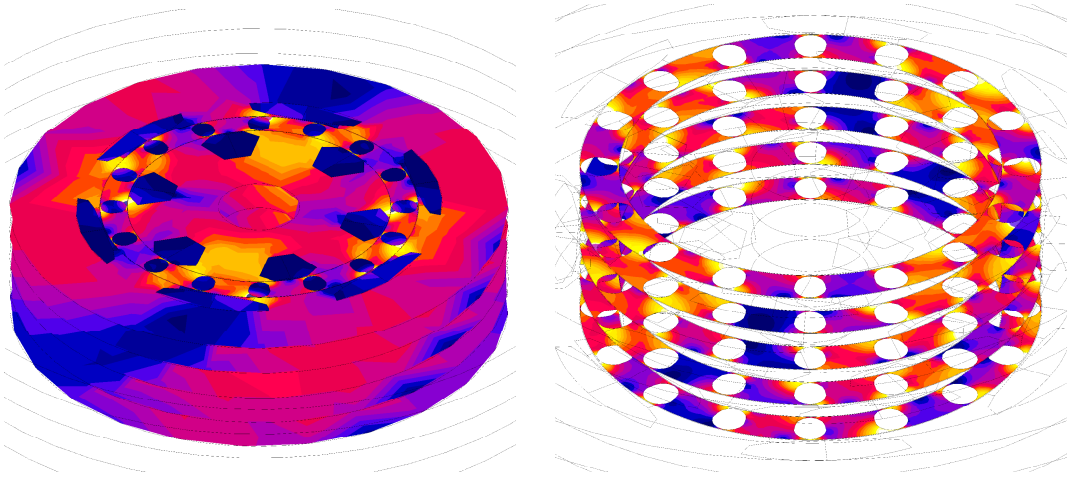

(a) Full geometry

(b) Rotor core

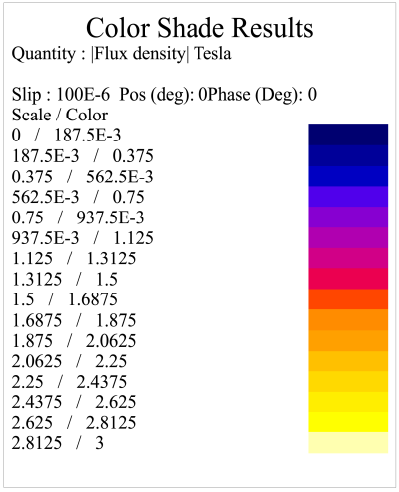

(c) Flux density value

Figure 4.28: Skew of the double modular stator induction motor under no load conditions

4.8 Solid rotor core induction motor

Solid rotor induction motors are used for very high speed applications because of the requirements on structural rotor integrity. The main requirement of the solid steel rotor is its mechanical strength with the electrical resistivity of secondary importance. Figure 4.29 shows a rotor design with the laminated rotor core replaced by a low carbon solid steel but retaining the copper cage. The geometry is the same as the 5.5 kW benchmark machine.

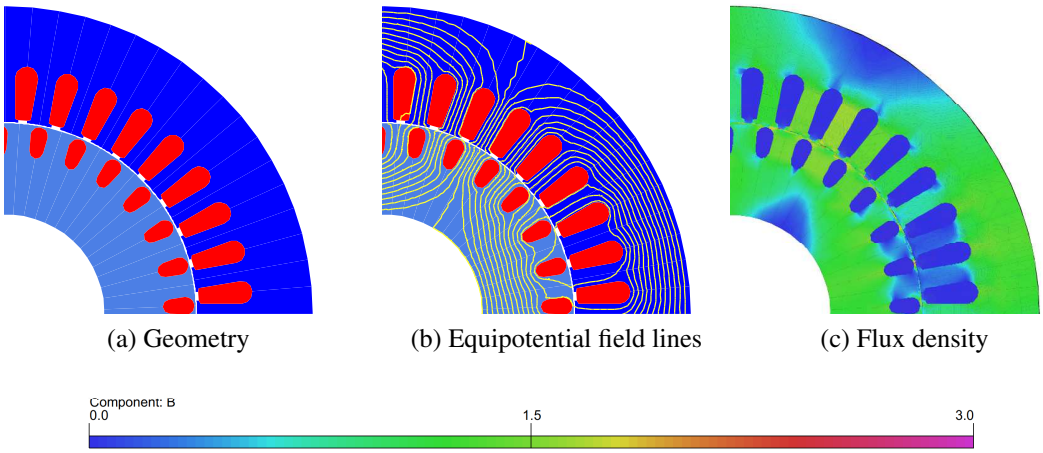

(a) Geometry (b) Equipotential field lines (c) Flux density

(d) Flux density value (T)

Figure 4.29: Solid rotor core induction motor under no load conditions

The steady state simulations suggested a higher torque whilst the transient simulations of the solid rotor core motor however showed in Figure 4.30 that there is no apparent improvement in the torque. The difference in these results might be explained by the fact that the steady state modelling of the induction motor assumes that the rotor and stator are fixed while using Opera 2D the stator is excited at the slip frequency [21]. Although this is a quick method used for routine design, the effects produced by the movement between stator and rotor are ignored [21].

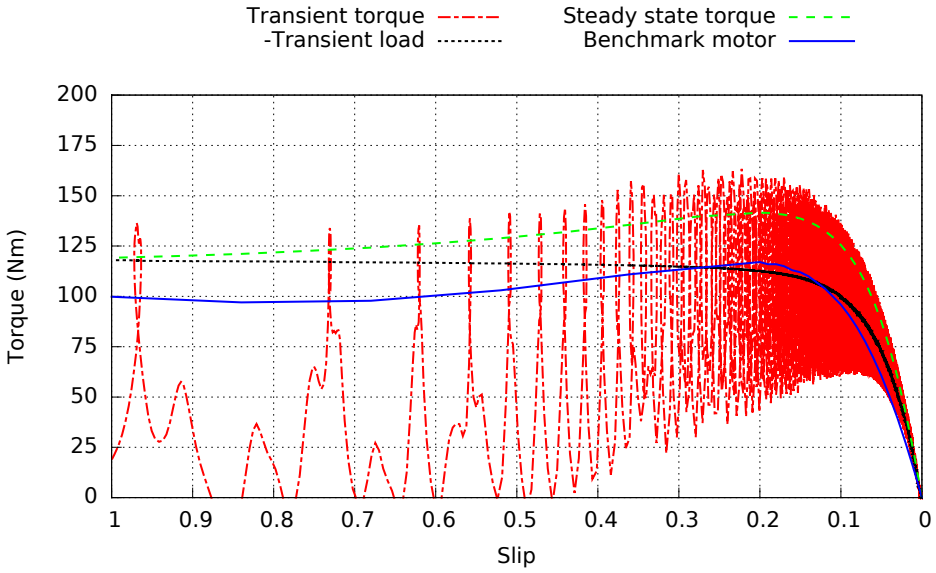

Figure 4.30: Torque-slip curves of the solid rotor core induction motor

Currents appear even at no load on the rotor as shown in Figure 4.31 and these are highly concentrated on the rotor surface. These currents are not modelled in steady state and are thought to be responsible for the difference in the torque results.

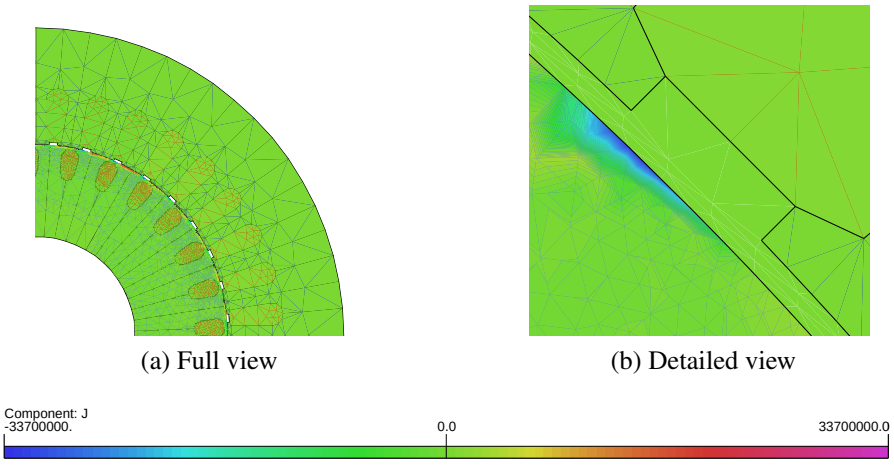

(a) Full view (b) Detailed view

(c) Current density value (A/m^2)

Figure 4.31: Transient current in the solid rotor core induction motor at no load

4.9 Induction motor with grain oriented laminations

Grain oriented steel laminations were modelled using segmented stator magnetic cores. The basic geometry is the same as the 7.5 kW benchmark motor but the stator lamination segments have an axis aligned with the best magnetic properties in the radial direction. Figure 4.32 illustrates the machine developed in Opera 2D.

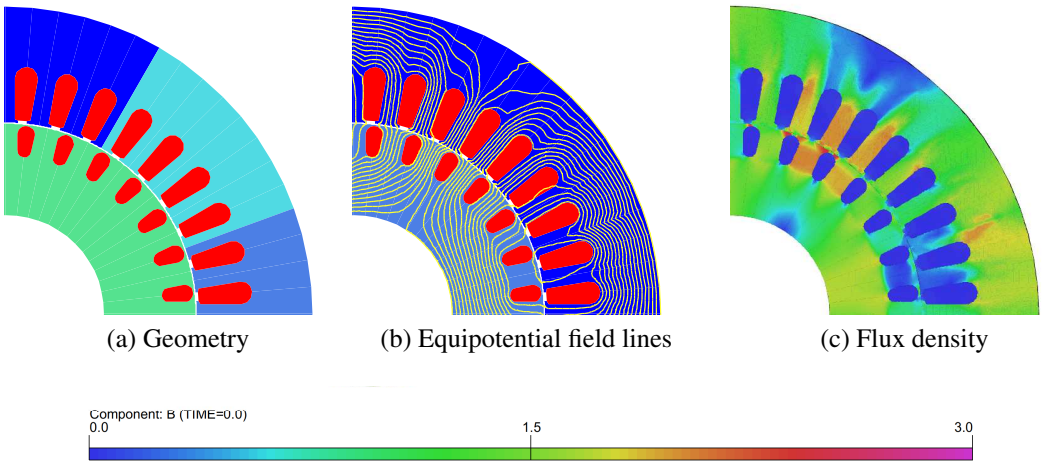

(a) Geometry (b) Equipotential field lines (c) Flux density

(d) Flux density value (T)

Figure 4.32: Induction motor with grain oriented iron under no load conditions

Voltage excitation was increased in order to increase the flux density of the magnetic materials to 1.8 T and 2.1 T in the benchmark and modified motors respectively. As a result, torque production improved as illustrated in Figure 4.33 whilst the remaining performance parameters suffered probably due to the higher flux density values in the coreback: lower power factor; higher magnetizing current and losses.

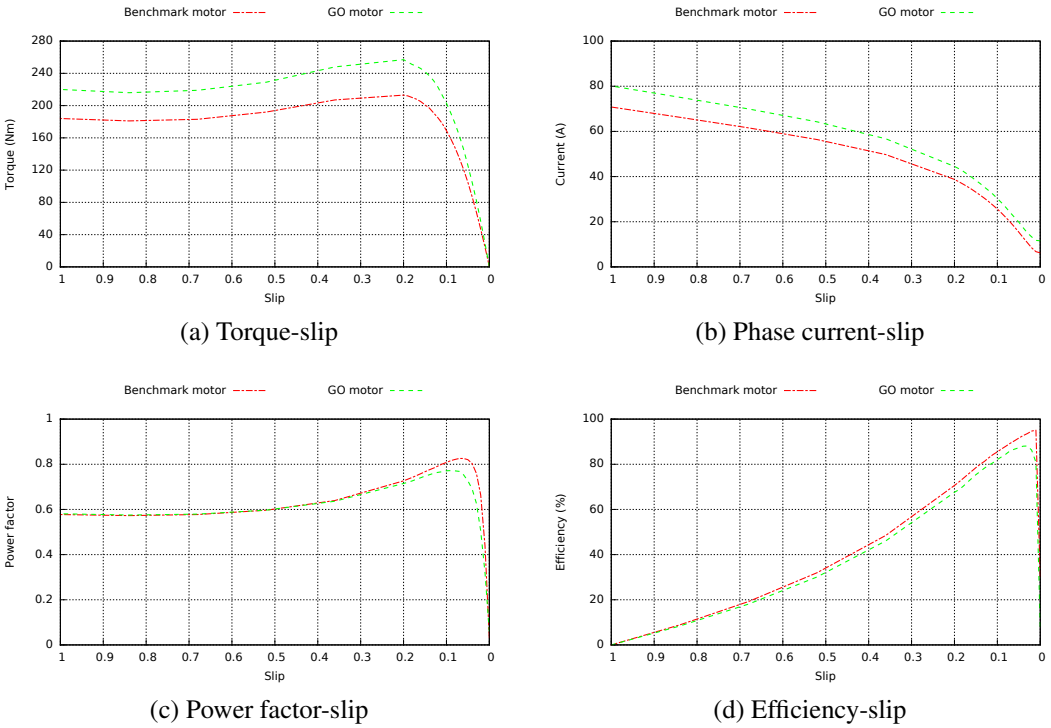

(a) Torque-slip

(b) Phase current-slip

(c) Power factor-slip

(d) Efficiency-slip

Figure 4.33: Performance curves of the induction motor with grain oriented laminations

4.10 Canned rotor induction motor

The use of a larger airgap in an induction motor brings benefits in terms of better torque production and lower harmonics in the airgap field distribution [22]. However the performance is also affected by the higher current required to magnetise the machine.

This simple design modification was selected and a surface copper can was included to utilise the additional space in the airgap. The can was expected to improve the torque production but at the expense of higher losses [23]. Figure 4.34 presents the canned induction machine design based on the 5.5 kW benchmark motor.

Figure 4.35 shows the performance curves and the torque has increased as expected, however the other performance parameters again deteriorate. The required phase current is higher and the power factor and efficiency are lower compared to the benchmark motor. The 2D finite element model of the rotor can is approximate. The 2D model constraints the current to flow axially effectively removing the end-ring resistance paths. The current distribution in a solid can on the surface of the rotor is 3D. It is thought that slitting the can to create a cage structure might improve the performance but the 2D finite element model needs to incorporate additional resistance to represent the current paths at the end of the can [23].

Further torque improvements could be obtained if the rotor core is substituted by low-silicon content laminations and the rotor slots modified to take into account the properties of these materials [24]. The specific torque would improve because the rotor tooth width

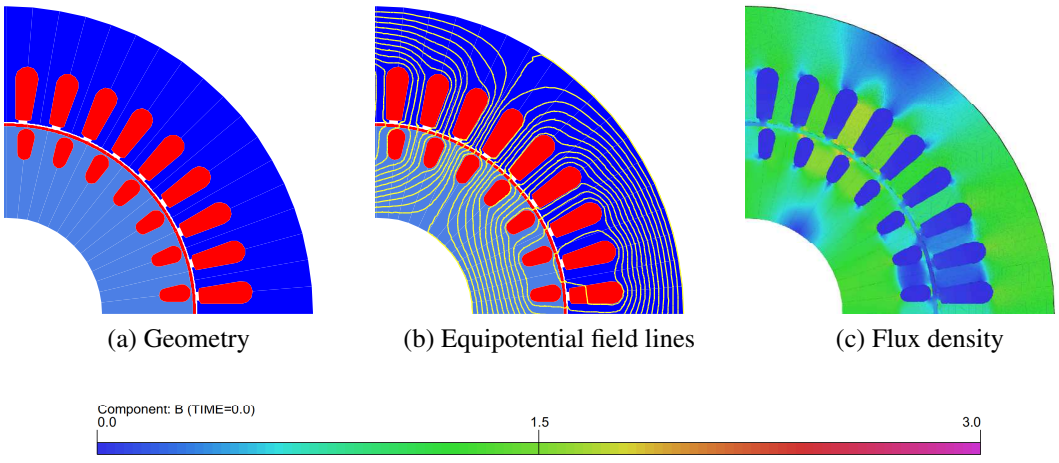

(a) Geometry (b) Equipotential field lines (c) Flux density

(d) Flux density value (T)

Figure 4.34: Canned rotor induction motor under no load conditions

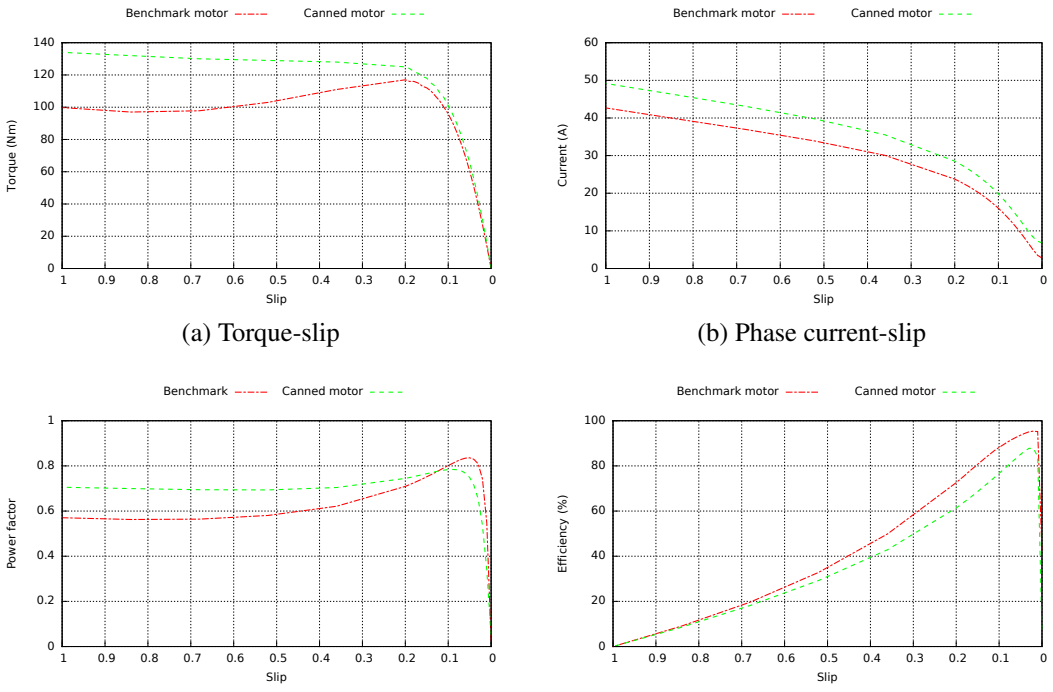

(a) Torque-slip (b) Phase current-slip

(c) Power factor-slip (d) Efficiency-slip

Figure 4.35: Performance curves of the canned rotor induction motor

could be reduced allowing wider rotor slots and reduced depth. These changes in the slot shape would reduce the slot leakage.

4.11 Toroidal induction motor

Another potential design examined was the use of toroidal windings in the stator, based on the 55 kW benchmark motor. Toroidal windings have been known since the XIX century but they have found little application in industrial machines [25]. These windings were

implemented without seeking to improve the specific torque, but instead looking for a wider speed range through pole changing as shown in Figure 4.36.

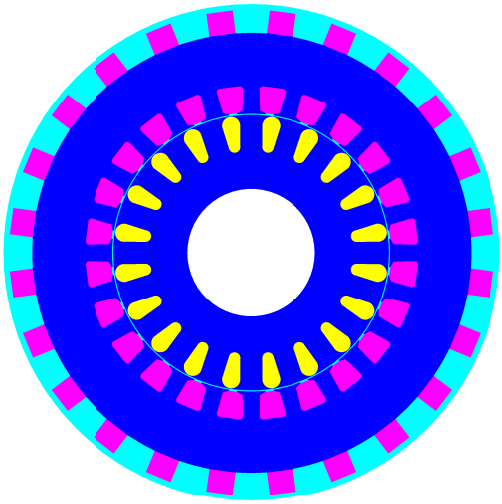

(a) Geometry

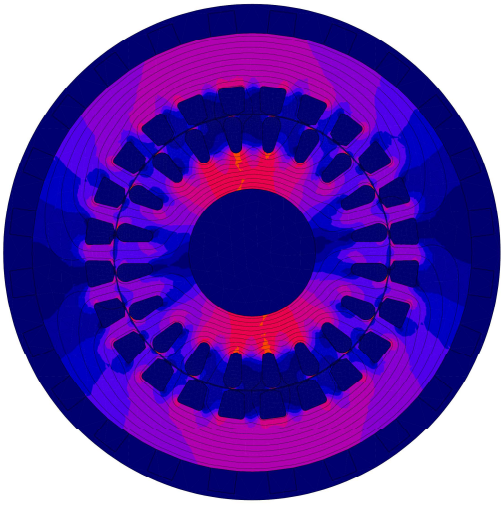

(b) 2 pole

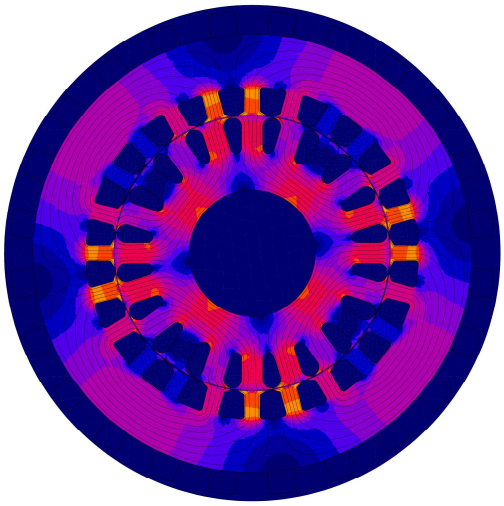

(c) 4 pole

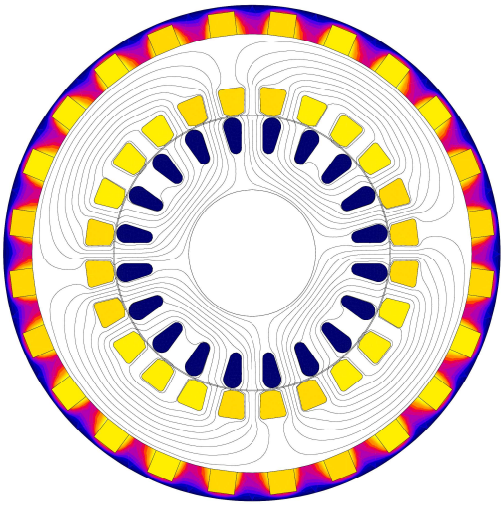

(d) Current density

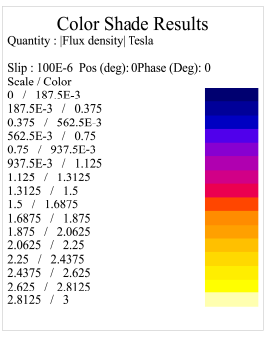

(e) Flux density value

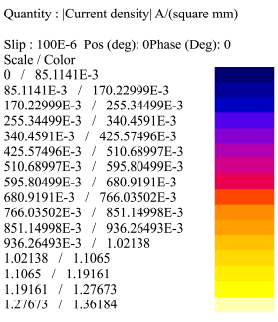

(f) Current density value

Figure 4.36: Toroidal induction motor under no load conditions

Electronically pole changing techniques in industrial motors improve the pull out torque and allow a wide speed range. Toroidal windings also offer the opportunity to reduce the end winding dimensions which was expected to have a positive impact on torque

production. Higher slot fill factors are also expected due to the removal of coil overlap in the end-windings. The disadvantage of a toroidal winding as shown in Figure 4.36 is that the end-winding effectively passes close to the stator core and this could increase the stator end-winding leakage significantly and reduce the torque capability of the machine.

Unfortunately, the support material needed for the outer coil sides was also a significant issue due to induced eddy currents as shown in Figure 4.36d. These degrade the performance of the machine. The containment was modelled as a 2D short circuit solid conductor.

Pole changing could be attractive but in this particular case the excitation voltage had to be restricted to avoid saturation in the coreback. Unfortunately, when the machine operates in the 2 pole mode, the coreback was saturated when the airgap flux density was approximately half of the 4 pole value. This particular motor design requires an increased coreback depth to operate at full flux level in the airgap for both pole numbers. Figure 4.37 illustrates the operation of the machine in both 4 and 2 poles modes at 50 Hz compared to the desired torque.

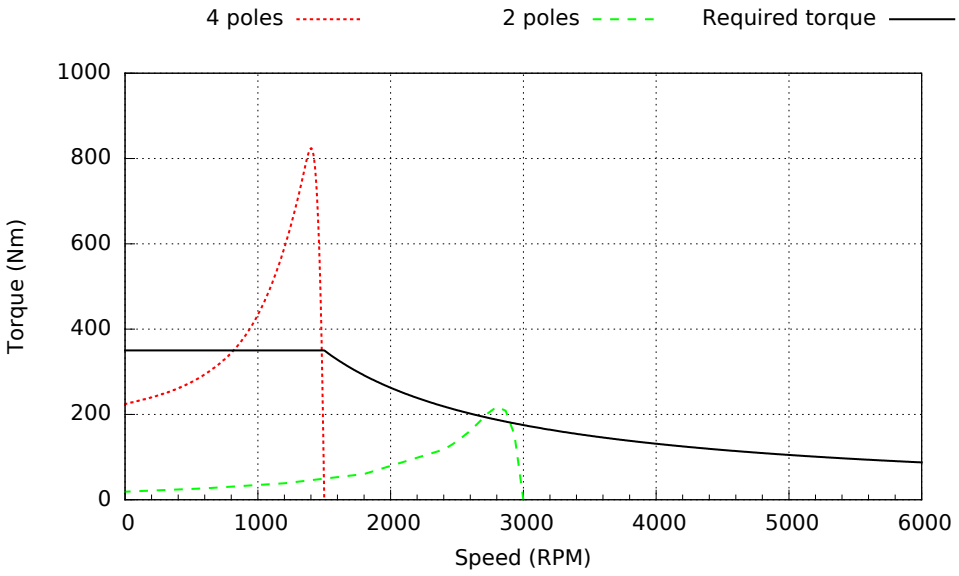

Figure 4.37: Torque-speed curves of the toroidal pole-change induction motor

4.12 Conclusions

This chapter summarises a series of new potential induction motor designs aimed specially at increasing the specific torque. Each design was described including some constructional detail, advantages and weaknesses. The performance of each new motor design was compared with a benchmark motor based on a industrial induction motor in order to assess the improved performance in terms of higher specific torque.

The machines presented in this chapter helped to identify the topology for the design of

an experimental induction motor with a higher specific torque. The detailed comparison, selection, design refinement, prototype manufacture, test and analysis are presented in the following chapter.

4.13 References

[1] J.S. Hsu et al., "Losses influenced by third-harmonic flux in induction motors", *Energy Conversion, IEEE Transactions on*. 6, 461–468. (1991).

[2] M. Akroune et al., "Characterisation of nonoriented electric alloys under nonconventional conditions", *Science, Measurement and Technology, IEE Proceedings* -. 143, 35 –40. (1996).

[3] D. Casadei et al. "Torque maximization in high-torque density multiphase drives based on induction motors". In: *Energy Conversion Congress and Exposition (ECCE), 2010 IEEE*. 2010, pp. 3896 –3902.

[4] D. Casadei et al. "Control of a high torque density seven-phase induction motor with field-weakening capability". In: *Industrial Electronics (ISIE), 2010 IEEE International Symposium on*. 2010, pp. 2147 –2152.

[5] L. Zarri et al. "Maximum-torque-per-ampere control of high torque-density multiphase drives based on induction motors". In: *Energy Conversion Congress and Exposition (ECCE), 2012 IEEE*. 2012, pp. 495 –502.

[6] H.A. Toliyat, T.A. Lipo, and J.C. White, "Analysis of a concentrated winding induction machine for adjustable speed drive applications. I. Motor analysis", *Energy Conversion, IEEE Transactions on*. 6, 679 –683. (1991).

[7] H.A. Toliyat, T.A. Lipo, and J.C. White, "Analysis of a concentrated winding induction machine for adjustable speed drive applications. II. Motor design and performance", *Energy Conversion, IEEE Transactions on*. 6, 684 –692. (1991).

[8] S.L. Ho, Shuangxia Niu, and W.N. Fu, "A Novel Solid-Rotor Induction Motor With Skewed Slits in Radial and Axial Directions and Its Performance Analysis Using Finite Element Method", *Applied Superconductivity, IEEE Transactions on*. 20, 1089 –1092. (2010).

[9] Ronghai Qu and T.A. Lipo, "Design and parameter effect analysis of dual-rotor, radial-flux, toroidally wound, permanent-magnet machines", *Industry Applications, IEEE Transactions on*. 40, 771 –779. (, May/Jun, 2004).

[10] Ronghai Qu and T.A. Lipo. "Dual-rotor, radial-flux, toroidally-wound, permanent-magnet machines". In: *Industry Applications Conference, 2002. 37th IAS Annual Meeting. Conference Record of the*. Vol. 2. 2002, 1281 –1288 vol.2.

[11] Y. Shibata, N. Tsuchida, and K. Imai, “Performance of induction motor with free-rotating magnets inside its rotor”, *Industrial Electronics, IEEE Transactions on*. 46, 646 –652. (1999).

[12] Yoshiyuki Shibata, Nuio Tsuchida, and Koji Imai, “High torque induction motor with rotating magnets in the rotor”, *Electrical Engineering in Japan*. 117, 102–109. (1996).

[13] J. Cros and P. Viarouge, “New structures of polyphase claw-pole machines”, *Industry Applications, IEEE Transactions on*. 40, 113 –120. (, Jan/Feb, 2004).

[14] J. Cros, J.R. Figueroa, and P. Viarouge. “Analytical design method of polyphase claw-pole machines”. In: *Industry Applications Conference, 2004. 39th IAS Annual Meeting. Conference Record of the 2004 IEEE*. Vol. 3. 2004, 1397 –1404 vol.3.

[15] S.K. Tidblad Lundmark and E.S. Hamdi. “Designs of Claw-Pole Motors for Industrial Applications”. In: *Power Electronics, Machines and Drives, 2006. The 3rd IET International Conference on*. 2006, pp. 111 –115.

[16] F. Jurca, C. Martis, and K. Biro. “Comparative analysis of the claw-pole rotor dimensions influence on the performances of a claw -pole generator for wind applications”. In: *Clean Electrical Power, 2009 International Conference on*. 2009, pp. 715 –720.

[17] L. Melcescu et al. “Claw-pole line-start permanent-magnet synchronous motor design and development”. In: *Advanced Electromechanical Motion Systems Electric Drives Joint Symposium, 2009. ELECTROMOTION 2009. 8th International Symposium on*. 2009, pp. 1 –5.

[18] F.N. Jurca et al. “Design and development of a three-phase permanent magnet claw pole synchronous”. In: *Electrical Machines (ICEM), 2010 XIX International Conference on*. 2010, pp. 1 –6.

[19] Y. Kuroda et al. “Improvement of a claw pole motor using additional ferrite magnets for hybrid electric vehicles”. In: *Electrical Machines (ICEM), 2010 XIX International Conference on*. 2010, pp. 1 –3.

[20] A.S. Abdel-Khalik and S. Ahmed, “Performance Evaluation of a Five-Phase Modular Winding Induction Machine”, *Industrial Electronics, IEEE Transactions on*. 59, 2654 –2669. (2012).

[21] Cobham Technical Services. *Opera2d User Guide*. Cobham CTS Litmited, 2011.

[22] I. Hirotsuka et al. “Characteristics of high-speed constant-voltage operation of squirrel-cage induction motors -the influence of gap length in 4- and 8-pole induction-”. In: *Electrical Machines and Systems, 2007. ICEMS. International Conference on*. 2007, pp. 1094 –1098.

[23] R.L. Russell and K.H. Norsworthy, “Eddy currents and wall losses in screened-rotor induction motors”, *Proceedings of the IEE - Part A: Power Engineering*. 105, 163 –175. (1958).

[24] K.M. Rahman and S.E. Schulz, “Design of high-efficiency and high-torque-density switched reluctance motor for vehicle propulsion”, *Industry Applications, IEEE Transactions on*. 38, 1500 –1507. (, Nov/Dec, 2002).

[25] W.B. Esson, “Notes on the design of multipolar dynamos”, *Electrical Engineers, Journal of the Institution of*. 20, 265–289. (1891).

CHAPTER

FIVE

RESULTS ANALYSIS AND DESIGN REFINEMENT

5.1 Introduction

This chapter assesses the simulation results from the previous chapter. It defines the criteria used to compare all the designs considered. A more detailed description of the selected topologies for prototyping is presented as part of the fuller design process. It also includes a detailed evaluation of the expected performance as a result of modifications necessary to facilitate the prototype build.

The experimental test system was prepared whilst the prototype machines were being constructed. A reduced voltage test was undertaken for each prototype to obtain the performance at different slip conditions. This chapter concludes with a comparison of the experimental and simulation results.

5.2 Comparison of simulated results

In order to compare all the designs developed during this research, a simple methodology was established:

- Obtain the pull out or maximum torque from the simulation results.
- Calculate the nominal or rated torque. This was set at a quarter of the maximum torque in order to achieve the speed range (4 times the base speed). For designs with the option to use a pole changing strategy, the nominal torque was half of the maximum torque in order to achieve half of the speed range before the pole change was applied.

- Calculate the active mass which is the mass of the magnetic cores plus the active part of the windings.
- Calculate the specific torque by dividing the nominal torque by the active mass.
- In order to normalize the results because of the different machine sizes, the normalized specific torque was used. This was defined as the ratio between the specific torque of the design divided by the specific torque of the machine used as the benchmark for that design. The calculated specific torque for the benchmarks are 0.9917 Nm/kg, 1.2683 Nm/kg, 2.20 Nm/kg for the 5.5 kW, 7.5 kW and 55 kW benchmarks respectively.

Table 5.2 shows a summary table of the simulated results. It was found that the machines with the highest normalized specific torque were those involving the injection of third harmonic currents, with the highest being the combination of a wound rotor design with third harmonic technique. After these two designs, the following three machines with the highest normalized specific torque were the grain-oriented laminated stator core, distributed bars and the wound rotor machines. The three worst designs were the slitted tooth, toroidal stator winding and the modular stator winding machines. The worst one (induction machine with tooth slits) had even a slightly lower performance than its respective benchmark.

Table 5.1 shows the equivalent circuit parameters of some of the machine designs which were obtained using the simulation results presented in the previous chapter and some additional simulations as described in [1]. These results provide some useful information in analysing the results in Table 5.2. For example, in the case of the worst design - the induction motor with tooth slits - this was designed to reduce the stator slot leakage. Although this was achieved however, the benefits were degraded by an increment in the rotor leakage.

Table 5.1: Equivalent circuit parameters of the designed machines

Figure	**Machine**	R_1 (Ω)	R_2' (Ω)	X_1 (Ω)	X_2' (Ω)	X_m (Ω)
4.7	Benchmark 5.5 kW	3.00	2.5675	2.0796	10.7581	143.4724
4.7	Double cage	3.00	1.3135	2.1003	6.6567	48.8804
4.35	Canned rotor	3.00	2.9032	2.0819	0.8212	56.4334
4.13	Benchmark 7.5 kW	2.02	1.5904	1.3856	6.5666	103.2695
4.13	Wound rotor	2.02	2.5262	2.8571	0.8579	167.2977
4.33	With GO laminations	2.02	1.3591	1.1150	5.6803	42.2135
4.19	Double stator	1.8062	1.2570	1.3174	2.1742	10.4916
4.15	Benchmark 55 kW	0.145	0.2312	0.3548	2.2287	27.8857
4.2	Distributed bar	0.145	0.4929	0.2632	2.2017	21.4279
4.15	With tooth slits	0.145	0.2518	0.0816	2.7514	26.4859

Most of the designs achieved a higher torque by reducing the leakage inductance in either or both of the rotor and stator. However, most of them suffered from a reduction of the

Table 5.2: Comparison of the designed machines

Figure	Machine	Benchmark machine (kW)	Pull out torque (Nm)	Nominal torque (Nm)	Active mass (kg)	Specific torque (Nm/kg)	Normalized specific torque
4.2	Distributed bar	55	1660	415	149.6	2.7740	1.2609
4.7	Double cage	5.5	130	32.5	27.4	1.1861	1.1960
4.9	With TH	55	2221	555.25	165.3	3.3590	1.5268
4.13	Wound rotor	7.5	234	58.5	38.04	1.5378	1.2125
4.13	Wound rotor TH	7.5	328	82	38.04	2.1556	1.6996
4.15	With tooth slits	55	1420	355	163.5	2.1712	0.9869
4.19	Double stator	7.5	217	54.25	35.9	1.5111	1.1914
4.27	Modular	55	829	414.5	178.1	2.3273	1.0578
4.30	Solid rotor core	5.5	118	29.5	27.73	1.0638	1.0727
4.33	With GO laminations	7.5	257	64.25	34.1	1.8842	1.4856
4.35	Canned rotor	5.5	134	33.5	28.2	1.1879	1.1978
4.37	Toroidal	55	818	409	176.6	2.3160	1.0527

magnetizing leakage which means an increase in the phase current which in turn would also be reflected in a lower efficiency and power factor.

The thermal performance as well as the electromechanical performance is an important parameter to consider during the design of an induction machine. Table 5.3 shows the temperature rise of some of the machine designs at nominal rating. All of them have a higher temperature rise but are within a reasonably safe margin as the thermal time constants are large and the induction machine will not normally operate continuously at the nominal rating level for large periods of time.

Table 5.3: Temperature rise of the designed machines

Figure	Machine	Temperature rise (°C)
4.7	Benchmark 5.5 kW	73.02
4.7	Double cage	107.20
4.35	Canned rotor	97.74
4.13	Benchmark 7.5 kW	77.44
4.13	Wound rotor	103.48
4.33	With GO laminations	143.97
4.15	Benchmark 55 kW	118.99
4.2	Distributed bar	109.76
4.15	With tooth slits	126.68

5.3 Selection criteria

The next stage in the design process consists of a prototype build and experimental test program in order to validate and refine the new designs. These activities require a lot of time and resources. For this reason, the number of prototypes that could be constructed was limited.

Previous chapters presented different designs with the target of increasing the specific torque. Each one has its own potential and limitations for further development and improvement. While the previous chapter focused on the improvement of the performance as the main target, this chapter is focused more on the practical considerations for the manufacturing and test processes. The designer needs to consider the following points in the final selection:

Time. The total prototype motor build time was estimated to be 6 to 12 months. For this reason, the manufacture and test stages could only be undertaken once in the design process.

Economic considerations. This relates to the materials and manufacturing costs. They were considered to be high enough to only consider building one or two prototypes.

Test rig. This relates to the test equipment and tools available in the laboratory. This forced the change from a 55 kW to a 5.5 kW rating in the benchmark machine.

Modelling issues. This relates to the accuracy of the models for each specific design. It needs to consider where a design could have important sources of inaccuracy in the results. For example, the canned motor design requires 3D models to improve the accuracy of the performance results but 2D models have been employed successfully despite their limitations.

Final costs. This relates to the evaluation of which designs have the potential to offer important savings to the costumers when they are mass produced.

Maintenance requirements. This relates to identifying the designs which would require lower maintenance during their operational life and identify potential issues during operation.

The first selection criterion used to decide which motor type would be manufactured was choosing the designs which offered the key advantage of using the same stator as the benchmark machine, avoiding the need to manufacture a new stator. This allowed a reduction in manufacture cost and time leaving enough resources for the construction of two rotors. This criteria also permitted a more direct comparison with the industrial induction motor.

Half of the design proposals presented in the previous chapter were discarded using this selection criterion. The first potential design discarded under this constraint was the induction motor with tooth slits because the dimensions and geometry of the stator core are different from the benchmark. The wound rotor, toroidal and modular induction motor designs were also discarded due to their topological differences in the stator with respect to the benchmark. The induction motor with grain-oriented laminations design had very similar geometry and dimensions to the benchmark but the core material was completely different.

From the remaining designs, the third harmonic current injection had been highlighted as a technique which has the main attractiveness of potentially being combined with other proposed designs. However, it was discarded due to the fact that potential torque improvements alone had already been covered by other researchers. The double stator motor was also discarded because the expected torque improvements were not predicted by the finite element models and due to the issues of the mechanical coupling between the rotor and the shaft. The solid rotor core motor design was also discarded because it required transient simulations in order to predict the torque accurately. Finally, a double cage rotor, a very simplified version of the distributed bar motor, and a canned rotor induction motor were the final selected prototype designs based on the previously discussed criteria.

5.4 Detailed performance evaluation

Before manufacture of the prototypes, a more detailed analysis of the selected machines was undertaken to provide a more complete evaluation of the performance and also to assess any modifications if required.

5.4.1 Double cage rotor induction motor

The double cage rotor induction motor developed in the previous chapter did not required any additional modification for prototyping or testing. Its rotor bars have simple geometries which were appropriate for ease of construction. For this reason, this section focuses on further analysis of this design to complement the results obtained previously.

Figure 5.1 shows the harmonic analysis of the airgap flux distribution on no-load and rated load in the airgap of the double cage rotor. These are compared with the values for the 5.5 kW benchmark motor. It has a slightly higher harmonic content than the benchmark in general but particularly with the harmonics associated with the stator and rotor slotting. This might be a result of the saturation in the rotor tooth between the circular and rectangular bars. The 5th and 7th harmonic however are lower which suggest an improved rotor current distribution due to the increase in the number of rotor bars. The fundamental field is also a little lower on full load but the reduction seems to be small so should not impact on the torque improvement in this design.

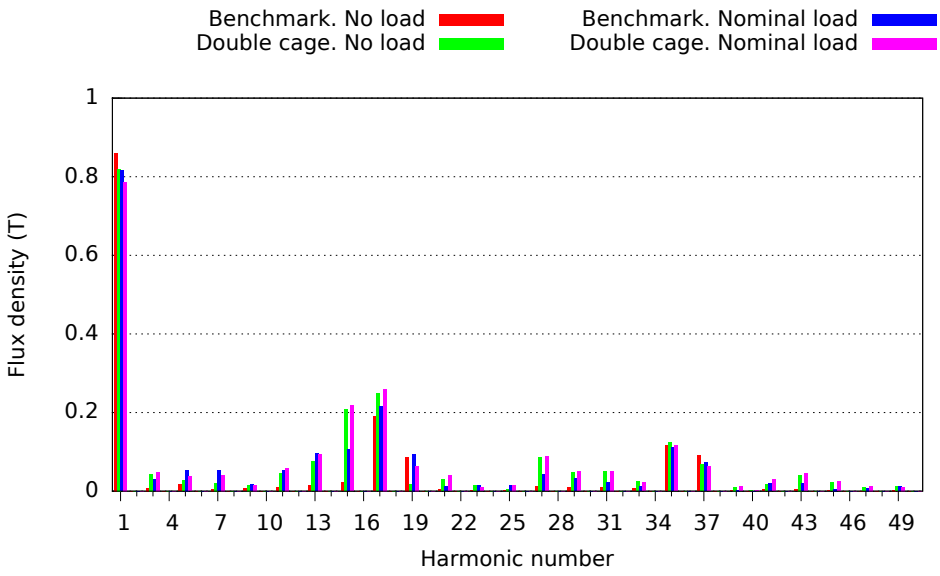

Figure 5.1: Harmonic analysis of benchmark and double cage machines

Figure 5.2 shows the torque speed curves for this machine at different frequencies and was subject to the same considerations for Figure 3.11. Although this motor does not satisfy the power requirements at high speed during the constant power region, its overall performance is better than the benchmark machine as described in Figure 3.11. While

the maximum frequency at which the benchmark satisfied the constant power region requirements is 125 Hz at 3750 RPM nominal speed, the double cage rotor induction motor achieved the required torque up to 150 Hz at 4500 RPM nominal speed.

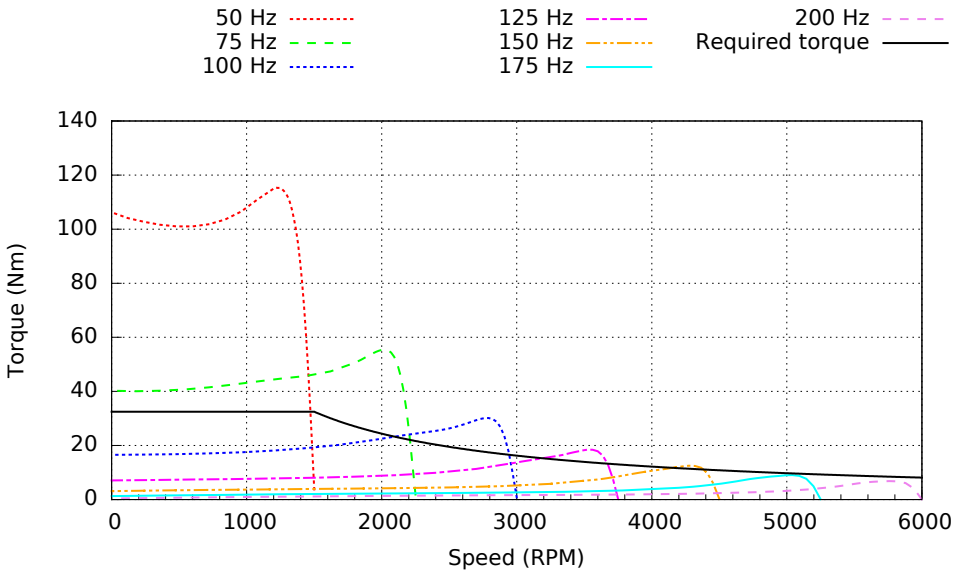

Figure 5.2: Torque speed characteristics of the double cage machine

5.4.2 Canned rotor induction motor

The canned rotor induction motor design offers a simple construction which is very similar to the benchmark motor. It has a larger airgap because of the copper can mounted on the rotor surface. The rotor bar shape however was more suitable for copper die-casting. For this reason, the rotor bar shape was changed to rectangular bars in order to facilitate workshop manufacture. Figure 5.3 illustrates this change and also includes the equipotential lines and flux density distribution at no load. These pictures show similar field paths and distribution to the original rotor slot shape as shown in Figure 4.34.

Figure 5.4 shows the simulated torque, phase current, power factor and efficiency for the canned motor with the rectangular rotor bars. The performance is similar to the previous rotor slot shape as illustrated in Figure 4.35 and better than the benchmark machine.

Figure 5.5 shows the Fourier harmonic analysis of the airgap field for the canned rotor induction motor for no-load and nominal load. Although the fundamental field is again reduced, most of the harmonics are also reduced particularly during rated load conditions. This improvement in the airgap field distribution suggest a reduction of the differential leakage due to the larger airgap.

Figure 5.6 shows the torque speed curves of the canned rotor machine at different frequencies. The performance is better than the benchmark machine and also the double

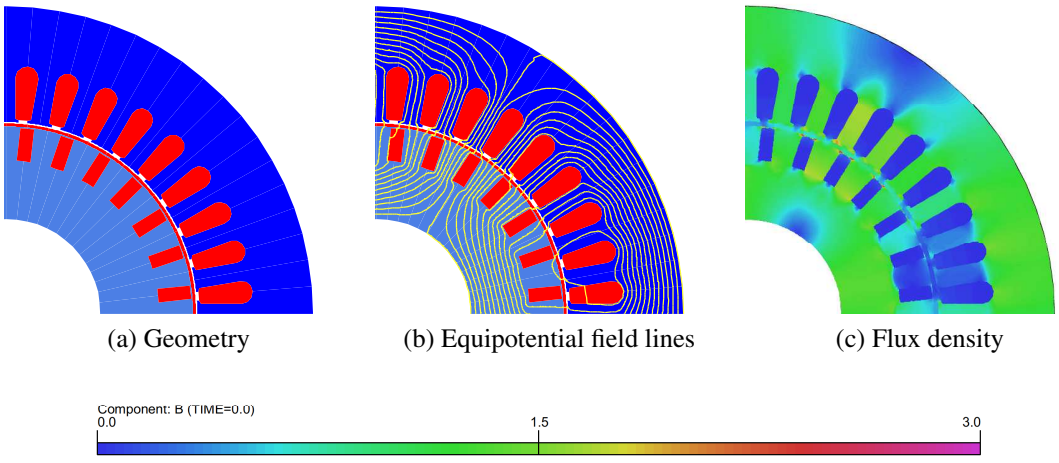

(a) Geometry (b) Equipotential field lines (c) Flux density

(d) Flux density value (T)

Figure 5.3: Canned rotor induction motor

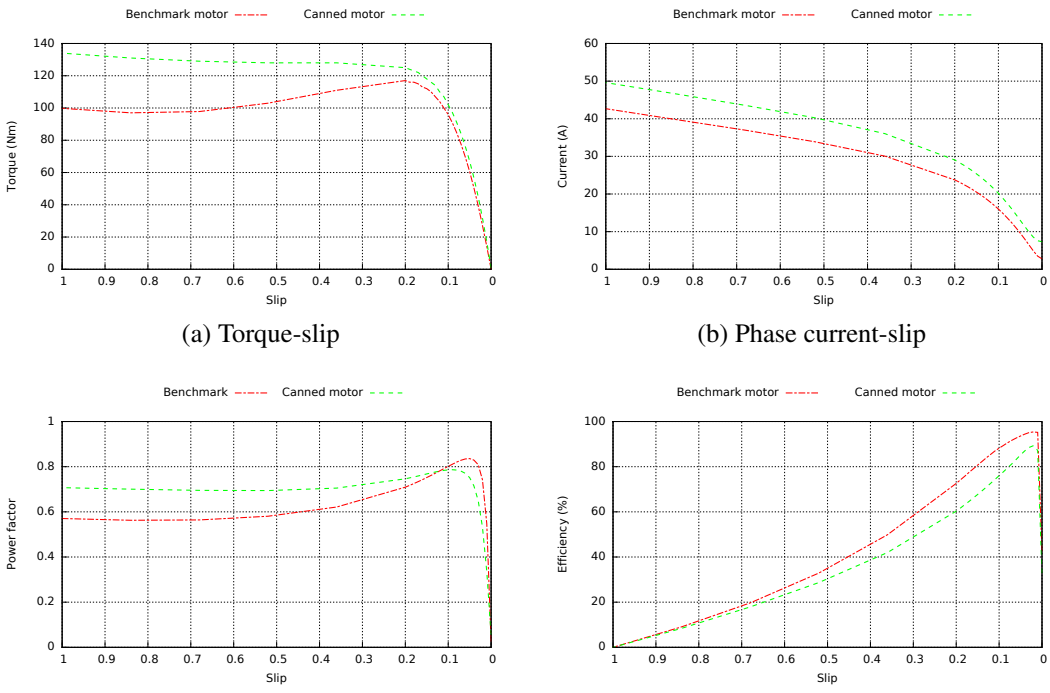

(a) Torque-slip (b) Phase current-slip

(c) Power factor-slip (d) Efficiency-slip

Figure 5.4: Performance curves of the canned rotor motor

cage prototype design. This motor satisfied the torque requirements in the constant power region up to a operating frequency of 175 Hz corresponding to a speed of 5250 RPM which is higher than the speed range for the other machines. This motor almost achieved the full speed range up to 6000 RPM at 200 Hz.

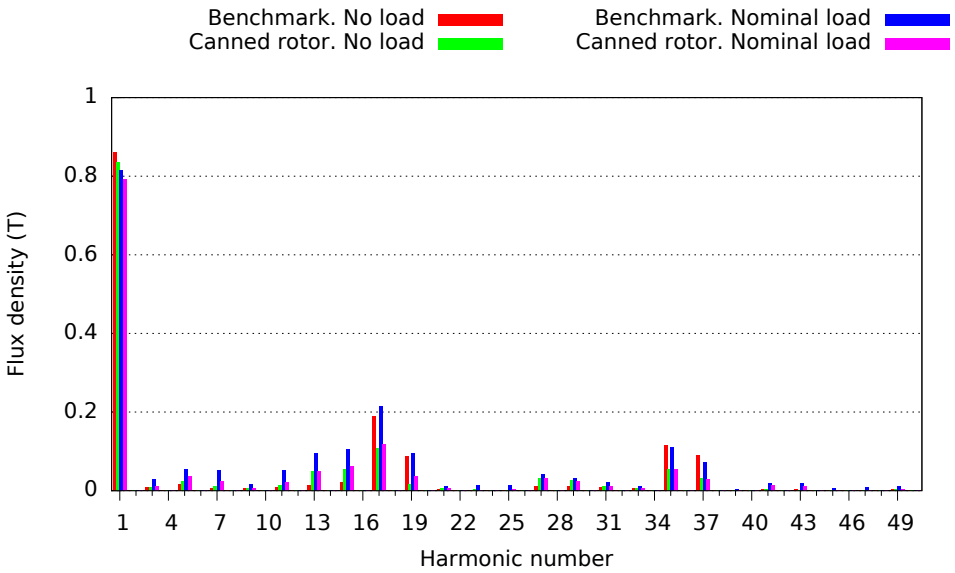

Figure 5.5: Harmonic analysis of the airgap field

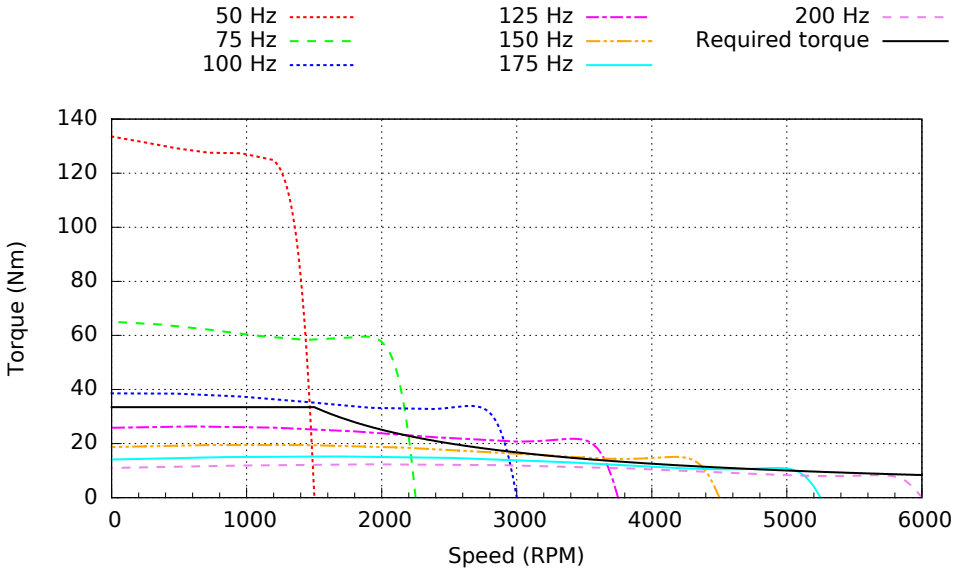

Figure 5.6: Torque speed characteristics of the canned rotor motor

5.5 Prototype construction

Appendix E presents a detailed description of the prototype dimensions used for manufacture. It covers the stator which was the same as the 5.5 kW benchmark induction motor. Each rotor is then described in detail including general core, slot and end-ring dimensions. This section presents a brief description of the building of the two rotor prototypes. Figure 5.7 shows the stator of the benchmark industrial induction motor and the original aluminium cage rotor which was also tested for comparison with the new designs.

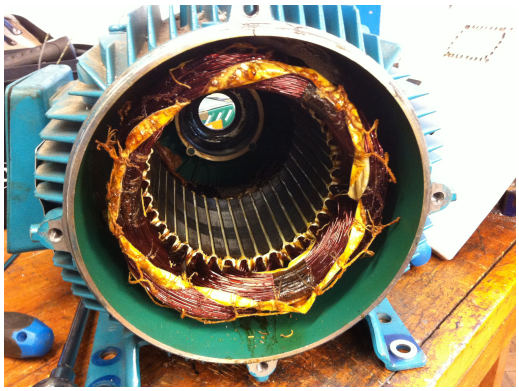

(a) Stator

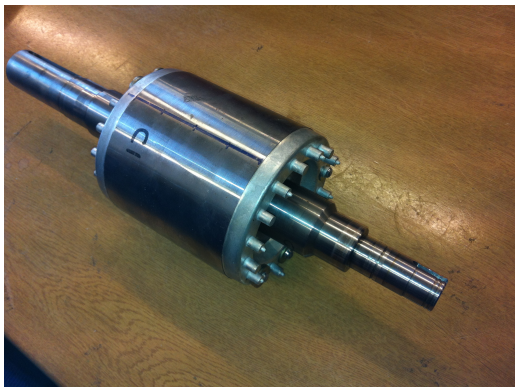

(b) Rotor

Figure 5.7: 5.5 kW industrial induction motor

5.5.1 Rotor 1 – Double Cage Rotor

The first part of the rotor manufacture consisted in building of the core. Figure 5.8 shows the finished core. The laminations were laser cut, stacked and bonded by S&S Windings LTD. The axial markings on the outer rotor surface are assumed to be a result of local heating of the thin slot bridges during the cutting process.

(a)

(b)

(c)

Figure 5.8: Rotor 1 core

The next stage in the rotor build was the construction of the copper cage. Copper die-casting would be the preferred method for industrial production but it was not practical for this prototype because of the cost. For this reason, the copper double cage was fabricated in the mechanical workshop. The round and rectangular rotor bars were cut individually from solid copper. The end-rings were also machined separately. The copper bars were inserted into the slots and soldered together with the end-rings using silver solder. Figure 5.9 shows the finished double cage rotor, including the shaft.

(a) (b)

Figure 5.9: Rotor 1 – Double cage rotor

5.5.2 Rotor 2 – Canned Rotor

The build process for rotor 2 was very similar to that for rotor 1. Figure 5.10 shows the laminated core for rotor 2. It was manufactured by the same company and the same axial markings on the rotor surface are evident.

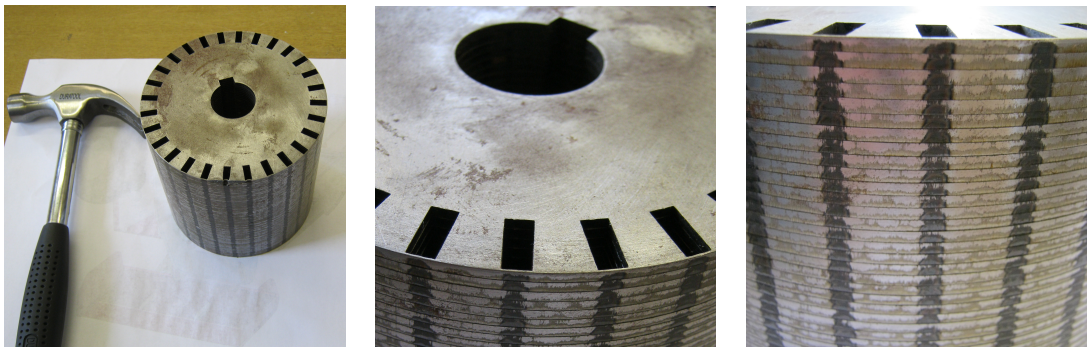

(a) (b) (c)

Figure 5.10: Rotor 2 core

The rotor cage was also machined instead of die-cast. The end-rings were also soldered to the bars using silver solder as shown in Figure 5.11a. The prototype rotor was built using a single sheet of copper (1-mm thick) which was wrapped around the rotor and the joint soldered to hold the can in place and to provide an electrical connection across the joint. Unfortunately during final machining of the rotor outer diameter (including the can), the joint separated and a section of the copper was torn away - see photo in Figure 5.11b.

The only available solution was to cut out a section of the can and insert a patch which was again soldered in. The only copper available for this patch was unfortunately thinner (approx. 0.5-mm) than the original can. This severely weakened the rotor structure so the test procedures were modified accordingly. Although this might impact on the performance, a higher torque was still expected compared to the industrial motor. Figure 5.12 illustrates the finished rotor including the shaft which was machined from

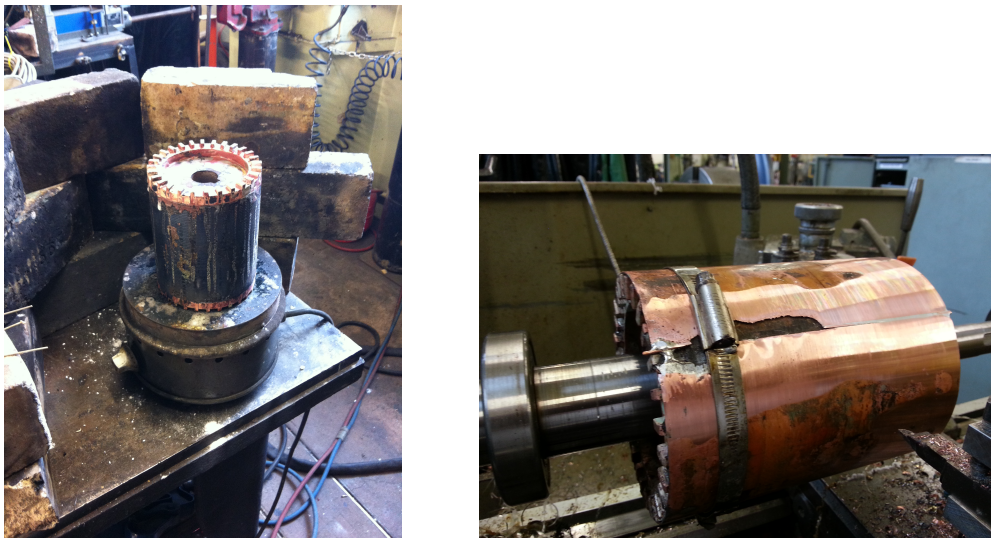

(a) Soldering (b) Damaged can

Figure 5.11: Construction of the canned rotor motor

carbon steel and used in both rotors.

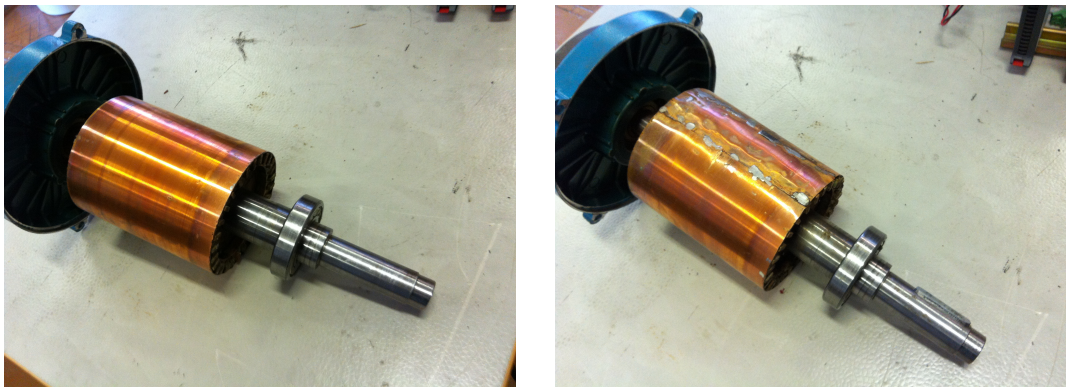

(a) (b)

Figure 5.12: Rotor 2 – Canned rotor

The can construction process was selected mainly in terms of the time and resources available. Mounting a can on the surface of the rotor can be undertaken in several ways. The most common method is to heat shrink the can onto the rotor. Electro-deposition of copper directly onto the rotor surface would be another choice.

5.6 Experimental test results

This section describes, compares and discusses the results obtained from the finite element simulations and the experimental tests. This stage is key in the design process because it closes the cycle on refining the methodology.

5.6.1 Rotor 1 – Double Cage Rotor

The double-cage rotor was designed to increase the torque developed by the machine by adding more copper area in the form of a second cage winding. The rectangular outer cage was designed so that the copper area was the same as the industrial aluminium bar area scaled for electrical conductivity. The inner round bar cage had a reduced bar area due to the space constraints and also to limit the slot leakage. The bridge depth between the round copper bars and the rectangular bars was designed to saturate and present a magnetic short-circuit by using the same bridge depth as that at the top of the rectangular bars. The round bars were placed between the rectangular bars to increase the number of effective rotor bars which would reduce the harmonic (or differential) leakage reactance of the rotor.

The experimental procedure was performed at two test voltages (100 V and 200 V). Figure 5.13a shows the simulated and test results for rotor 1 and the original industrial motor at 100 V. The simulated and test results for the industrial motor shows good correlation at low slip values. Rotor 1 showed a higher torque than the industrial motor but the improvement was not as high as calculated.

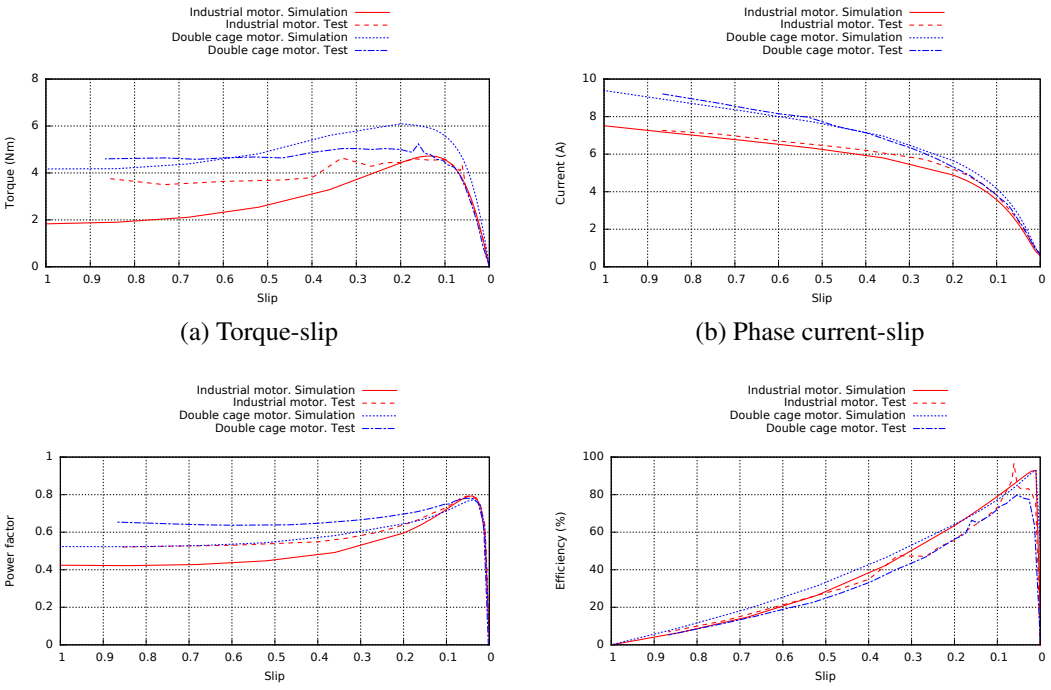

(a) Torque-slip

(b) Phase current-slip

(c) Power factor-slip

(d) Efficiency-slip

Figure 5.13: Performance curves for rotor 1 at 100 V

Figure 5.14a shows the torque behaviour for rotor 1 at 200 V. Both measured torque profiles are lower than expected by simulation with the rotor 1 torque very similar to that for the aluminium cage rotor. This lower than expected performance might be attributed to further heating specially at high load conditions. The soldering between the bars and end-rings is also an area of concern because it would increase the rotor resistance R'_2

especially at higher temperatures.

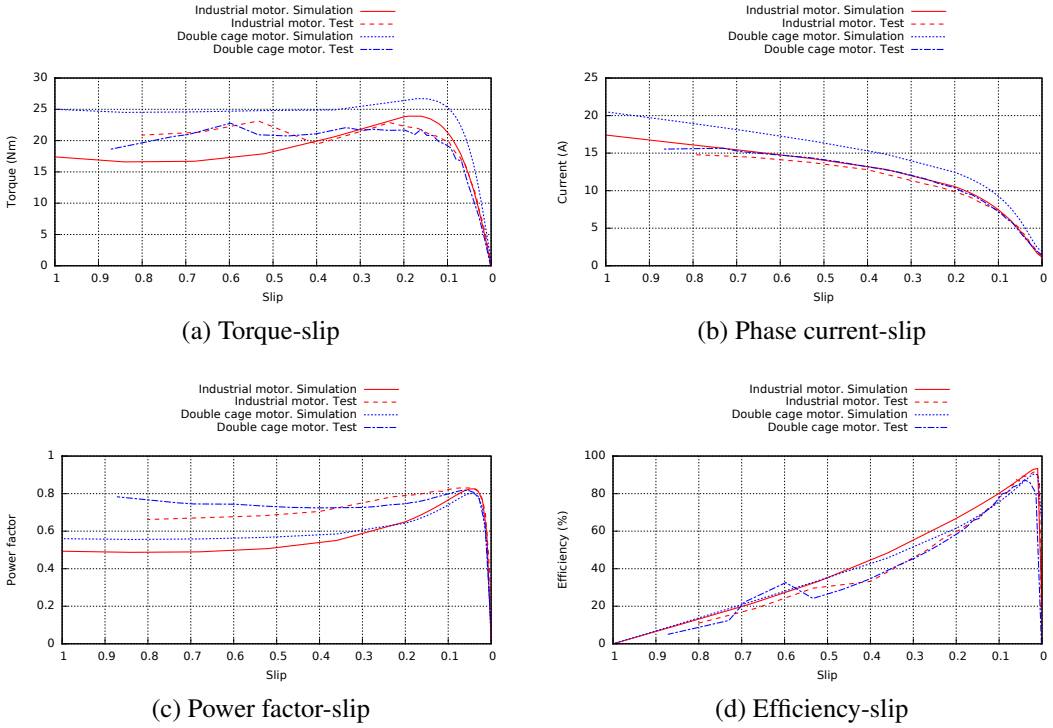

(a) Torque-slip

(b) Phase current-slip

(c) Power factor-slip

(d) Efficiency-slip

Figure 5.14: Performance curves for rotor 1 at 200 V

Figures 5.13b and 5.14b show the phase current-slip curves for the tests at 100 V and 200 V respectively. The test results at 100 V have similar phase-current values to those predicted for both the industrial and the double cage motors. At 200 V, only the industrial motor showed good agreement between the measured and simulated current results whilst the measured current for the double cage motor produced a behaviour similar to the industrial induction motor instead of the calculated performance.

Figure 5.15a shows the characteristic of the torque per amp squared (T/I^2) at 100 V where I is the rotor current calculated from the measured current using the equivalent circuit parameters of Table 5.2. Ignoring harmonic torques, T/I^2 is directly proportional to R'_2/s using the simple equivalent circuit of an induction machine and it provides a good estimate of the rotor resistance R'_2 at fixed speed (slip). The test results at 100 V suggest that R'_2 is lower for the double cage motor than in the industrial motor at low slip (under about 0.4) whilst the opposite at high slips. This increase in R'_2 in the double cage rotor at higher slip values might be a result of more severe heating of the rotor during testing. Again an area of concern is the performance of the soldering between the bars and end-rings.

Figure 5.15b presents the factor (T/I^2) for the 200 V tests. The test results suggest that the rotor resistance R'_2 measured is lower than expected for the industrial motor. However the measured rotor resistance R'_2 of the double cage motor was higher than calculated for most values of slip. This might be also associated with the soldered joints.

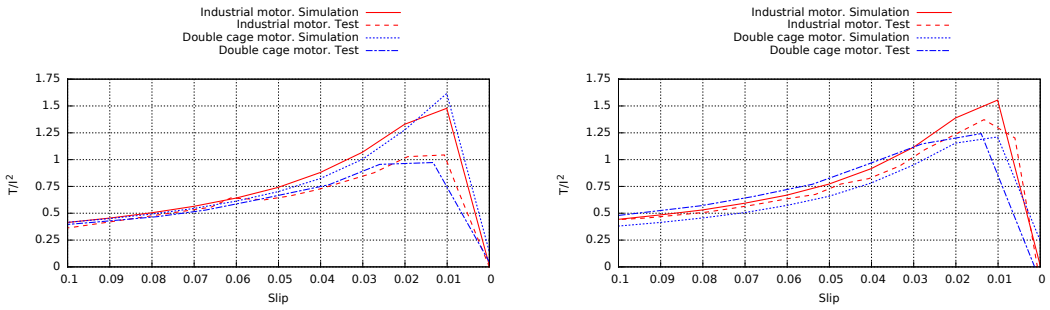

(a) At 100 V

(b) At 200 V

Figure 5.15: T/I^2-slip curve for rotor 1

The net rotor resistance increases with bar number unless the rotor end-ring area is also increased to accommodate the increased end-ring current. Figure 5.15a shows that the simulated rotor resistance for the industrial and double-cage rotors are very similar but the experimental measured values are lower. This is thought to be due to a number of possible factors but the principal factor is commonly the assumption that the input current is totally rotor-referred torque producing current (I_2'). Assuming that the effective rotor resistance is the approximately the same for both rotors then the rotor leakage reactance would explain the difference seen in the torque-slip curves in Figure 5.13a. The rotor leakage reactance is composed of several components: slot leakage; harmonic leakage and end-ring leakage. The double-cage concept doubles the number of effective rotor bars which reduces the harmonic leakage. Reducing the rotor leakage reactance has the effect of increasing the peak torque capability of the motor but the peak torque occurs at a higher slip value. This is evident in Figure 5.13a. The input current curves, Figures 5.13b and 5.14b, also indicate that the double cage rotor has a lower impedance. The greatest area of uncertainty however was the slot leakage of the rotor particularly around the inner cage and there is some evidence in Figures 5.13b and 5.14b that the rotor impedance of the double-cage rotor is increasing as the voltage increases. The key area of concern here is the effect of saturation in the bridge between the rectangular and round bars. This suggest that although the rotor harmonic leakage of the double-cage rotor is reduced, the rotor slot leakage might be increased. The end-ring reactance could also be increased because of the larger end-ring cross-sectional area.

Figures 5.13c and 5.14c present the power factor-slip curves for rotor 1 showing good agreement between the results at low slip. The higher than calculated power factor at high slip values might be a consequence of the rotor overheating. The motor resistances increases with temperature which in turn increases the active power because of the associated higher copper losses. A higher active power with the same reactive power consumption would be reflected in a higher power factor.

Figures 5.13d and 5.14d illustrate the efficiency-slip curves for the rotor 1 at different voltage level tests. The results again show good agreement between them. As with

power factor, the measured results suggest that the efficiency is also affected by higher temperature which is reflected in a lower efficiency.

The expected performance degradation resulting from the higher temperature was confirmed when the machine was disassembled as shown in Figure 5.16. The stator end winding ties and binding were damaged because of overheating. Some marks were evident in the joints between the end-rings and the bars suggesting some heating around the soldered joints. There were also evidence of discolouration of the shaft again as a consequence of overheating during the tests.

(a) (b) (c)

Figure 5.16: Overheating effects in the double cage motor

5.6.2 Rotor 2 – Canned Rotor

Canned rotor motors are commonly found in sealless pump applications where the rotor is immersed in the pump fluid (often corrosive) and leak-free operation is needed. The rotor cans are usually composed of materials resistant to such environments, for instance stainless steel. However, the design presented in this project was not required to protect the rotor windings allowing the use of a material (copper) with better electrical properties for this application.

The test procedure would normally have been the same as that used for the double cage rotor, however the methodology had to be modified because of problems encountered in the rotor build. The rotor can now consisted of two copper sections which were soldered together to the rotor surface. The initial concern related to the possible mechanical unbalance as a result of the difference in the thickness of the two copper sheets. There was also a potential risk of the solder joints separating if the temperature become excessively high. Finally, the resistive effect of the soldered joints in the can as well as the reduced copper area in the thinner section of the can would electrically unbalance the rotor leading to potential torque pulsations and vibration. For these reasons, the tests were only conducted at low values of slip and after each measurement was recorded, the speed was increased to the nominal 1500 RPM for a period to allow the rotor to cool down before continuing with the next step.

Figure 5.17a shows the torque measured at 100 V for the canned rotor machine. It also

includes the simulated results for this motor and the industrial induction motor. The peak torque achieved by this machine is higher than in the industrial one. The measured torque curve of the canned rotor motor suggests a higher rotor resistance compared to the simulated rotor.

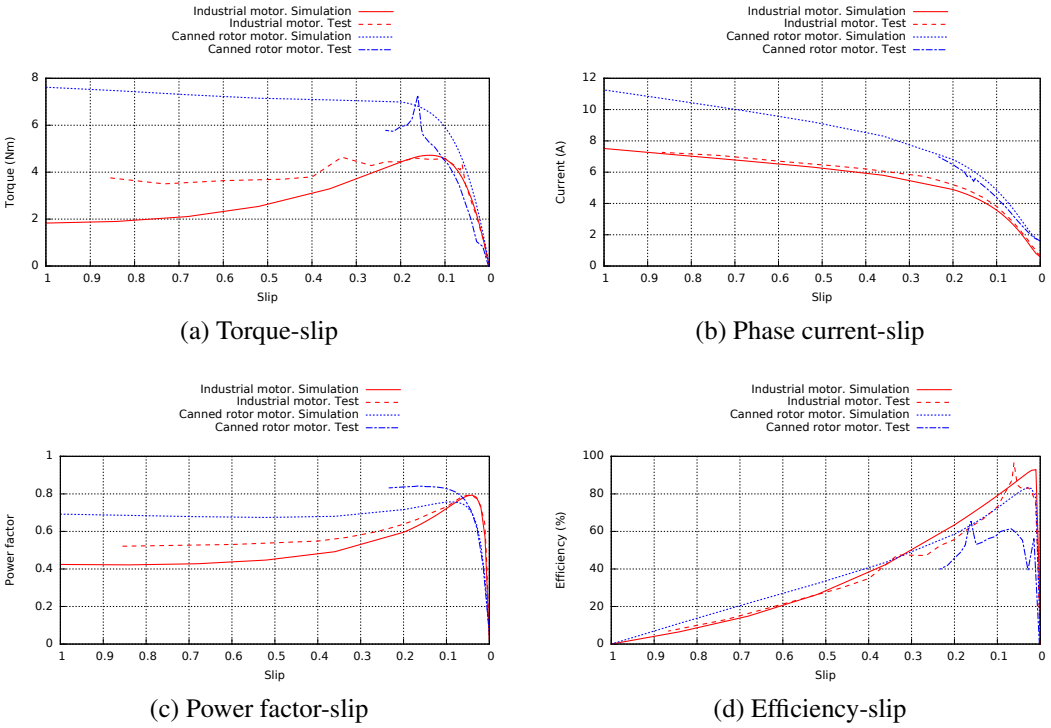

(a) Torque-slip

(b) Phase current-slip

(c) Power factor-slip

(d) Efficiency-slip

Figure 5.17: Performance curves for rotor 2 at 100 V

The results obtained at 200 V showed only a very slightly higher peak torque for the canned rotor machine as shown in Figure 5.18a. The peak torque also occurs at a higher than expected slip which again suggests a higher than predicted resistance. This is very likely as a result of the problems with the rotor can construction. There was also evidence of over-heating during the test which would also serve to increase the rotor resistance.

Similar to the double cage motor, there is a good agreement between the calculated and measured phase currents during the test at the lower voltage test as illustrated in Figure 5.17b. The higher no load current is a result of the larger airgap because of the canned rotor design.

At 200 V, Figure 5.18b however showed that the measured phase currents of the canned rotor machine started at the expected no load value but then showed a lower than expected values as the slip increased tending to follow the values for the industrial motor phase current. Rotor overheating leading to higher rotor resistance was though to be the likely cause of this.

The coefficient T/I^2 was used again as an indirect method of estimating the rotor resistance R_2'. At 100 V, this coefficient showed mostly the expected results with the simulated resistance being generally lower for the canned rotor motor than for the

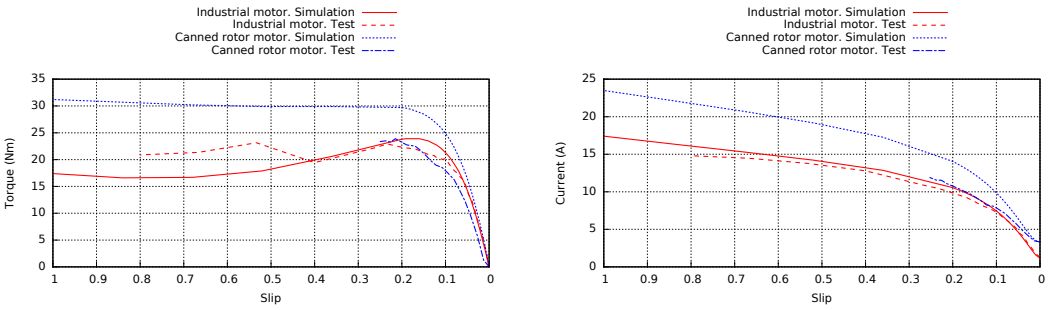

(a) Torque-slip

(b) Phase current-slip

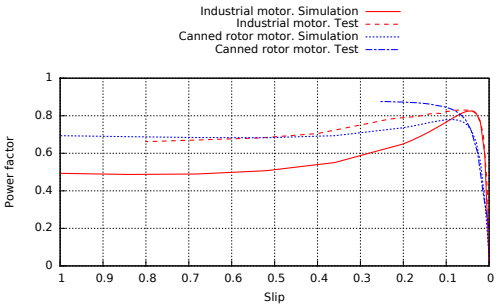

(c) Power factor-slip

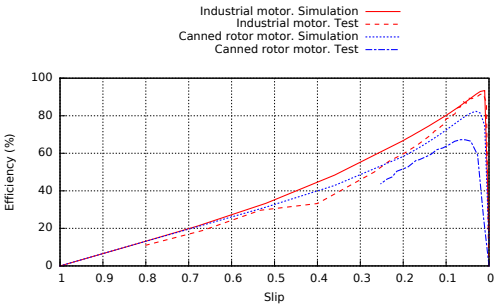

(d) Efficiency-slip

Figure 5.18: Performance curves for rotor 2 at 200 V

industrial induction machine as shown in Figure 5.19a. This is probably caused by the additional magnetizing current needed in the canned rotor. The test coefficient is further reduced and this is possibly caused by the additional harmonic losses expected in the rotor can.

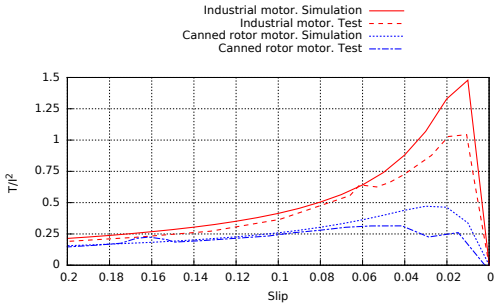

(a) At 100 V

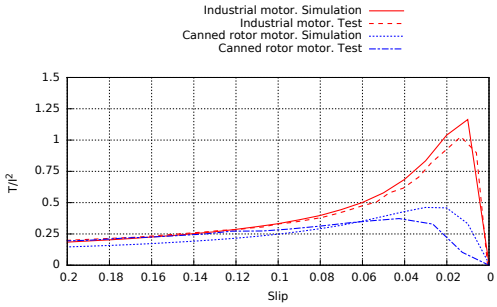

(b) At 200 V

Figure 5.19: T/I^2-slip curve for rotor 2

Figure 5.19b shows similar trends for the coefficient T/I^2 at 200 V. Again it is thought harmonic losses in the copper can are leading to a reduced coefficient on test.

The power factor shows a reasonable agreement between the calculated and measured values obtained for values of slip lower than about 0.05. For higher values, the measured power factor of the canned motor was higher than calculated. This might be a result of the higher copper losses as in the canned rotor. This behaviour was seen at both test voltages as shown in Figures 5.17c and 5.18c.

The measured efficiency of the canned motor was lower than expected for both voltage levels as illustrated by Figures 5.17d and 5.18d. This is associated in part with the higher copper losses incurred due to the reduced thickness section of the copper can, the soldering of the can and end-rings, and the harmonic losses in the can. Higher iron losses might have also contributed as a result of the 2-mm mild steel laminations employed for the manufacture of this prototype rotor.

It was also evident during testing that the canned rotor was a little noisier than the previous rotors which would confirm the expected electrical and mechanical asymmetry of the rotor. Figure 5.20 shows the canned rotor in detail after testing. Figures 5.20a and 5.20b show the rotor surface at the undamaged and patched sections respectively. Figure 5.20c shows the soldered end-ring and bars whilst Figure 5.20d shows the joint in the can where the solder joint was damaged. The canned rotor expanded during test as a result of overheating and this resulted in a slight contact between the stator and rotor as shown in Figures 5.20e and 5.20f. The rotor-stator contact represents an extra friction torque which in turn might explain the lower than expected torque in the 200 V test.

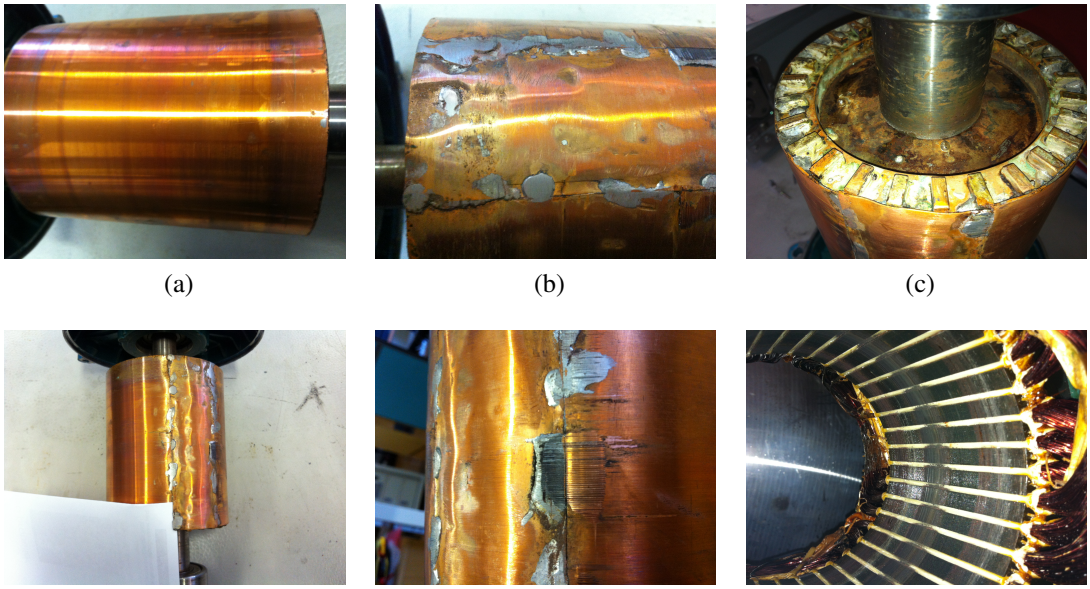

(a) (b) (c)

(d) (e) (f)

Figure 5.20: Canned rotor after testing

5.7 Summary

This chapter presents a summary of the simulations results in a manner that facilitates a comparison between the proposed motor designs using a parameter denominated normalized specific torque. It also includes calculations of the equivalent circuit parameters and temperature rises in some of the designs.

This chapter describes the criteria used to select the designs for prototyping and testing

to further the design process. A detailed analysis of the selected machines was then presented including any modifications required to facilitate manufacture.

The manufacture and testing of two prototype rotors designed to produce a higher specific torque induction motor was also presented. The finite element models used in the design process were validated and used to identify improvements in the design process.

5.8 References

[1] O. Chiver, E. Micu, and C. Barz. “Stator winding leakage inductances determination using finite elements method”. In: *Optimization of Electrical and Electronic Equipment, 2008. OPTIM 2008. 11th International Conference on*. 2008, pp. 69–74.

CHAPTER

SIX

CONCLUSIONS AND FURTHER WORK

6.1 Introduction

This project has looked at a complete cycle of the design process for the induction motor from the basic proposed topology though to the comparison of simulated and experimental test results. This chapter summarises the research developed during this process highlighting the contributions of this work to the field of knowledge. This final part of the thesis also includes comments about areas for further research related to the improvement of the specific torque in electrical machines for electric traction in light ground vehicles, with special emphasis on the induction motor.

6.2 Review of presented work

This work has presented a complete review of the background concerning electric vehicles and the role of the traction motor. This included the identification of the characteristics that these traction machines must meet, focusing mainly on the specific torque. Permanent magnet, switched reluctance and induction motors were identified as the main candidates for this application. Permanent magnet machines offer torque densities higher than the other machines resulting in a predominance in commercial electrical vehicles.

However, concerns about the production of the rare earth materials employed as permanent magnets has encouraged the research for alternatives. The induction motor represents an attractive competitor due to its robustness, lower raw material costs and manufacturing costs, but its main disadvantage is a lower specific torque. This project conducted a search to identify methodologies and designs for improved specific torque.

The first step undertaken was a detailed analysis of the induction motors already used

in electric vehicles. Most of these machines were found to be very similar to industrial designs. For this reason, it was decided to extend the literature review to other type of electrical machines with high torque/power density or wide speed range focusing on the technologies which could be implemented in an induction motor.

Once the state of the art on high power/torque dense electric machines was covered, the next stage consisted of reviewing the design process of induction motors including its historical evolution. This allowed the identification of the basis of the methodology to be followed in this project:

- The specific performance requirements were summarized for the designs developed during this research with a focus on the torque and speed range necessary for driving a light ground vehicle.
- The benchmark induction motors were selected for a direct comparison of the new designs. These motors were based on industrial induction motor designs with the only difference being the cage material was replaced by copper. In some cases, the rotor slot area was adjusted by the copper to aluminium conductivity ratio.
- A large part of this research was dedicated to the identification of potential designs with improved specific torque. The approach followed for this purpose consisted mainly in the proposal of topologies which in many cases differed from the standard industrial induction motor.
- The initial design dimensions were derived from the benchmark motors and/or calculated using analytical expressions. A finite element analysis was then employed to refine the designs until a satisfactory performance was achieved. All the finite element models were coded in Opera 2D or Flux 2D in order to facilitate their analysis and use for further development.
- The different topologies considered for achieving a higher specific torque were simulated in both steady-state and transient conditions. Their performance was assessed in terms of torque, phase current, efficiency and power factor. Further refinement was conducted in some designs and two rotor designs were selected for prototyping and testing.
- The construction of the prototypes was also an important task. The selected designs used the same stator as the benchmark machine which reduced time and costs. Two rotors were built consisting of a double cage rotor and a canned rotor. Some severe difficulties were encountered during the construction process and repairs had to be undertaken to try and minimize any adverse effect on the performance.
- An experimental test rig and test procedure were developed to obtain the torque-slip curves. Although tests were conducted at reduced voltage to avoid any excessive rise in temperature, there was some evidence of rotor overheating during test.

- The experimental results obtained were compared with their respective finite element simulations. The tests were conducted as quickly as possible but there were still indications of rotor overheating at low slip speeds. Nevertheless, the torque showed some improvements at the lower voltage test.
- The design cycle concluded with a review of the results obtained identifying areas for further improvement.

6.3 Conclusions

In this research, the main aim was to take a radical approach to the design process of the induction motor for its application on electric vehicles. This was achieved by developing ten different topology designs of induction machine and performing an analysis of their performance directly using the finite element analysis. Analytical methods were used only to calculate the initial dimensions for these designs. Other completed objectives included:

- A review of the literature about electric motors for electric vehicles focusing on induction motors and high power/torque machines. Motors with wide speed range were also included.
- Specification of the requirements for an induction motor for automotive applications in terms of performance.
- Review and identification of the materials suitable for electrical motors in light ground vehicles.
- Design, construction and test of two prototype induction machines which had the potential to increase the specific torque for their application in electric vehicles.
- Analysis and review of the methodology used during this research in order to validate and recommend further improvements.

The finite element analysis was the key tool used during this research (Opera 2D and Flux 2D). Methodologies using this technique are more common today because of the growing computing capabilities. The tendency goes even further and 3D design models will improve the results of the existing machines and open up new possibilities with more complex topologies. Nevertheless, analytical methods are still an important tool at the beginning of the design process in obtaining the base design before refinement using the finite element analysis.

The main objective was to examine the design of conventional induction machines and develop new designs to increase the torque produced for the same motor volume. As expected, it is difficult to find ways of increasing the torque without some loss of performance in terms of current, power factor and efficiency. A large number of

potential new designs were examined and a number of these were shown to provide more torque than the equivalent benchmark industrial design. Some of the more novel designs would prove difficult to manufacture and would require some innovation in manufacturing methods to make them more realistic alternatives. The designs developed in this thesis are ranked below in terms of their normalized specific torque (in brackets) as the key figure of merit:

Wound rotor induction motor with third harmonic current injection (1.6996). The performance was improved by combining two design techniques.

Induction motor with third harmonic current injection (1.5268). This is a technique which allows an increase in the fundamental of the airgap field by changing its distribution through the injection of third harmonic currents. The main advantage of this technique is that it can be combined with other designs.

Induction motor with grain oriented laminations (1.4856). The stator core of the benchmark motor was replaced by a segmented core of grain-oriented laminations oriented in the radial direction. Although the mechanical structure is weaker, there was an improvement in the specific torque.

Distributed rotor bar induction motor (1.2609). The rotor bars were replaced by distributed small elements forming a mesh with the intention of increasing the effective number of bars without increasing the slot leakage. Although the specific torque found was higher, the complex manufacture represented the main difficulty.

Wound rotor induction motor (1.2125). A wound outer rotor was designed which would not respond to all the mmf harmonics produced by the stator. However, it was constrained by the space available for the rotor windings.

Canned rotor (1.1978). An induction machine which used a normal cage but added a copper can on the rotor surface to develop more torque.

Double cage (1.1960). This was designed to have two electrically isolated rotor cages, one sitting inside the other. The idea behind this was a reduction of the rotor harmonic (differential) reactance by placing the second cage one half a rotor slot pitch from the first cage. This effectively doubled the number of rotor bars, reducing the rotor differential reactance and increasing the peak torque capability of the machine. Design of the inner cage to avoid increasing the slot leakage reactance was difficult but the finite elements models demonstrated a net increase in the peak torque

Double stator induction motor (1.1914). A series of designs were analysed in order to use the space inside the rotor cage by placing an additional stator. This was expected to improve the electrical loading of the machine but there was insufficient space to implement this concept for small power ratings.

Solid rotor core induction motor (1.0727). The laminated rotor core was replaced by solid carbon steel. The initial steady state simulations suggested an improved specific torque but the transient simulations showed that the torque was not improved due to harmonic effects not included in the steady state model. These machines are more suited to very high-speed operation.

Modular induction motor (1.0578). Induction motors designed with modular windings require more volume for the same rating. However a double stator version with these windings was proposed in order to improve specific torque but only achieved the same as the benchmark machine.

Toroidal induction motor (1.0527). Toroidal windings are more compact offering a higher fill factor but require about the double the turns of conventional windings. This increased the stator winding leakage reactance and resistance which restricts the improvement in the torque. Toroidal windings however offer the option of electronic pole changing which unfortunately could not be fully exploited because of the saturation in the coreback.

Induction motor with tooth slits (0.9869). This machine had radial slits in the middle of the tooth in order to reduce the leakage. Only a slightly higher torque was achieved which did not justify the mechanical weakness introduced by the teeth slits.

Two rotor designs were selected for prototyping: a double-cage rotor; and a canned cage rotor. Experimental tests on the double-cage rotor demonstrated that the increased torque was lower than the simulated values but higher than the industrial motor at 100 V and closely similar at 200 V. The reduced torque output was thought to be due to rotor overheating during the test and increased rotor reactance with increasing voltage. The canned rotor encountered a serious problem during build and a section of the rotor can had to be removed and replaced with another section of copper of reduced thickness. The testing was restricted to low slip values as a result. Again rotor overheating and additional rotor harmonic losses in the surface-mounted can were thought to be the main reason.

In both cases the test confirmed a small loss in the other performance measures: current, power factor and efficiency. However there was evidence to suggest that these designs could provide more torque with an improved and more consistent means of manufacturing the rotors.

The combination of the designs presented also offers an opportunity to improve further the torque. Some are easily to implement, for example the third harmonic current injection could be combined with practically all the rest of the designs and would represent an improvement performance in torque. However, some cases might face special challenges for example the combination of the third harmonic current injection

with the grain oriented segmented stator. This combination might require a very large magnetizing current because of the airgaps between stator core segments and the saturation in the coreback produced by the third harmonics.

Others combinations should be analysed in more detail to evaluate their convenience, for example it is possible to combine modular and toroidal windings but little advantage is expected at first glance from such complex stator and/or rotor. Combining methods or techniques to increase the torque is a complex process because calculating the contribution of each technique is not straightforward.

6.4 Further work

A large number of induction motor designs were examined in this work. A number of these were not considered for prototyping because of the difficulty in constructing them. However it would be worth pursing some of these further particularly if good rapid prototyping facilities were available for example.

One of the areas not considered in this thesis and would be worth exploring is short-term overloading to increase torque as these machines would be operating at a lower load depending on the typical driving cycle used. This makes use of the long thermal time constants to enable short-periods of high current and torque. Designs could be examined to enhance this capability.

In general during this research, the efforts were focused on the electromagnetic design leaving the thermal design on second plane. Although, the obtained designs satisfy the thermal operational requirements, further work is necessary in the thermal rating design.

Some more radical concepts might be worthy of consideration. For example, the use of ferrofluids (a colloidal liquid with ferromagnetic properties [1]) or the use of heat pipes for direct cooling of the rotor [2]. The later could be used in conjunction with the short-term overloading mentioned above.

The canned rotor design could also be improved. The harmonic losses in the can were thought to be problematic. One way to improve this would be cut axial slits into the rotor can as shown in Figure 6.1. This forces the induced current pattern to flow more like a conventional cage current distribution and would prevent some of the harmonic currents from circulating in the can. The slits would not extend along the full length of the rotor as shown in Figure 6.1 to provide an 'end-ring' path for the currents. The spacing of the slits would pose an interesting design challenge and would influence the performance of the rotor can.

The double-cage rotor could also be improved in larger motor sizes where there would be more space to integrate the second cage into the rotor without increasing the rotor

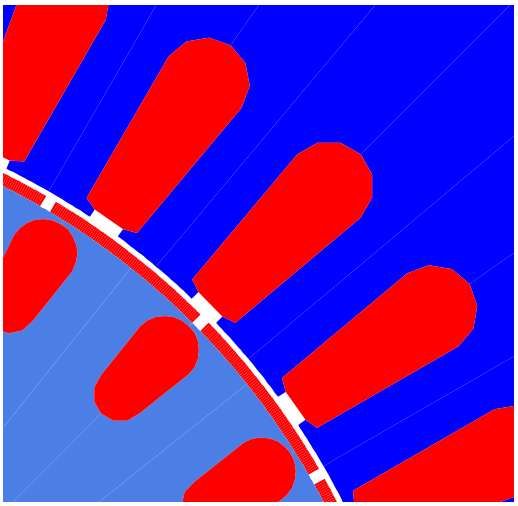

Figure 6.1: Canned rotor with slits

slot leakage. This also applies to the double-stator concept – larger motor ratings would provide more space to accommodate an effective second inner stator and increase the torque capability of the motor.

During this research, most of the simulations were carried out at nominal speed in order to reduce the simulation time. A more detailed approach could include the simulation of the designs over the full speed range at the expense of much higher computing times.

One final of improvement would be the development of the models using 3D finite elements which would provide more accurate modelling of effects such as the end-windings. However, it would be a trade off between time and available resources (computational, economical and software licenses). the new generation of multi-physics finite element packages would also be worthy of developing: this would directly link the electromagnetic and thermal performance for example of any given design.

6.5 References

[1] S. Engelmann et al., “Concept of a new type of electric machines using ferrofluids”, *Journal of Magnetism and Magnetic Materials*. 293, 685 –689. (2005).

[2] J.C. Corman et al., “Heat Pipe Cooled Induction Motor”, *Power Apparatus and Systems, IEEE Transactions on*. PAS-93, 1069 –1075. (1974).

APPENDIX

A

SPECIFICATIONS OF THE BENCHMARK MOTORS

This appendix details the specification of the industrial induction motors used as the benchmark machines. It also includes details of the modified rotor slots used in the benchmark machines. All dimensions are in mm unless otherwise specified.

A.1 55 kW industrial induction motor

Table A.1: Stator data of the 55 kW industrial induction motor

Description	Value	Unit
Poles	4	-
Output	55	kW
Voltage	400	V
Phases	3	-
Frequency	50	Hz
Winding connection	Delta	-
Temperature	120	°C
Lamination material	China steel	-
Number of slots	48	-
Core length	235	mm
Bore diameter	234.95	mm
Core back depth	35.17	mm
Stacking factor	0.96	-

Table A.2: Stator winding data of the 55 kW industrial induction motor

Description		Value	Unit
Winding type		Whole coil concentric	-
Coils per slot		1	-
Tiers		2	-
Coils per group		4	-
Turns per coil		19	-
No of parallels		2	-
Step		1-10,12,14,16	-
Wires	Size 1	1/1.18	mm
	Size 2	6/1.12	mm
Wire material		Copper wire	-
Slot fill (%)		79.39 (square wire + insulation)	-
Mean turn length		1100	mm

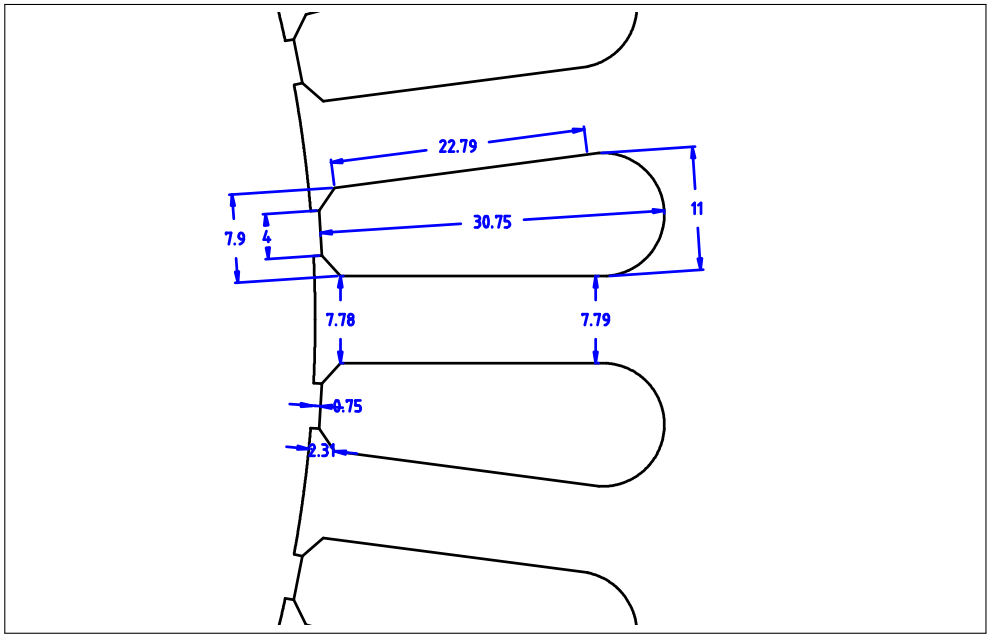

Figure A.1: Stator slot dimensions of the 55 kW industrial induction motor

Table A.3: Rotor data of the 55 kW industrial induction motor

Description	Value	Unit
Lamination material	China steel	-
Number of slots	40	-
Core length	232	mm
Core back depth	31.4	mm
Stacking factor	0.97	-
Airgap	0.8	mm
Skew	1.5	Degrees at shaft OD
Conductor material	Aluminium	-
Shaft material	Carbon steel	-
Temperature	120	°C

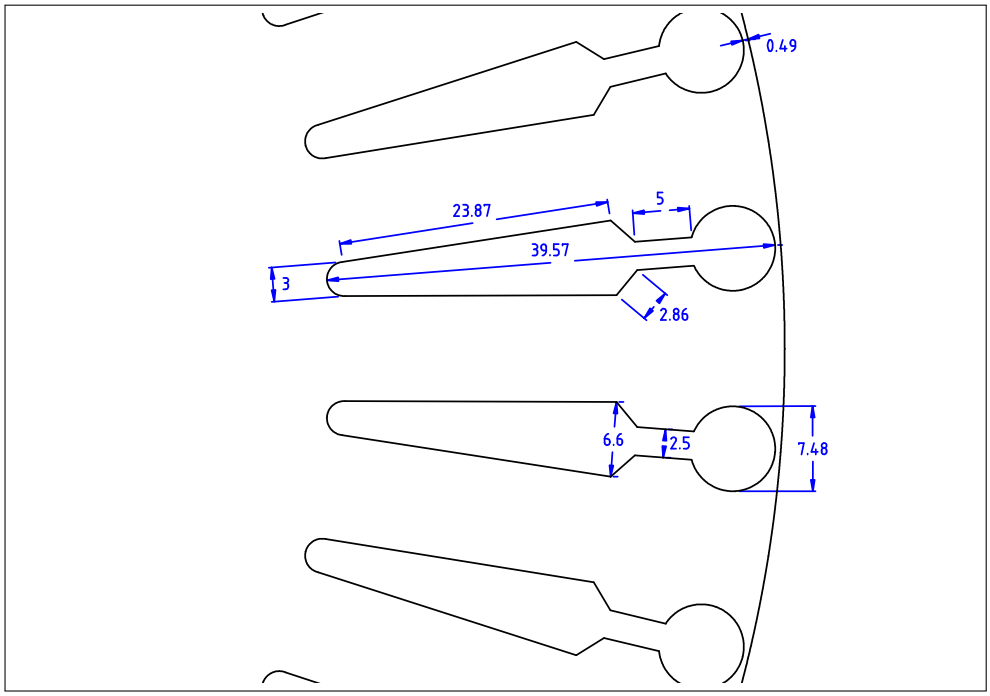

Figure A.2: Rotor slot dimensions of the 55 kW industrial induction motor

Table A.4: Performance data of the 55 kW industrial induction motor (Data provided by the manufacturer)

Slip (P.U.)	**Output (kW)**	**Current (A)**	**Input (kW)**	**Speed (RPM)**	**Torque (Nm)**	**Effy (%)**	**Power factor**
0.0001	0.00	28.28	1.108	1499.9	0.0	0.0	0.0570
0.0036	13.77	36.37	15.11	1494.6	88.0	91.11	0.600
0.0072	27.49	52.77	29.24	1489.2	176.0	94.03	0.800
0.0111	41.23	72.80	43.87	1483.4	265.0	93.99	0.870
0.0151	54.97	94.76	58.87	1477.4	355.0	93.38	0.897
0.0195	68.71	118.3	74.28	1470.8	446.0	92.50	0.906
1.0000	0.00	755.60	234.00	0.0	857.0	0.00	0.447

Table A.5: Equivalent circuit data of the 55 kW industrial induction motor (Data provided by the manufacturer)

	Reference	**Cold**
R_1	0.145@120°C	0.104@20°C

	No load	**Full load**	**Locked rotor**
X_1	0.335	0.335	0.335
R_2'@120°C	0.116	0.116	0.269
X_2'	4.37	0.989	0.465
R_m	700	576	901
X_m	24.1	24.0	18.1

Table A.6: Lamination properties of the 55 kW industrial induction motor

B (T)	**H (A/m)**
0	0
0.5360205	0.34794634
0.8035629	0.695892681
1.010403	1.179151438
1.155757	1.783224539
1.261454	2.538316386
1.340343	3.48218151
1.4005	4.662012914
1.447272	6.136800913
1.484359	7.980287482
1.514426	10.28464444
1.539463	13.16509534
1.561023	16.76564955
1.580366	21.26634545
1.598574	26.89222161
1.618062	33.92456367
1.641464	42.71499124
1.669321	53.70301314
1.702105	67.43805622
1.740152	84.60686007
1.783566	106.0678586
1.832092	132.8941445
1.884979	166.4268761
1.940851	208.342885
1.997595	260.7379902
2.052309	326.2317776
2.1013	408.0989176
2.140156	510.4329053
2.163835	638.3505157
2.170218	702.1855421

A.2 55 kW benchmark induction motor

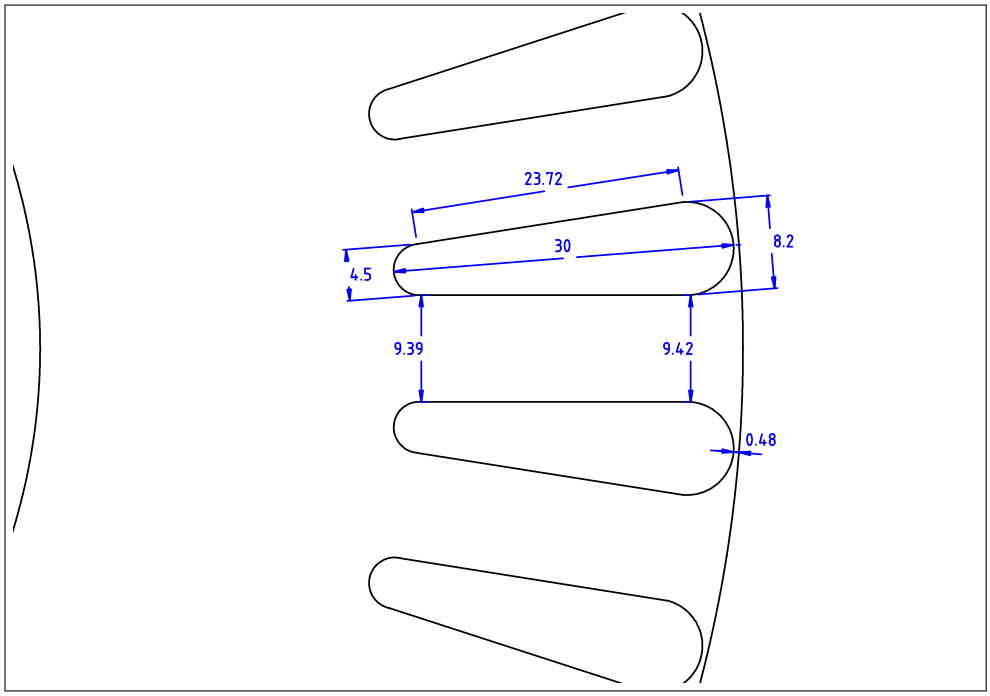

Figure A.3: Rotor slot dimensions of the 55 kW benchmark induction motor

A.3 7.5 kW industrial induction motor

Table A.7: Stator data of the 7.5 kW industrial induction motor

Description	Value	Unit
Poles	4	-
Output	7.5	kW
Voltage	400	V
Phases	3	-
Frequency	50	Hz
Winding connection	Delta	-
Temperature	75	°C
Lamination material	Newcor 660-50	-
Number of slots	36	-
Core length	160	mm
Bore diameter	127	mm
Core back depth	19.76	mm
Stacking factor	0.96	-

Table A.8: Stator winding data of the 7.5 kW industrial induction motor

Description		Value	Unit
Winding type		Whole coil concentric	-
Coils per slot		1	-
Tiers		2	-
Coils per group		3	-
Turns per coil		34	-
No of parallels		1	-
Step		1-8,10,12	-
Wires	Size 1	1/0.80	mm
	Size 2	2/0.75	mm
Wire material		Copper wire	-
Slot fill (%)		42.20 (true wire area only)	-
Mean turn length		644	mm

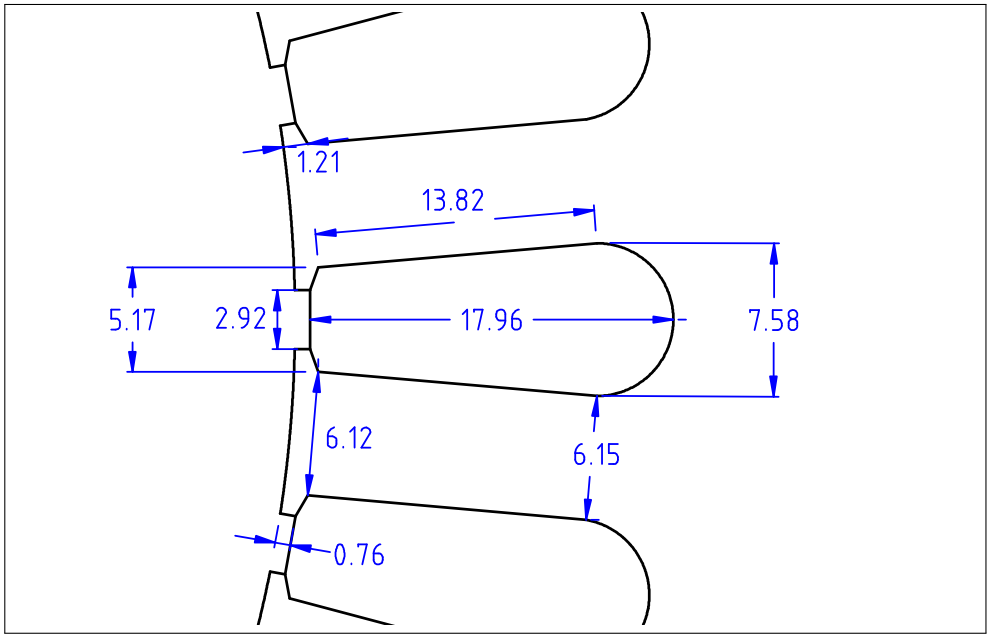

Figure A.4: Stator slot dimensions of the 7.5 kW industrial induction motor

Table A.9: Rotor data of the 7.5 kW industrial induction motor

Description	Value	Unit
Lamination material	Newcor 660-50 unannealed	-
Number of slots	28	-
Core length	160	mm
Core back depth	19.46	mm
Stacking factor	0.97	-
Airgap	0.45	mm
Skew	1.15	Rotor bars
Conductor material	Aluminium	-
Shaft material	Carbon steel	-
Temperature	75	°C

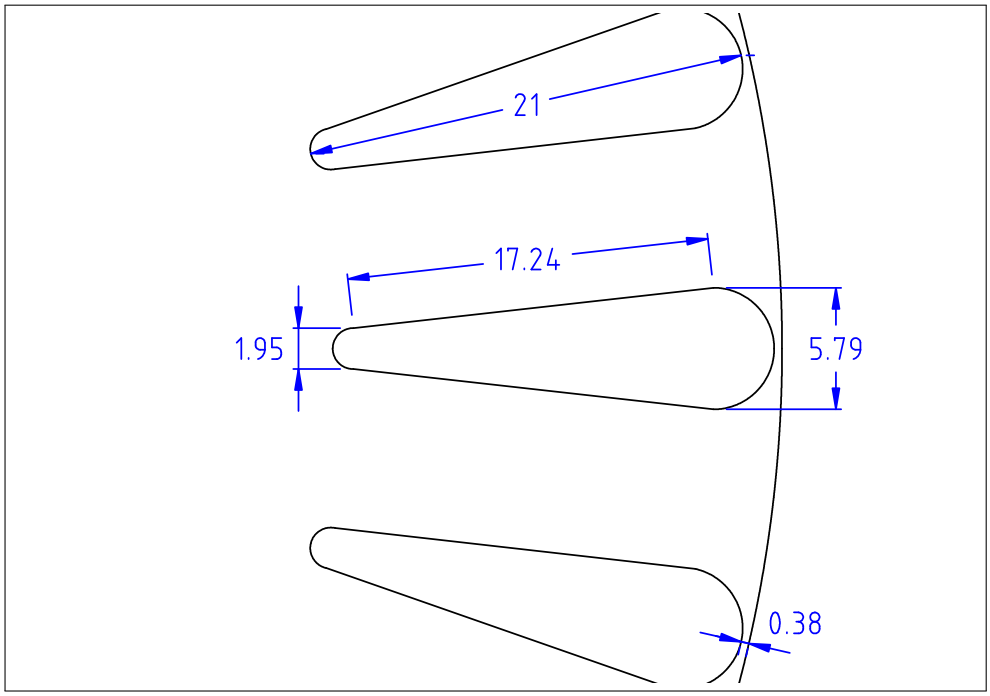

Figure A.5: Rotor slot dimensions of the 7.5 kW industrial induction motor

Table A.10: Performance data of the 7.5 kW industrial induction motor (Data provided by the manufacturer)

Slip (P.U.)	**Output (kW)**	**Current (A)**	**Input (kW)**	**Speed (RPM)**	**Torque (Nm)**	**Effy (%)**	**Power factor**
0.0002	0.000	5.951	0.282	1499.7	0.0	0.00	0.000
0.0070	1.876	6.768	2.196	1489.5	12.0	85.44	0.468
0.0143	3.747	8.747	4.187	1478.6	24.2	89.50	0.691
0.0221	5.619	11.38	6.272	1466.9	36.6	89.60	0.796
0.0307	7.492	14.45	8.461	1454.0	49.2	88.55	0.845
0.0403	9.363	17.91	10.77	1439.6	62.1	86.92	0.868
1.0000	0.000	89.69	35.57	0.0	115.0	0.00	0.572

Table A.11: Equivalent circuit data of the 7.5 kW industrial induction motor (Data provided by the manufacturer)

	Reference	**Cold**	
R_1	2.02@75°C	1.66@20°C	
	No load	**Full load**	**Locked rotor**
X_1	1.73	1.73	1.73
R_2'@75°C	1.62	1.62	2.60
X_2'	29.9	8.13	4.50
R_m	2926	2518	4164
X_m	114	114	91.5

Table A.12: Lamination properties of the 7.5 kW industrial induction motor

B (T)	**H (A/m)**
0	0
0.099817	0.556872933
0.199615	0.751059173
0.299635	0.888865763
0.399138	0.991168712
0.499445	1.101472041
0.599185	1.209399069
0.699795	1.323852065
0.798947	1.477463379
0.898636	1.66488954
0.999416	1.932309447
1.098478	2.317325449
1.199293	2.971342208
1.299129	4.226823163
1.399837	7.155140631
1.496727	14.85788599
1.59605	33.82468615
1.697686	69.80280841
1.747747	94.16087059
1.808	125.6637061
1.948	251.3274123
2.014	376.9911184
2.086	628.3185307
2.186	1256.637061
2.331	2513.274123
2.464	3769.911184

A.4 7.5 kW benchmark induction motor

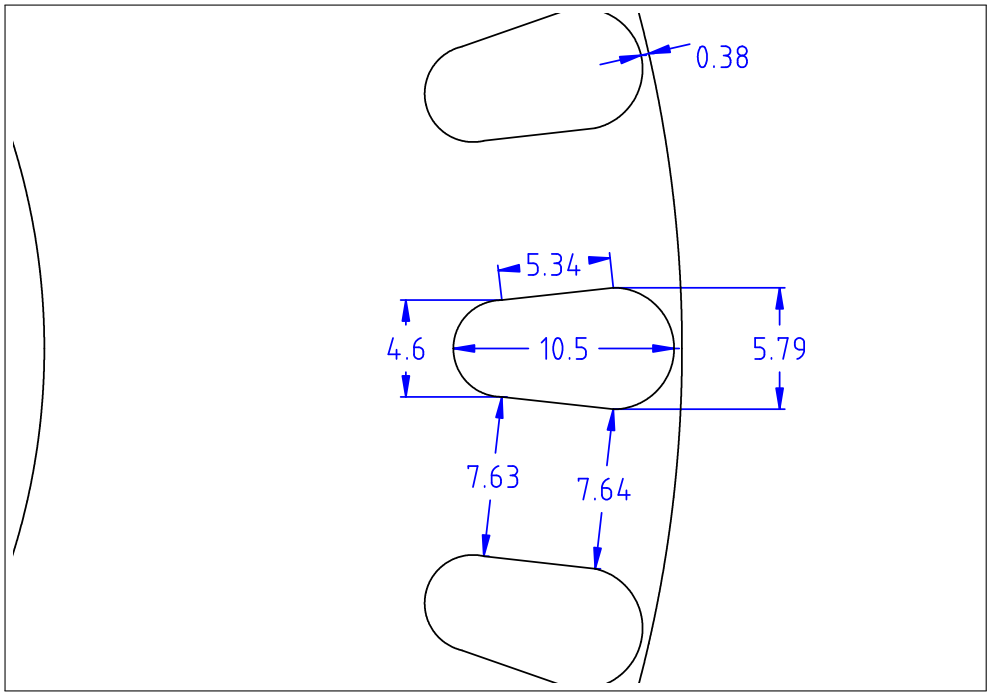

Figure A.6: Rotor slot dimensions of the 7.5 kW benchmark induction motor

A.5 5.5 kW industrial induction motor

Table A.13: Stator data of the 5.5 kW industrial induction motor

Description	Value	Unit
Poles	4	-
Output	5.5	kW
Voltage	400	V
Phases	3	-
Frequency	50	Hz
Winding connection	Delta	-
Temperature	75	°C
Lamination material	Newcor 660-50	-
Number of slots	36	-
Core length	130	mm
Bore diameter	127	mm
Core back depth	19.76	mm
Stacking factor	0.96	-

Table A.14: Stator winding data of the 5.5 kW industrial induction motor

Description		Value	Unit
Winding type		Whole coil concentric	-
Coils per slot		1	-
Tiers		2	-
Coils per group		3	-
Turns per coil		43	-
No of parallels		1	-
Step		1-8,10,12	-
Wires	Size 1	1/0.80	mm
	Size 2	1/0.85	mm
Wire material		Copper wire	-
Slot fill (%)		41.20 (true wire area only)	-
Mean turn length		584	mm

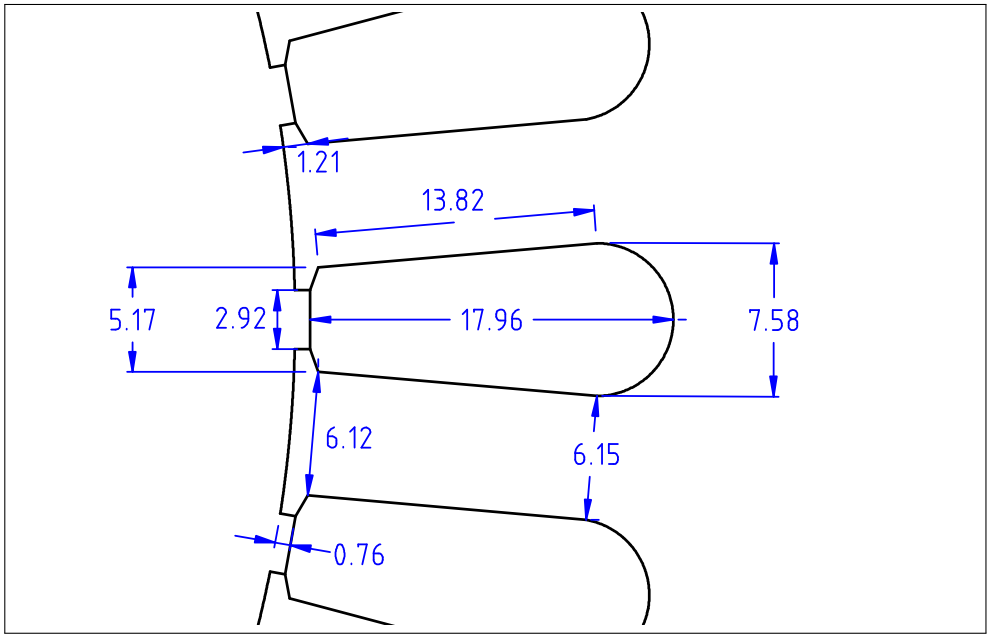

Figure A.7: Stator slot dimensions of the 5.5 kW industrial induction motor

Table A.15: Rotor data of the 5.5 kW industrial induction motor

Description	Value	Unit
Lamination material	Newcor 660-50 unannealed	-
Number of slots	28	-
Core length	130	mm
Core back depth	19.46	mm
Stacking factor	0.97	-
Airgap	0.45	mm
Skew	1.15	Rotor bars
Conductor material	Aluminium	-
Shaft material	Carbon steel	-
Temperature	75	°C

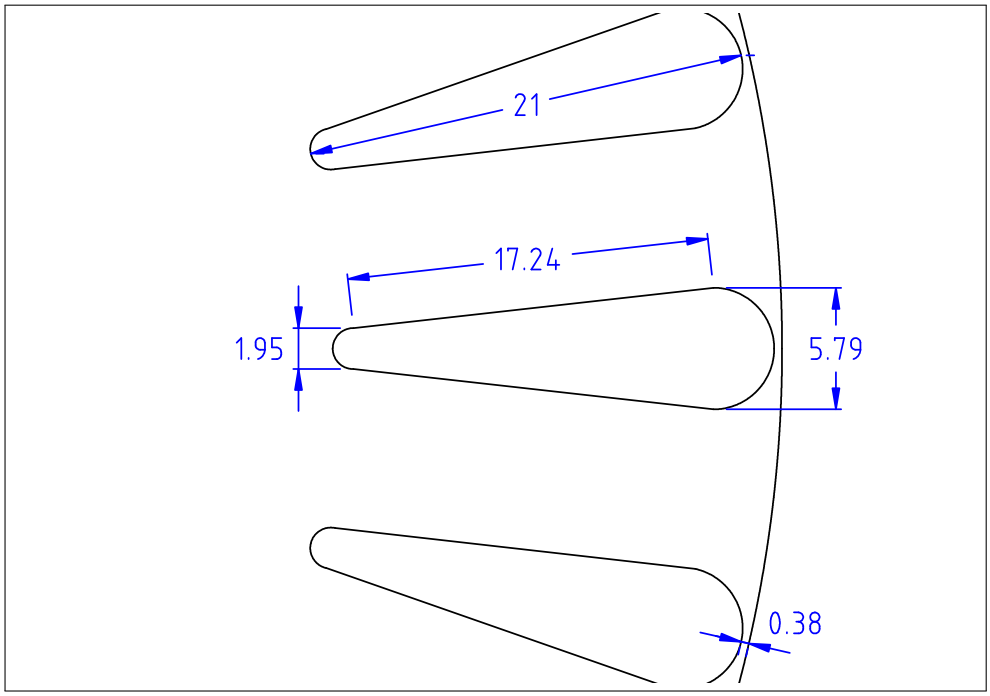

Figure A.8: Rotor slot dimensions of the 5.5 kW industrial induction motor

Table A.16: Performance data of the 5.5 kW industrial induction motor (Data provided by the manufacturer)

Slip (P.U.)	**Output (kW)**	**Current (A)**	**Input (kW)**	**Speed (RPM)**	**Torque (Nm)**	**Effy (%)**	**Power factor**
0.0002	0.000	4.547	0.234	1499.7	0.0	0.00	0.074
0.0070	1.376	5.130	1.638	1489.5	8.82	84.00	0.461
0.0142	2.748	6.554	3.103	1478.7	17.7	88.56	0.683
0.0221	4.120	8.476	4.637	1466.9	26.8	88.86	0.790
0.0307	5.494	10.73	6.253	1454.0	36.1	87.85	0.841
0.0404	6.866	13.28	7.966	1439.4	45.5	86.18	0.866
1.0000	0.000	64.62	25.52	0.0	77.4	0.00	0.570

Table A.17: Equivalent circuit data of the 5.5 kW industrial induction motor (Data provided by the manufacturer)

	Reference	**Cold**
R_1	3.00@75°C	2.46@20°C

	No load	**Full load**	**Locked rotor**
X_1	2.40	2.40	2.40
R'_2@75°C	2.19	2.19	3.38
X'_2	41.9	11.0	6.30
R_M	3833	3344	5595
X_M	149	150	123

Table A.18: Lamination properties of the 5.5 kW industrial induction motor

B (T)	**H (A/m)**
0	0
0.099817	0.556872933
0.199615	0.751059173
0.299635	0.888865763
0.399138	0.991168712
0.499445	1.101472041
0.599185	1.209399069
0.699795	1.323852065
0.798947	1.477463379
0.898636	1.66488954
0.999416	1.932309447
1.098478	2.317325449
1.199293	2.971342208
1.299129	4.226823163
1.399837	7.155140631
1.496727	14.85788599
1.59605	33.82468615
1.697686	69.80280841
1.747747	94.16087059
1.808	125.6637061
1.948	251.3274123
2.014	376.9911184
2.086	628.3185307
2.186	1256.637061
2.331	2513.274123
2.464	3769.911184

A.6 5.5 kW benchmark induction motor

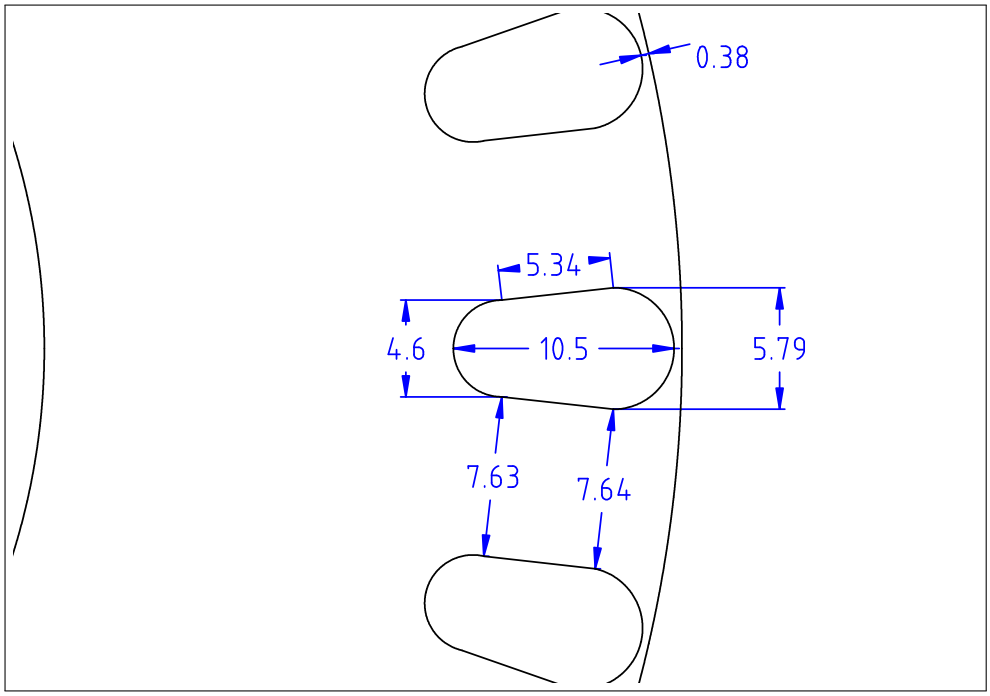

Figure A.9: Rotor slot dimensions of the 5.5 kW benchmark induction motor

APPENDIX

B

ANALYTICAL EXPRESSIONS FOR THE DESIGN OF INDUCTION MOTORS

This appendix includes some additional equations employed to obtain the initial design dimensions or parameters.

B.1 Rotor dimensions

Equations for the calculation of the rotor tooth width (t_{wr}) and the rotor core-back depth (y_{dr}) [1].

$$\hat{B}_{tr} = \frac{\hat{B}_g D}{p t_{wr}} \sin\left(\frac{p\pi}{N_r}\right) \tag{B.1}$$

where

$\hat{B}_{tr}$ is the peak rotor tooth flux density (T)

N_r is the number of rotor slots

$$\hat{B}_{cr} = \frac{\hat{B}_g D}{2 p y_{dr}} \tag{B.2}$$

where

$\hat{B}_{cr}$ is the peak rotor core flux density (T)

B.2 End-winding inductance

The end winding inductance can be calculated by [2]:

$$L_{ew} = 8\frac{k_{d1}^2 k_{p1}^2 N_p^2 h}{P}\left(L_{ew1} + L_{ew2} + L_{ew3} + L_{ew4}\right) \tag{B.3}$$

where

L_{ew} is the end winding inductance (H)

k_{d1} is the distribution factor

k_{p1} is the pitch factor

$N_p h$ is the total number of series connected turns per phase

P is the number of poles

The remaining coefficients:

$$L_{ew1} = \mu_0 \left(\frac{l_{ew} - p_w \tau_p}{2\pi}\right) \ln\left(\frac{p_w \tau_{p1}}{\Delta R}\right) \tag{B.4}$$

where

l_{ew} is the total perimeter of the end winding on one side (m)

p_w is the winding pitch

τ_p is the pole pitch (m)

ΔR is the radius of an equivalent circle of the same cross sectional area as the coil

$\Delta R = \sqrt{\frac{A_c}{\pi}}$

A_c is the coil cross sectional area

$$L_{ew2} = 0 \tag{B.5}$$

L_{ew} is zero when the end-winding shape is close to a rectangle [2].

$$L_{ew3} = \frac{\mu_0}{\pi}\left(\frac{p_w \tau_p}{2}\right)\left[\ln\left(\frac{l_{e2}}{2\Delta R}\right)\right] \tag{B.6}$$

where

l_{e2} is the straight portion of the end winding (m)

$$L_{ew4} = \frac{\mu_0}{8\pi} l_{ew} \tag{B.7}$$

B.3 End-ring parameters

The end-ring resistance [3]:

$$R_i = \rho \frac{L_i}{A_i} \tag{B.8}$$

where

R_i is the end-ring segment resistance (Ω)
ρ is the end-ring material resistivity (Ωm)
L_i is the end-ring segment length (m)
A_i is the end-ring cross-section (m^2)

$$L_i = \pi \frac{D_i}{N_r} \tag{B.9}$$

where

D_i is the stator bore

The end-ring inductance [3]:

$$L_{ei} = \mu_0 L_i \lambda_{ei} \tag{B.10}$$

where

L_{ei} is the inductance of a end-ring segment (H)
μ_0 is the magnetic permeability of free space ($4\pi \times 10^{-7} N/A^{-2}$)
λ_{ei} is the geometrical permeance of end ring segment

When the end-ring is attached to the rotor [3]:

$$\lambda_{ei} = \frac{2.3 D_{ir}}{4 N_r L_e \sin^2\left(\frac{\pi P}{N_r}\right)} \log \frac{4.7 D_i}{a + 2b} \tag{B.11}$$

where

D_{ir} is the average end-ring diameter (m)
L_e is the stack length (m)
P is the pole number
a is the end-ring radial thickness (m)
b is the end-ring axial width (m)

When the end-ring is distanced from the rotor [3]:

$$\lambda_{ei} = \frac{2.3 D_{ir}}{4 N_r L_e \sin^2\left(\frac{\pi P}{N_r}\right)} \log \frac{4.7 D_i}{2(a+b)} \tag{B.12}$$

B.4 Iron Losses

B.4.1 Flux 2D

Flux 2D makes use of the theory of Bertotti for computing the magnetic losses as a function of the frequency and of the peak value of the magnetic flux density [4, 5].

$$d_{P_{TOT}} = k_h B_m^2 f + \frac{\pi^2 \sigma d_t^2}{6} (B_m f)^2 + 8.67 k_e (B_m f)^{3/2} \tag{B.13}$$

where

$d_{P_{TOT}}$ is the core loss density (W/m^3)
k_h is the coefficient of hysteresis loss $(W.s/T^2/m^3)$
B_m is the maximum flux density at the node concerned (T)
f is the the frequency
σ is the electrical steel conductivity $(\Omega m)^{-1}$
d_t is the lamination sheet thickness (m)
k_e is the coefficient of excess loss $(W/(Ts^{-1})^{3/2}/m^3)$

B.5 Recommended slot combinations

Table B.1: Recommended slot combinations [2, 6]

Pole number	Stator/Rotor slot combination							
2	18/23 54/46	36/22 60/52	36/24	36/28	36/32	42/32	48/38	54/34
4	24/17 60/76	24/33 72/58	48/40	48/56	48/60	60/42	60/44	60/52
6	36/40 72/58	36/44 72/88	48/44 72/84	54/38	54/42	54/66	72/54	72/56
8	54/70	72/52	72/58	72/60	72/88			
10	72/88	72/92						
12	72/92							

B.6 References

[1] A C Smith. *Design of Electrical Machines, Lecture notes*. 2012.

[2] T.A. Lipo. *Introduction to AC Machine Design*. Wisconsin Power Electronics Research Center, University of Wisconsin, 2004.

[3] I. Boldea and S.A. Nasar. *The Induction Machine Handbook*. Electric Power Engineering Series. Taylor & Francis, 2001.

[4] Cedrat. *Induction Machine Tutorial*. Magsoft corporation, 2006.

[5] Cedrat. *User Guide Flux*. 2012.

[6] E.S. Hamdi. *Design of small electrical machines*. Design and measurement in electronic engineering. Wiley, 1994.

APPENDIX

C

SCRIPT EXAMPLES

This appendix shows the model of the 7.5 industrial induction motor using the programming languages for Flux 2D (PyFlux) and Opera 2D.

C.1 Model of the 7.5 kW industrial induction motor in Flux 2D

C.1.1 Main file

Listing C.1: Main file

```
1  #! Flux2D 11.1
2
3  #Script for the HIGH TORQUE DENSITY INDUCTION MOTOR PROJECT
4
5  ##SS=STANDARD STATOR
6
7  stator='SS'
8
9  #CR=CAGE ROTOR
10
11 rotor='CR'
12
13 #Calling the PARAMETERS files
14
15 executeBatchSpy(stator+'para.py')
16
17 executeBatchSpy(rotor+'para.py')
18
19 #Calling the GEOMETRY files
20
21 executeBatchSpy(rotor+'geom.py')
22
23 executeBatchSpy(stator+'geom.py')
24
25 #Calling the MESH files
26
27 executeBatchSpy(stator+'mesh.py')
28
29 executeBatchSpy(rotor+'mesh.py')
30
31 #Calling the PHYSICS files
32
33 executeBatchSpy(stator+'phys.py')
34
35 executeBatchSpy(rotor+'phys.py')
36
37 #Calling the CIRCUIT files
38
```

```
executeBatchSpy(rotor+'pt1.py')

executeBatchSpy(stator+'circ.py')

executeBatchSpy(rotor+'circ.py')

#Calling the REGION files

executeBatchSpy(stator+'regi.py')

executeBatchSpy(rotor+'regi.py')
```

C.1.2 Parameters files

Listing C.2: Stator parameters file

```
#! Flux2D 11.1

newProject()

import math

##STATOR PARAMETERS

ParameterGeom(name='SF_:_STATOR_FREQUENCY',
              expression='50')

ParameterGeom(name='SDD_:_STATOR_DOMAIN_DEPTH',
              expression='160')

ParameterGeom(name='SFF_:_STATOR_FILL_FACTOR',
              expression='0.4220')

ParameterGeom(name='STN_:_STATOR_TURNS_NUMBER',
              expression='204')

ParameterGeom(name='SID_:_STATOR_INNER_DIAMETER',
              expression='127')

ParameterGeom(name='SS_:_STATOR_SLOTS',
              expression='36')

ParameterGeom(name='SCPS_:_STATOR_COIL_PITCH_SLOTS',
              expression='7')

ParameterGeom(name='SSO_:_STATOR_SLOT_OPENING',
              expression='2.92')

ParameterGeom(name='STTD_:_STATOR_TOOTH_TIP_DEPTH',
              expression='0.762')

ParameterGeom(name='STD_:_STATOR_TOP_DEPTH',
              expression='0.409')

ParameterGeom(name='STW_:_STATOR_TOP_WIDTH',
              expression='5.169')

ParameterGeom(name='SBW_:_STATOR_BOTTOM_WIDTH',
              expression='7.552')

ParameterGeom(name='SSD_:_STATOR_SLOT_DEPTH',
              expression='17.96')

ParameterGeom(name='SCB_:_STATOR_CORE_BACK',
              expression='19.76')

ParameterGeom(name='SPN_:_STATOR_POLES_NUMBER',
              expression='4')

ParameterGeom(name='SP_:_STATOR_PHASES',
              expression='3')

ParameterGeom(name='AIRGAP_:_AIRGAP',
              expression='0.45')

ParameterGeom(name='INF_:_INFINITE',
              expression='20')

##CIRCUIT PARAMETERS

ParameterGeom(name='CPV_:_VOLTAGE',
              expression='400')

ParameterGeom(name='CPWR_:_WINDING_RESISTANCE',
              expression='2.02')

ParameterGeom(name='CPWL_:_WINDING_LEAKAGE',
              expression='0.00275')

ParameterGeom(name='SCT_:_STATOR_CONDUCTOR_TEMPERATURE',
              expression='75')

```

```
##STATOR AUXILIAR PARAMETERS

ParameterGeom(name='ZSY0 : STATOR AUXILIAR PARAMETER Y0',
              expression='SSO/2')

ParameterGeom(name='ZSX0 : STATOR AUXILIAR PARAMETER X0',
              expression='SQRT((SID/2)^2-ZSY0^2)')

ParameterGeom(name='ZSY1 : STATOR AUXILIAR PARAMETER Y1',
              expression='ZSY0')

ParameterGeom(name='ZSX1 : STATOR AUXILIAR PARAMETER X1',
              expression='ZSX0+STTD')

ParameterGeom(name='ZSX2 : STATOR AUXILIAR PARAMETER X2',
              expression='ZSX1+STD')

ParameterGeom(name='ZSY2 : STATOR AUXILIAR PARAMETER Y2',
              expression='STW/2')

ParameterGeom(name='ZSX3 : STATOR AUXILIAR PARAMETER X3',
              expression='ZSX1+SSD-SBW/2')

ParameterGeom(name='ZSY3 : STATOR AUXILIAR PARAMETER Y3',
              expression='SBW/2')
```

Listing C.3: Rotor parameters file

```
#! Flux2D 11.1

#CAGE ROTOR PARAMETERS

##ROTOR PARAMETERS

ParameterGeom(name='RS : ROTOR SLOTS',
              expression='28')

ParameterGeom(name='RTBW : ROTOR TOP BAR WITH',
              expression='5.786')

ParameterGeom(name='RTBD : ROTOR TOP BAR DEPTH',
              expression='2.893')

ParameterGeom(name='RTB : ROTOR TOP BRIDGE',
              expression='0.377')

ParameterGeom(name='RSD : ROTOR SLOT DEPTH',
              expression='10.5')

ParameterGeom(name='RBBW : ROTOR BOTTOM BAR WIDTH',
              expression='4.6')

ParameterGeom(name='RBBD : ROTOR BOTTOM BAR DEPTH',
              expression='2.3')

ParameterGeom(name='RCB : ROTOR CORE BACK',
              expression='19.46')

ParameterGeom(name='SKA : SKEW ANGLE',
              expression='19.28')

VariationParameterPilot(name='SLIP : SLIP',
                        referenceValue=1.0E-4)

##ROTOR CIRCUIT PARAMETERS

ParameterGeom(name='CPERR : ENDRING RESISTANCE',
              expression='2E-6')

ParameterGeom(name='CPERL : ENDRING INDUCTANCE',
              expression='7.4e-8')

ParameterGeom(name='RCT : ROTOR CONDUCTOR TEMPERATURE',
              expression='75')

##ROTOR AUXILIAR PARAMETERS

ParameterGeom(name='ZRY1 : ROTOR AUXILIAR PARAMETER Y1',
              expression='RTBW/2')

ParameterGeom(name='ZRX1 : ROTOR AUXILIAR PARAMETER X1',
              expression='SID/2-AIRGAP-RTB-RTBD')

ParameterGeom(name='ZRX2 : ZRX2',
              expression='SID/2-AIRGAP-RTB-RSD+RBBD')

ParameterGeom(name='ZRY2 : ZRY2',
              expression='RBBW/2')

ParameterGeom(name='ZRBC : ZR BOTTOM C',
              expression='SQRT(RBBW^2/4+RBBD^2)')

ParameterGeom(name='ZRBS : ZR BOTTOM SEMIPERIMETER',
              expression='(RBBW+2*ZRBC)/2')

ParameterGeom(name='ZRBR : ZR BOTTOM RADIUS',
              expression='(RBBW*ZRBC^2)/(4*SQRT(ZRBS*(ZRBS-RBBW)*(ZRBS-ZRBC)^2))')

ParameterGeom(name='ZRTC : ZR TOP C',
```

```
72                  expression='SQRT(RTBW^2/4+RTBD^2)')
73
74  ParameterGeom(name='ZRTS : ZR_TOP_SEMIPERIMETER',
75                  expression='(RTBW+2*ZRTC)/2')
76
77  ParameterGeom(name='ZRTR : ZR_TOP_RADIUS',
78                  expression='(RTBW*ZRTC^2)/(4*SQRT(ZRTS*(ZRTS-RTBW)*(ZRTS-ZRTC)^2))')
```

C.1.3 Geometry files

Listing C.4: Stator geometry file

```
1   #! Flux2D 11.1
2
3   #STATOR COORDINATE SYSTEMS
4
5   CoordSysCartesian(name='STATOR : GLOBAL_STATOR_COORDINATE_SYSTEM',
6                     parentCoordSys=GlobalUnits(lengthUnit=LengthUnit['MILLIMETER'],
7                                                angleUnit=AngleUnit['DEGREE']),
8                     origin=['0',
9                             '0'],
10                    rotationAngles=RotationAngles(angleZ='0'))
11
12  CoordSysCartesian(name='STATOR1 : AUXILIAR_STATOR_COORDINATE_SYSTEM_1',
13                    parentCoordSys=Local(coordSys=CoordSys['STATOR']),
14                    origin=['0',
15                            '0'],
16                    rotationAngles=RotationAngles(angleZ='180/SS'))
17
18  #STATOR TRANSFORMATIONS
19
20  TransfRotation3AnglesPivotCoord(name='TRANSF_STATOR : TRANSFORMATION_TO_CREATE_STATOR_SLOTS',
21                                  coordSys=CoordSys['STATOR'],
22                                  pivotCoord=['0',
23                                              '0'],
24                                  rotationAngles=RotationAngles(angleZ='360/SS'))
25
26  #DRAWING
27
28  ##DRAWING STATOR COILS
29
30  for i in range(0,4):
31
32          PointCoordinates(color=Color['White'],
33                           visibility=Visibility['VISIBLE'],
34                           coordSys=CoordSys['STATOR1'],
35                           uvw=['ZSX'+str(i),
36                                '-ZSY'+str(i)],
37                           nature=Nature['STANDARD'])
38
39  for i in range(0,4):
40
41          PointCoordinates(color=Color['White'],
42                           visibility=Visibility['VISIBLE'],
43                           coordSys=CoordSys['STATOR1'],
44                           uvw=['ZSX'+str(3-i),
45                                'ZSY'+str(3-i)],
46                           nature=Nature['STANDARD'])
47
48  for i in range(1,4):
49
50          LineSegment(color=Color['White'],
51                      visibility=Visibility['VISIBLE'],
52                      defPoint=[Point[AUXP3+i],
53                                Point[AUXP3+i+1]],
54                      nature=Nature['STANDARD'])
55
56  LineArcRadius(color=Color['White'],
57                visibility=Visibility['VISIBLE'],
58                coordSys=CoordSys['STATOR1'],
59                radius='SBW/2',
60                defPoint=[Point[AUXP3+4],
61                          Point[AUXP3+5]],
62                nature=Nature['STANDARD'])
63
64  for i in range(1,4):
65
66          LineSegment(color=Color['White'],
67                      visibility=Visibility['VISIBLE'],
68                      defPoint=[Point[AUXP3+i+4],
69                                Point[AUXP3+i+5]],
70                      nature=Nature['STANDARD'])
71
72  LineSegment(color=Color['White'],
73              visibility=Visibility['VISIBLE'],
74              defPoint=[Point[AUXP3+2],
75                        Point[AUXP3+7]],
76              nature=Nature['STANDARD'])
77
78  AUXS=int(ParameterGeom['SS'].expression)
79  AUXSCL=8
80  AUXSCP=8
```

```
AUXSCF=1

for i in range(1,AUXS):

        for k in range(1,AUXSCL+1):

                LineSegment[AUXL3+AUXSCL*(i-1)+k].propagate(transformation=Transf['TRANSF_STATOR'],
                        repetitionNumber=1)

AUXP4=AUXP3+AUXSCP*AUXS
AUXL4=AUXL3+AUXSCL*AUXS
AUXF4=AUXF3+AUXSCF*AUXS

buildFaces()

##DRAWING AIRGAP

for i in range(1,AUXS+1):

        LineArcPivotCoord(color=Color['White'],
                          visibility=Visibility['VISIBLE'],
                          coordSys=CoordSys['STATOR'],
                          pivotCoord=['0',
                                      '0'],
                          defPoint=[Point[AUXP3+AUXSCP*(i-1)+1],
                                    Point[AUXP3+AUXSCP*i]],
                          nature=Nature['STANDARD'])

for i in range(1,AUXS+1):

        LineArcPivotCoord(color=Color['White'],
                          visibility=Visibility['VISIBLE'],
                          coordSys=CoordSys['STATOR'],
                          pivotCoord=['0',
                                      '0'],
                          defPoint=[Point[AUXP3+AUXSCP*i],
                                    Point[AUXP3+AUXSCP*i%(AUXSCP*AUXS)+1]],
                          nature=Nature['STANDARD'])

AUXL5=AUXL4+2*AUXS
AUXP5=AUXP4
AUXF5=AUXF4+AUXS+1

buildFaces()

##DRAWING STATOR CORE

PointCoordinates(color=Color['White'],
                 visibility=Visibility['VISIBLE'],
                 coordSys=CoordSys['STATOR'],
                 uvw=['ZSX3+SBW/2+SCB',
                      '0'],
                 nature=Nature['STANDARD'])

PointCoordinates(color=Color['White'],
                 visibility=Visibility['VISIBLE'],
                 coordSys=CoordSys['STATOR'],
                 uvw=['-(ZSX3+SBW/2+SCB)',
                      '0'],
                 nature=Nature['STANDARD'])

LineArcPivotCoord(color=Color['White'],
                  visibility=Visibility['VISIBLE'],
                  coordSys=CoordSys['STATOR'],
                  pivotCoord=['0',
                              '0'],
                  defPoint=[Point[AUXP5+1],
                            Point[AUXP5+2]],
                  nature=Nature['STANDARD'])

LineArcPivotCoord(color=Color['White'],
                  visibility=Visibility['VISIBLE'],
                  coordSys=CoordSys['STATOR'],
                  pivotCoord=['0',
                              '0'],
                  defPoint=[Point[AUXP5+2],
                            Point[AUXP5+1]],
                  nature=Nature['STANDARD'])

AUXL6=AUXL5+2
AUXP6=AUXP5+2
AUXF6=AUXF5+1

buildFaces()

##DRAWING INFINITE REGION

PointCoordinates(color=Color['White'],
                 visibility=Visibility['VISIBLE'],
                 coordSys=CoordSys['STATOR'],
                 uvw=['ZSX3+SBW/2+SCB+INF',
                      '0'],
                 nature=Nature['STANDARD'])

PointCoordinates(color=Color['White'],
                 visibility=Visibility['VISIBLE'],
                 coordSys=CoordSys['STATOR'],
                 uvw=['-(ZSX3+SBW/2+SCB+INF)',
                      '0'],
                 nature=Nature['STANDARD'])

LineArcPivotCoord(color=Color['White'],
                  visibility=Visibility['VISIBLE'],
```

```
                    coordSys=CoordSys['STATOR'],
                    pivotCoord=['0',
                                '0'],
                    defPoint=[Point[AUXP6+1],
                              Point[AUXP6+2]],
                    nature=Nature['STANDARD'])

LineArcPivotCoord(color=Color['White'],
                    visibility=Visibility['VISIBLE'],
                    coordSys=CoordSys['STATOR'],
                    pivotCoord=['0',
                                '0'],
                    defPoint=[Point[AUXP6+2],
                              Point[AUXP6+1]],
                    nature=Nature['STANDARD'])

buildFaces()
```

Listing C.5: Rotor geometry file

```
#! Flux2D 11.1

#COORDINATE SYSTEMS

CoordSysCartesian(name='ROTOR : GLOBAL ROTOR COORDINATE SYSTEM',
                    parentCoordSys=GlobalUnits(lengthUnit=LengthUnit['MILLIMETER'],
                                               angleUnit=AngleUnit['DEGREE']),
                    origin=['0',
                            '0'],
                    rotationAngles=RotationAngles(angleZ='0'))

CoordSysCartesian(name='ROTOR1 : AUXILIAR ROTOR COORDINATE SYSTEM 1',
                    parentCoordSys=Local(coordSys=CoordSys['ROTOR']),
                    origin=['0',
                            '0'],
                    rotationAngles=RotationAngles(angleZ='180/RS'))

#PERIODICITY

#TRANSFORMATIONS

TransfRotation3AnglesPivotCoord(name='TRANSF_ROTOR : TRANSFORMATION TO CREATE ROTOR SLOTS',
                                coordSys=CoordSys['ROTOR'],
                                pivotCoord=['0',
                                            '0'],
                                rotationAngles=RotationAngles(angleZ='360/RS'))

#DRAWING

##DRAWING ROTOR COILS

for i in range(1,3):

        PointCoordinates(color=Color['White'],
                         visibility=Visibility['VISIBLE'],
                         coordSys=CoordSys['ROTOR1'],
                         uvw=['ZRX'+str(i),
                              '-ZRY'+str(i)],
                         nature=Nature['STANDARD'])

for i in range(1,3):

        PointCoordinates(color=Color['White'],
                         visibility=Visibility['VISIBLE'],
                         coordSys=CoordSys['ROTOR1'],
                         uvw=['ZRX'+str(3-i),
                              'ZRY'+str(3-i)],
                         nature=Nature['STANDARD'])

LineSegment(color=Color['White'],
            visibility=Visibility['VISIBLE'],
            defPoint=[Point[1],
                      Point[2]],
            nature=Nature['STANDARD'])

LineArcRadius(color=Color['White'],
              visibility=Visibility['VISIBLE'],
              coordSys=CoordSys['ROTOR'],
              radius='ZRBR',
              defPoint=[Point[3],
                        Point[2]],
              nature=Nature['STANDARD'])

LineSegment(color=Color['White'],
            visibility=Visibility['VISIBLE'],
            defPoint=[Point[3],
                      Point[4]],
            nature=Nature['STANDARD'])

LineArcRadius(color=Color['White'],
              visibility=Visibility['VISIBLE'],
              coordSys=CoordSys['ROTOR'],
              radius='ZRTR',
              defPoint=[Point[1],
                        Point[4]],
              nature=Nature['STANDARD'])

AUXR=int(ParameterGeom['RS'].expression)
AUXRCL=4
```

```
AUXRCP=4
AUXRCF=1

for i in range(1,AUXR):

        for k in range(1,AUXRCL+1):

                LineSegment[AUXRCL*(i-1)+k].propagate(transformation=Transf['TRANSF_ROTOR'],
                        repetitionNumber=1)

AUXP1=AUXRCP*AUXR
AUXL1=AUXRCL*AUXR
AUXF1=AUXRCF*AUXR

buildFaces()

##DRAWING SHAFT

PointCoordinates(color=Color['White'],
                 visibility=Visibility['VISIBLE'],
                 coordSys=CoordSys['ROTOR'],
                 uvw=['ZRX2-RCB-RBBD',
                      '0'],
                 nature=Nature['STANDARD'])

PointCoordinates(color=Color['White'],
                 visibility=Visibility['VISIBLE'],
                 coordSys=CoordSys['ROTOR'],
                 uvw=['-(ZRX2-RCB-RBBD)',
                      '0'],
                 nature=Nature['STANDARD'])

LineArcPivotCoord(color=Color['White'],
                  visibility=Visibility['VISIBLE'],
                  coordSys=CoordSys['ROTOR'],
                  pivotCoord=['0',
                              '0'],
                  defPoint=[Point[AUXP1+1],
                            Point[AUXP1+2]],
                  nature=Nature['STANDARD'])

LineArcPivotCoord(color=Color['White'],
                  visibility=Visibility['VISIBLE'],
                  coordSys=CoordSys['ROTOR'],
                  pivotCoord=['0',
                              '0'],
                  defPoint=[Point[AUXP1+2],
                            Point[AUXP1+1]],
                  nature=Nature['STANDARD'])

AUXP2=AUXP1+2
AUXL2=AUXL1+2
AUXF2=AUXF1+1

buildFaces()

##DRAWING ROTOR CORE

PointCoordinates(color=Color['White'],
                 visibility=Visibility['VISIBLE'],
                 coordSys=CoordSys['ROTOR'],
                 uvw=['SID/2-AIRGAP',
                      '0'],
                 nature=Nature['STANDARD'])

PointCoordinates(color=Color['White'],
                 visibility=Visibility['VISIBLE'],
                 coordSys=CoordSys['ROTOR'],
                 uvw=['-(SID/2-AIRGAP)',
                      '0'],
                 nature=Nature['STANDARD'])

LineArcPivotCoord(color=Color['White'],
                  visibility=Visibility['VISIBLE'],
                  coordSys=CoordSys['ROTOR'],
                  pivotCoord=['0',
                              '0'],
                  defPoint=[Point[AUXP2+1],
                            Point[AUXP2+2]],
                  nature=Nature['STANDARD'])

LineArcPivotCoord(color=Color['White'],
                  visibility=Visibility['VISIBLE'],
                  coordSys=CoordSys['ROTOR'],
                  pivotCoord=['0',
                              '0'],
                  defPoint=[Point[AUXP2+2],
                            Point[AUXP2+1]],
                  nature=Nature['STANDARD'])

AUXP3=AUXP2+2
AUXL3=AUXL2+2
AUXF3=AUXF2+1

buildFaces()
```

C.1.4 Mesh files

Listing C.6: Stator mesh file

```
#! Flux2D 11.1

#MESH

##STATOR MESH LINES

MeshLineArithmetic(name='MLINF ': 'MESH LINE FOR INFINITE',
                   color=Color['White'],
                   number=12)

MeshLineArithmetic(name='MLSC ': 'MESH LINE FOR STATOR CORE',
                   color=Color['White'],
                   number=24)

MeshLineArithmetic(name='MLSSAB ': 'MESH LINE FOR STATOR SLOT AB',
                   color=Color['White'],
                   number=1)

MeshLineArithmetic(name='MLSSBC ': 'MESH LINE FOR STATOR SLOT BC',
                   color=Color['White'],
                   number=2)

MeshLineArithmetic(name='MLSSCD ': 'MESH LINE FOR STATOR SLOT CD',
                   color=Color['White'],
                   number=4)

MeshLineArithmetic(name='MLSSBB ': 'MESH LINE FOR STATOR SLOT BB',
                   color=Color['White'],
                   number=3)

MeshLineArithmetic(name='MLSSDD ': 'MESH LINE FOR STATOR SLOT DD',
                   color=Color['White'],
                   number=4)

MeshLineArithmetic(name='MLSSAA ': 'MESH LINE FOR STATOR SLOT AA',
                   color=Color['White'],
                   number=3)

MeshLineArithmetic(name='MLSSAAA ': 'MESH LINE FOR STATOR SLOT AAA',
                   color=Color['White'],
                   number=10)

##ASSIGN MESH LINES

###STATOR SLOT MESH LINES

for i in range(1,AUXS+1):

        LineSegment[AUXL3+AUXSCL*(i-1)+1].assignMeshLine(meshLine=MeshLine['MLSSAB'])
        LineSegment[AUXL3+AUXSCL*(i-1)+2].assignMeshLine(meshLine=MeshLine['MLSSBC'])
        LineSegment[AUXL3+AUXSCL*(i-1)+3].assignMeshLine(meshLine=MeshLine['MLSSCD'])
        LineSegment[AUXL3+AUXSCL*(i-1)+4].assignMeshLine(meshLine=MeshLine['MLSSDD'])
        LineSegment[AUXL3+AUXSCL*(i-1)+5].assignMeshLine(meshLine=MeshLine['MLSSCD'])
        LineSegment[AUXL3+AUXSCL*(i-1)+6].assignMeshLine(meshLine=MeshLine['MLSSBC'])
        LineSegment[AUXL3+AUXSCL*(i-1)+7].assignMeshLine(meshLine=MeshLine['MLSSAB'])
        LineSegment[AUXL3+AUXSCL*(i-1)+8].assignMeshLine(meshLine=MeshLine['MLSSBB'])
        LineSegment[AUXL4+i].assignMeshLine(meshLine=MeshLine['MLSSAA'])
        LineSegment[AUXL4+AUXS+i].assignMeshLine(meshLine=MeshLine['MLSSAAA'])

###STATOR CORE MESH LINES

LineSegment[AUXL5+1,AUXL5+2].assignMeshLine(meshLine=MeshLine['MLSC'])

###INFINITE MESH LINES

LineSegment[AUXL6+1,AUXL6+2].assignMeshLine(meshLine=MeshLine['MLINF'])
```

Listing C.7: Rotor mesh file

```
#! Flux2D 11.1

#MESH

##ROTOR MESH LINES

MeshLineArithmetic(name='MLRSAB ': 'MESH LINE FOR ROTOR SLOT AB',
                   color=Color['White'],
                   number=4)

MeshLineArithmetic(name='MLRSBB ': 'MESH LINE FOR ROTOR SLOT BB',
                   color=Color['White'],
                   number=3)

MeshLineArithmetic(name='MLRSAA ': 'MESH LINE FOR ROTOR SLOT AA',
                   color=Color['White'],
                   number=12)

MeshLineArithmetic(name='MLS ': 'MESH LINE FOR SHAFT',
                   color=Color['White'],
```

```
                        number=8)

MeshLineArithmetic(name='MLRC_:_MESH_LINE_FOR_ROTOR_CORE',
                        color=Color['White'],
                        number=240)

##ASSIGN MESH LINES

####ROTOR COIL MESH LINES

for i in range(1,AUXR+1):

        LineSegment[AUXRCL*(i-1)+1].assignMeshLine(meshLine=MeshLine['MLRSAB'])
        LineSegment[AUXRCL*(i-1)+2].assignMeshLine(meshLine=MeshLine['MLRSBB'])
        LineSegment[AUXRCL*(i-1)+3].assignMeshLine(meshLine=MeshLine['MLRSAB'])
        LineSegment[AUXRCL*(i-1)+4].assignMeshLine(meshLine=MeshLine['MLRSAA'])

###SHAFT MESH LINES

LineSegment[AUXL1+1,AUXL1+2].assignMeshLine(meshLine=MeshLine['MLS'])

###ROTOR CORE MESH LINES

LineSegment[AUXL2+1,AUXL2+2].assignMeshLine(meshLine=MeshLine['MLRC'])

GeomMeshOptions[1].automaticMesh=AutomaticMeshInactivated()

meshDomain()
```

C.1.5 Physics files

Listing C.8: Stator physics file

```
#! Flux2D 11.1

##PHYSICS

##DEFINING APPLICATION

ApplicationMagneticAC2D(frequency='SF',
                        domain2D=Domain2DPlane(lengthUnit=LengthUnit['MILLIMETER'],
                                               depth='SDD'),
                        coilCoefficient=CoilCoefficientAutomatic())

##MATERIALS

Material(name='SCM_:_STATOR_CONDUCTOR_MATERIAL',
        propertyBH=PropertyBhLinear(mur='1'),
        propertyJE=PropertyJeTLinearFunction(slope='0.00427',
                                             rhoConstant='0.1564E-07',
                                             referenceTemperature=Temperature(temperature='0',
                                                                              unit=Unit['CELSIUS_DEGREE']),
                                             temperature=Temperature(temperature='SCT',
                                                                     unit=Unit['CELSIUS_DEGREE'])),
        thermalConductivity=KtIsotropic(k='394'),
        specificHeat=RhoCpConstant(rhoCp='3518000'))

Material(name='SIM_:_STATOR_IRON_MATERIAL',
        propertyBH=PropertyBhNonlinearSpline(splinePoints=[BHPoint(h=0.0,
                                                                   b=0.0),
                                                           BHPoint(h=44.31454,
                                                                   b=0.099817),
                                                           BHPoint(h=59.76739,
                                                                   b=0.199615),
                                                           BHPoint(h=70.73369,
                                                                   b=0.299635),
                                                           BHPoint(h=78.8747,
                                                                   b=0.399138),
                                                           BHPoint(h=87.65236,
                                                                   b=0.499445),
                                                           BHPoint(h=96.24092,
                                                                   b=0.599185),
                                                           BHPoint(h=105.3488,
                                                                   b=0.699795),
                                                           BHPoint(h=117.5728,
                                                                   b=0.798947),
                                                           BHPoint(h=132.4877,
                                                                   b=0.898636),
                                                           BHPoint(h=153.7683,
                                                                   b=0.999416),
                                                           BHPoint(h=184.4069,
                                                                   b=1.098478),
                                                           BHPoint(h=236.4519,
                                                                   b=1.199293),
                                                           BHPoint(h=336.3599,
                                                                   b=1.299129),
                                                           BHPoint(h=569.388,
                                                                   b=1.399837),
                                                           BHPoint(h=1182.353,
                                                                   b=1.496727),
                                                           BHPoint(h=2691.683,
                                                                   b=1.59605),
```

```
                                                                BHPoint(h=5554.731,
                                                                        b=1.697686),
                                                                BHPoint(h=7493.084,
                                                                        b=1.747747),
                                                                BHPoint(h=10000.0,
                                                                        b=1.808),
                                                                BHPoint(h=20000.0,
                                                                        b=1.948),
                                                                BHPoint(h=30000.0,
                                                                        b=2.014),
                                                                BHPoint(h=50000.0,
                                                                        b=2.086),
                                                                BHPoint(h=100000.0,
                                                                        b=2.186),
                                                                BHPoint(h=200000.0,
                                                                        b=2.331),
                                                                BHPoint(h=300000.0,
                                                                        b=2.464)]))


Material(name='SWM_:_STATOR_WEDGE_MATERIAL',
        propertyBH=PropertyBhLinear(mur='1'))

Material(name='AM_:_AIRGAP_MATERIAL',
        propertyBH=PropertyBhLinear(mur='1'))

Material(name='IM_:_INF_MATERIAL',
        propertyBH=PropertyBhLinear(mur='1'))

##MECHANICAL SETS

MechanicalSetFixed(name='STATOR_:_MECHANICAL_SET_FOR_STATOR')
```

Listing C.9: Rotor physics file

```
#! Flux2D 11.1

##PHYSICS

##MATERIALS

Material(name='RCM_:_ROTOR_CONDUCTOR_MATERIAL',
        propertyBH=PropertyBhLinear(mur='1'),
        propertyJE=PropertyJeTLinearFunction(slope='0.00427',
                                             rhoConstant='0.1564E-07',
                                             referenceTemperature=Temperature(temperature='0',
                                                                              unit=Unit['CELSIUS_DEGREE']),
                                             temperature=Temperature(temperature='RCT',
                                                                     unit=Unit['CELSIUS_DEGREE'])),
        thermalConductivity=KtIsotropic(k='235'),
        specificHeat=RhoCpConstant(rhoCp='2530000'))

Material(name='RIM_:_ROTOR_IRON_MATERIAL',
        propertyBH=PropertyBhNonlinearSpline(splinePoints=[BHPoint(h=0.0,
                                                                   b=0.0),
                                                           BHPoint(h=44.31454,
                                                                   b=0.099817),
                                                           BHPoint(h=59.76739,
                                                                   b=0.199615),
                                                           BHPoint(h=70.73369,
                                                                   b=0.299635),
                                                           BHPoint(h=78.8747,
                                                                   b=0.399138),
                                                           BHPoint(h=87.65236,
                                                                   b=0.499445),
                                                           BHPoint(h=96.24092,
                                                                   b=0.599185),
                                                           BHPoint(h=105.3488,
                                                                   b=0.699795),
                                                           BHPoint(h=117.5728,
                                                                   b=0.798947),
                                                           BHPoint(h=132.4877,
                                                                   b=0.898636),
                                                           BHPoint(h=153.7683,
                                                                   b=0.999416),
                                                           BHPoint(h=184.4069,
                                                                   b=1.098478),
                                                           BHPoint(h=236.4519,
                                                                   b=1.199293),
                                                           BHPoint(h=336.3599,
                                                                   b=1.299129),
                                                           BHPoint(h=569.388,
                                                                   b=1.399837),
                                                           BHPoint(h=1182.353,
                                                                   b=1.496727),
                                                           BHPoint(h=2691.683,
                                                                   b=1.59605),
                                                           BHPoint(h=5554.731,
                                                                   b=1.697686),
                                                           BHPoint(h=7493.084,
                                                                   b=1.747747),
                                                           BHPoint(h=10000.0,
                                                                   b=1.808),
                                                           BHPoint(h=20000.0,
                                                                   b=1.948),
                                                           BHPoint(h=30000.0,
                                                                   b=2.014),
                                                           BHPoint(h=50000.0,
                                                                   b=2.086),
```

```
                                                                BHPoint(h=100000.0,
                                                                        b=2.186),
                                                                BHPoint(h=200000.0,
                                                                        b=2.331),
                                                                BHPoint(h=300000.0,
                                                                        b=2.464)]))

Material(name='RWM_:_ROTOR_WEDGE_MATERIAL',
         propertyBH=PropertyBhLinear(mur='1'))

Material(name='SM_:_SHAFT_MATERIAL',
         propertyBH=PropertyBhLinear(mur='1'))

##MECHANICAL SETS

MechanicalSetRotation1Axis(name='ROTOR_:_MECHANICAL_SET_FOR_ROTOR',
                           kinematics=RotatingMultiStatic(slip='SLIP'),
                           rotationAxis=RotationZAxis(coordSys=CoordSys['ROTOR'],
                                                      pivot=['0',
                                                             '0'])))
```

C.1.6 Circuit files

Listing C.10: Auxiliary circuit file

```
#! Flux2D 11.1

# Equipotential 1 :

##STATOR EQUIPOTENTIALS

Equipotential(name='PT1',
              potential=ElectricPotential(connexions=[Connexion(points=[ConnexionPoint(uvw=[100.0,
                                                                                            100.0]),
                                                                        ConnexionPoint(uvw=[100.0,
                                                                                            200.0])]),
                                                      Connexion(points=[ConnexionPoint(uvw=[100.0,
                                                                                            200.0]),
                                                                        ConnexionPoint(uvw=[100.0,
                                                                                            300.0])]),
                                                      Connexion(points=[ConnexionPoint(uvw=[100.0,
                                                                                            300.0]),
                                                                        ConnexionPoint(uvw=[100.0,
                                                                                            400.0])]),
                                                      Connexion(points=[ConnexionPoint(uvw=[100.0,
                                                                                            400.0]),
                                                                        ConnexionPoint(uvw=[100.0,
                                                                                            500.0])]),
                                                      Connexion(points=[ConnexionPoint(uvw=[100.0,
                                                                                            500.0]),
                                                                        ConnexionPoint(uvw=[100.0,
                                                                                            600.0])]),
                                                      Connexion(points=[ConnexionPoint(uvw=[100.0,
                                                                                            600.0]),
                                                                        ConnexionPoint(uvw=[100.0,
                                                                                            700.0])]),
                                                      Connexion(points=[ConnexionPoint(uvw=[100.0,
                                                                                            700.0]),
                                                                        ConnexionPoint(uvw=[100.0,
                                                                                            800.0])]),
                                                      Connexion(points=[ConnexionPoint(uvw=[100.0,
                                                                                            800.0]),
                                                                        ConnexionPoint(uvw=[100.0,
                                                                                            900.0])]),
                                                      Connexion(points=[ConnexionPoint(uvw=[100.0,
                                                                                            900.0]),
                                                                        ConnexionPoint(uvw=[100.0,
                                                                                            1000.0])]),
                                                      Connexion(points=[ConnexionPoint(uvw=[100.0,
                                                                                            1000.0]),
                                                                        ConnexionPoint(uvw=[100.0,
                                                                                            1100.0])]),
                                                      Connexion(points=[ConnexionPoint(uvw=[100.0,
                                                                                            1100.0]),
                                                                        ConnexionPoint(uvw=[100.0,
                                                                                            1200.0])]),

                                                      Connexion(points=[ConnexionPoint(uvw=[100.0,
                                                                                            1200.0]),
                                                                        ConnexionPoint(uvw=[100.0,
                                                                                            1250.0])]),
                                                      Connexion(points=[ConnexionPoint(uvw=[100.0,
                                                                                            1250.0]),
                                                                        ConnexionPoint(uvw=[260.0,
                                                                                            1250.0])]),
                                                      Connexion(points=[ConnexionPoint(uvw=[260.0,
                                                                                            1250.0]),
                                                                        ConnexionPoint(uvw=[260.0,
                                                                                            1200.0])]),
##BEGIN OF ROTOR PART
                                                      Connexion(points=[ConnexionPoint(uvw=[260.0,
                                                                                            1250.0]),
```

```
                                                                ConnexionPoint(uvw=[300.0,
                                                                                    1250.0])]),
##END OF ROTOR PART
                                                    Connexion(points=[ConnexionPoint(uvw=[260.0,
                                                                                          100.0]),
                                                                      ConnexionPoint(uvw=[260.0,
                                                                                          200.0])]),
                                                    Connexion(points=[ConnexionPoint(uvw=[260.0,
                                                                                          200.0]),
                                                                      ConnexionPoint(uvw=[260.0,
                                                                                          300.0])]),
                                                    Connexion(points=[ConnexionPoint(uvw=[260.0,
                                                                                          300.0]),
                                                                      ConnexionPoint(uvw=[260.0,
                                                                                          400.0])]),
                                                    Connexion(points=[ConnexionPoint(uvw=[260.0,
                                                                                          400.0]),
                                                                      ConnexionPoint(uvw=[260.0,
                                                                                          500.0])]),
                                                    Connexion(points=[ConnexionPoint(uvw=[260.0,
                                                                                          500.0]),
                                                                      ConnexionPoint(uvw=[260.0,
                                                                                          600.0])]),
                                                    Connexion(points=[ConnexionPoint(uvw=[260.0,
                                                                                          600.0]),
                                                                      ConnexionPoint(uvw=[260.0,
                                                                                          700.0])]),
                                                    Connexion(points=[ConnexionPoint(uvw=[260.0,
                                                                                          700.0]),
                                                                      ConnexionPoint(uvw=[260.0,
                                                                                          800.0])]),
                                                    Connexion(points=[ConnexionPoint(uvw=[260.0,
                                                                                          800.0]),
                                                                      ConnexionPoint(uvw=[260.0,
                                                                                          900.0])]),
                                                    Connexion(points=[ConnexionPoint(uvw=[260.0,
                                                                                          900.0]),
                                                                      ConnexionPoint(uvw=[260.0,
                                                                                          1000.0])]),
                                                    Connexion(points=[ConnexionPoint(uvw=[260.0,
                                                                                          1000.0]),
                                                                      ConnexionPoint(uvw=[260.0,
                                                                                          1100.0])]),
                                                    Connexion(points=[ConnexionPoint(uvw=[260.0,
                                                                                          1100.0]),
                                                                      ConnexionPoint(uvw=[260.0,
                                                                                          1200.0])])]))
```

Listing C.11: Stator circuit file

```
#! Flux2D 11.1

# STATOR CIRCUIT

##STATOR EQUIPOTENTIALS

AUXSP=int(ParameterGeom['SP'].expression)

for i in range(1,int(ParameterGeom['SP'].expression)+1):

        Equipotential(name='PT'+str(i+1),
                      potential=ElectricPotential(connexions=[Connexion(points=[ConnexionPoint(uvw=[140.0,
                                                                                                    100.0*i]),
                                                                                ConnexionPoint(uvw=[160.0,
                                                                                                    100.0*i])])]))

        Equipotential(name='PT'+str(i+int(ParameterGeom['SP'].expression)+1),
                      potential=ElectricPotential(connexions=[Connexion(points=[ConnexionPoint(uvw=[200.0,
                                                                                                    100.0*i]),
                                                                                ConnexionPoint(uvw=[220.0,
                                                                                                    100.0*i])])]))

##STATOR INDUCTORS

for i in range(1,int(ParameterGeom['SP'].expression)+1):

        Inductor(name='LL'+str(i),
                 inductance='CPWL',
                 terminals=[Equipotential['PT'+str(i+int(ParameterGeom['SP'].expression)+1)],
                            Equipotential['PT1']],
                 visibility=Visibility['VISIBLE'],
                 color=Color['Turquoise'],
                 graphicDescription=GraphicComponent(rotationAngle=0.0,
                                                     centerCoordinates=[float(240.0),
                                                                        float(100*i)],
                                                     connectionNumbers=[1,
                                                                        0,
                                                                        1,
                                                                        0]))

# VoltageSource objects :

        FormulaVoltageSource(name='V'+str(i),
                             terminals=[Equipotential['PT1'],
                                        Equipotential['PT'+str(i+1)]],
                             visibility=Visibility['VISIBLE'],
                             color=Color['Turquoise'],
                             rmsModulus='CPV',
                             phase=str(180-i*360/int(ParameterGeom['SP'].expression)),
```

```
                                graphicDescription=GraphicComponent(rotationAngle=0.0,
                                                                    centerCoordinates=[float(120.0),
                                                                                       float(100.0*i)],
                                                                    connectionNumbers=[1,
                                                                                       0,
                                                                                       1,
                                                                                       0]))

# CoilConductor objects :

        CircuitStrandedCoil(name='B'+str(i),
                            terminals=[Equipotential['PT'+str(i+1)],
                                       Equipotential['PT'+str(i+int(ParameterGeom['SP'].expression)+1)]],
                            resistanceFormula='CPWR',
                            graphicDescription=GraphicComponent(rotationAngle=0.0,
                                                                centerCoordinates=[float(180.0),
                                                                                   float(100.0*i)],
                                                                connectionNumbers=[1,
                                                                                   0,
                                                                                   1,
                                                                                   0]))

#GROUND

Ground(name='GROUND_1',
       terminal=Equipotential['PT1'],
       graphicDescription=GraphicComponent(rotationAngle=0.0,
                                           centerCoordinates=[100.0,
                                                              1260.0]))
```

Listing C.12: Rotor circuit file

```
#! Flux2D 11.1

#ROTOR CIRCUIT

# SquirrelCage objects :

SquirrelCage(name='SQUIRRELCAGE_1',
             barsNumber=int(ParameterGeom['RS'].expression),
             endRingResistance='CPERR*(1+SLIP)',
             endRingInductance='CPERL*(1-0.5555*SLIP)',
             terminal=Equipotential['PT1'],
             graphicDescription=GraphicComponent(rotationAngle=0.0,
                                                 centerCoordinates=[320.0,
                                                                    1250.0]))
```

C.1.7 Region files

Listing C.13: Stator region file

```
#! Flux2D 11.1

##REGION FACES

for i in range(1,int(ParameterGeom['SP'].expression)+1):

        RegionFace(name='PHASE'+str(i)+'P_:_PHASE'+str(i)+'_POSITIVE',
                   magneticAC2D=MagneticAC2DFaceCoilConductor(coilConductor=CoilConductor2DPositive(turnNumber='STN',
                                                                                                    seriesParallel=
                                                                                                        AllInSeries
                                                                                                        (),
                                                                                                    electricComponent=
                                                                                                        CoilConductor
                                                                                                        ['B'+str(i)
                                                                                                        ],
                                                                                                    fillFactor='SFF'),
                                                              material=Material['SCM']),
                   color=Color['Turquoise'],
                   visibility=Visibility['VISIBLE'],
                   mechanicalSet=MechanicalSet['STATOR'])

        RegionFace(name='PHASE'+str(i)+'N_:_PHASE'+str(i)+'_NEGATIVE',
                   magneticAC2D=MagneticAC2DFaceCoilConductor(coilConductor=CoilConductor2DNegative(turnNumber='STN',
                                                                                                    seriesParallel=
                                                                                                        AllInSeries
                                                                                                        (),
                                                                                                    electricComponent=
                                                                                                        CoilConductor
                                                                                                        ['B'+str(i)
                                                                                                        ],
                                                                                                    fillFactor='SFF'),
                                                              material=Material['SCM']),
                   color=Color['Turquoise'],
                   visibility=Visibility['VISIBLE'],
                   mechanicalSet=MechanicalSet['STATOR'])

```

```
RegionFace(name='AIRGAP : AIRGAP',
           magneticAC2D=MagneticAC2DFaceMagnetic(material=Material['AM']),
           color=Color['Turquoise'],
           visibility=Visibility['VISIBLE'],
           mechanicalSet=MechanicalSet['STATOR'])

RegionFace(name='SCORE : STATOR_CORE',
           magneticAC2D=MagneticAC2DFaceMagnetic(material=Material['SIM']),
           color=Color['Black'],
           visibility=Visibility['VISIBLE'],
           mechanicalSet=MechanicalSet['STATOR'])

RegionFace(name='INF : INFINITE',
           magneticAC2D=MagneticAC2DFaceMagnetic(material=Material['IM']),
           color=Color['Turquoise'],
           visibility=Visibility['VISIBLE'],
           mechanicalSet=MechanicalSet['STATOR'])

RegionFace(name='SWEDGE : STATOR_WEDGE',
           magneticAC2D=MagneticAC2DFaceMagnetic(material=Material['SWM']),
           color=Color['Turquoise'],
           visibility=Visibility['VISIBLE'],
           mechanicalSet=MechanicalSet['STATOR'])

RegionLine(name='BOUNDARY : BOUNDARY',
           magneticAC2D=MagneticAC2DLineTangentField(),
           color=Color['Turquoise'],
           visibility=Visibility['VISIBLE'],
           mechanicalSet=MechanicalSet['STATOR'])


##ASSIGN REGION TO FACES

l=2*int(ParameterGeom['SCPS'].expression)

if l<0:
        l=l+AUXS*2

AUXN=int(ParameterGeom['SS'].expression)/(int(ParameterGeom['SP'].expression)*int(ParameterGeom['SPN'].expression))

AUXSP=int(ParameterGeom['SP'].expression)

for k in range(1,int(ParameterGeom['SPN'].expression)/2+1):

        for i in range(1,AUXSP+1):

                for n in range(1,AUXN+1):

                        assignRegionToFaces(face=[Face[AUXF3+(n+2*(k-1)*AUXN*AUXSP+2*(i-1)*AUXN-1)%(AUXS)+1]],
                                            region=RegionFace['PHASE'+str(i)+'P'])

                        assignRegionToFaces(face=[Face[AUXF3+(n+(2*k-1)*AUXN*AUXSP+2*(i-1)*AUXN-1)%(AUXS)+1]],
                                            region=RegionFace['PHASE'+str(i)+'N'])

for i in range(1,AUXS+1):

        assignRegionToFaces(face=[Face[AUXF4+1+i]],
                            region=RegionFace['SWEDGE'])

assignRegionToFaces(face=[Face[AUXF4+1]],
                    region=RegionFace['AIRGAP'])

assignRegionToFaces(face=[Face[AUXF5+1]],
                    region=RegionFace['SCORE'])

assignRegionToFaces(face=[Face[AUXF6+1]],
                    region=RegionFace['INF'])

LineArcPivotCoord[AUXL6+1].assignRegion(region=RegionLine['BOUNDARY'])
LineArcPivotCoord[AUXL6+2].assignRegion(region=RegionLine['BOUNDARY'])
```

Listing C.14: Rotor region file

```
#! Flux2D 11.1

##REGION FACES

for i in range(1,int(ParameterGeom['RS'].expression)+1):

        RegionFace(name='BAR'+str(i)+' : ROTOR_BAR'+str(i),
                   magneticAC2D=MagneticAC2DFaceSolidConductor(material=Material['RCM'],
                                                               circuitType=Circuit(orientation=PositiveOrientation(),
                                                                                   component=SolidConductor2Terminals[
                                                                                             'BAR_'+str(i)+'
                                                                                             _SQUIRRELCAGE_1'])),
                   color=Color['Turquoise'],
                   visibility=Visibility['VISIBLE'],
                   mechanicalSet=MechanicalSet['ROTOR'])

RegionFace(name='RCORE : ROTOR_CORE',
           magneticAC2D=MagneticAC2DFaceMagnetic(material=Material['RIM']),
           color=Color['Black'],
           visibility=Visibility['VISIBLE'],
           mechanicalSet=MechanicalSet['ROTOR'])

RegionFace(name='SHAFT : SHAFT',
           magneticAC2D=MagneticAC2DFaceMagnetic(material=Material['SM']),
           color=Color['Turquoise'],
           visibility=Visibility['VISIBLE'],
```

```
            mechanicalSet=MechanicalSet['ROTOR'])

##ASSIGN REGION TO FACES

for i in range(1,int(ParameterGeom['RS'].expression)+1):

        assignRegionToFaces(face=[Face[i]],
                            region=RegionFace['BAR'+str(i)])

assignRegionToFaces(face=[Face[AUXF1+1]],
                    region=RegionFace['SHAFT'])

assignRegionToFaces(face=[Face[AUXF2+1]],
                    region=RegionFace['RCORE'])
```

C.2 Model of the 7.5 kW industrial induction motor in Opera 2D

C.2.1 Main file

Listing C.15: Main file

```
/HIGH TORQUE DENSITY INDUCTION MOTOR

CLEAR
YES

/STATOR PARAMETERS

$ COMI SSpara.COMI

/ROTOR PARAMETERS

$ COMI CRpara.COMI

/STATOR WINDING

$ COMI SSslot.COMI

/STATOR CORE

$ COMI SScore.COMI

/ROTOR SLOT

$ COMI CRslot.COMI

/ROTOR CORE

$ COMI CRcore.COMI

/SOLVER AND AIRGAP

$ COMI SSsolv.COMI

/SOLUTION

$ COMI SSsolu.COMI

SECTION FIXEDASPECT=YES
RECONSTRUCT XMIN=1 XMAX=-1
```

C.2.2 Parameters files

Listing C.16: Stator parameters file

```
/STATOR PARAMETERS AND MATERIAL DATA

/STATOR PARAMETER

$PARAMETER NAME=#SF VALUE=50.0 DESCRIPTION='STATOR FREQUENCY'
$PARAMETER NAME=#SDD VALUE=160E-3 DESCRIPTION='STATOR DOMAIN DEPTH'
$PARAMETER NAME=#SFF VALUE=0.4220 DESCRIPTION='STATOR FILL FACTOR'
```

```
$PARAMETER NAME=#STN VALUE=34 DESCRIPTION='STATOR TURNS NUMBER PER COIL'
$PARAMETER NAME=#SID VALUE=127E-3 DESCRIPTION='STATOR INNER DIAMETER'
$PARAMETER NAME=#SS VALUE=36 DESCRIPTION='STATOR SLOTS'
$PARAMETER NAME=#SSO VALUE=2.92E-3 DESCRIPTION='STATOR SLOT OPNENING'
$PARAMETER NAME=#STTD VALUE=0.762E-3 DESCRIPTION='STATOR TOOTH TIP DEPTH'
$PARAMETER NAME=#STD VALUE=0.409E-3 DESCRIPTION='STATOR TOP DEPTH'
$PARAMETER NAME=#STW VALUE=5.169E-3 DESCRIPTION='STATOR TOP WIDTH'
$PARAMETER NAME=#SBW VALUE=7.552E-3 DESCRIPTION='STATOR BOTTOM WIDTH'
$PARAMETER NAME=#SSD VALUE=17.96E-3 DESCRIPTION='STATOR SLOT DEPTH'
$PARAMETER NAME=#SCB VALUE=19.76E-3 DESCRIPTION='STATOR CORE BACK'
$PARAMETER NAME=#SPN VALUE=4 DESCRIPTION='STATOR POLES NUMBER'
$PARAMETER NAME=#SP VALUE=3 DESCRIPTION='STATOR PHASES'
$PARAMETER NAME=#AIRGAP VALUE=0.45E-3 DESCRIPTION='AIRGAP'
$PARAMETER NAME=#INFINITE VALUE=20E-3 DESCRIPTION='INFINITE'

/CIRCUIT PARAMETERS
$PARAMETER NAME=#CPV VALUE=400 DESCRIPTION='VOLTAJE'
$PARAMETER NAME=#CPWR VALUE=2.02 DESCRIPTION='WINDING RESISTANCE'
$PARAMETER NAME=#CPWL VALUE=0.00275 DESCRIPTION='WINDING LEAKAGE'
$PARAMETER NAME=#SCT VALUE=75 DESCRIPTION='STATOR CONDUCTOR TEMPERATURE'

/STATOR AUXILIAR PARAMETERS

$PARAMETER NAME=#ZSY0 VALUE=#SSO/2 DESCRIPTION='STATOR AUXILIAR PARAMETER Y0'
$PARAMETER NAME=#ZSX0 VALUE=SQRT((#SID/2)**2-#ZSY0**2) DESCRIPTION='STATOR AUXILIAR PARAMETER X0'
$PARAMETER NAME=#ZSY1 VALUE=#ZSY0 DESCRIPTION='STATOR AUXILIAR PARAMETER Y1'
$PARAMETER NAME=#ZSX1 VALUE=#ZSX0+#STTD DESCRIPTION='STATOR AUXILIAR PARAMETER X1'
$PARAMETER NAME=#ZSX2 VALUE=#ZSX1+#STD DESCRIPTION='STATOR AUXILIAR PARAMETER X2'
$PARAMETER NAME=#ZSY2 VALUE=#STW/2 DESCRIPTION='STATOR AUXILIAR PARAMETER Y2'
$PARAMETER NAME=#ZSX3 VALUE=#ZSX1+#SSD-#SBW/2 DESCRIPTION='STATOR AUXILIAR PARAMETER X3'
$PARAMETER NAME=#ZSY3 VALUE=#SBW/2 DESCRIPTION='STATOR AUXILIAR PARAMETER Y3'
$PARAMETER NAME=#ZSX4 VALUE=#ZSX1+#SSD DESCRIPTION='STATOR AUXILIAR PARAMETER X4'
$PARAMETER NAME=#ZSY4 VALUE=0 DESCRIPTION='STATOR AUXILIAR PARAMETER Y4'

/STATOR BH data

BHDATA MATERIAL=3 TYPE=ISOTROPIC PHASE=0 PACK=1
DELETEBH N1=1 N2=*
ADD BVALUE=0 HVALUE=0
ADD BVALUE=0.099817 HVALUE=44.31454
ADD BVALUE=0.199615 HVALUE=59.76739
ADD BVALUE=0.299635 HVALUE=70.73369
ADD BVALUE=0.399138 HVALUE=78.8747
ADD BVALUE=0.499445 HVALUE=87.65236
ADD BVALUE=0.599185 HVALUE=96.24092
ADD BVALUE=0.699795 HVALUE=105.3488
ADD BVALUE=0.798947 HVALUE=117.5728
ADD BVALUE=0.898636 HVALUE=132.4877
ADD BVALUE=0.999416 HVALUE=153.7683
ADD BVALUE=1.098478 HVALUE=184.4069
ADD BVALUE=1.199293 HVALUE=236.4519
ADD BVALUE=1.299129 HVALUE=336.3599
ADD BVALUE=1.399837 HVALUE=569.388
ADD BVALUE=1.496727 HVALUE=1182.353
ADD BVALUE=1.59605 HVALUE=2691.683
ADD BVALUE=1.697686 HVALUE=5554.731
ADD BVALUE=1.747747 HVALUE=7493.084
ADD BVALUE=1.808 HVALUE=10000.0
ADD BVALUE=1.948 HVALUE=20000.0
ADD BVALUE=2.014 HVALUE=30000.0
ADD BVALUE=2.086 HVALUE=50000.0
ADD BVALUE=2.186 HVALUE=100000.0
ADD BVALUE=2.331 HVALUE=200000.0
ADD BVALUE=2.464 HVALUE=300000.0
DEMAGQUAD COMMAND=CLEAR
QUITBH

/STATOR MESH PARAMETERS

$PARAMETER NAME=#MLSSAB VALUE=1 DESCRIPTION='MESH LINE FOR STATOR SLOT AB'
$PARAMETER NAME=#MLSSBC VALUE=2 DESCRIPTION='MESH LINE FOR STATOR SLOT BC'
$PARAMETER NAME=#MLSSCD VALUE=3 DESCRIPTION='MESH LINE FOR STATOR SLOT CD'
$PARAMETER NAME=#MLSSBB VALUE=3 DESCRIPTION='MESH LINE FOR STATOR SLOT BB'
$PARAMETER NAME=#MLSSDE VALUE=3 DESCRIPTION='MESH LINE FOR STATOR SLOT DE'
$PARAMETER NAME=#MLSSEF VALUE=5 DESCRIPTION='MESH LINE FOR STATOR SLOT EF'
$PARAMETER NAME=#MLSSFG VALUE=1 DESCRIPTION='MESH LINE FOR STATOR SLOT FG'
$PARAMETER NAME=#MLSSGH VALUE=8 DESCRIPTION='MESH LINE FOR STATOR SLOT GH'
$PARAMETER NAME=#MLSSHI VALUE=3 DESCRIPTION='MESH LINE FOR STATOR SLOT HI'
$PARAMETER NAME=#MLSSIJ VALUE=3 DESCRIPTION='MESH LINE FOR STATOR SLOT IJ'
$PARAMETER NAME=#MLSSJA VALUE=12 DESCRIPTION='MESH LINE FOR STATOR SLOT JA'
$PARAMETER NAME=#MLSSINFI1 VALUE=2 DESCRIPTION='MESH LINE FOR STATOR SLOT INFI1'
$PARAMETER NAME=#MLSSINFI2 VALUE=16 DESCRIPTION='MESH LINE FOR STATOR SLOT INFI2'
$PARAMETER NAME=#MLAIRGAP VALUE=400 DESCRIPTION='MESH LINE FOR AIRGAP'

$PARAMETER NAME=#MLSSABB VALUE=0.5 DESCRIPTION='MESH LINE FOR STATOR SLOT AB BIAS'
$PARAMETER NAME=#MLSSBCB VALUE=0.5 DESCRIPTION='MESH LINE FOR STATOR SLOT BC BIAS'
$PARAMETER NAME=#MLSSCDB VALUE=0.5 DESCRIPTION='MESH LINE FOR STATOR SLOT CD BIAS'
$PARAMETER NAME=#MLSSBBB VALUE=0.5 DESCRIPTION='MESH LINE FOR STATOR SLOT BB BIAS'
$PARAMETER NAME=#MLSSDEB VALUE=0.5 DESCRIPTION='MESH LINE FOR STATOR SLOT DE BIAS'
$PARAMETER NAME=#MLSSEFB VALUE=0.15 DESCRIPTION='MESH LINE FOR STATOR SLOT EF BIAS'
$PARAMETER NAME=#MLSSFGB VALUE=0.5 DESCRIPTION='MESH LINE FOR STATOR SLOT FG BIAS'
$PARAMETER NAME=#MLSSGHB VALUE=0.85 DESCRIPTION='MESH LINE FOR STATOR SLOT GH BIAS'
$PARAMETER NAME=#MLSSHIB VALUE=0.5 DESCRIPTION='MESH LINE FOR STATOR SLOT HI BIAS'
$PARAMETER NAME=#MLSSIJB VALUE=0.5 DESCRIPTION='MESH LINE FOR STATOR SLOT IJ BIAS'
$PARAMETER NAME=#MLSSJAB VALUE=0.5 DESCRIPTION='MESH LINE FOR STATOR SLOT JA BIAS'
$PARAMETER NAME=#MLSSINFI1B VALUE=0.85 DESCRIPTION='MESH LINE FOR STATOR SLOT INFI1 BIAS'
$PARAMETER NAME=#MLSSINFI2B VALUE=0.5 DESCRIPTION='MESH LINE FOR STATOR SLOT INFI2 BIAS'
```

Listing C.17: Rotor parameters file

```
/CAGE ROTOR PARAMETERS AND MATERIAL DATA

/ROTOR PARAMETERS

$PARAMETER NAME=#RS VALUE=28 DESCRIPTION='ROTOR SLOTS'
$PARAMETER NAME=#RTBD VALUE=2.893E-3 DESCRIPTION='ROTOR TOP BAR DEPTH'
$PARAMETER NAME=#RTBW VALUE=5.786E-3 DESCRIPTION='ROTOR TOP BAR WIDTH'
$PARAMETER NAME=#RBBD VALUE=2.3E-3 DESCRIPTION='ROTOR BOTTOM BAR DEPTH'
$PARAMETER NAME=#RBBW VALUE=4.6E-3 DESCRIPTION='ROTOR BOTTOM BAR WIDTH'
$PARAMETER NAME=#RTB VALUE=0.377E-3 DESCRIPTION='ROTOR TOP BRIDGE'
$PARAMETER NAME=#RBD VALUE=10.5E-3 DESCRIPTION='ROTOR BAR DEPTH'
$PARAMETER NAME=#RCB VALUE=19.46E-3 DESCRIPTION='ROTOR CORE BACK'
$PARAMETER NAME=#SLIP VALUE=1E-4 DESCRIPTION='SLIP'
$PARAMETER NAME=#MINSLIP VALUE=1E-4 DESCRIPTION='MINIMUM SLIP'
$PARAMETER NAME=#MAXSLIP VALUE=0.2 DESCRIPTION='MAXIMUM SLIP'
$PARAMETER NAME=#STEPSLIP VALUE=20 DESCRIPTION='STEPS FOR SLIP'
$PARAMETER NAME=#MAXSLIP2 VALUE=1 DESCRIPTION='MAXIMUM SLIP2'
$PARAMETER NAME=#STEPSLIP2 VALUE=10 DESCRIPTION='STEPS FOR SLIP2'

/ROTOR CIRCUIT PARAMETERS

$PARAMETER NAME=#CPERR VALUE=2E-6 DESCRIPTION='ENDRING RESISTANCE'
$PARAMETER NAME=#CPERL VALUE=7.4E-8 DESCRIPTION='ENDRING INDUCTANCE'
$PARAMETER NAME=#RCT VALUE=75 DESCRIPTION='ROTOR CORE TEMPERATURE'
$PARAMETER NAME=#RMC VALUE=4.8429E7 DESCRIPTION='ROTOR MATERIAL CONDUCTIVITY'

/ROTOR AUXILIAR PARAMETERS

$PARAMETER NAME=#ZRX0 VALUE=#SID/2-#AIRGAP-#RTB DESCRIPTION='ROTOR AUXILIAR PARAMETER X0'
$PARAMETER NAME=#ZRY0 VALUE=0 DESCRIPTION='ROTOR AUXILIAR PARAMETER Y0'
$PARAMETER NAME=#ZRY1 VALUE=#RTBW/2 DESCRIPTION='ROTOR AUXILIAR PARAMETER Y1'
$PARAMETER NAME=#ZRX1 VALUE=#SID/2-#AIRGAP-#RTB-#RTBD DESCRIPTION='ROTOR AUXILIAR PARAMETER X1'
$PARAMETER NAME=#ZRX2 VALUE=#SID/2-#AIRGAP-#RTB-#RBD+#RBBD DESCRIPTION='ROTOR AUXILIAR PARAMETER X2'
$PARAMETER NAME=#ZRY2 VALUE=#RBBW/2 DESCRIPTION='ROTOR AUXILIAR PARAMETER Y2'
$PARAMETER NAME=#ZRX3 VALUE=#SID/2-#AIRGAP-#RTB-#RBD DESCRIPTION='ROTOR AUXILIAR PARAMETER X3'
$PARAMETER NAME=#ZRY3 VALUE=0 DESCRIPTION='ROTOR AUXILIAR PARAMETER Y3'
$PARAMETER NAME=#ZRBC VALUE=SQRT(#RBBW**2/4+#RBBD**2) DESCRIPTION='ROTOR AUXILIAR PARAMETER ZR BOTTOM C'
$PARAMETER NAME=#ZRBS VALUE=(#RBBW+2*#ZRBC)/2 DESCRIPTION='ROTOR AUXILIAR PARAMETER ZR BOTTOM SEMIPERIMETER'
$PARAMETER NAME=#ZRBR VALUE=(#RBBW*#ZRBC**2)/(4*SQRT(#ZRBS*(#ZRBS-#RBBW)*(#ZRBS-#ZRBC)**2)) DESCRIPTION='ROTOR
      AUXILIAR PARAMETER ZR BOTTOM RADIUS'
$PARAMETER NAME=#ZRTC VALUE=SQRT(#RTBW**2/4+#RTBD**2) DESCRIPTION='ROTOR AUXILIAR PARAMETER ZR TOP C'
$PARAMETER NAME=#ZRTS VALUE=(#RTBW+2*#ZRTC)/2 DESCRIPTION='ROTOR AUXILIAR PARAMETER ZR TOP SEMIPERIMETER'
$PARAMETER NAME=#ZRTR VALUE=(#RTBW*#ZRTC**2)/(4*SQRT(#ZRTS*(#ZRTS-#RTBW)*(#ZRTS-#ZRTC)**2)) DESCRIPTION='ROTOR
      AUXILIAR PARAMETER ZR TOP RADIUS'

/ROTOR BH data

BHDATA MATERIAL=4  TYPE=ISOTROPIC  PHASE=0  PACK=1
DELETEBH N1=1  N2=*
ADD  BVALUE=0  HVALUE=0
ADD  BVALUE=0.099817  HVALUE=44.31454
ADD  BVALUE=0.199615  HVALUE=59.76739
ADD  BVALUE=0.299635  HVALUE=70.73369
ADD  BVALUE=0.399138  HVALUE=78.8747
ADD  BVALUE=0.499445  HVALUE=87.65236
ADD  BVALUE=0.599185  HVALUE=96.24092
ADD  BVALUE=0.699795  HVALUE=105.3488
ADD  BVALUE=0.798947  HVALUE=117.5728
ADD  BVALUE=0.898636  HVALUE=132.4877
ADD  BVALUE=0.999416  HVALUE=153.7683
ADD  BVALUE=1.098478  HVALUE=184.4069
ADD  BVALUE=1.199293  HVALUE=236.4519
ADD  BVALUE=1.299129  HVALUE=336.3599
ADD  BVALUE=1.399837  HVALUE=569.388
ADD  BVALUE=1.496727  HVALUE=1182.353
ADD  BVALUE=1.59605  HVALUE=2691.683
ADD  BVALUE=1.697686  HVALUE=5554.731
ADD  BVALUE=1.747747  HVALUE=7493.084
ADD  BVALUE=1.808  HVALUE=10000.0
ADD  BVALUE=1.948  HVALUE=20000.0
ADD  BVALUE=2.014  HVALUE=30000.0
ADD  BVALUE=2.086  HVALUE=50000.0
ADD  BVALUE=2.186  HVALUE=100000.0
ADD  BVALUE=2.331  HVALUE=200000.0
ADD  BVALUE=2.464  HVALUE=300000.0
DEMAGQUAD  COMMAND=CLEAR
QUITBH

/ROTOR MESH PARAMETERS

$PARAMETER NAME=#MLRSAB VALUE=6 DESCRIPTION='MESH LINE FOR ROTOR SLOT AB'
$PARAMETER NAME=#MLRSBC VALUE=3 DESCRIPTION='MESH LINE FOR ROTOR SLOT BC'
$PARAMETER NAME=#MLRSCD VALUE=3 DESCRIPTION='MESH LINE FOR ROTOR SLOT CD'
$PARAMETER NAME=#MLRSDE VALUE=5 DESCRIPTION='MESH LINE FOR ROTOR SLOT DE'
$PARAMETER NAME=#MLRSEF VALUE=1 DESCRIPTION='MESH LINE FOR ROTOR SLOT EF'
$PARAMETER NAME=#MLRSFG VALUE=10 DESCRIPTION='MESH LINE FOR ROTOR SLOT FG'
$PARAMETER NAME=#MLRSGH VALUE=2 DESCRIPTION='MESH LINE FOR ROTOR SLOT GH'
$PARAMETER NAME=#MLRSHI VALUE=3 DESCRIPTION='MESH LINE FOR ROTOR SLOT HI'
$PARAMETER NAME=#MLRSIJ VALUE=12 DESCRIPTION='MESH LINE FOR ROTOR SLOT IJ'
$PARAMETER NAME=#MLRSJA VALUE=1 DESCRIPTION='MESH LINE FOR ROTOR SLOT JA'
$PARAMETER NAME=#MLRSSHA VALUE=3 DESCRIPTION='MESH LINE FOR ROTOR SLOT SHAFT'

$PARAMETER NAME=#MLRSABB VALUE=0.5 DESCRIPTION='MESH LINE FOR ROTOR SLOT AB BIAS'
$PARAMETER NAME=#MLRSBCB VALUE=0.5 DESCRIPTION='MESH LINE FOR ROTOR SLOT BC BIAS'
$PARAMETER NAME=#MLRSCDB VALUE=0.5 DESCRIPTION='MESH LINE FOR ROTOR SLOT CD BIAS'
$PARAMETER NAME=#MLRSDEB VALUE=0.15 DESCRIPTION='MESH LINE FOR ROTOR SLOT DE BIAS'
$PARAMETER NAME=#MLRSEFB VALUE=0.5 DESCRIPTION='MESH LINE FOR ROTOR SLOT EF BIAS'
$PARAMETER NAME=#MLRSFGB VALUE=0.85 DESCRIPTION='MESH LINE FOR ROTOR SLOT FG BIAS'
$PARAMETER NAME=#MLRSGHB VALUE=0.5 DESCRIPTION='MESH LINE FOR ROTOR SLOT GH BIAS'
$PARAMETER NAME=#MLRSHIB VALUE=0.5 DESCRIPTION='MESH LINE FOR ROTOR SLOT HI BIAS'
$PARAMETER NAME=#MLRSIJB VALUE=0.5 DESCRIPTION='MESH LINE FOR ROTOR SLOT IJ BIAS'
$PARAMETER NAME=#MLRSJAB VALUE=0.5 DESCRIPTION='MESH LINE FOR ROTOR SLOT JA BIAS'
$PARAMETER NAME=#MLRSSHAB VALUE=0.5 DESCRIPTION='MESH LINE FOR ROTOR SLOT SHA BIAS'
```

C.2.3 Stator files

Listing C.18: Stator windings file

```
/STATOR SLOT

$PARAMETER NAME=#XA VALUE=0 DESCRIPTION='AUXILIAR VARIABLE XA'
$PARAMETER NAME=#YA VALUE=0 DESCRIPTION='AUXILIAR VARIABLE YA'
$PARAMETER NAME=#A VALUE=180/#SS DESCRIPTION='AUXILIAR VARIABLE A'

$CONSTANT NAME=#I VALUE=0 DESCRIPTION='AUXILIAR VARIABLE I'

$DO #I 1 #SS 1

  DRAW SHAPE=POLYGON,
  DRAW +DEFAULTS SHAPE=POLYGON TOLERANCE=5.0E-05 MATERIAL=1 PERM=1 DENS=0 CONDUCTIVITY=0 PHASE=0 VELOCITY=0 N=#I
       SYMMETRY=0 XCEN=0 YCEN=0 ANGLE=0 NX=1 DX=0 NY=1 DY=0 ROTATIONS=1 TROTATION=0 MIRROR=NO

  #XA=#ZSX1*COSD(#A)-#ZSY1*SIND(#A)
  #YA=#ZSX1*SIND(#A)+#ZSY1*COSD(#A)
  POLYGON -RELATIVE POLAR=NO X=#XA Y=#YA OPTION=TEXT +DATA
  POLYGON -DATA -SIZE N=#MLSSBC BIAS=#MLSSBCB LINESHAPE=CURVATURE CURVATURE=0 F=NO

  #XA=#ZSX2*COSD(#A)-#ZSY2*SIND(#A)
  #YA=#ZSX2*SIND(#A)+#ZSY2*COSD(#A)
  POLYGON -RELATIVE POLAR=NO X=#XA Y=#YA OPTION=TEXT +DATA
  POLYGON -DATA -SIZE N=#MLSSCD BIAS=#MLSSCDB LINESHAPE=CURVATURE CURVATURE=0 F=NO

  #XA=#ZSX3*COSD(#A)-#ZSY3*SIND(#A)
  #YA=#ZSX3*SIND(#A)+#ZSY3*COSD(#A)
  POLYGON -RELATIVE POLAR=NO X=#XA Y=#YA OPTION=TEXT +DATA
  POLYGON -DATA -SIZE N=#MLSSDE BIAS=#MLSSDEB LINESHAPE=CURVATURE CURVATURE=2/#SBW F=NO

  #XA=#ZSX4*COSD(#A)-#ZSY4*SIND(#A)
  #YA=#ZSX4*SIND(#A)+#ZSY4*COSD(#A)
  POLYGON -RELATIVE POLAR=NO X=#XA Y=#YA OPTION=TEXT +DATA
  POLYGON -DATA -SIZE N=#MLSSDE BIAS=1-#MLSSDEB LINESHAPE=CURVATURE CURVATURE=2/#SBW F=NO

  #XA=#ZSX3*COSD(#A)+#ZSY3*SIND(#A)
  #YA=#ZSX3*SIND(#A)-#ZSY3*COSD(#A)
  POLYGON -RELATIVE POLAR=NO X=#XA Y=#YA OPTION=TEXT +DATA
  POLYGON -DATA -SIZE N=#MLSSCD BIAS=1-#MLSSCDB LINESHAPE=CURVATURE CURVATURE=0 F=NO

  #XA=#ZSX2*COSD(#A)+#ZSY2*SIND(#A)
  #YA=#ZSX2*SIND(#A)-#ZSY2*COSD(#A)
  POLYGON -RELATIVE POLAR=NO X=#XA Y=#YA OPTION=TEXT +DATA
  POLYGON -DATA -SIZE N=#MLSSBC BIAS=1-#MLSSBCB LINESHAPE=CURVATURE CURVATURE=0 F=NO

  #XA=#ZSX1*COSD(#A)+#ZSY1*SIND(#A)
  #YA=#ZSX1*SIND(#A)-#ZSY1*COSD(#A)
  POLYGON -RELATIVE POLAR=NO X=#XA Y=#YA OPTION=TEXT +DATA
  POLYGON -DATA -SIZE N=#MLSSBB BIAS=#MLSSBBB LINESHAPE=CURVATURE CURVATURE=0 F=NO

  POLYGON OPTION=CLOSE

  #A=#A+360/#SS

$END DO
```

Listing C.19: Stator core file

```
/STATOR CORE

#A=180/#SS

DRAW SHAPE=POLYGON,
DRAW +DEFAULTS SHAPE=POLYGON TOLERANCE=5.0E-05 MATERIAL=3 PERM=10000 DENS=0 CONDUCTIVITY=0 PHASE=0 VELOCITY=0 N=0
     SYMMETRY=0 XCEN=0 YCEN=0 ANGLE=0 NX=1 DX=0 NY=1 DY=0 ROTATIONS=#SS TROTATION=360/#SS MIRROR=YES TMIRROR=180/#SS

#XA=#ZSX0*COSD(#A)+#ZSY0*SIND(#A)
#YA=#ZSX0*SIND(#A)-#ZSY0*COSD(#A)
POLYGON -RELATIVE POLAR=NO X=#XA Y=#YA OPTION=TEXT +DATA
POLYGON -DATA -SIZE N=#MLSSAB BIAS=#MLSSABB LINESHAPE=CURVATURE CURVATURE=0 F=NO

#XA=#ZSX1*COSD(#A)+#ZSY1*SIND(#A)
#YA=#ZSX1*SIND(#A)-#ZSY1*COSD(#A)
POLYGON -DATA OPTION=PICK +EXIST
POLYGON X=#XA Y=#YA -POLAR -RELATIVE

#XA=#ZSX2*COSD(#A)+#ZSY2*SIND(#A)
#YA=#ZSX2*SIND(#A)-#ZSY2*COSD(#A)
POLYGON -DATA OPTION=PICK +EXIST
POLYGON X=#XA Y=#YA -POLAR -RELATIVE

#XA=#ZSX3*COSD(#A)+#ZSY3*SIND(#A)
#YA=#ZSX3*SIND(#A)-#ZSY3*COSD(#A)
```

```
POLYGON -DATA OPTION=PICK +EXIST
POLYGON X=#XA Y=#YA -POLAR -RELATIVE

#XA=#ZSX4*COSD(#A)+#ZSY4*SIND(#A)
#YA=#ZSX4*SIND(#A)-#ZSY4*COSD(#A)
POLYGON -DATA OPTION=PICK +EXIST
POLYGON X=#XA Y=#YA -POLAR -RELATIVE

#XA=(#ZSX4+#SCB)*COSD(#A)+0*SIND(#A)
#YA=(#ZSX4+#SCB)*SIND(#A)-0*COSD(#A)
POLYGON -DATA -SIZE N=#MLSSEF BIAS=#MLSSEFB LINESHAPE=CURVATURE CURVATURE=0 F=NO
POLYGON -RELATIVE POLAR=NO X=#XA Y=#YA OPTION=TEXT +DATA

POLYGON -DATA -SIZE N=#MLSSFG BIAS=#MLSSFGB LINESHAPE=CURVATURE CURVATURE=1/(#ZSX4+#SCB) F=V V=0
POLYGON -RELATIVE POLAR=NO X=#ZSX4+#SCB Y=0 OPTION=TEXT +DATA

POLYGON -DATA -SIZE N=#MLSSGH BIAS=#MLSSGHB LINESHAPE=CURVATURE CURVATURE=0 F=NO
POLYGON -RELATIVE POLAR=NO X=#ZSX3 Y=0 OPTION=TEXT +DATA

POLYGON -DATA -SIZE N=#MLSSHI BIAS=#MLSSHIB LINESHAPE=CURVATURE CURVATURE=0 F=NO
POLYGON -RELATIVE POLAR=NO X=#ZSX2 Y=0 OPTION=TEXT +DATA

POLYGON -DATA -SIZE N=#MLSSIJ BIAS=#MLSSIJB LINESHAPE=CURVATURE CURVATURE=0 F=NO
POLYGON -RELATIVE POLAR=NO X=#SID/2 Y=0 OPTION=TEXT +DATA

POLYGON -DATA -SIZE N=#MLSSJA BIAS=#MLSSJAB LINESHAPE=CURVATURE CURVATURE=-2/#SID F=NO
POLYGON OPTION=CLOSE
```

C.2.4 Rotor files

Listing C.20: Rotor windings file

```
/ROTOR SLOT

#A=180/#RS

$DO #I 1 #RS 1

  DRAW SHAPE=POLYGON,
  DRAW +DEFAULTS SHAPE=POLYGON TOLERANCE=5.0E-05 MATERIAL=1 PERM=1 DENS=0 CONDUCTIVITY=#RMC PHASE=0 VELOCITY=0 N=#I+#
       SS SYMMETRY=0 XCEN=0 YCEN=0 ANGLE=0 NX=1 DX=0 NY=1 DY=0 ROTATIONS=1 TROTATION=0 MIRROR=NO

  #XA=#ZRX0*COSD(#A)-#ZRY0*SIND(#A)
  #YA=#ZRX0*SIND(#A)+#ZRY0*COSD(#A)
  POLYGON -RELATIVE POLAR=NO X=#XA Y=#YA OPTION=TEXT +DATA
  POLYGON -DATA -SIZE N=#MLRSAB BIAS=#MLRSABB LINESHAPE=CURVATURE CURVATURE=-1/#ZRTR F=NO

  #XA=#ZRX1*COSD(#A)-#ZRY1*SIND(#A)
  #YA=#ZRX1*SIND(#A)+#ZRY1*COSD(#A)
  POLYGON -RELATIVE POLAR=NO X=#XA Y=#YA OPTION=TEXT +DATA
  POLYGON -DATA -SIZE N=#MLRSBC BIAS=#MLRSBCB LINESHAPE=CURVATURE CURVATURE=0 F=NO

  #XA=#ZRX2*COSD(#A)-#ZRY2*SIND(#A)
  #YA=#ZRX2*SIND(#A)+#ZRY2*COSD(#A)
  POLYGON -RELATIVE POLAR=NO X=#XA Y=#YA OPTION=TEXT +DATA
  POLYGON -DATA -SIZE N=#MLRSCD BIAS=#MLRSCDB LINESHAPE=CURVATURE CURVATURE=-1/#ZRBR F=NO

  #XA=#ZRX3*COSD(#A)-#ZRY3*SIND(#A)
  #YA=#ZRX3*SIND(#A)+#ZRY3*COSD(#A)
  POLYGON -RELATIVE POLAR=NO X=#XA Y=#YA OPTION=TEXT +DATA
  POLYGON -DATA -SIZE N=#MLRSCD BIAS=1-#MLRSCDB LINESHAPE=CURVATURE CURVATURE=-1/#ZRBR F=NO

  #XA=#ZRX2*COSD(#A)+#ZRY2*SIND(#A)
  #YA=#ZRX2*SIND(#A)-#ZRY2*COSD(#A)
  POLYGON -RELATIVE POLAR=NO X=#XA Y=#YA OPTION=TEXT +DATA
  POLYGON -DATA -SIZE N=#MLRSBC BIAS=1-#MLRSBCB LINESHAPE=CURVATURE CURVATURE=0 F=NO

  #XA=#ZRX1*COSD(#A)+#ZRY1*SIND(#A)
  #YA=#ZRX1*SIND(#A)-#ZRY1*COSD(#A)
  POLYGON -RELATIVE POLAR=NO X=#XA Y=#YA OPTION=TEXT +DATA
  POLYGON -DATA -SIZE N=#MLRSAB BIAS=1-#MLRSABB LINESHAPE=CURVATURE CURVATURE=-1/#ZRTR F=NO

  POLYGON OPTION=CLOSE

  #A=#A+360/#RS

$END DO
```

Listing C.21: Rotor core file

```
/ROTOR CORE

#A=180/#RS

DRAW SHAPE=POLYGON,
DRAW +DEFAULTS SHAPE=POLYGON TOLERANCE=5.0E-05 MATERIAL=4 PERM=10000 DENS=0 CONDUCTIVITY=0 PHASE=0 VELOCITY=0 N=0
     SYMMETRY=0 XCEN=0 YCEN=0 ANGLE=0 NX=1 DX=0 NY=1 DY=0 ROTATIONS=#RS TROTATION=360/#RS MIRROR=YES TMIRROR=180/#RS
```

```
7
8  #XA=#ZRX0*COSD(#A)+#ZRY0*SIND(#A)
9  #YA=#ZRX0*SIND(#A)-#ZRY0*COSD(#A)
10 POLYGON -DATA OPTION=PICK +EXIST
11 POLYGON X=#XA Y=#YA -POLAR -RELATIVE
12
13 #XA=#ZRX1*COSD(#A)+#ZRY1*SIND(#A)
14 #YA=#ZRX1*SIND(#A)-#ZRY1*COSD(#A)
15 POLYGON -DATA OPTION=PICK +EXIST
16 POLYGON X=#XA Y=#YA -POLAR -RELATIVE
17
18 #XA=#ZRX2*COSD(#A)+#ZRY2*SIND(#A)
19 #YA=#ZRX2*SIND(#A)-#ZRY2*COSD(#A)
20 POLYGON -DATA OPTION=PICK +EXIST
21 POLYGON X=#XA Y=#YA -POLAR -RELATIVE
22
23 #XA=#ZRX3*COSD(#A)+#ZRY3*SIND(#A)
24 #YA=#ZRX3*SIND(#A)-#ZRY3*COSD(#A)
25 POLYGON -DATA OPTION=PICK +EXIST
26 POLYGON X=#XA Y=#YA -POLAR -RELATIVE
27
28 #XA=(#ZRX3-#RCB)*COSD(#A)+0*SIND(#A)
29 #YA=(#ZRX3-#RCB)*SIND(#A)-0*COSD(#A)
30 POLYGON -DATA -SIZE N=#MLRSDE BIAS=#MLRSDEB LINESHAPE=CURVATURE CURVATURE=0 F=NO
31 POLYGON -RELATIVE POLAR=NO X=#XA Y=#YA OPTION=TEXT +DATA
32
33 POLYGON -DATA -SIZE N=#MLRSEF BIAS=#MLRSEFB LINESHAPE=CURVATURE CURVATURE=1/(#ZRX3-#RCB) F=V V=0
34 POLYGON -RELATIVE POLAR=NO X=#ZRX3-#RCB Y=0 OPTION=TEXT +DATA
35
36 POLYGON -DATA -SIZE N=#MLRSFG BIAS=#MLRSFGB LINESHAPE=CURVATURE CURVATURE=0 F=NO
37 POLYGON -RELATIVE POLAR=NO X=#ZRX2 Y=0 OPTION=TEXT +DATA
38
39 POLYGON -DATA -SIZE N=#MLRSGH BIAS=#MLRSGHB LINESHAPE=CURVATURE CURVATURE=0 F=NO
40 POLYGON -RELATIVE POLAR=NO X=#ZRX1 Y=0 OPTION=TEXT +DATA
41
42 POLYGON -DATA -SIZE N=#MLRSHI BIAS=#MLRSHIB LINESHAPE=CURVATURE CURVATURE=0 F=NO
43 POLYGON -RELATIVE POLAR=NO X=#SID/2-#AIRGAP Y=0 OPTION=TEXT +DATA
44
45 #XA=(#SID/2-#AIRGAP)*COSD(#A)+0*SIND(#A)
46 #YA=(#SID/2-#AIRGAP)*SIND(#A)-0*COSD(#A)
47 POLYGON -DATA -SIZE N=#MLRSIJ BIAS=#MLRSIJB LINESHAPE=CURVATURE CURVATURE=-1/(#SID/2-#AIRGAP) F=NO
48 POLYGON -RELATIVE POLAR=NO X=#XA Y=#YA OPTION=TEXT +DATA
49
50 POLYGON -DATA -SIZE N=#MLRSJA BIAS=#MLRSJAB LINESHAPE=CURVATURE CURVATURE=0 F=NO
51 POLYGON OPTION=CLOSE
```

C.2.5 Solver files

Listing C.22: Solver file

```
1  /SOLVER AND AIRGAP
2
3  /SOLVER
4
5  SOLVE TYPE=AC
6  CASE COMM=CLEAR
7  CASE COMM=ADD POSITION=1 VALUE=#SF*#SLIP
8  DATA LINEAR=NO TOLERANCE=1.0E-03 NITERATION=50 CMU=NO LOSSYD=NO ADIT=0
9  QUIT
10
11 /AIRGAP
12
13 GAP INCLUDE=ONE SYMMETRY=1 RADIUS=(#SID-#AIRGAP)/2 SLICES=1 SKEW=0 SKEW2=0 BACKGROUND=YES N=#MLAIRGAP
14
15 /GENERATE MESH
16
17 SET ELEMENT=QUADRATIC
18 MESH +ERRORCHECK -DISPLAY TOLERANCE=5.0E-05
19 NO
20
21 /CIRCUIT
22
23 CEDITOR OPTION=LOAD FILE=SScirc.vfc
24 CEDITOR OPTION=UPDATE
```

C.2.6 Auxiliary solution files

Listing C.23: Auxiliary solution file

```
1  /SOLUTION
2
```

```
3  WRITE FILE=BENCHMARK.op2
4
5  $ open 0 fields.dat overwrite
6  $ constant #output openstream
7  $ format 1 string 1 STRING=' '
8  $ format 2 exponential 0
9  $ assign 2 1 2
10
11 $string label BENCHMARKxxx.op2
12
13 $DO #I #MINSLIP #MAXSLIP (#MAXSLIP-#MINSLIP)/#STEPSLIP
14
15    #SLIP=#I
16
17    SOLVE TYPE=AC
18    CASE COMM=REPLACE POSITION=1 VALUE=#SF*#SLIP
19    DATA LINEAR=NO TOLERANCE=1.0E-03 NITERATION=50 CMU=NO LOSSYD=NO ADIT=0 |QUIT
20
21    WRITE FILE=%replace<&label&><xxx><%real(#SLIP)> +SOLVENOW
22
23    RMTORQUE
24
25    $ write #output #SLIP TORQUE*#SDD
26
27 $END DO
28
29 $DO #I #MAXSLIP+(#MAXSLIP2-#MAXSLIP)/#STEPSLIP2 #MAXSLIP2 (#MAXSLIP2-#MAXSLIP)/#STEPSLIP2
30
31    #SLIP=#I
32
33    SOLVE TYPE=AC
34    CASE COMM=REPLACE POSITION=1 VALUE=#SF*#SLIP
35    DATA LINEAR=NO TOLERANCE=1.0E-03 NITERATION=50 CMU=NO LOSSYD=NO ADIT=0 |QUIT
36
37    WRITE FILE=%replace<&label&><xxx><%real(#SLIP)> +SOLVENOW
38
39    RMTORQUE
40
41    $ write #output #SLIP TORQUE*#SDD
42
43 $END DO
44
45 $ close #output
```

APPENDIX

D

EQUATIONS USED IN THE THERMAL MODEL

Table D.1: Equations for the thermal model [1]

Model parameter	Equation		Variables
R_{sy1}: Inner half of the radial conduction thermal resistance of the stator yoke (°C/W)	$R_{sy1} = \frac{1}{2\pi k_{ir} L_s} \ln\left(\frac{r_m}{r_{iy}}\right)$	(D.1)	r_m - average stator yoke radius (m) r_{iy} - inner stator yoke radius (m) L_s - stator core length (m) k_{ir} - iron thermal conduction coefficient (W/(m°C))

Continued on next page

Table D.1 – continued from previous page

Model parameter	Equation		Variables
R_{sy2}: Outer half of the radial conduction thermal resistance of the stator yoke (°C/W)	$R_{sy2} = \frac{1}{2\pi k_{ir} L_s} \ln\left(\frac{r_{oy}}{r_m}\right)$	(D.2)	r_{oy} - outer stator yoke radius (m)
$R_{s,ag}$: Convection thermal resistance between stator and airgap (°C/W)	$R_{s,ag} = \frac{1}{A_{ist} h_{ag}}$	(D.3)	A_{ist} - inner stator surface (m^2) h_{ag} - forced convection coefficient of the airgap (W/(m^2 °C)), $h_{ag} = \frac{\text{Nu} k_{air}}{2 l_{ag}}$ Nu - Nusselt number If Re $<$ RE$_{cr}$ then Nu $= 2$ else: Nu $= 0.386 \frac{1}{\sqrt{r_i s l_{ag}}}Pr^{0.27}$ Pr - Pradtl number, Pr $= c_p \mu / k$ c_p - fluid specific heat capacity (kJ/(kg°C)) k - fluid thermal conductivity ($W/(m^2 \cdot^\circ C)$) Re$_{cr}$ - Reynolds critical number, Re$_{cr} = 100\sqrt{r_{is} l_{ag}}$ l_{ag} - radial thickness of the airgap (m) Re - Reynolds number, Re $= \rho \upsilon L / \mu$ υ - fluid speed (m/s) μ - fluid dynamic viscosity ($kg/(m \cdot s)$), $\mu =$ 5.128x10^{-8}T + 310x10^{-8} ρ: Air density (kg/m^3), $\rho = -0.00475T + 2.5725$ T - temperature (K)

Continued on next page

Table D.1 – continued from previous page

Model parameter	Equation		Variables
$R_{r,ag}$: Convection thermal resistance between rotor and airgap (°C/W)	$R_{r,ag} = \frac{1}{A_{ort} h_{ag}}$	(D.4)	A_{ort} - outer rotor surface (m^2)
R_{airgap} equivalent airgap thermal resistance (°C/W)	$R_{airgap} = \frac{1}{2\pi k_{air} L_s} \ln\left(\frac{r_{is}}{r_{or}}\right)$	(D.5)	r_{or} - outer rotor radius (m)
R_{st} radial conduction thermal resistance of the stator radius (°C/W)	$R_{st} = \frac{1}{2\pi k_{ir} L_s p_{ir}} \ln\left(\frac{r_{iy}}{r_{is}}\right)$	(D.6)	p_{ir} - percentage of the teeth iron volume respect of the total teeth plus slots volume
R_{shf} axial conduction thermal resistance of the shaft (°C/W)	$R_{shf} = \frac{1}{2\pi k_{ir} L_s} \ln\left(\frac{r_{ory}}{r_{iry}}\right) + \frac{1}{4}\left(\frac{0.5 L_s}{k_{ir}\pi r_{iry}^2}\right) + \frac{1}{2}\left(\frac{0.5(L_{shf} - L_s)}{k_{ir}\pi r_{iry}^2}\right)$	(D.7)	L_{shf} - shaft length (m) r_{iry} - inner rotor yoke radius (m) r_{ory} - outer rotor yoke radius (m)

Continued on next page

Table D.1 – continued from previous page

Model parameter	Equation	Variables
$R_{ew,ec}$ conduction thermal resistance between stator winding external connection and external case (°C/W)	$R_{ew,ec} = \frac{1}{2\pi k(L_{ec} - L_s)} \ln\left(\frac{r_{oy}}{r_{oy} - \alpha t_{sy}}\right)$ (D.8)	L_{ec} - external case length (m) L_s - stator core length (m) r_{oy} - outer stator yoke radius (m) α - reduction coefficient (0.4-0.7)
$R_{ew,ia}$ conduction thermal resistance between stator winding external connections and inner air (°C/W)	$R_{ew,ia} = \frac{1}{A_{ew} h_{ew}}$ (D.9)	A_{ew} - total end winding connections surface in constant contact with inner air in movement (m^2) $A_{ew} = 2\pi r_{is}(L_{ec} - Ls)$ h_{ew} - convection coefficient for the air between end-windings and inner air (W/(m^2 °C)) $h_{ew} = 15.5(0.29\upsilon + 1)$ $\upsilon = r_{or}\omega\eta$ η - endring fan efficiency ($\eta \approx 0.5$)
$R_{ia,ec}$ conduction thermal resistance between inner air and external endcaps (°C/W)	$R_{ia,ec} = \frac{1}{A_{ec} h_{ec}}$ (D.10)	A_{ec} - endcaps external surface (m^2) $A_{ec} = 2\pi(r_{oy} + t_{ec})^2$ t_{ec} - external case thickness (m) h_{ec} - convection coefficient between inner air and endcaps (W/(m^2 °C)), $h_{ec} \approx h_{ew}$

Continued on next page

Table D.1 – continued from previous page

Model parameter	Equation		Variables
$R_{cu,ir}$ conduction thermal resistance between stator copper and iron (°C/W)	$R_{cu,ir} = \frac{t_{eq}}{k_{cu,ir} A_{slot}}$	(D.11)	A_{slot} - interior slot surface (m^2) $k_{cu,ir}$ - equivalent conductivity coefficient of the air and insulation material in the stator slots (W/(m °C)) $t_{eq} = \frac{S_{slot} - S_{cu}}{l_{sb}}$ S_{slot} - stator slot cross-sectional area (m^2) S_{cu} - copper section in the stator slot (m^2) l_{sb} - stator slot perimeter (m)
R_{sig} interface gap conduction thermal resistance between stator core and external case (°C/W)	$R_{sig} = \frac{l_{ig}}{2 k_{air} \pi r_{oy} L_s}$	(D.12)	l_{sig} - stator interface gap length (m)
R_0 natural convection thermal resistance between external case and external air (°C/W)	$R_0 = \frac{T_{case} - T_{air}}{P_{DC}}$	(D.13)	T_{case} - external case temperature (°C) T_{air} - air temperature (°C)
R_{eca} forced convection thermal resistance between external case and external air (°C/W)	$R_{eca} = \frac{1}{A_c h_{ea}}$	(D.14)	A_c - total external surface of the motor case (m^2) h_{ea} - forced convection coefficient (W/(m^2 °C)) $h_{ea} = \frac{\text{Nu} k_{air}}{L_{ec}}$ $\text{Re} = \frac{L_{ec} \upsilon_{air} \rho_{air}}{\mu_{air}}$ If Re $< 10^4$ then Nu $= 0.66\text{Re}^{0.5}\text{Pr}^{0.33}$ If Re $> 10^4$ then Nu $= 0.066\text{Re}^{0.75}\text{Pr}^{0.33}$

D.1 References

[1] A. Boglietti et al., "A simplified thermal model for variable-speed self-cooled industrial induction motor", *Industry Applications, IEEE Transactions on*. 39, 945 –952. (, Jul/Aug, 2003).

APPENDIX

E

FINAL PROTOTYPE DIMENSIONS

E.1 Stator

Tables E.1 and E.2 present a detailed description of the core and winding details of the benchmark stator of the industrial motor. Figure E.1 shows the dimensions of the stator slots (All dimensions are in millimetres).

Table E.1: Stator data

Description	Value	Unit
Poles	4	-
Output	5.5	kW
Voltage	400	V
Phases	3	-
Frequency	50	Hz
Winding connection	Delta	-
Lamination material	Newcor 660-50	-
Number of slots	36	-
Core length	130	mm
Bore diameter	127	mm
Core back depth	19.76	mm
Stacking factor	0.96	-

E.2 Rotor 1 – Double Cage Rotor

Table E.3 shows the main data of the rotor of the double cage prototype which was labelled number 1. Mild steel laminations, 2 mm thick, were used because it offered reduced manufacturing costs without compromising the test results significantly. A slightly lower efficiency might be expected as a result of higher rotor core losses.

Table E.2: Stator winding data

Description		Value	Unit
Winding type		Whole coil concentric	-
Coils per slot		1	-
Tiers		2	-
Coils per group		3	-
Turns per coil		43	-
No of parallels		1	-
Step		1-8,10,12	-
Wires	Size 1	1/0.80	mm
	Size 2	1/0.85	mm
Wire material		Copper wire	-
Slot fill (%)		41.20 (true wire area only)	-
Mean turn length		584	mm

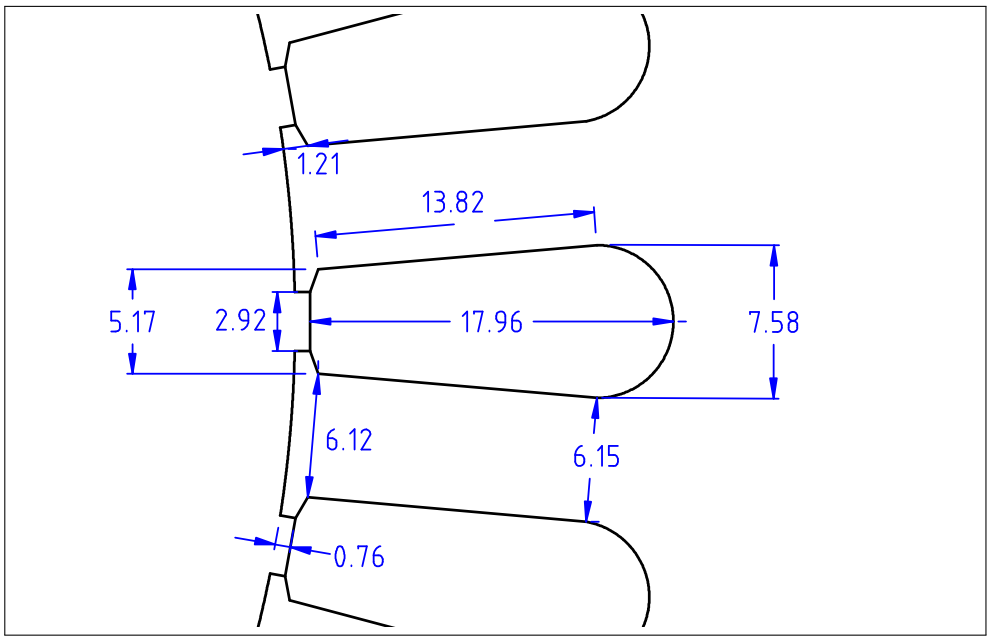

Figure E.1: Stator slot dimensions

Table E.3: Rotor 1 data

Description	Value	Unit
Lamination material	Mild steel	-
Lamination thickness	2	mm
Number of slots	56	-
Core length	130	mm
Stacking factor	0.97	-
Airgap	0.45	mm
Skew	0	Rotor bars
Conductor material	Copper	-
Shaft material	Carbon steel	-

Figure E.2 shows in detail the final dimensions of the prototype rotor including a full view of the laminations and a magnified view of the rotor slots. The inner rotor dimensions and

geometry were modified to interface to the test rig including a square key-way.

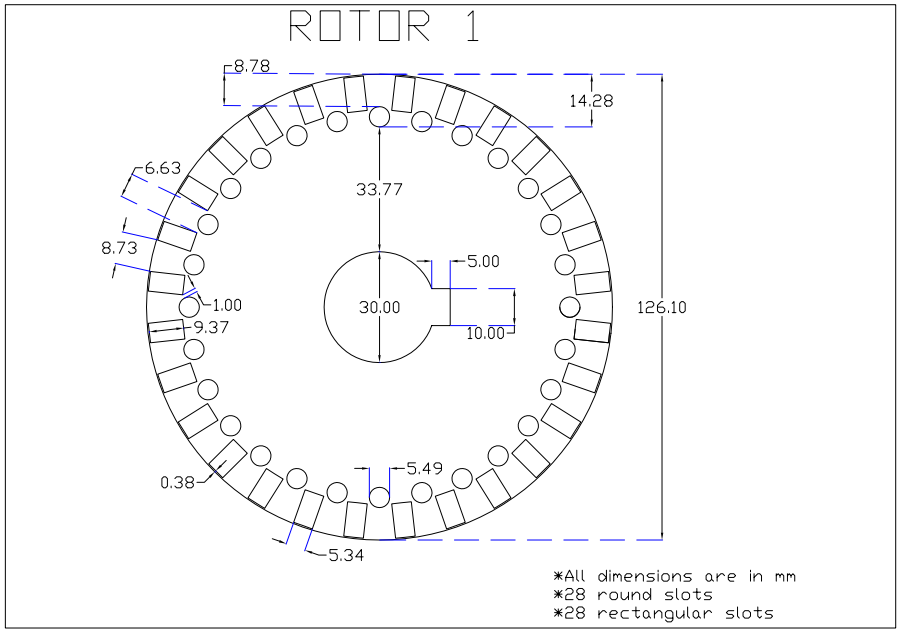

(a) Full view

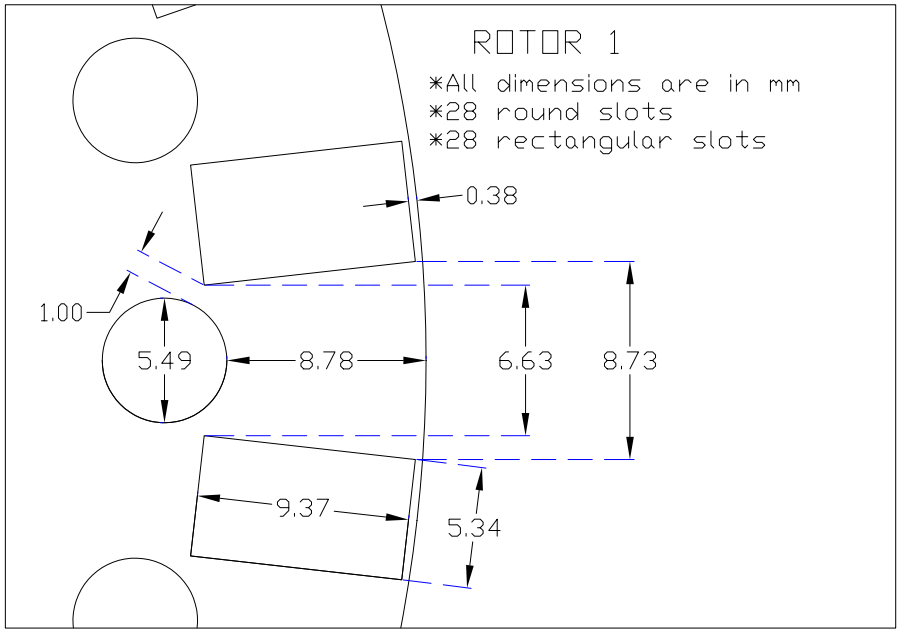

(b) Slots view

Figure E.2: Rotor 1 laminations

Figure E.3 illustrates the dimensions of the machined copper end-ring in plan and axial views. Yellow corresponds to the copper end-ring with the rotor bars in red. The rotor core is displayed in grey and the shaft, including the square key, in blue. Figure E.4 shows the 3D view of the double cage rotor after assembly.

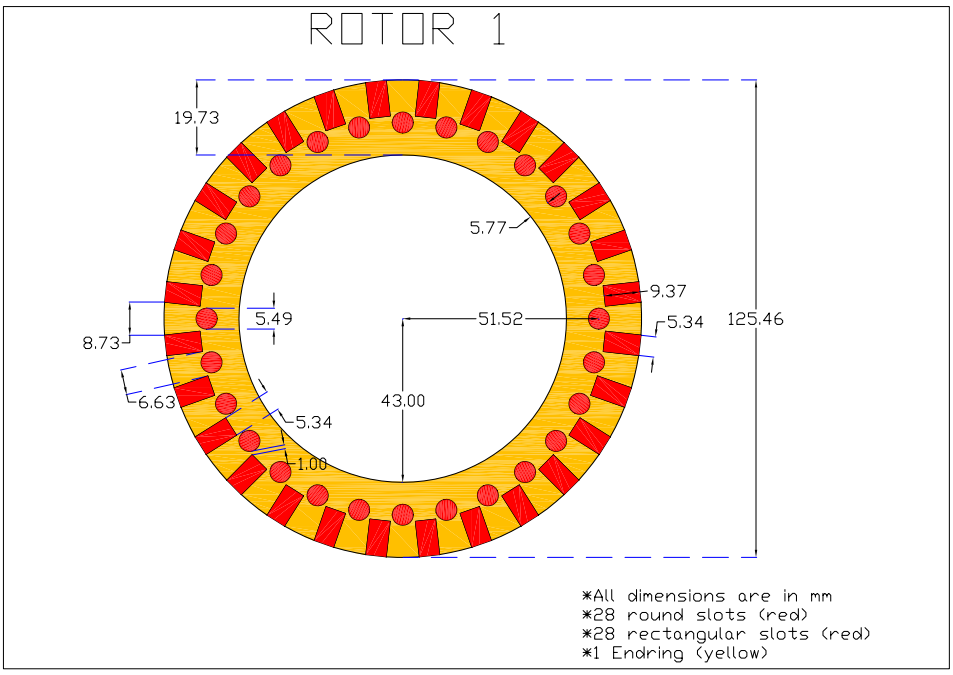

(a) Top view

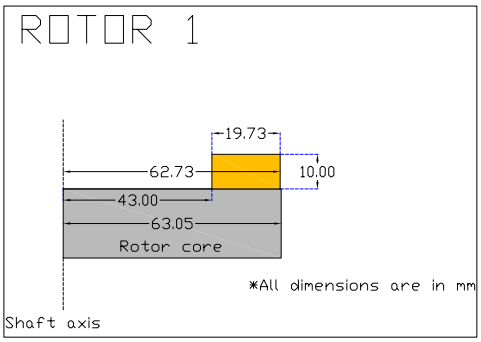

(b) Axial view

Figure E.3: Rotor 1 end-ring

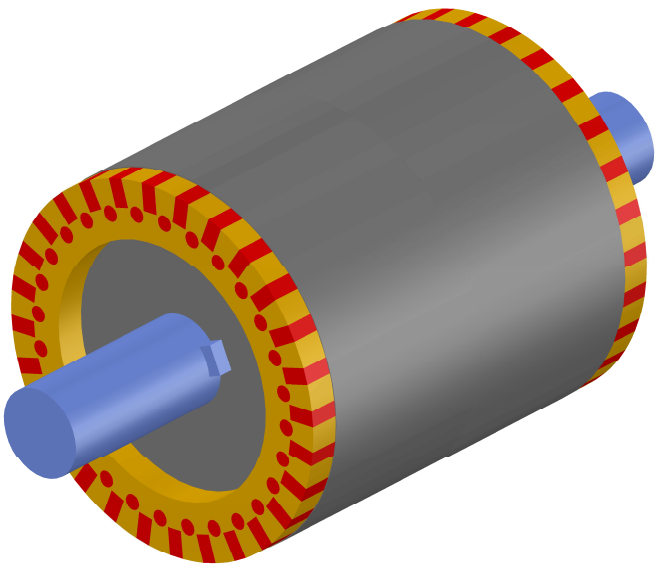

Figure E.4: 3D view of rotor 1

E.3 Rotor 2 – Canned Rotor

Table E.4 shows the data for rotor 2. This label corresponds to the canned rotor design. This rotor uses the same core laminations as the previous rotor but it includes a 1-mm copper can mounted on the surface of the rotor.

Table E.4: Rotor 2 data

Description	Value	Unit
Lamination material	Mild steel	-
Lamination thickness	2	mm
Number of slots	28	-
Core length	130	mm
Stacking factor	0.97	-
Airgap	0.45	mm
Skew	0	Rotor bars
Can thickness	1	mm
Can material	Copper	-
Conductor material	Copper	-
Shaft material	Carbon steel	-

Figure E.5 shows the detailed dimensions of the laminations for rotor 2. This rotor has been also modified with the same dimensions for the shaft and square key way so that one shaft can be used for both rotors.

Figure E.6 presents the dimensions of the copper end-ring for the canned rotor. The plan view shows the end-ring after soldering the rotor bars, only one rectangular rotor bar is displayed. Figure E.7 presents the 3D view of the rotor including the 1-mm copper can on the rotor surface in brown.

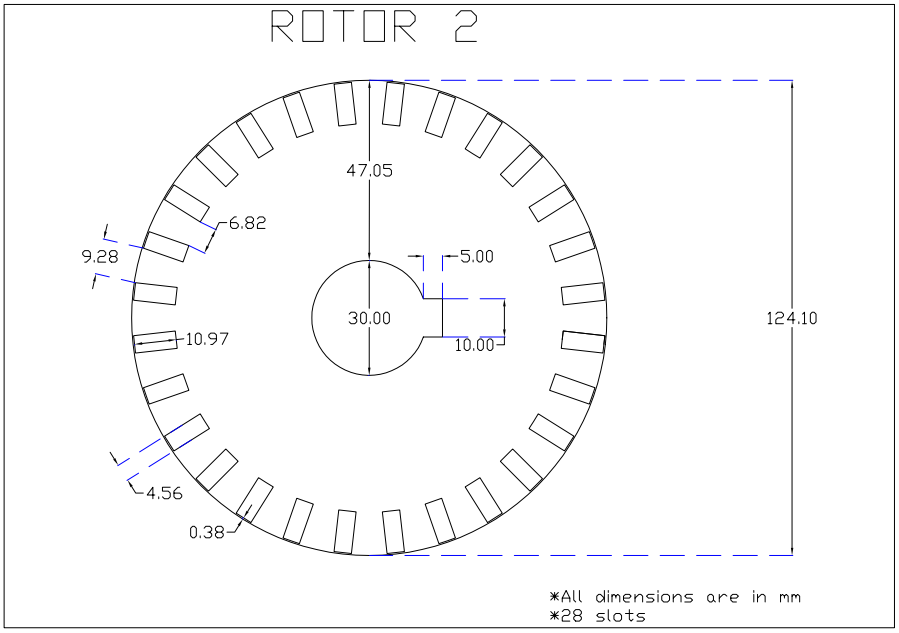

(a) Full view

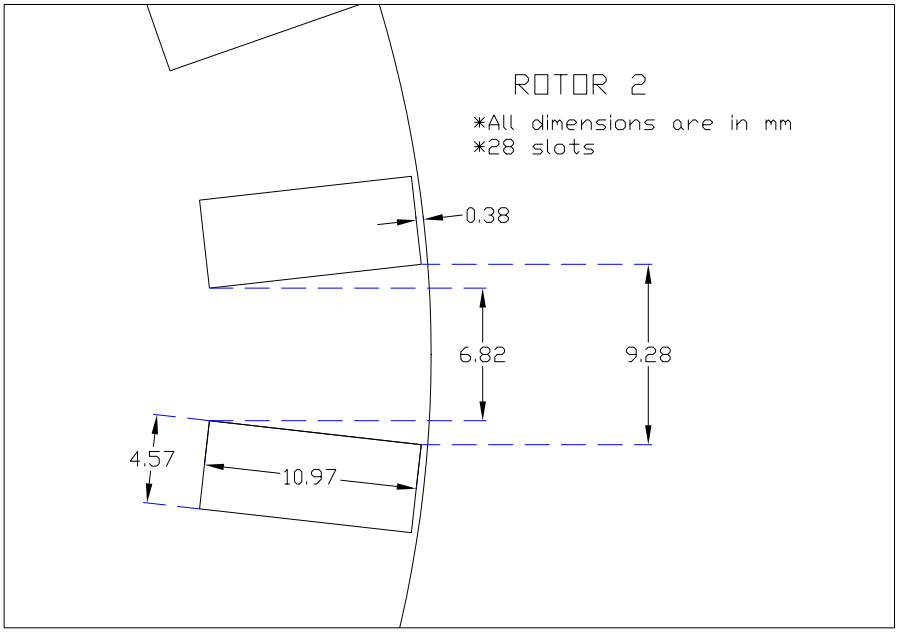

(b) Slots view

Figure E.5: Rotor 2 laminations

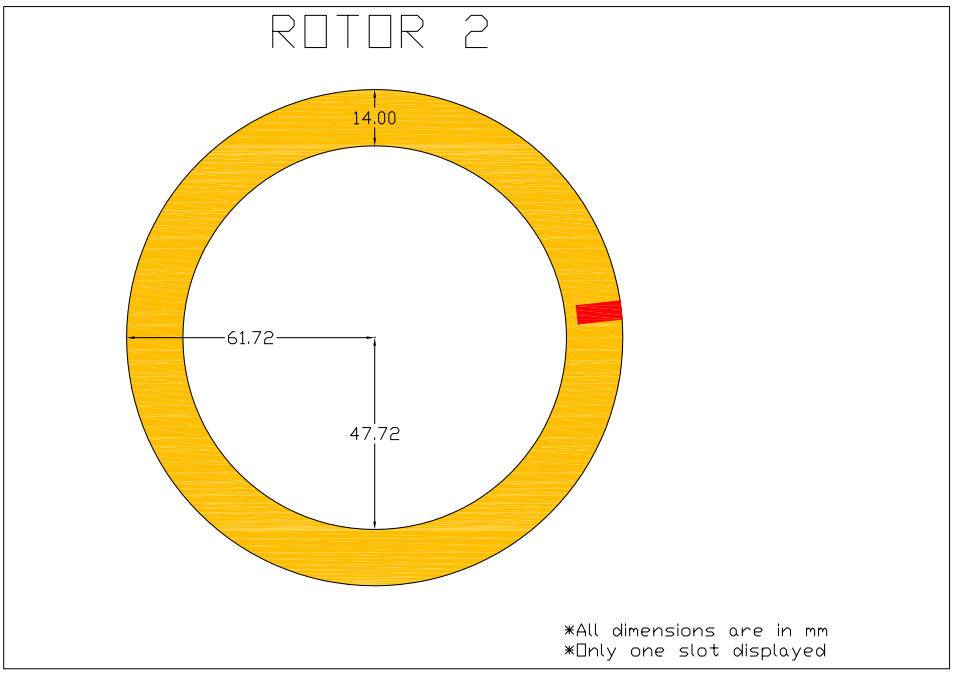

(a) Top view

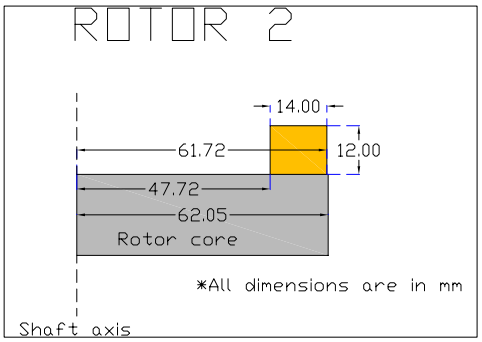

(b) Axial view

Figure E.6: Rotor 2 end-ring

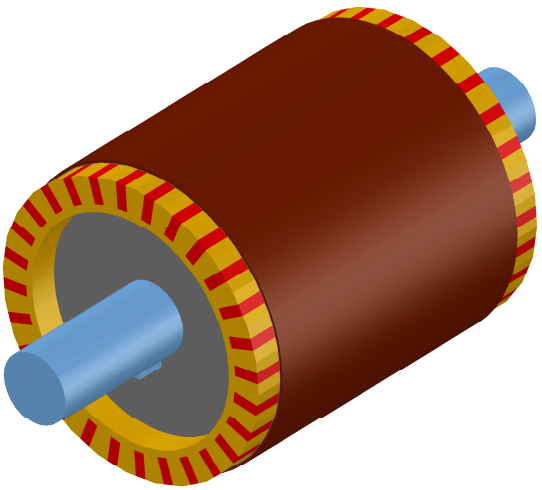

Figure E.7: 3D view of rotor 2

APPENDIX

F

PUBLICATIONS

During this research the following paper has been accepted to be presented at a conference:

- J. H. Ceron Guerrero, A. C. Smith, "Introduction to the Design of High Specific Torque Induction Motors for Electric Vehicles", 28 Reunion de Verano de Potencia, Aplicaciones Industriales y Exposicion Industrial, IEEE RVP-AI 2015, Mexico, July 19th-25th, 2015.